UNIVERSITY OF SOUTHAMPTON

AN ELECTROSTATIC MICRO ACTUATOR FOR ALIGNING AND TUNING AN OPTICAL CAVITY ON AN ATOM CHIP

by

Carsten Olaf Gollasch

A thesis submitted for the degree of

Doctor of Philosophy

FACULTY OF ENGINEERING, SCIENCE & MATHEMATICS

DEPARTMENT OF ELECTRONICS AND COMPUTER SCIENCE

November 2007

UNIVERSITY OF SOUTHAMPTON

ABSTRACT

FACULTY OF ENGINEERING, SCIENCE & MATHEMATICS

DEPARTMENT OF ELECTRONICS AND COMPUTER SCIENCE

Doctor of Philosophy

AN ELECTROSTATIC ACTUATOR FOR ALIGNING AND TUNING AN OPTICAL CAVITY ON AN ATOM CHIP

by Carsten Olaf Gollasch

In this thesis, a novel concept of a micro-optical and micro-actuated atom chip is presented. Atom chips are micro structured surfaces used for trapping, guiding and manipulating atom clouds. It is of greatest interest for physicists to integrate optical elements with atom chips for purposes of detection and quantum manipulation of cold atoms. In this work a nanopositioning system for an optical micro cavity on an atom chip has been designed. By combining optical micro mirrors, a fibre and an electrostatic comb drive actuator on wafer scale into one single chip a new generation of atom chip has been realized. The idea of an optical tunable micro cavity on an atom chip is original and has not been accomplished up-to-date.

Two inventive actuation design concepts have been investigated. First, a three-dimensional actuator utilizing the electrostatic force generated by four comb drives in *xy* direction and a parallel plate configuration in *z* direction to actuate a suspended mass. A micro mirror enclosed in the suspended mass and actuated in the wafer plane (*xy*) is used to align the optical cavity. The design incorporates a unique locking mechanism which allows the out of the wafer plane actuation to be carried out once the in the wafer plane alignment is completed. Secondly, a more simplified one-dimensional electrostatic comb drive actuator, which is only required to be actuated in the wafer plane in order to tune the optical micro cavity. Both non-standard actuators have been specifically designed and fabricated for atom chip applications. Their features and characteristics are novel and original in their design and function. The overall concept of the single chip solution is of high relevance for future atom chip experiments in the field of atom physics.

Analytical calculations and CoventorWare simulations have been carried out for both actuation designs to predict the physical behaviour of the actuation devices, including static deflections, spring constants and motion of accuracy. The fabrication of both actuation devices involved not only standard micromachining processes such as deep reactive ion etching, KOH etching, metal evaporation and anodic bonding of silicon wafers to pyrex wafers, but also involved extensive process development in order to realize high reflective atomically smooth sidewall mirrors and micro structures for fibre self-alignment. Lithography mask re-designs were necessary especially for the three-dimensional device structure due to its various lateral structure resolutions.

Contents

List of Figures

List of Tables

List of Symbols

a	-	length of small beam from the single serpentine beam element (3D actuator) $[m]$
A_L	-	total area of four electrodes of the locking mechanism for the 3D actuator $[m^2]$
A_z	-	area of one capacitor plate of the z actuation for the 3D actuator $[m^2]$
α	-	thermal expansion coefficient $[K^{-1}]$
b	-	length of large beam from the single serpentine beam element (3D actuator) $[m]$
C	-	capacity $[F]$
d	-	distance between two parallel plates $[m]$
δ_o	-	overlap between comb fingers $[m]$
δ_{max}	-	maximum stable linear deflection of the comb drive actuation for the 1D actuator $[m]$
$\delta_{max,d}$	-	maximum stable linear deflection of the comb drive actuation for the 1D actuator considering the axial stiffness upon deflection $[m]$
$\delta_{max,3D}$	-	maximum stable linear deflection of the comb drive actuation for the 3D actuator $[m]$
δ_x	-	deflection in x direction $[m]$
$\delta_{x,3D}$	-	maximum required deflection in x direction of the xy actuation for the 3D actuator $[m]$
δ_z	-	deflection in z direction $[m]$
E	-	elastic modulus of bulk silicon $[Nm^{-2}]$
E'	-	elastic modulus of beam material $[Nm^{-2}]$
E_j	-	electric field tensor $[Vm^{-1}]$
E_v	-	electric field between two parallel plates $[Vm^{-1}]$
ε_0	-	permittivity $[AsV^{-1}m^{-1}]$
ξ	-	spatial coordinate along the length of the single beam element $[m]$
ε_r	-	relative permittivity $[AsV^{-1}m^{-1}]$
f	-	fundamental resonance frequency $[Hz]$
f_{1D}	-	fundamental resonance frequency of 1D actuator $[Hz]$

f_{3D} - fundamental resonance frequency of 3D actuator [Hz]

$f_{o,1D}$ - fundamental resonance frequency of 1D actuator considering effective mass [Hz]

$f_{s,1D}$ - simulated fundamental resonance frequency of 1D actuator [Hz]

$F_{e,3D}$ - electrostatic actuation force of the xy actuation for the 3D actuator [N]

$F_{e,1D}$ - simluated maximum achievable electrostatic actuation force of the x actuation for the 1D actuator at 150 Volts [N]

F_g - force of gravitation [N]

$F_{c,1D}$ - theoretical maximum achievable electrostatic actuation force for the 1D actuator at 150 Volts [N]

$F_{c,3D}$ - electrostatic actuation force in the xy plane for the 3D actuator [N]

$F_{max,1D}$ - electrostatic actuation force for the maximum achievable translation of 20 μm [N]

$F_{min,1D}$ - electrostatic actuation force for the minimum required translation of 4 μm [N]

F_p - electrostatic force of the z actuation for the 3D actuator [N]

$F_{s,1D}$ - spring force for the 1D actuator [N]

F_x - force in x direction [N]

F_z - force in z direction [N]

g_1 - gap distance between the comb fingers of the 1D actuator [m]

g_2 - gap distance between the comb fingers of the 3D actuator [m]

g_3 - gap distance between the electrodes of the z actuation for the 3D actuator [m]

g_4 - gap distance between the electrodes of the locking mechanism for the 3D actuator [m]

g_a - gravitational acceleration [ms^{-2}]

g_v - gap between electrodes of z actuator after applying voltage (3D actuator) [m]

G - shear modulus [Pa]

h_1 - height of the comb structure for the 1D actuator [m]

h_2 - height of the comb structure for the 3D actuator [m]

h_s - height of silicon oxide stubs [m]

i - index of small beam element [1]

I_p - polar moment of inertia for the serpentine spring (3D actuator) [m^4]

I_x - moment of inertia in x direction of the small and large beam for the serpentine spring (3D actuator) [m^4]

I_z - moment of inertia in z direction of the small and large beam for the serpentine spring (3D actuator) [m^4]

$I_{z,1D}$ - moment of inertia in z direction of one suspension beam (1D actuator) [m^4]

I'_z - moment of inertia in z direction of beam cross section [m^4]

$I_{b,x}$ - moment of inertia in x direction of the single beam for the 3D actuator [m^4]

$I_{b,z}$ - moment of inertia in z direction of the single beam for the 3D actuator [m^4]

$I_{s,x}$ - moment of inertia in x direction of the double folded spring suspension beam for the 3D actuator [m^4]

$I_{s,z}$ - moment of inertia in z direction of the double folded spring suspension beam for the 3D actuator [m^4]

j - index of large beam element [1]

J - torsion constant [m^4]

k - spring constant [N/m]

k'_y - first elastic spring constant in y direction for the 1D actuator [N/m]

$k'_{y,3D}$ - first elastic spring constant in y direction for the 3D actuator [N/m]

$k''_{y,3D}$ - second elastic spring constant in y direction for the 3D actuator [N/m]

k''_y - second elastic spring constant in y direction for the 1D actuator [N/m]

$k_{b,y}$ - spring constant in y direction of the single beam suspension of the 3D actuator [N/m]

$k_{b,z}$ - spring constant in z direction of the single beam suspension for the 3D actuator [N/m]

$k_{b,z,tot}$ - total spring constant in z direction of the locking mechanism for the 3D actuator [N/m]

$k_{m,z}$ - spring constant in z direction of the z actuation (3D actuator) [N/m]

$k_{s,y}$ - spring constant in y direction of the double folded spring suspension for the 3D actuator [N/m]

$k_{s,z}$ - spring constant in z direction of the double folded spring suspension for the 3D actuator [N/m]

$k_{tot,y}$ - total spring constant in y direction of the xy actuation (3D actuator) [N/m]

$k_{tot,z}$ - total spring constant in z direction of the xy actuation (3D actuator) [N/m]

k_{ij} - tensor of the converse piezoelectric coefficients [9]

k_x - total spring constant in x direction of the spring suspension for the 1D actuator [N/m]

$k_{x,3D}$ - total spring constant in x direction of the spring suspension for the 3D actuator [N/m]

k_y - effective spring constant in y direction of spring suspension (1D actuator) [N/m]

$k_{y,3D}$ - total spring constant in y direction of the spring suspension for 3D actuator [N/m]

$k_{y,beam}$ - spring constant in y direction of one beam spring element (1D actuator) [N/m]

$k_{y,d}$ - total spring constant in y direction considering axial stiffness upon deflection (1D actuator) [N/m]

k_z - spring constant in z direction [N/m]

KE_{max} - maximum kinetic energy [J]

KE_s - maximum kinetic energy of shuttle [J]

KE_t - maximum kinetic energy of trusses [J]

KE_b - maximum kinetic energy of beams [J]

$KE_{[AB]}$ - kinetic energy of beam segment AB [J]

$KE_{[CD]}$ - kinetic energy of beam segment CD [J]

$KE_{[EF]}$ - kinetic energy of beam segment EF [J]
$KE_{[GH]}$ - kinetic energy of beam segment GH [J]
λ - wavelength of laser [m]
l - length of parallel plate [m]
l' - length of one beam segment [m]
l_1 - beam length of double-folded spring suspension for the 1D actuator [m]
l_2 - beam length of double folded spring suspension for the 3D actuator [m]
l_3 - beam length of center frame suspension for the 3D actuator [m]
l_F - length of comb fingers for 1D actuator [m]
l_s - length of polysilicon plate [m]
l_s' - length of polysilicon plate attached to the insulator [m]
L - separation length between two mirrors of the optical cavity [m]
ΔL_R - length change between two resonance modes of the intensity spectrum [m]
L_f - initial length of solid material before temperature change [m]
L_f - final length of solid material after temperature change [m]
δL_R - full width at half maximum of a resonance [m]
L_c - optical cavity translation [m]
L_0 - length of material [m]
M - mass [kg]
M_2 - movable structure mass of the xy actuation for the 3D actuator [kg]
M_b - mass of beam [kg]
M_{eff} - effective mass [kg]
M_s - mass of shuttle [kg]
M_t - mass of truss [kg]
$M_{[AB]}$ - mass of beam segment AB [kg]
$M_{[CD]}$ - mass of beam segment CD [kg]
$M_{[EF]}$ - mass of beam segment EF [kg]
$M_{[GH]}$ - mass of beam segment GH [kg]
M_o - external bending moment [Nm]
$M_{a,i}$ - moment of the ith connector from the small beam segment of the single serpentine beam element (3D actuator) [Nm]
$M_{b,j}$ - moment of the ith connector from the large beam segment of the single serpentine beam element (3D actuator) [Nm]
m - constant [1]
m_1 - magnitude of vetor [m]
n - number of single beam elements [1]
N_1 - number of comb fingers for the 1D actuator [1]
N_2 - number of comb fingers for the 3D actuator [1]
PE_{max} - maximum potential energy [J]
ν - poisson's ratio for silicon [1]
ϕ_0 - angle of rotation from bending moment [°]

Q - charge on capacitor [C]
ρ - mass density of bulk silicon [kg/m^3]
S_i - mechanical strain [9]
$T1$ - truss number one of double folded spring [1]
$T2$ - truss number two of double folded spring [1]
$T3$ - truss number three of double folded spring [1]
T_o - external torsion [Nm]
$T_{a,i}$ - torsion of the ith connector from small beam segment of the single serpentine beam element (3D actuator) [Nm]
$T_{b,j}$ - torsion of the ith connector from large beam segment of the single serpentine beam element (3D actuator) [Nm]
ΔT - temperature difference [K]
U - energy of the one entire serpentine spring [J]
v_s - maximum velocity of shuttle [m/s]
v_t - maximum velocity of trusses [m/s]
v_{t1} - velocity of truss number one T1 [m/s]
v_{t2} - velocity of truss number two T2 [m/s]
v_{t3} - velocity of truss number three T3 [m/s]
v_b - maximum velocity of beams [m/s]
V - voltage [V]
V_1 - maximum actuation voltage for the 1D actuator [V]
V_2 - maximum actuation voltage in the xy plane for the 3D actuator [V]
V_3 - volume of the xy actuation structure for the 3D actuator [m^3]
V_4 - actuation voltage of the z actuation for the 3D actuator [V]
$V_{L,pi}$ - pull-in voltage of the locking mechanism for the 3D actuator [V]
$V_{min,1D}$ - voltage for the minimum required translation of 4 μm [V]
$V_{min,xy}$ - voltage for the minimum required translation of 5 μm [V]
$V_{max,xy}$ - voltage for the maximum achievable translation of 15 μm [V]
$V_{max,1D}$ - voltage for the maximum achievable translation of 20 μm [V]
$V_{z,pi}$ - pull-in voltage of the z actuation for 3D actuator [V]
V_s - volume of shuttle [m^3]
V_t - volume of truss [m^3]
V_b - volume of beam [m^3]
w - width of beam for xyz-actuator (Design A) [m]
w_1 - width of beam of the spring suspension for the 1D actuator [m]
w_2 - width of beam of the suspensions for the 3D actuator [m]
w_3 - width of beam of the serpentine spring suspensions for the 3D actuator [m]
w_F - width of comb fingers for 1D actuator [m]
w_p - width of parallel plate [m]
W - potential energy [Ws]
ω - angular velocity

x	-	spatial coordinate [m]
Δx_s	-	step size of scratch drive actuator [m]
y	-	spatial coordinate [m]
ψ_0	-	angle of rotation from torsion moment [°]
z	-	spatial coordinate [m]
z_1	-	displacement in z direction of the xy actuation structure for the 3D actuator [m]

Chapter 1

Introduction

1.1 Background

Micro Technology - since it's first appearance in the 1960's - has been of immense interest to the IC Industry and Research Centres around the world. Realising the potential of applying existing batch fabrication processes in combination with silicon micromachining, Micro Technology also generally referred as MEMS (MicroElectroMechnical Systems) or MST (MicroSystemTechnology), is anticipated to undergo an evolution similar to the IC Technology. The cost effective mass production of Micro Technology devices is a key parameter for success in our faster than ever changing high-tech world of business.

Especially in the past two decades Micro Technology has become more and more dominant because noticeable advances in the technology and development of infrastructure occurred. As a result today Micro Technology devices can be found in nearly all automobiles as sensors e.g. accelerometers and gyroscopes for Airbags, Anti-Lock Braking Systems (ABS), Traction Control (ASR) or Electronic Stability Program (ESP). But not only sensors, also actuators have stepped up the ladder, ready for mass production and commercially available to Industry and end consumer. In particular the Telecommunication Industry and companies like LG Electronics or Lucent Technology already marketed successfully MEMS actuators. For example, the MEMS Variable Optical Attenuator (VOA) from LG Electronics [1] - a micro-actuated optical fibre switch.

Since the beginning of the Micro Technology era it has always been of great interest to researchers combining and integrating Micro Technology with other potential application areas. As a result of this effort MicroOptoElectroMechanical Systems (MOEMS) arose, as well as Bio-MEMS and Nanotechnology. Specifically MOEMS derive their functionality from the miniaturization of optics, electronics and mechanics. The combination of micromachining and optics allows a size reduction of optical elements on a wafer scale, as well as the motion of

optical elements in association with micromachined actuation elements.

Uniting MOEMS and atomic physics together is yet another very promising research field. Since Nobel prizes in physics were awarded to Cohen-Tannoudji, Chu, and Phillips in 1997 for laser cooling and trapping of atoms and to Ketterle, Cornell, and Wieman in 2001 for Bose-Einstein condensation (BEC) in dilute alkali gases, atomic physics manipulating neutral atoms has rapidly developed. A BEC can be generated on a surface of a so called "atom chip" - a microfabricated structure. Magnetic potentials created by microscopic wire structures on this surface have been used by various research groups to realize several atom optical elements such as atom traps, guides, beam splitters, mirrors and interferometers [2]. A more detailed review of "atom chips" and their application is given in chapter 2 [3],[4]. These devices fabricated by very non-standard MEMS processes will become a new tool box leading to new insights into the foundations of quantum theory and quantum information processing (QIP) on a chip [5],[6]. Atom chips are particularly attractive because trapped neutral atoms can have a long coherence times. Hence, the interaction between atoms and MEMS structures is advantageous. In addition, this technology is attractive because it appears to be robust and scalable.

1.2 Atom Chips and Their Link to MOEMS

Over the last 10 years atomic physics, particularly the field of cold atoms has continuously gained momentum in the world of research. Making use of the physical characteristic of neutral atoms, once they have been cooled down to μK temperatures their de Broglie wave nature becomes evident, cold atoms can be controlled and manipulated by atom optical elements such as mirrors, wave guides and beam splitters. Especially in an optical cavity it is possible to exchange quantum information between a single neutral atom and a photon [7],[8],[9],[10]. Optical cavities that can be integrated into atom chips hold therefore a great promise for scalabe quantum computing in the future. It is anticipated that with currently available MOEMS fabrication techniques the development of such atom-cavity systems is possible.

The ultimate goal of researchers is the incorporation of such optical cavities, wave guides, atom traps and guides into one single atom chip. One interesting approach is pursued by our group at the University of Southampton in the Electronics and Computer Science Department in collaboration with a cold atom physics group at the University of Imperial College in London - a new generation of atom chip with integrated micro-optical and micro-actuated elements combined with micro-fabricated wires packaged to a single atom chip and fabricated at wafer scale. The core of the atom chip is an integrated nanopositioning system, including a micromachined multi-dimensional actuation device, optical micro-mirrors and laser light, capable detecting and characterizing atom clouds as well as single atoms. Atom clouds guided by current carrying micro wires are exposed to laser light which is trapped in the optical cavity between the two opposing micro-mirrors. The laser light is used as a read-out source and acts as a feedback channel in order to establish a stable optical cavity. Essential for

the functionality of the envisioned atom chip is the alignment and tunability of the optical micro cavity achieved by the multi-dimensional actuator.

The new generation of atom chip presented in this thesis is a major contribution in the field of atomic physics, not only because it combines all the features and elements requested by physicits into one single chip, but also because it is fabricated utilizing general available silicon bulk micromachinig techniques. This novel concept of the atom chip will reveal new information about quantum optics and will extensively contribute to the understanding of quantum physics in the future. It may bring the quantum computer a step closer.

1.3 Motivation and Main Achievements

The motivation of our research group is the realisation of the new generation of atom chip. Integrating micro actuated and micro optical elements into one single atom chip in the micron scale regime is a key requirement of researchers at the moment that has not been achieved yet. This thesis proposes a novel atom chip, which is based on micro fabrication and integrates a nanopositioning system for an optical tunable micro cavity on a micro structured atom chip. In the following chapters it is shown that it is technologically possible to fabricate the envisaged new generation of atom chips. In particular, a novel micro actuator for optical cavity tuning is presented. The successful outcome of this research project is determined by the following achievements:

- Designing and fabricating a micro actuator for aligning and tuning an optical micro cavity on an atom chip.
- Comparing the theoretical model of the actuator with experimental results of the tunable optical cavity system.

1.4 Thesis Organisation

Chapter 2 gives a literature review of atom chips and their applications. Several atom chip systems are described and details of their micro structured surfaces and their functionality are discussed. Also the field of micro-actuators is reviewed. Various actuation principles are outlined, in particular piezoelectric, thermal and electrostatic actuators are discussed. Furthermore, a variety of multi-dimensional actuators and their applications are presented.

In chapter 3, the novel concept of a new generation of atom chips packaged in a multi-layered chip is introduced. The working principle of a tunable optical cavity is explained, using the example of a three-dimensional and a one-dimensional actuator. The three-dimensional actuator design is based on the alignment of an optical cavity in the wafer plane and tunability in the out-of the wafer plane. The one-dimensional actuator is used for tuning the optical cavity in the wafer plane.

In chapter 4, a theoretical analysis of the multi-dimensional actuators for cavity alignment and tuning are illustrated. Both actuator designs are optimized using a simulation model in CoventorWare and verifying the motion behaviour of the actuation designs.

Due to the novelty and geometric complexity of the nanopositioning system, a significant amount of process development work was necessary to devise a fabrication process for the three- and one-dimensional actuator. The entire fabrication process for the 3D and 1D actuator are described in chapter 5. Also critical aspects of the fabrication process are addressed. A process for atomically smooth mirror sidewalls with gold sidewall deposition was developed. In order to release the actuator structure a process for deep reactive ion etching (DRIE) had to be derived. Also the masking layers for the DRIE were optimised for the three-dimensional actuator design.

Chapter 6 describes a test and measurement of the one-dimensional actuator. Only the optical cavity characteristics of the partically fabricated one-dimensional actuator was evaluated, because towards the end of the 3D and 1D actuator fabrication a fire at the university destroyed every actuation device fabricated up to that point.

Chapter 7 is the conclusion and gives an outlook on further work.

Chapter 2

Literature Review

2.1 Introduction

One interesting field of atomic physics explores the behaviour of clouds of cold atoms above surfaces on microchips. Such microchips, also called "atom chips", use micro structures to generate magnetic and electrostatic fields, that can be used to guide, trap and manipulate neutral atoms at room temperature on a chip surface. Since the discovery of Bose-Einstein Condensation (BEC) by M.H. Anderson and his research group [11] in 1995, physicists have been working with a tremendous effort on implementing surface micro structures on atom chip surfaces. As a result of this effort researches have already proven that with the technologies available in micro- and nanofabrication it is possible to develop atom chips, which are capable of guiding, trapping, detecting and manipulating atom clouds as well as single atoms. Even though atomic physics is still in its infancy, future atom chips will ultimately lay the foundation for quantum information processing (QIP) and quantum computing [12],[13],[14].

It is not the intention of chapter 2.2 to give a complete review of all atom chips ever described in the literature since the discovery of the BEC. Rather an overview of the most important atom chips is provided, which had an high impact in atomic physics and are relevant for this work. The overview focuses on the fabrication of the surface micro structures for atom chips as well as their applications. The summary of the atom chip literature review in chapter 2.3 indicates that with current technology it is possible to fully integrate a micro actuated tunable optical cavity onto an atom chip. Hence, chapter 2.4 gives a review of micro actuators and their applications.

2.2 Atom Chips

The creation of Bose-Einstein Condensation (BEC) in 1995 was achieved by cooling and magnetically trapping neutral atoms. A so called "magneto-optical trap" (MOT) slows and cools down atoms to microklevin temperatures by lasers and traps them by magnetic fields generated from macroscopic coils [15]. Also in 1995 an ingenious publication by Weinstein and Libbrecht [16] laid the foundation for microscopic structures that can be utilized to magnetically trap neutral atoms. Although macroscopic coils are still used in magneto-optical traps today the idea of generating magnetic fields from microstructured surfaces in order to trap and guide atoms is the focus of research ever since. Before 1999 magnetic traps and guides for neutral atoms have been solely realized with thin, freestanding wires with a thickness between 50 μm and 100 μm [17],[18]. Proving that microstructured surfaces can be used for trapping and guiding neutral atoms two research groups from Austria and Germany raced neck to neck until late 1999. In October 1999 the research group from Haensel et al. succeeded and published their work on manipulation of neutral atoms using the magnetic field of microfabricated current-carrying conductors [19]. By applying microfabrication processes such as photolithography and electroplating they demonstrated an "atomic motor" using a wire structure as shown in figure 2-1. The "atomic motor" is capable of trapping and guiding neutral atoms. The microstructured wires are 2 cm in length with a minimum cross section of 3 by 3 μm. The electroplated gold wires are fabricated on a aluminium oxide substrate and sustain more than 2A.

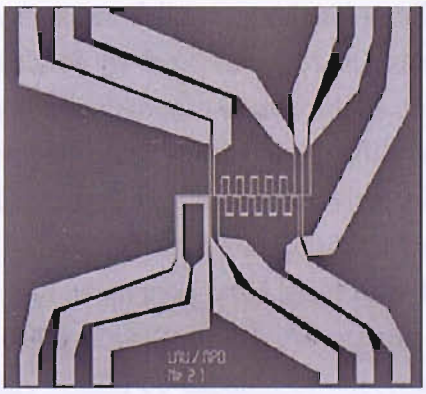

Figure 2-1: Microscope picture showing the wire layout (2 x 2 cm) of the "atomic motor". The larger gold areas extending to the edges are used to feed the system with current. The meander in the middle of the device is the actual "atomic motor" [19].

Following in 2000 the second research group from Austria with Folman et al. succeeded as well and published their work with the title "Controlling Cold Atoms using Nanofabricated Surfaces: Atom Chips" [20]. Even though they lost the race, they were the first naming such microstructured surfaces "atom chips". Since then the synonym "atom chip(s)" is used around the world for this kind of surface structured chips. Figure 2-2 is showing the mounted atom

chip from the Austrian research group with a size of 2 x 2 cm before it is introduced into the vacuum chamber. The chip is made of a 2.5 μm gold layer patterned using microlithography on a 600 μm GaAs substrate creating 10 μm U-shaped gold wires, which withstand also a maximum current of 2A.

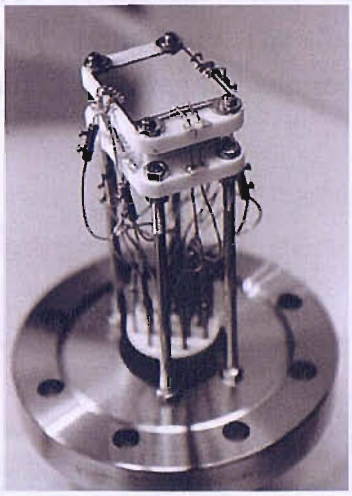

Figure 2-2: Mounted "atom chip", ready to be put into the vacuum chamber. At the top is the microstructured chip with wires attached at the edges in order to drive current through the device during the experiments [20].

Both research groups have successfully trapped and guided cold atoms and showed that with current microfabrication technology the concept of an atom chip clearly works. Researchers were encouraged by the results and soon had new ideas of utilizing such microstructured wires. One idea is a microfabricated beam splitter for guiding atoms using microscopic magnetic guides on an atom chip [21],[22],[23]. Current carrying micro wires on a chip surface are fabricated in a Y-shape which are able to split and combine clouds of atoms. One promising application of such a system would be an integrated atom interferometer on a chip as proposed by several research groups in 2001 [24],[25],[26]. An atomic gyroscope developed by such atomic interferometry technology would be capable of unprecedented sensitivity of a ten billionth of the Earth's rotation rate. Although this goal has not been achieved yet, Wang et al. demonstrated in 2004 the first on-chip atom Michelson interferometer employing a Bose-Einstein condensate (BEC) [27]. The atom chip contains lithographically patterned wires on an aluminium substrate and a pair of reflective prism-shaped mirrors, as shown in figure 2-3. The wires generate the magnetic fields on the atom chip surface enabling a cloud of ^{87}Rb atoms to be guided into the trapping region between the two prism. A linearly polarized laser beam is reflected by the inward-facing surfaces of the two prism, which are mirror-coated and aligned within 2 degrees, producing standing waves and allowing the observation of atom interference on the chip surface.

Trapping and guiding atoms with microstructured wires on a chip is not the only method researchers investigate. For example, trapping cold atoms on magnetic films such as video-tapes [28] and hard drive disc [29] have also been successfully demonstrated. Also, electro-static fields can be used in order to trap and manipulate neutral atoms. Krueger et al. demonstrated a novel type of three-dimensional trap, which was formed by modulating a magnetic guide using electrostatic fields. The electrostatic fields were produced by charging a set of electrodes distributed along current carrying wires. The electrodes and wires have been fabricated on silicon substrates with micromachining techniques [30].

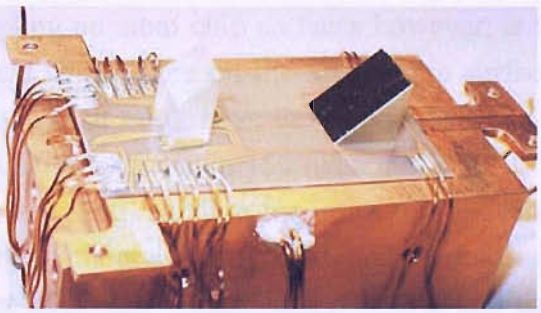

Figure 2-3: A photo image of the 5 cm by 2 cm atom chip glued onto a copper holder. The two cubes on top on the chip surface are the prism mirrors [27].

One major interest in the research of atomic physics is the integration of micro optical elements on atom chips for purposes of detection as well as trapping. Since Birkl et al. proposed the development of miniaturized and integrated atom optical devices in 2001 researchers focused on this new direction of atom optics. Birkl's new approach arises from the application of one- or two-dimensional arrays of spherical microfabricated lenses for atom trapping [31]. It was conceivable that state-of-the art micro- and nanofabrication techniques can be utilized to create versatile and integrated atom optical devices within atom chips. Thus, researchers started developing micro optical elements on atom chips allowing them to detect and manipulate atom clouds as well as single atoms.

A good example of integration of optical elements has already been shown in figure 2-3. However, the optical mirrors illustrated in the interferometric atom chip (see picture above) are around 1 cm in size forming a relatively large and bulky optical cavity making an integration on chip level in the micron scale regime impossible. The design also lacks the ability of tuning the cavity into resonance, because the mirrors are fixed to the surface. Recently two research groups, Teper et al. [32] and Haase et al. [33], presented tunable Fabry-Perot (FP) cavities with superpolished, concave mirrors suitable for atom detection. The mirrors for both designs are up to 1 cm in diameter with a cavity length between 10 to 30 mm and mounted on a piezoelectric stage actuator. The tunable cavity system is then positioned above the atom chip on which the

atoms are magnetically trapped and guided into the optical cavity. However, the macroscopic structure of the optical cavities remains, making them incompatible with the microscopic atom chip.

An alternative method of forming an optical cavity is by using two fibre-tip ends of an optical fibre which act as mirrors. The idea of using optical fibres for atom detection was introduced in 2003 by Horak et. al. [34]. In 2004, Quinto-Su et al. presented the first on-chip optical detection of laser cooled atoms [35] using two solid core optical fibres chemically bonded onto a microfabricated atom chip. By coupling laser light from the "source" fibre into the "detection" fibre they were able to detect ~10^5 atoms. One of the biggest difficulties of using optical fibres for atom-cavity coupling on atom chip surfaces however, is the accuracy of alignment during the mounting process of the fibre on the actual chip surface. Facing the problem of accurate fibre alignment Wilzbach et al. have developed a precise lithographic method that allows robust positioning of fibres to within 150 nanometres [36]. The high accuracy allows very reliable fibre-to-fibre coupling, suitable for integration of fibre cavities. The fibre are mounted on the atom chip by lithographically patterned photoresist called SU-8. SU-8 is an epoxy based negative resist with high mechanical, chemical and thermal stability. The SU-8 structures, as shown in figure 2-4a, align and fix the optical fibre cavity in between two 125 μm thick and 6000 μm long fibres. Figure 2.4b represents a layout of the cross section of the fibre in the SU-8 structure.

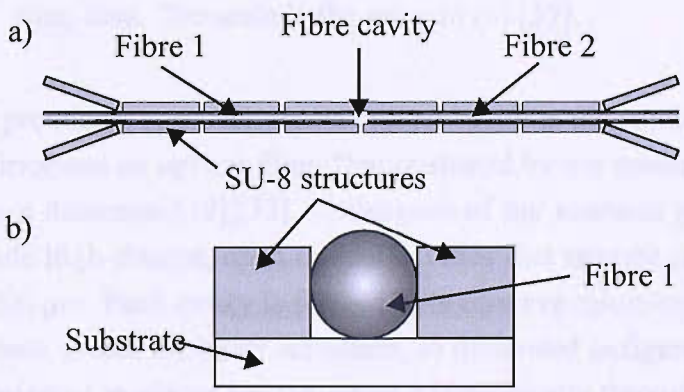

Figure 2-4: Schematic layout of the SU-8 photoresist structure along with the optical fibre cavity [36].

Addressing the same problem our research group at Southampton University fabricated v-grooves into a silicon substrate, which establishes good mechanical stability and alignment of the fibres on the atom chip. The v-grooves are wet-etched; near the centre, where the fibres come to within a few tens of micrometers of one another, the groove become narrower to support the tapered fibre ends as shown in figure 2-5 [37].

Stabilizing and aligning optical fibres by introducing mechanical structures on an atom chip is viable, nevertheless addressing the tunability of such a system is yet another challenge. So far only Steinmetz and his research group tackled the problem and presented at the end of 2006 a fibre-based tunable Fabry-Perot cavity [38]. Even though they have managed to align and tune two fibres forming a Fabry-Perot cavity capable of detecting less than 50 neutral atoms at a temperature of 70 μK, one major drawback of the system is, that the cavity tuning is achieved by gluing each fibre onto a piezoelectric actuator. Again, the macroscopic dimensions of the piezos do not match the microscopic scale of the atom chip.

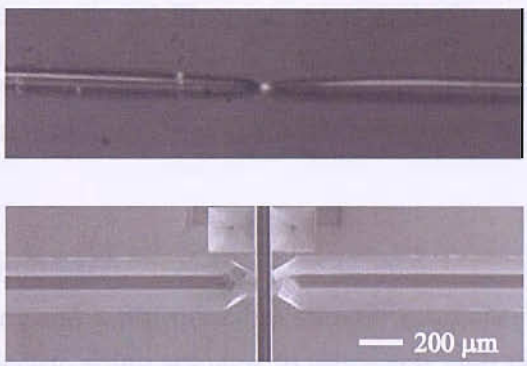

Figure 2-5: Tapered optical fibres. (a) microscope image of two opposing fibres with propagating laser light between them. (c) SEM micrograph of silicon v-grooves for mounting fibres in an atom chip. The scale is the same in (b) [37].

Another very promising approach for an optical cavity is the combination of a microfabricated spherical mirror and an optical fibre. Demonstrated by our research group this setup is also suitable for atom detection [39],[37]. Colleagues of my research group at Southampton University have made high-finesse, open optical cavities that operate in length at a range of approximately 20-200 μm. Each cavity is formed by a concave micro-mirror and the plane tip of an optical fibre, both coated for better reflection, as illustrated in figure 2-6a. Arrays of concave mirrors are fabricated in silicon by wet-etching isotropically through circular apertures in a lithography mask using a mixture of HF and HNO_3 in acetic acid. The etch bath in which the wafer is immersed undergoes continuous agitation during the etching process, resulting in

spherical surface profiles as shown in figure 2-6b.

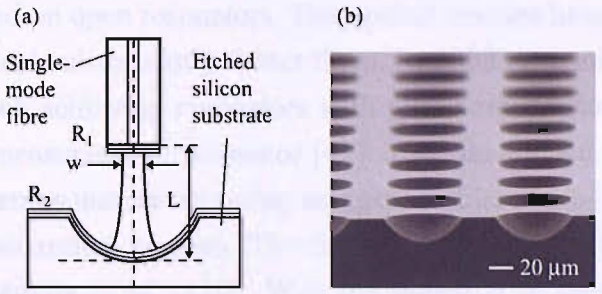

Figure 2-6: The optical microcavity. (a) Plano-concave optical microcavity. The plane mirror is formed on the fibre tip by applying a pull-off coating. The concave mirror is formed by sputtering gold onto the etched silicon wafer. (b) SEM micrograph of an array of isotropically etched spherical mirros on a silicon wafer [37],[39].

Depending on the etching parameters we have produced wafers with a range of mirror radii between 30 and 250 µm and a reproducible surface roughness of 5 nm. However, this setup also requires a piezoelectric stage actuator to align and tune the optical fibre above the silicon surface of the spherical micro-mirrors.

Recently, other members of our research group have shown that pyramidal micromirrors also can be used as a micro optical trap (MOT) suitable for integration into micro-optoelectro-mechanical systems (MOEMS) and atom chips [40]. The concave pyramids are created in the (100) surface of a silicon wafer by anisotropic etching with potassium hydroxide (KOH) into square opening of oxide, which were lithographically patterned and opened by a dry-etch process. Due to the nature of the crystallographic orientation of (100) silicon subtrate and the application of an anisotropic etchant pyramids are formed with pyramidal sidewalls, where the angle between opposing faces is 70.5°. The square pyramids have 30 µm sides corresponding to a perpendicular depth of 21.3 µm and are arranged in a square lattice with a pitch of 100 µm as shown in figure 2-7. For good mirror reflectivity a layer of sputtered gold is chosen, which increases the surface roughness to 3 nm rms.

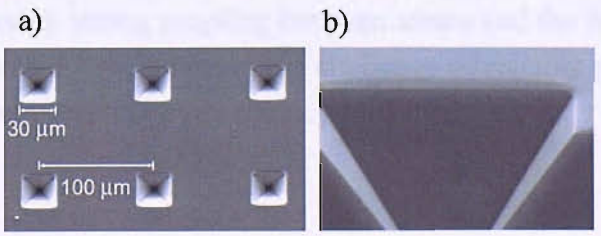

Figure 2-7: SEM micrographs of etched and gold coated pyramids. (a) Top view of pyramid array. (b) Cross-sectional view of a single pyramid [40].

One final method of creating an optical cavity (resonator) is presented below before concluding the review on atom chips. All the atom chips and their integrated optical cavities described so far are based on open resonators. The optical cavities have open access in order to guide atoms into them and subsequently detect them. In 2003 Armani et al. presented a completely different approach achieving resonators with Q factors in excess of 100 million - the highest Q factors ever measured in a resonator [41]. They developed a process for producing silica toroid-shaped microresonators-on-a-chip using a combination of lithography, dry etching and a selective CO_2 laser reflow process. The figure 2-8 shows this toroidal microresonator, which has an intrinsic cavity Q of $1x10^8$. With the potential of detecting single atoms, M. Rosenblit et al. demonstrated in 2004 that the whispering gallery mode (WGM) of such microdisk resonators can be used for optical detection of single atoms on atom chips [42]. WGM microcavities have unprecendented quality factors, but one major drawback of such WGM microcavities is that they are closed resonators. In order to use a WGM microcavity for atom detection, the atom must interact with the resonator mode of the microdisk. Since the resonator is a closed structure the intense part of the mode is localized inside the solid material of the resonator and only the weaker evanescent field outside the microdisk allows coupling to the resonator mode. The electromagnetic field outside the microdisk decays expontially with a decay constant of order $\lambda/2\pi$ [43].

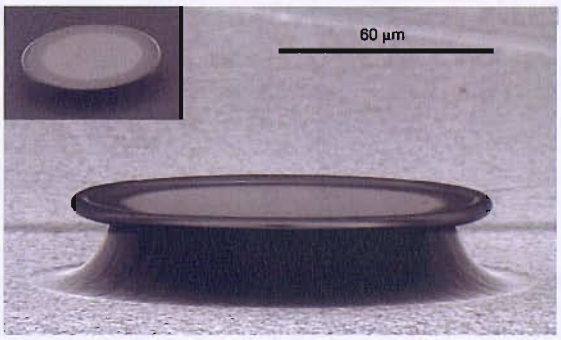

Figure 2-8: SEM micrograph of the toroidal microresonator [41].

As a result the atom requires to be positioned within a small fraction of a wavelength to the resonator surface to strongly interact with the resonator mode. At such a small distances the (attractive) van der Waals interaction between the atom and the resonator surface must be taken into account. Recently strong coupling between atoms and the field of a microdisk resonator has been demonstrated [44], however the challenge of reliably positioning single atoms in the evanescent field with the required accuracy remains.

Atom chips have undergone an intensive development in the past few years. Microstructures have been integrated on atom chip surfaces by applying micro- and nanofabrication technologies able to guide, trap, detect and manipulate several thousands of atoms down to individual atoms. Detecting atoms or even one single atom reliably with micro optical cavities is a key requirement for implementing quantum information on atom chips. The ability to detect single atoms with optical cavities has been demonstrated in the past [45],[46],[47], but only with large and macroscopic cavity systems unsuitable for microintegration. Cavity systems in general can be realized in many different ways, however the biggest challenge to date is the implementation of a tunable optical micro cavity that is small enough to be integrated onto surface structures of current atom chips. The scalability of such micro optical cavity systems remains still a problem, because the actuation systems of these tunable cavities are based on large macroscopic piezoelectric stage actuators. However, this thesis will show, that with current technology it is possible to build actuated optical cavities in the micron scale regime, which can be integrated onto atom chips. Actuators in MEMS offer a variety of micro actuation principles, which are known and well understood and transferable to atom chips. In the following a review is given about several actuation principles as well as micro actuators which might be suitable for integration on atom chips. Providing a micro actuated optical cavity system would be a major contribution in the research of atomic physics. Combined with batch microfabrication techniques and capable of detecting single atoms one could build entire arrays, that can be used for quantum information processing, which ultimately could lead to quantum computers.

2.3 Micro Actuators

Micro-Opto-Electro-Mechanical-Systems (MOEMS), in particular micro actuators integrated on micro structured atom chips, are very appealing for atomic physicists for many reasons. MOEMS are scalable and can be realized on chip surfaces in very small and confined areas. Also their potential of providing an open access architecture is certainly advantageous for guiding and trapping atoms. Especially the batch fabrication process of MOEMS is applicable to current existing micro structures on atom chips making a seamless integration viable.

Most actuators convert one form of energy, which can be electrical, chemical, thermal, magnetic or radiation energy, into mechanical work. In the macroscopic world typical examples of such mechanical actuators are combustion engines, electro motors and human muscles. Since the 1980s Micro Technology paved the way for actuators in the microscopic world. Nowadays advanced micro fabrication processes enable industry and researches to build actuators of sub-millimetre dimensions, commonly referred to as micro actuators.

The following literature review on micro actuators investigates actuators with emphasis on their fabrication and integration as well as their actuation principle. The intention is to find a practical actuation solution in order to realize a tunable optical cavity on an atom chip. First,

several actuation principles are discussed. Secondly, two-dimensional (2D) actuators and three-dimensional (3D) actuators and their applications are reviewed. The main focus is on electrostatic actuators and is limited to the field of linear actuators since they are the most relevant to the work presented here.

2.3.1 Actuation Principles

Piezoelectric Actuators

Piezoelectric actuators are solid state actuators (ceramics) that convert electrical energy directly into motion (mechanical energy) of extremely high resolution with a high force capability and short reaction times. Their major disadvantage is the relatively small movement in the order several nm/V. Piezoelectricity is a phenomenon that occurs in a certain class of anisotropic crystals subjected to mechanical deformation. When a mechanical pressure is applied to such materials, the crystalline structure produces a charge proportional to the strain. Conversely, when an electric field is applied to it, the crystalline structure changes shape, producing dimensional changes in the material. The effect was first discovered in single crystals such as quartz in 1880's by the Curie brothers. However, scientist discovered around 50 years later that polycrystalline materials, e.g. barium titanate could be made piezoelectric by application of an electric field; a process which is called poling. This led to the discovery of a number of piezoelectric ceramics, and the lead zirconate titanate (PZT) family, which are still the most widely used piezoelectric ceramics today. Also the piezoelectric material ZnO (zinc oxide) is commonly used, because it can be sputtered as a polycrystalline film very easily, whereas the ceramics barium titanate and PZT are more difficult to deposit as a film.

In general, a poled ceramic exhibits the direct and converse piezoelectric effects. Piezoelectric actuation is based in the converse piezoelectric effect. The converse effect can be defined as the deformation of the piezoceramic or as the strain on the material caused by the application of an external electric field. The electric field (tensor E_j) produces a mechanical strain S_i as given by [48],

$$S_i = k_{ij} E_j \tag{2.1}$$

where k_{ij} is the tensor of the converse piezoelectric coefficients.

Piezoelectric actuators can be divided in two groups. The first group achieves actuation by using only a single piezoelectric ceramic layer between two metal electrodes. For example, a piezoelectric actuated micropump as shown in figure 2-9. A voltage applied between the electrodes results in the deformation of the silicon membrane, which has the piezoelectric material fabricated on top, pumping liquid through the device [49],[50]. The major disadvantage of this technique is the limited displacement one can achieve using only one single piezoelectric ceramic layer.

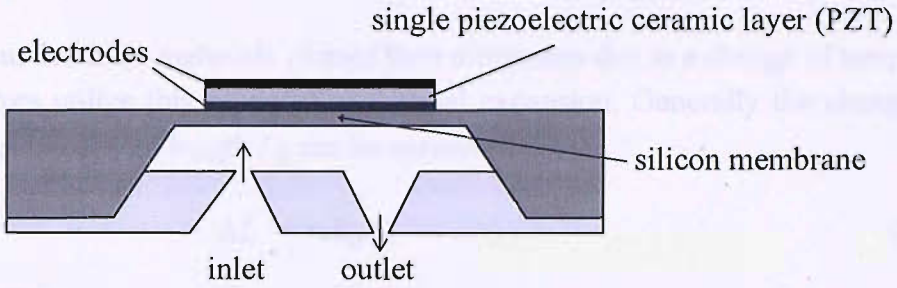

Figure 2-9: Piezoelectric actuated micropump [48].

The other group of piezoelectric actuators are fabricated as a stack or multi-layered actuator as shown in figure 2-10. Several piezoelectric ceramic layers are sandwiched between two metal electrodes and placed on top of each other. In this configuration the layers are mechanically stacked with a strain proportional to the number of layers or to the total thickness of the piezoelectric ceramic layers [51]. Generally the maximum actuation range is directly related to the number or overall thickness of the piezoelectric ceramic layers used. For example, a displacement of 5 μm can be achieved with a stack that is around 5 mm in thickness.

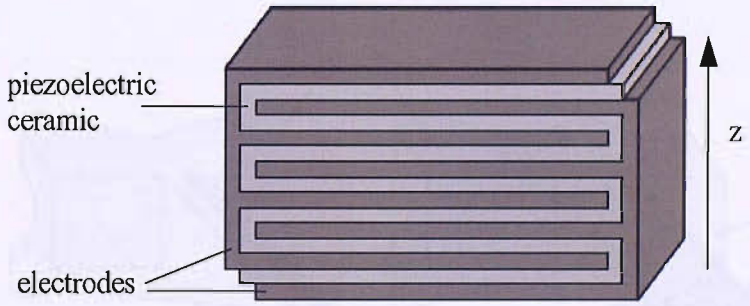

Figure 2-10: Piezoelectric multi-layered actuator [48].

The majority of applications for such multi-layered actuators are positioning systems, as used in atomic force microscopy (AFM) and scanning tunnelling microscopy (STM). Konishi et al. [52] fabricated a parallel linear actuator system providing a high accuracy (nm order) due to piezoactuation. However, the entire system is rather large in size (around 40 mm by 50 mm) because of an integrated multi-layer piezoactuator of approximately 10 mm in length. A more compact actuator using a smaller piezoelectric stack in combination with a linear inchworm actuator has been demonstrated recently by Yokokawa et. al and his research group [53]. The micro syringe pump presented is using a piezo stack element to drive a linear actuator with a minimum step displacement of 180 nm. In general, the rather large dimensions is a major drawback for actuation systems using piezoelectric stacks and makes them unsuitable for the integration along microstructures on wafer scale.

Thermal Actuators

It is well known, that most materials change their dimension due to a change of temperature. Thermal actuators utilize this property of thermal expansion. Generally the change in length ΔL of an object initially of length L_0 can be expressed by,

$$\Delta L = \alpha L_0 \Delta T \tag{2.2}$$

where α is the thermal expansion coefficient, which is specific for each material, and ΔT is the change in temperature. The thermal expansion coefficients of materials generally available for micromaching are in the range of $2 \cdot 10^{-6} K^{-1}$ to $25 \cdot 10^{-6} K^{-1}$. In order to obtain large displacements with thermal actuators practical implementations include amplification mechanisms. For bimorph or bimetallic actuators two materials are used which have different thermal expansions coefficients. Depending on their layer arrangement they are grouped in horizontal and vertical bimorph actuators as shown in figure 2.11. A horizontal bimetallic actuator [54] normally has a planar layer arrangement allowing actuation normal to the wafer plane only (z-direction). Applying this technique Mohamed et al. [55] demonstrated a maximum displacement of 5 µm at 5 Volts. A vertical bimetallic actuator as fabricated by Sehr et al. [56] has a direction of movement in the wafer plane (x and y direction) and with a 1000 µm long beam a displacement of about 4.5 µm is obtained at an input power of 3 mW.

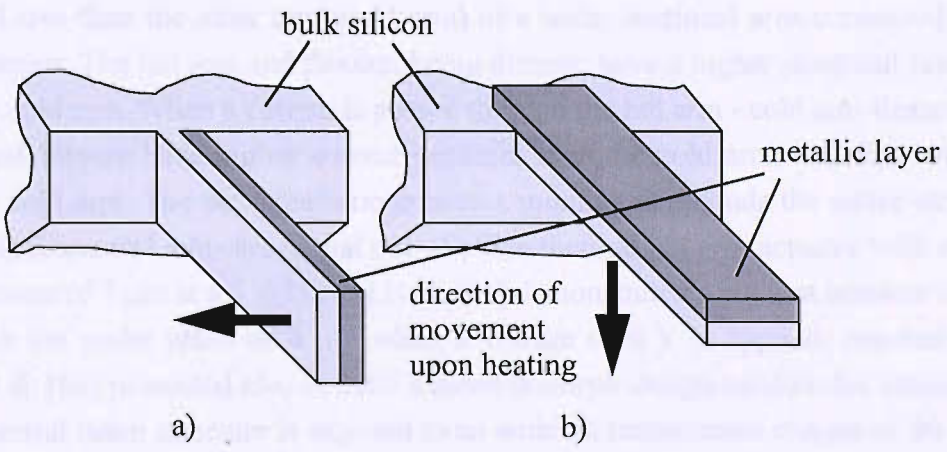

Figure 2-11: Vertical (a) and horizontal (b) bimorph actuator [55].

Thermal actuators, such as bent-beam actuators and hot arm actuators, fabricated only with one material can make use of constraints or asymmetrical design to amplify the movement. A bent-beam actuator as illustrated in figure 2-12a is a V-shaped beam anchored at two ends. Passing an electric current through thermal expansion caused by joule heating pushes the apex outward. The displacement of the apex in the wafer plane is a function of the beam dimensions and slope, and can be increased by cascading several actuators together as shown

in figure 2-12b.

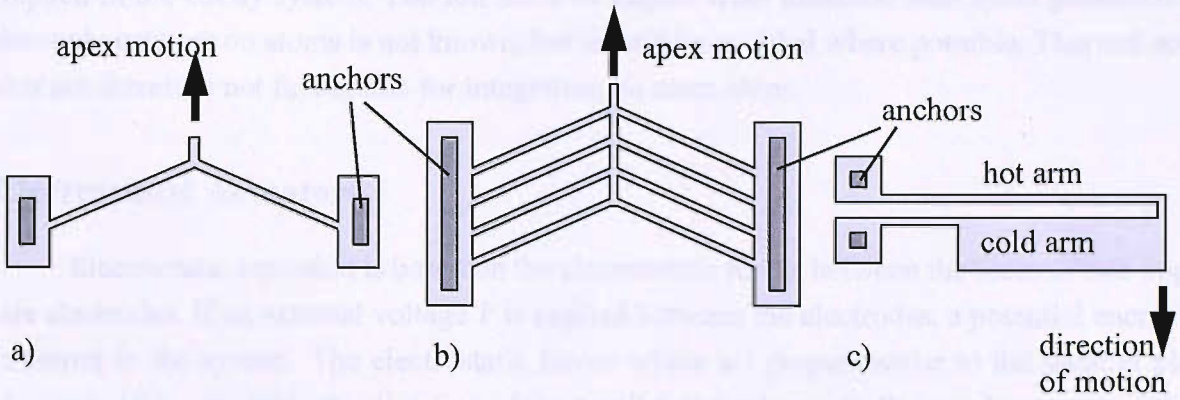

Figure 2-12: Bent-beam (a), cascaded bent-beam (b) and hot arm (c) thermal actuator.

Que et al. demonstrated cascaded bent-beam actuators [57] with a displacement of 6 μm and an input power of 220 mW at 13V. Similar work has been realized by Sinclair [58] with an array of bent-beam actuators achieving a deflection of up to 14 μm at a power consumption of 240 mW.

Also illustrated in figure 2.12c is a thermal hot arm actuator [59] which consist of asymmetric parallel arms connected at one end. One arm (hot arm) is long and thin with a smaller cross sectional area than the other arm (cold arm) of a wider sectional area connected with a shorter thin flexure. The hot arm and flexure, being thinner, have a higher electrical resistance than the wider cold arm. When a current is passed through the hot arm - cold arm flexure loop, the hot arm and flexure have higher current densities than the cold arm; and thus will heat more than the cold arm. The net expansion creates a moment that bends the entire structure. Chen et al. [60] fabricated a bi-directional out-of-plane thermal hot arm actuator with a maximum displacement of 7 μm at a 5 Volts. Lai et al. [61] demonstrated a hot arm actuator that has a translation in the wafer plane of 6 μm when a voltage of 6 V is applied. Another group around Lim et al. [62] presented also in 2005 a novel bimorph design suitable for actuation. A flip-over bimaterial beam structure is exposed to an ambient temperature change of 30 degree celsius resulting in a 5 μm translation of a mirror stage. Applications for bimorph actuators are for example 3D Micromirrors [63], RF-MEMS Inductors [64] or RF-MEMS tunable capacitors [65].

Micro thermal actuators offer several advantages compared to other actuation methods. They can produce a force output >100 μN at low voltages <30 V. They are also capable of relatively large displacements >10 μm in amplitude. However, the disadvantage of thermal actuators is that they require a greater amount of power in their operation, which is due to the energy loss from the heated elements to the surrounding interfaces such as air and substrate. Especially for atom chip integration the power dissipation is disadvantegous. It is antisipated that an increase in ambient temperature near the thermal actuation structure and in close proximity to

the actuated optical cavity will negatively affect the characteristics and behaviour of the atoms trapped in the cavity system. The full scale of impact from localised heat spots generated by thermal acutators on atoms is not known, but should be avoided where possible. Thermal actuator are therefore not favourable for integration on atom chips.

Electrostatic Actuators

Electrostatic actuation is based on the electrostatic forces between the faces of two opposite electrodes. If an external voltage V is applied between the electrodes, a potential energy W is stored in the system. The electrostatic forces which act perpendicular to the parallel plate electrode (F_z) and within the direction of the parallel plate electrode (F_x) can be represented by

$$F_z = -\frac{\partial W}{\partial d} = -\frac{1}{2}\varepsilon_r\varepsilon_o\frac{lw_pV^2}{d^2} \tag{2.3}$$

$$F_x = \frac{\partial W}{\partial x} = \frac{1}{2}\varepsilon_r\varepsilon_o\frac{w_pV^2}{d} \tag{2.4}$$

where ε_0 is the permittivity in vacuum, ε_r the relative permittivity, w_p the plate width, l the length of a plate and d the distance between the two plates as shown in figure 2-13. The equations above are derived on parallel plate capacitors neglecting the capacitances due to fringing fields.

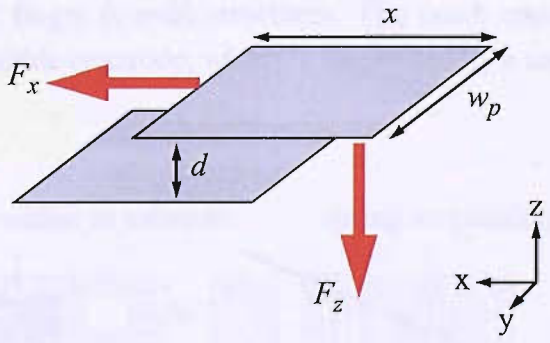

Figure 2-13: Parallel plate capacitor.

Since the force F_z perpendicular to the plates is proportional to the square of the gap distance, electrostatic forces turn out to be useful for micromachined applications where the electrode separation d is small in the order of microns. While the lateral force F_x is constant with respect to the displacement in the x direction, the vertical force F_z is highly nonlinear with respect to the displacement in z direction. A typical vertical motion parallel-plate electrostatic actuator is controlled by voltage sources and becomes instable when the displacement in z-direction exceeds 1/3 of initial distance d [66],[67]. Successful attempts have been demon-

strated by several groups in surpassing this 1/3 gap limitation by applying for example leverage and non-linear, stiffening springs [68] or using a feedback system controlling the voltage based on measured capacitance [69]. In 2006 Rocha et al. were able to demostrate a 90% gap travel range of a parallel plate electrostatic actuator using a dynamic voltage drive [70]. Yet, controlling the charge on parallel-plate actuators has been found to be practical as well [71]. Figure 2-14 shows an example of an application as parallel-plate electrostatic microgrippers [72].

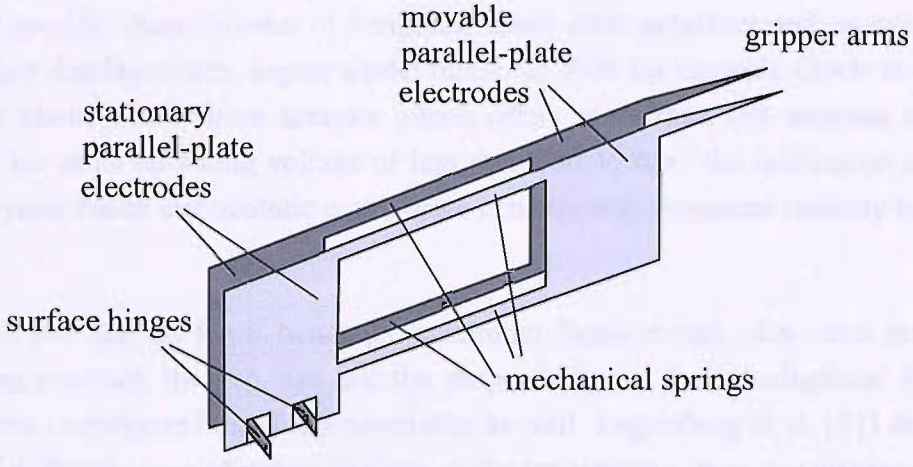

Figure 2-14: Parallel-plate electrostatic microgrippers [72].

Utilizing the constant lateral force F_x the first comb drive actuator was demonstrated in 1990 by W.C Tang [73]. A planar microstructure parallel to the substrate is driven electrostatically using interdigitated finger (comb) structures. The comb capacitor consists of a fixed comb electrode and a movable electrode, which is suspended by a spring as shown in figure 2-15.

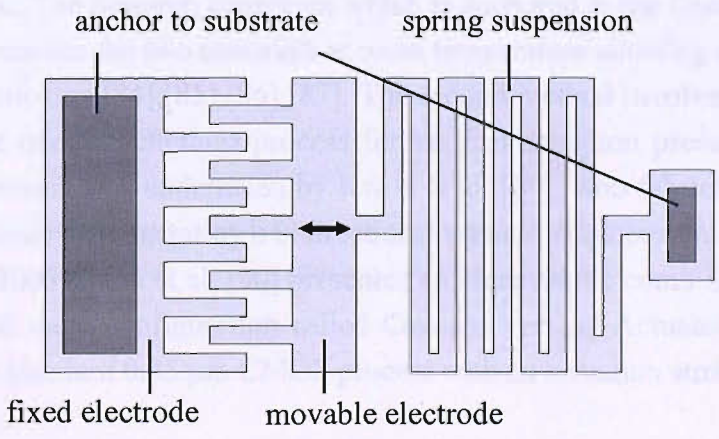

Figure 2-15: Comb drive actuator [73].

When a voltage is applied between the electrodes the movable element moves towards the fixed part of the comb drive actuator according to equation 2.3. Comb drive actuators have been fabricated from polysilicon by surface micromachining techniques [74],[75] and from single crystal silicon using Deep Reactive Ion Etching (DRIE) processes [76],[77],[78].

Since the first appearance of a comb drive in 1990 the main interest of research was focused on comb drive actuators with a horizontal motion in the wafer plane (*xy* direction). During the following years development efforts were made by various research groups to improve specific characteristics of horizontal comb drive actuators such as lower driving voltages, larger displacements, higher aspect ratios. In 2003 for example Grade et al. [79] demonstrated a planar comb drive actuator which offers more than 150 microns of displacement within 1 ms at an operating voltage of less than 150 V. Also the fabrication of a high aspect ratio polymer based electrostatic comb drive actuator was presented recently by Zhao and Cui [80].

The fact that the force, hence the maximum displacement, of a comb drive is related to the spring constant, the gap size and the shape design of the interdigitated finger structures researchers investigated these characteristics as well. Legtenberg et al. [81] demonstrated the effect of different types of spring designs on the maximum achievable displacement of a horizontal driven comb drive. Also the optimal shape design of an electrostatic comb drive was studied by Ye et al. [82] and submicron gap comb drive microactuators were successfully fabricated by Hirano et al. [83].

Besides horizontal driven comb drives a number of comb drive actuators can be found in the literature which allow a vertical motion in *z* direction out of the wafer plane. In order to displace the movable comb a vertical offset between the fixed comb and the movable comb has to be introduced. There are two methods providing this vertical offset. The first method involves a bimorph cantilever made of thermal coefficient mismatch materials i.e., silicon oxide and single crystal silicon. The bimorph cantilever which is anchored to the fixed comb is deflected by residual stress between the two materials at room temperature allowing an effective vertical motion of several microns [84],[85],[86],[87]. The second method involves a novel, extended SBM (surface bulk micromachining) process for vertical actuation presented by Kim et al. [88]. A similar approach was undertaken by Kwon et al. [89], who fabricated a vertical actuated micro lens scanner demonstrating a bidirectional vertical displacement from -6.5 to +9 μm at 12 Volts DC. In 2006 Chiou et al. [90] presented an electrostatic comb drive actuator with a novel cascade multi-stage configuration called Cascade Vertical Actuator (CVA). The CVA was fabricated by a standard 0.35 μm CMOS process with an actuation stroke length of 2.6 μm at 90 Volts.

Comb drive actuators are advantageous, because they are easy to fabricate with basic surface micro machining techniques such as DRIE. Comb drive actuators have also a low dynamic response time which make them suitable for high speed applications such as optical fibre switching [91]. Another advantage of comb drive actuators is their low power consumption. Nevertheless, disadvantages of comb drive actuators are low forces and higher operating voltages. Although Saheb et al. [92] recently reported a system integration for high voltage MEMS with high output voltages up to 300 Volts controlling MEMS capacitive loads between 1 to 50 pF. Applications for comb drive actuators range from linear micro vibromotors [93], micro-grippers [94], optical microscopy probes [95] and precision positioning systems [96] to optical switching devices [97].

Another group of electrostatic actuator is known as Scratch Drive Actuator (SDA). The basic idea of a SDA was originally reported in 1993 by Akiyama et al. [98]. Both a polysilicon stepping motor and slider which employed the SDA as a transducer were demonstrated. A cross-sectional view of a Scratch Drive Actuator (SDA) is represented in fig. 2-16. The SDA has a polysilicon plate and bushing which is fabricated on an insulator film of a silicon substrate. The device is driven by an AC voltage with a peak to peak amplitude of a few volts and can move on the wafer by repeating a step motion. A diagramatic illustration of the step motion which can be observed in the SDA is illustrated in fig. 2-16a-c.

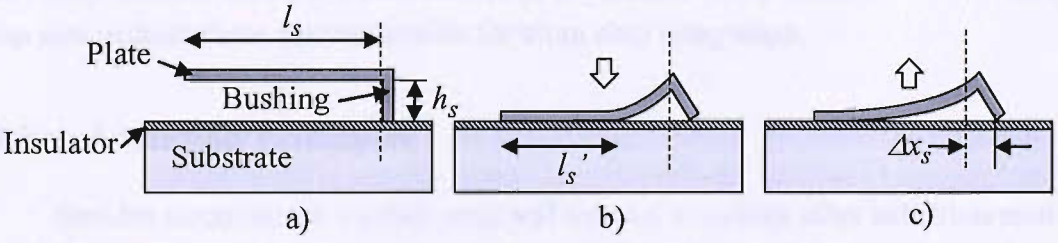

Figure 2-16: Cross-sectional view of the Scratch Drive Actuator (SDA).

The plate is pulled down to the insulator layer by the electrostatic force when the electric pulse is applied between the plate and the substrate as shown in fig. 2-16b. In this state a length l_s' of the plate is attached to the insulator, whereas part of the polysilicon plate which is connected to the bushing is deformed storing temporarily an elastic strain energy in the plate structure. In the following state as shown in fig. 2-16c the elastic strain energy is released again and the plate begins to return to its original shape. During this transition, the end of the plate towards the bushing side shifts forward by a distance Δx_s. The geometric relation given by T. Akiyama [99],

$$\Delta x_s = \frac{h_s^2}{2(l_s - l_s')} \tag{2.5}$$

gives the step value Δx_s. The minimum step values observed were in the range of 10-30 nm for a bushing height of h_s = 1.0 μm.

Polysilicon SDAs produce a step motion in the wafer plane (*x* and *y* direction) [100], but can also be used for out-of wafer plane actuation (*z* direction). A vertical actuation can be achieved by beam buckling in *z* direction induced by integrated Scratch Drive Actuators (SDAs). This vertical movement can be used to self-assemble three dimensional polysilicon structures such as micro mirrors for optical applications [101]. With this technique another group of researchers realized micro-*xyz* stages for a free-space micro optical bench [102] which has an optical beam adjustment with three degrees of freedom. A positioning accuracy of 11 nm is achieved by the integrated SDAs, with the travel distance of 30 μm in each direction.

SDAs can easily be arrayed due to their compact size producing forces on the order of mN. As an example for an integrated SDA array is the surface micro machined free-space fibre optic switch presented by Lee et al. [103]. The switch consists of an out-of-plane micro mirror driven by an array of SDAs. In general, Scratch Drive Actuators (SDAs) offer a high force actuation with a minimum step size of around 10 nm. For optical cavity actuation on atom chips the minimum step size is the biggest disadvantage of SDAs. The actuated optical cavities on the integrated atom chip requires a strong coupling between the resonator mode and the trapped atoms inside the optical cavity. The strong coupling is achieved by tuning and locking the cavity mirrors within 2-4 nanometers of a resonant cavity mode. SDAs are limited in their step size making them also unsuitable for atom chip integration.

Other Actuation Principles

Besides electrostatic, piezoelectric and thermal actuators other actuation methods can be used. For example electromagnetic actuators, which utilize the physical principle of the Lorenzforce. Well established in the macro world are electro-motors, but also in the micron scale electromagnetic actuators such as stepping motor are demonstrated [104]. Further actuation principles have been used for microactuation including magnetostrictive, shape memory alloy, chemical and biological actuators. However, fabrication difficulties of such devices remain challenges researchers struggle with.

2.3.2 Multi-Dimensional Actuators

A multi dimensional actuation can be achieved by applying either one of the actuation principles as described earlier to all translation axes or by applying a combination of different actuation principles to different axes. In the following paragraphs a variety of *xy* and *xyz* actuators and their applications are presented.

Two-dimensional (2D) Actuators

The first multi dimensional actuators were demonstrated in two dimensions in the early 1990s allowing a displacement in the wafer plane in the *x* and *y* direction. Not only was the realisation of such micro-machined two dimensional actuators easier than fabricating devices in all three dimensions, but it was also important for researches to demonstrate two dimensional actuators which could be used in a wide range of applications. The most commonly used actuation principle for two dimensional actuators is the electrostatic principle. In 1992, Yao et al. fabricated an *xy* translation actuator for scanning probe devices measuring only 40 μm by 40μm [105]. It incorporates four parallel plate actuators, which allow a movement of up to 200 nm for a driving voltage of 55 V. Also based on electrostatic actuation is the *xy* micropositioner fabricated by Indermuehle et al. [106]. However, this design includes four electrostatic comb drive actuators which enable a microstage to be scanned over an area of about 3 μm x 3 μm with voltages of 150 V. The *xy* microstage has an integrated tip on top to perform topographic AFM measurements. Yet, another group of researchers, Sun et al., also utilize electrostatic comb drive actuators demonstrating a two axis microactuator for precision manipulation [107]. The fabrication process involves deep reactive ion etching (DRIE) on silicon-on-insulator (SOI) wafers. The manipulator, as shown in figure 2-17 has a travel range of around 4 μm with voltages up to 70 V.

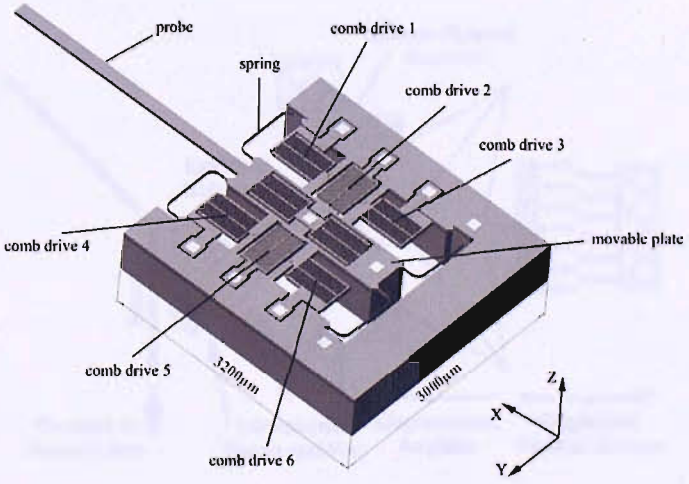

Figure 2-17: Two axis micromanipulator [107].

A similar fabrication process but on a silicon-on-glass (SOG) wafer has been used by Kim et al. [108] to realize a *xy* microstage with high aspect ratio structures as illustrated in figure 2-18. Four identical electrostatic comb drives arranged perpendicular to each other have been used to achieve a two dimensional active driving region of 50 μm by 50 μm. In order to show the feasibility of application as a micro optical system an integrated micro lens was formed on the shuttle.

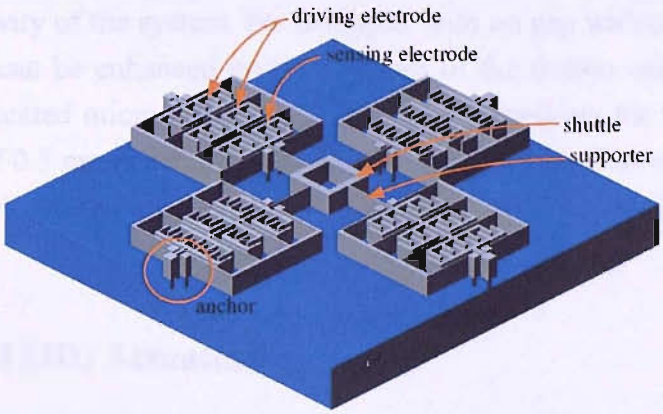

Figure 2-18: XY microstage with an integrated Fresel lens [108].

Besides comb drive actuators also scratch drives actuators (SDA's) have been used to actuate microstages in x and y direction. An integrated xy motion system has been fabricated and operated by Langlet et al. [100]. The system uses four SDAS with a step motion of 25 nm in order to move a stage with a maximum displacement of 50 μm along the x axis and 40 μm along the y axis. Apart from electrostatic actuation also other actuation principles such as electrothermal actuation have been successfully implemented moving microstages in the wafer plane (Fig. 2.19).

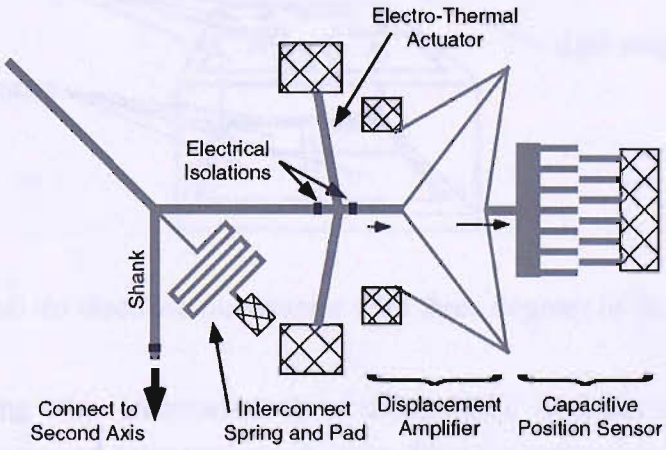

Figure 2-19: An electrothermal 2D micropositioner [109].

Chu et al. demonstrated a micro machined 2D positioner with electrothermal actuation [109]. The two axis micropositioner has a travel range of around 40 μm at a driving voltage of 20 V. Additionally, an integrated sensing comb drive structure acts as a capacitive sensor providing a sub-nanometre position feedback. The electrical set-up of the system uses standard laboratory instruments that can reliably measure 0.1 fF. This sensitivity corresponds to a displacement accuracy of 0.3 nm. The fabrication process of the micropositioner includes a DRIE process, which defines the mechanical structure of the thermal acuator and the sensing comb

drive. Important to notice is that the gap widening of the comb fingers during the DRIE process reduces the sensitivity of the system. For example, with no gap widening due to DRIE, the capacitive sensitivity can be enhanced up to 3.9 times of the design value. Even though the sensitivity of the fabricated micropositioner is reduced by applying the DRIE process a displacement accuracy of 0.3 nm is achieved. The work presented by Chu et al. shows that electrostatic comb drive structures are well suitable for atom chip integration, in particular for optical cavity tuning.

Three-dimensional (3D) Actuators

The first three dimensional actuator was presented in 1990 by Fukuda and Tanaka [110]. It consists of four parallel plate electrodes allowing a probe attached to a stage which is sitting on top of the movable structure to be moved in a rotational *yz* and *xz* direction or in *z* direction. The micro electrostatic actuator with three degrees of freedom has two major disadvantages. First, the device is not capable of independent motions in the axes *x*, *y* and *z*, because of the structural design as shown in figure 2-20. Secondly, the physical dimensions of the entire actuation device are quite large with 30 mm in length, 21 mm in width and 3.5 mm in thickness.

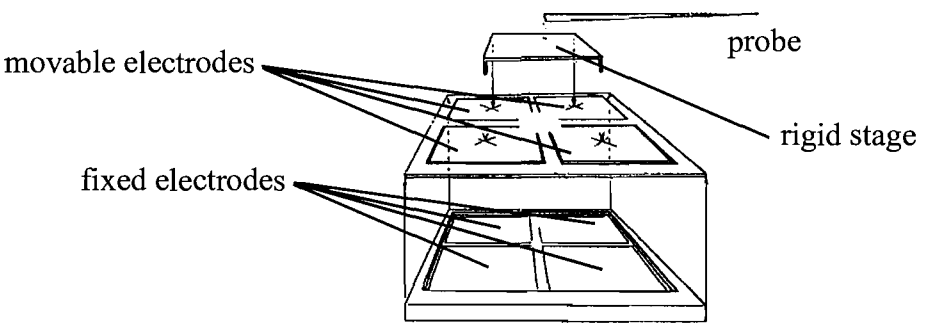

Figure 2-20: Micro electrostatic actuator with three degrees of freedom [110].

In years following other electrostatic three dimensional actuators have been presented. Xu and MacDonald fabricated a micro scanning tunnelling microscope (micro STM) and demonstrated the operation of the STM by obtaining a STM image of a 200 nm metal conductor on a silicon chip [111]. The micro STM includes integrated *xy* comb drive actuators for scanning and a torsional *z* actuator with an integrated cantilever and tip. Another group of researchers, Zhou et al. [112], fabricated a MEMS 3D optical mirror which has both out-of-plane *x* and *y* rotations and in-plane *x* and *y* translations. Lateral electrostatic comb drive actuators control the *x* and *y* translation of the optical mirror up to 4 μm. Whereas the *xy* plane tilt angle up to 3

degrees is achieved by electrostatic parallel plate configurations (Fig. 2-21).

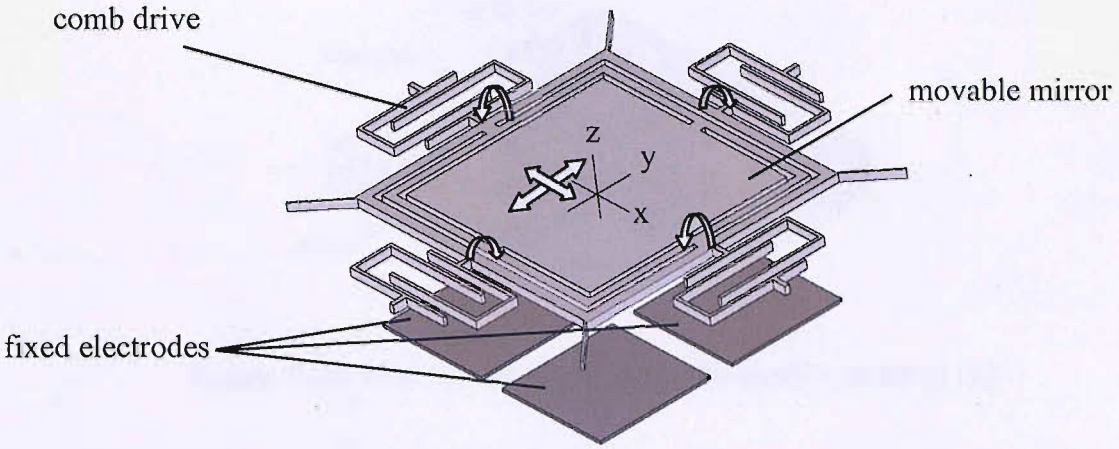

Figure 2-21: MEMS 3D optical mirror [112].

The biggest drawback of the majority of electrostatic three dimensional actuators is the lack of controllable motion independently in all three axes. Addressing exactly this problem Ando developed three dimensional electrostatic stages driven by comb drive actuators [113]. The translation along the *z* axis is achieved by the geometry of the suspensions, which incorporate a pair of leaf springs inclined to the substrate. A maximum displacement of 1.0 μm for *x*, 0.13 μm for *y* and 0.4 μm for *z* at a driving voltage of approximately 100 V has been demonstrated. Independent motion in three-degree-of freedom (3-DOF) has also been realized by Chang et al. [114]. They demonstrated a 3-DOF positioning micro-manipulator by using the integration of two linear comb actuators and one vertical comb actuator. They achieved an out-of-plane angular displacement of 0.05 degree at 50 Volts and an in-plane displacement in both *x* and *y* directions of 6 μm at 50 V.

In addition to electrostatic actuators a number of three dimensional thermal actuators have been fabricated. Niblock et al. [115] fabricated a three dimensional actuator based on planar bimorphs. It consists of two orthogonal silicon bridges with four independently addressable heating resistors. On the back of the silicon bridges aluminium is deposited to obtain the

bimorph structure (Fig. 2-22).

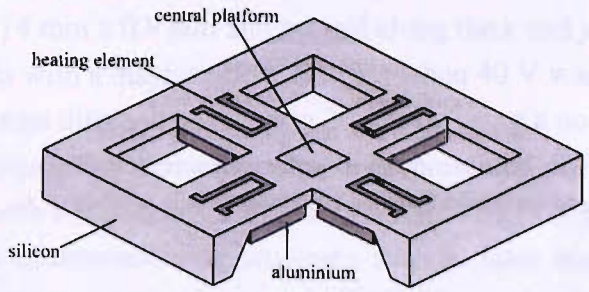

Figure 2-22: Three dimensional planar bimorph actuator [115].

The bimorph actuator delivers an out-of plane movement of up to 100 µm. However, the in-plane movement is limited to approximately 500 nm in each direction. Another disadvantage lies in the high power consumption of 0.5 W for 100 µm. In order to overcome the limitation for the in plane actuation Sehr et al. [116] have proposed a three dimensional scanning stage for an integrated AFM as shown in figure 2-23. It combines four vertical bimorphs (marked x) performing a movement in *x* direction, another set of four vertical bimorphs (marked y) moves the central platform in *y* direction, and two planar bimorphs (marked z) performing a movement in *z* direction. The central platform is designed to house an AFM tip.

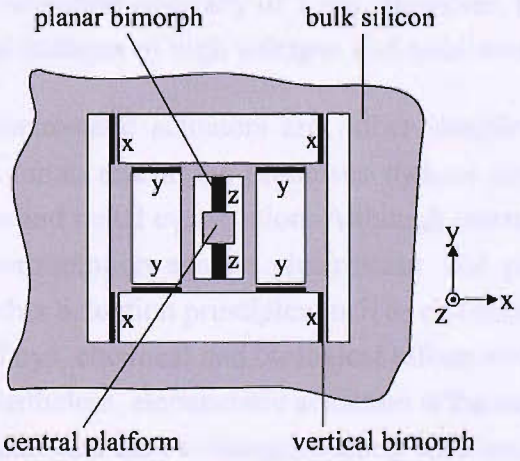

Figure 2-23: A three dimensional scanner for an integrated AFM [116].

Also multi-dimensional piezoelectric actuators have been demonstrated in the past. For example in 2003 Zhang et al. demonstrated a piezoelectric *xy* actuator for multiprobe nanorecording [117]. Proposing a novel planar fabrication method they were able to fabricate a piezo-driven *xy* microstage in a PZT plate achieving a *xy* displacement of up to 26 µm at 150 Volts.

Just two years later the same group demonstrated a *xyz* microstage [118]. By modifying and improving their planar fabrication method on monolithic PZT plates they developed integrated piezoactuators constructed with a double-layered piezo-stack actuator. The size of the *xyz* microstage is 14 mm x 14 mm x 0.8 mm and moved along the *x* and *y* axis with a displacement of 2 μm as well as *z* axis with a displacement of 2 μm when 40 V was applied. The piezo actuator is able to achieve large displacements up to 26 μm by using a novel parallelogram mechanism. However, the large displacements were only presented for the *xy* microstage. The fabrication process of both microstages is based on monolithic PZT plates, which require non-standard and expensive micromachining processes such as laser machining. The use of PZT plates makes single wafer processing and batch fabrication quite difficult, especially if integrated along other microstructures on atom chips.

2.4 Summary

Actuators but also sensors play a significant role in the world of today's micro regime. They are necessary components in many microsystems and have been implemented in various applications employing different actuation principles. Piezoelectric actuators in comparison to electrostatic actuators provide higher forces, but with a very limited translation ranging from 1 nm to maximum of several microns. Yet, electrostatic actuators can have translation ranges up to 150 μm. Piezoelectric actuators require higher actuation voltages (up to 1kV for a stacked PZT) than thermal and electrostatic actuators in order to achieve a translation of several micron. The resolution of piezoelectric actuators are superior to thermal and electrostatic actuators, easily achieving an actuation accuracy of 1 nm. However, the benefit of higher resolution is masked by the disadvantages of high voltages and small translations.

Thermal actuators and electrostatic actuators are rather straight forward in fabrication by applying standard surface micro machining processes such as deep dry etching (DRIE), wet etching, plasma deposition and metal evaporation. Although thermal actuators have the disadvantage of high power consumption against electrostatic and piezoelectric actuators. Also microactuators based on other actuation principles such as electromagnetic or magnetostrictive effect, memory effect of alloys, chemical and biological effects are feasible, but quite demanding in manufacturing. Nevertheless, electrostatic actuation is the most explored principle of all. After all electrostatic actuators are easy to integrate along other micro structures - especially in the form of comb drive structures - and scalable without difficulties to achieve forces large enough for actuation. Due to their structural design comb drive actuators are open access architectures. For example, a single comb drive actuating in $+x$ direction provides an open access in $-x$, $+y$, $-y$, $+z$ and $-z$ direction, which can be utilized to integrate additional micro structures. The ability of the open access architecture in the wafer plane makes these electrostatic actuation structures in particular suitable for integration on an atom chip. The optical cavity as well as guiding and trapping atoms can easily integrated around the comb drive actuator and within the wafer plane. In comparision to the piezoelectric actuation for example in the form of a pie-

zoelectric micropump the open access is limited due to the out of the wafer plane actuation making the integration of the tunable optical cavity difficult.

Table 2-1 summarizes the advantages and disadvantages of the most important actuation principles - electrostatic, piezoelectric and thermal actuation.

	Electrostatic	Piezoelectric	Thermal
Open access	very good	bad	good
Scalability	easy	difficult	not easy
Fabrication	easy	not easy	easy
Forces	medium	high	medium
Voltages	medium	high	low
Power consumption	low	low	high
Translation	large	small	large
Resolution	high	very high	medium
Integration on atom chips	very good	not good	good

Table 2-1: An overview of the most important actuation principles summarizing their pros and cons for atom chip integration.

In principle, the actuation of a cavity system can be achieved by magnetic, thermal or electrostatic actuators. However, magnetic actuation is not suitable, because the magnetic fields applied will interfere with the magnetic atom guiding fields from the micro wires. Thermal actuation is also not suitable, because the heat dissipation from the thermal actuation is likely to interrupt the guiding and trapping of atoms. Electrostatic actuation is the most feasible solution. Also by comparing each actuation principle in table 2-1 it becomes clear that electrostatic actuation is a good solution for integration on atom chips. Nevertheless, the final decision on which actuation principle to be used is also dependant on dominant factors such as costs, required development work and available facility machinery and processes at Southampton.

As a result of the literature review and the evaluation of pros and cons for different actuation principles, our research group decided to realize the new generation of atom chips by accommodating electrostatic actuation into the atom chip design. The design idea of a three-dimensional actuator is based on electrostatic actuation employing comb drives structures and parallel plate configurations for optical cavity alignment and tuning.

Chapter 3

Concept of the Atom Chip

3.1 Introduction

In this chapter a new concept of an atom chip is presented. Section 3.2 describes two atom chip designs, which are both capable of guiding, trapping and detecting neutral atoms by using integrated micro wires and micro actuated optical cavities. One atom chip is based on an one-dimensional actuator, which is used to tune an optical micro cavity in the wafer plane. The other atom chip integrates a three-dimensional actuator, which aligns the optical cavity in the wafer plane and tunes the cavity out of the wafer plane. In section 3.3 the micro structured components such as wires, cavities and actuators for both atom chips are described. For the actuators in section 3.3 the design requirements are collected and summarized. Controlling the atom chip actuator is a key requirement of a successful atom chip experiment and is also described in section 3.3. Finally, chapter 3 closes with a summary in section 3.4.

3.2 General Context

The combination of atom physics and MOEMS in this project requires a considerable amount of resources, needed to build the envisioned new generation of atom chips. Hence, this project is based on a collaboration between Southampton University and Imperial College in London. The realisation of BEC on board the new generation of atom chips is being pursued by our collaborators [119], whereas the group in Southampton will design and fabricate the actual atom chip. Linking the scientific know-how and facility equipment of both research institutions will determine the successful outcome of this project.

The optical MEMS atom chip project is aimed at the investigation of using micromachining techniques to design and realise a new generation of atom chips. Clouds of atoms are positioned and guided above a silicon surface along dedicated pathways by magnetic forces.

This is accomplished by passing a high current through micro-wires creating the magnetic fields. Furthermore, atom clouds are cooled with laser light of a specific wavelength [120]. Then laser light is coupled into an optical cavity through a wave guide confining the photons and allowing manipulation and characterization of the trapped atom clouds. The integration of the high-current density wires on a silicon substrate with an actuated micro-mirror for cavity tuning requires a variety of suitable MEMS fabrication techniques to be developed. Exactly this seamless integration of a optical micro electro mechanical system along with atom optics is the novelty of this project.

The envisaged new generation of atom chip will consist of three major, individually micromachined parts:

- the micro-wires,
- the optical cavity,
- and the actuator.

A typical example of an envisaged atom chip is shown in figure 3-1. The micro-wires will be electroplated on the surface of a silicon wafer. Gold is chosen to achieve high current density wires. The optical cavity consists of a planar-concave mirror configuration formed by a planar mirror and a concave mirror at the tip of an optical fibre. The fibre functions also as an optical read-out.

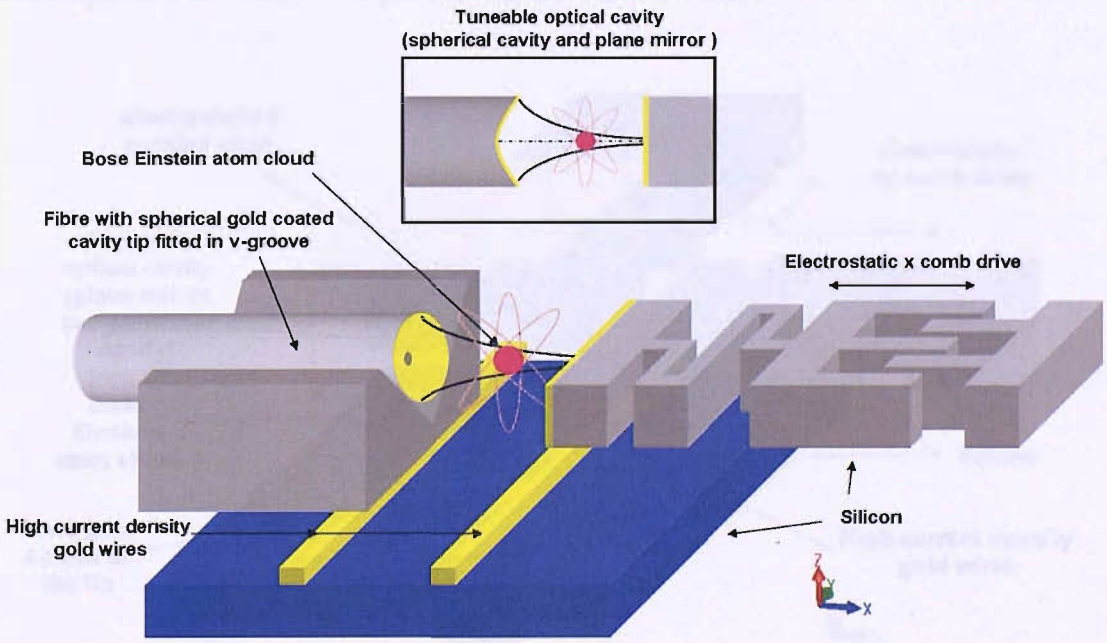

Figure 3-1: Schematic architecture of the 1D atom chip including the one-dimensional actuator, the gold wires and the tunable optical cavity (not to scale). The optical cavity consists of a planar-concave mirror configuration. The atom clouds are guided by current carrying electroplated gold wires between the concave fibre and movable planar gold mirror.

The concave fibre is buried in a v-groove and positioned opposite to the planar mirror. Since the optical axis lies within the wafer plane the tunability of the established optical cavity and its planar mirror can be achieved using a single one-dimensional (1D) electrostatic comb drive actuator. A high quality cavity is obtained from a planar mirror which is gold coated and atomically smooth using the (111) crystallographic planes of (110) silicon wafers. The major advantage of the one-dimensional atom chip design (1D referring to the actuator) is the open architecture of the system allowing easy access to atom chip from above. Another advantage of this setup is that no alignment of the optical mirrors is required, because the v-groove for the concave fibre is fabricated on the same silicon substrate as the actuation device and the planar mirror providing self-alignment and stability to the optical cavity system. However, there are also disadvantages. The fabrication process of an atomically smooth side wall mirror is not straight forward considering that the mirror needs to be integrated with the actuator structure. Implementing the v-groove as a mechanical alignment structure along with mirror and actuator is yet another challenge. But the most difficult task is the fabrication of the concave fibre. At the beginning of the project in 2003 the fabrication of those concave fibres proofed to be very difficult and time consuming making a practical implementation on atom chips in the foreseeable future uncertain. The availability of such concave fibres is the main reason why a second atom chip design idea is proposed in the following.

The 3D atom chip, as shown in figure 3-2, is based on an out-of the wafer plane cavity actuation. The fabrication of the 3D atom chip involves a more complicated three layer wafer process compared to a two wafer process for the 1D atom chip.

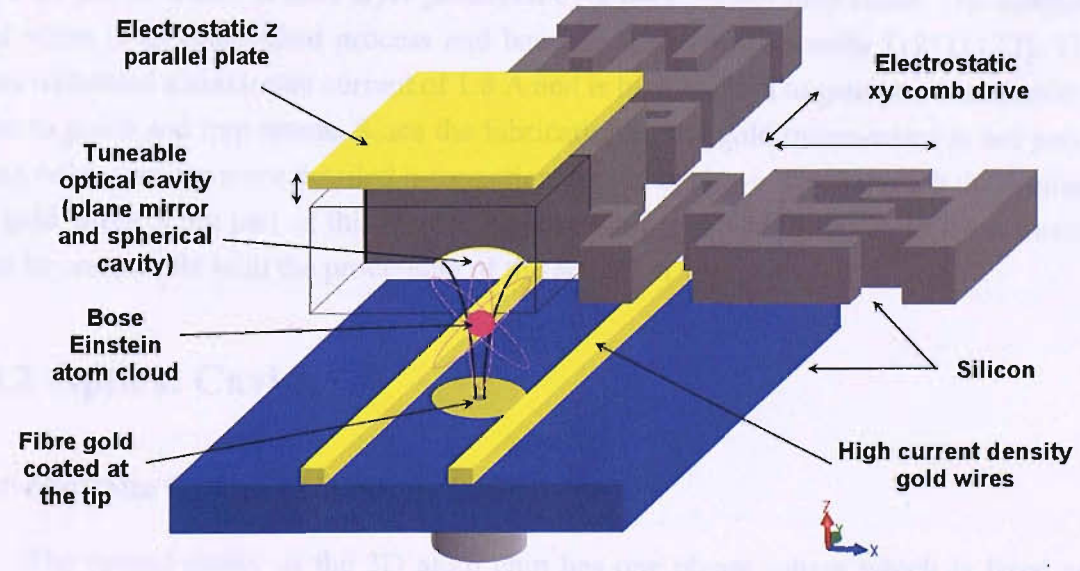

Figure 3-2: Schematic architecture of the 3D atom chip including the two-dimensional in-plane actuator to compensate an assembly misalignment, the one-dimensional out-of-plane actuator for cavity tuning, the gold wires (not to scale). The optical cavity consists of a planar-concave mirror configuration with a planar fibre mirror and a movable spherical mirror.

The electroplated gold wires are integrated along with the optical fibre on one silicon wafer. The optical fibre, which is gold coated at the tip obtaining a high reflectivity, acts as a planar mirror forming one part of the optical cavity. The opposite mirror of the optical cavity is embedded in a movable mass on a second separate silicon wafer. This spherical shaped and gold coated mirror together with the planar fibre mirror provides a high quality optical cavity. The tunability of the high quality cavity is reached by an electrostatic actuation fabricated on a third silicon wafer, which enables an out-of the wafer plane cavity actuation. Because of the misalignment during the assembling process of the cavity mirror wafers a second in-plane actuation is necessary. A two axis electrostatic actuator is introduced to compensate any deviation from the optical cavity axis between the two aligned mirrors. The introduction of the second actuator solely used for cavity alignment complicates the 3D atom chip design. Especially the combination of the *xyz* actuated tunable optical cavity, fibre and micro-wires increase the complexity of the system. Integrating all these elements on a single chip is challenging and requires a complicated fabrication process leading to a single, multi-layered atom chip. However, apart from the disadvantages mentioned above the biggest advantage of the 3D atom chip is the fact that simple and easily available planar fibre mirrors can be used.

3.3 Atom Chip Components

3.3.1 Micro-Wires

The micro-wires used for the atom chip are formed by electroplating gold of a thickness of 10-20 μm on a Cr/Au seed layer patterned by a photolithography resist. The fabrication of gold wires is an established process and has been published recently [121],[122]. The gold wires withstand a maximum current of 1.8 A and is high enough to generate a magnetic field in order to guide and trap atoms. Since the fabrication of the gold micro-wires is not part of this thesis references for more detailed information are given above. Even though the realisation of the gold wires is not part of this thesis, the processes involved to fabricate these micro-wires must be compatible with the processing of the actuation structures.

3.3.2 Optical Cavities

Out-of-plane Cavity (3D Atom Chip)

The optical cavity of the 3D atom chip has one planar mirror which is fixed and one spherical mirror which is movable. The fabrication of the planar gold or dielectric coated fibre mirror is a well known and established process [37],[39]. Cleaving the fibre and coating the fibre tip with evaporation techniques is straight forward. Whereas, fabricating the spherical mirror on a silicon surface in the scale of a few tens of microns in diameter is a novel approach and requires to be investigated and a proper fabrication process has to be developed. Other

researchers in Southampton have demonstrated spherical cavity mirrors on silicon surfaces. The mirrors are fabricated by applying a combination of dry anisotropic and wet isotropic etching techniques to achieve the sphericity of the cavity mirror as shown in figure 2-6 on page 11. However, for further details of this approach see the following reference [123]. It is important that the processes involved to fabricate the spherical mirrors are compatible to the fabrication processes of the atom chip including micro-wires and actuation structures.

In-plane Cavity (1D Atom Chip)

The optical cavity of the 1D atom chip has also one planar mirror and one spherical mirror. However, the spherical mirror is fixed and consists of a gold coated concave fibre tip. Whereas, the planar mirror is a movable gold coated vertical silicon side wall. Vertical silicon side wall microstructures with high aspect ratios can be fabricated by using (110) silicon wafers [124]. A (110) silicon wafer has its (111) planes perpendicular to its surface. When etched in KOH, the (111) planes are effectively not etched compared to other planes. As a results of the high selectivity between (111) and (110) planes vertical side walls can be obtained [125],[126]. Of critical importance is the precise alignment of the crystallographic (111) planes during the processing. If the alignment is very accurate (~0.1°) atomically smooth walls with a surface roughness of a few nanometers can be achieved. Yet, misalignment can lead to undercutting of features, as well as surface steps [127],[128]. Additionally to the fabrication of the vertical side walls, an evaporation process is applied to coat the side walls with gold. The combination of the gold coated atomically smooth planar mirror and the gold coated concave fibre mirror results in a high quality optical cavity.

3.3.3 Actuators

In the following the design requirements for the 1D and 3D actuators are presented. The design requirements are derived from the atom chips and their components introduced in the previous sections and by addressing certain design aspects, which are important for the realization of the new generation of atom chip. The design requirements are summarized in table 3-1. At last the controlling scheme of the actuators is described.

Actuator Requirements

A key functionality of the new generation of atom chip is an integrated tunable optical micro cavity. As described earlier the tuning of the optical cavity can be achieved by an actuation in the wafer plane (1D) or out of the wafer plane (3D). In the atom chip experiment laser light at a wavelength of $\lambda = 780$ nm is coupled via a fibre into the micro cavity. When the separation L between the two mirrors of the optical cavity is varied by the actuator, the cavity resonance modes can be captured in the reflected intensity of the optical fibre. Two successive resonance modes taken from the intensity spectrum are separated by length changes of $\Delta L_R =$

λ/2 (390nm). In order to bring the optical cavity in resonance a translation over a minimum two successive resonance modes of 780 nm is required [129]. If the actuator translation of 780 nm cannot be achieved the atom chip experiment will fail. Therefore, it is very important that the design of the actuator has a minimum travel range of 780 nm. However, it is advantageous to increase the actuator translation beyond 780 nm. For example, with an actuation of the optical cavity over a length of 4 μm it is possible to scan over ten resonance modes. Hence, the probability of finding 2 two successive resonance modes is five times higher. Consequently the experiment is more controllable making it easier to align and set up. In summary, the optical cavity actuator requires a coarse tuning travel range L_c between 780 nm and 4 μm. Since the full width at half maximum δL_R [130] of the resonances is expected in the order of 4 nm, the actuation accuracy for fine tuning and stabilizing the optical cavity system is required to be 2 nm [129]. If the actuation accuracy of 2 nm cannot be achieved it becomes more difficult to set up the atom chip experiment and lock the optical cavity in resonance. However, it is estimated that with an actuation accuracy greater than 4 nm it becomes almost impossible. Additionally for the 3D atom chip a separate in plane actuation of up to 5 μm in the x and y direction is required due to the misalignment of the cavity mirrors as a result of the wafer bonding process. For the cavity alignment an in plane actuation accuracy of 0.1 μm is proposed [129]. However, it is estimated that an alignment accuracy up to 0.2 μm is acceptable.

The processing of electrostatic actuators is compatible with the fabrication of micro wires and micro cavities. Electrostatic actuators are simple to implement, not difficult to scale in size and the fabrication resources are available. Especially electrostatic comb drive actuators for an in-plane actuation in the x and y direction are easy to fabricate using deep dry etching techniques. They are scalable and deliver the actuation range required without difficulty. The z actuation range of the 3D actuator is difficult to achieve with vertical translated comb drive structures. Their fabrication process is more complex with increasing translation range. Therefore a parallel plate actuator for the out of plane actuation of the 3D actuator is chosen. Parallel plate actuators are the most classic electrostatic actuation structures and also easy to fabricate. They are scalable as well and can be integrated by multi layered wafer processing as proposed in the 3D atom chip design. However, the major disadvantage is that their actuation range is limited to 1/3 of the initial gap distance of the parallel plates. The reason for the 1/3 gap limitation is explained in the following theoretical chapter 4. Since the alignment of the 3D actuator in xy direction is followed by tuning the optical cavity in z direction separate operations of these translations would be advantageous. As for the 1D actuator using a comb drive structure in the wafer plane is the most favourable actuation solution as well.

According to W. Tang [73], inventor of the comb drive actuators, the actuation force, thus the travel range of a comb drive actuator is proportional to the height of the comb structure, the number of comb fingers and the square of the actuation voltage, but inverse proportional to the gap size of the comb fingers and the spring constant of the system. Hence, increasing the height and number of comb fingers and decreasing the gap size and spring constant maximizes the travel range or lowers the actuation voltage by keeping the same actuation

range. Throughout the atom chip experiments a maximum actuation voltage of 150 Volts is allowed due to safety regulations and power limitations of the equipment used. Even though the maximum actuation voltage is limited to 150 Volts it is preferred to keep the voltage as low as possible. Maintaining the required travel range of the comb drive actuators of the 1D and 3D design an actuation voltage below 100 Volts is feasible and can be achieved by a low spring constant in the region of 50 to 100 N/m. Additionally, comb structure heights of up to 120 μm with around 300 comb fingers and gap sizes from 3 to 5 μm produce estimated electrostatic forces of up to 1 N, which are high enough for translations up to 4 μm.

For the out-of-plane tuning actuation of the 3D actuator the parallel plate configuration is required to translate up to 4 μm allowing the optical cavity to become resonant. The actuation force, hence the actuation range of a parallel plate actuator mainly depends on the actuation voltage, the spring constant and the initial gap distance between the parallel plates as well as their size. In order to actuate 4 μm a gap distance of 21 μm is chosen. With a gap distance of 21 μm and a 1/3 gap limitation a maximum translation of 7 μm between the two parallel plates can be achieved. The operating point for the coarse tuning of the optical cavity is at a maximum translation of 4 μm. Regarding the translation limit of the parallel plate actuator the operating point of 4 μm is at an advisable distance away from actuator limit of 7 μm improving the stability of the actuation system. In order to achieve the maximum achievable travel range of 7 μm the parallel plate actuator is applied with a low spring constant and the parallel plates are sized as large as possible. In this configuration a low actuation voltage is obtained. It is estimated that a spring constant of around 1 N/m and parallel plates of 200 μm in size achieves a translation of 7 μm with an actuation voltage of less than 100 Volts.

The 1D actuator also requires a minimum translation of 780 nm in order to scan over a minimum of two resonance modes. However, the 1D actuator and its comb drive actuation structure can easily be scaled up increasing the preferred translation from 4 μm up to 20 μm at a voltage around 150 Volts without any difficulties in the device design and fabrication. With a maximum achievable translation of 20 μm the 1D actuator is capable of scanning over 51 resonance modes simplifying the set up of the atom chip experiment even further. However, the travel range up to 4 μm is the maximum required translation and operating point of the atom chip experiment.

Another important requirement of the electrostatic actuators is that not only their fabrication process must be compatible with the fabrication processes of the optical cavity and micro wires, but they must also be compatible with high vacuum operations. The atom chip experiments is conducted in a high vacuum chamber at around 10^{-11} mbar. The vacuum chamber is designed to hold atom chips with a maximum size of 2 cm by 2 cm. Around 50 - 70% of the surface area of the atom chip is used to create ultra-cold atoms as well as trapping and guiding them from the location of the BEC to the location where the optical cavity is situated. Therefore only an area of 1 cm by 1 cm is available for the actuation system.

The electrostatic actuation is carried out in a static direct current (DC) operation. Since there is no operation with alternating currents (AC operation), no specific requirement on bandwidth is required. Nevertheless, the dynamic behaviour of the actuation system is important. A successful detection and characterization of the trapped atoms require the cavity to be robust against external perturbation. Although the mechanical stability can be optimized by the physical dimensions of the actuator, the requirement of spring constants as low as 1 N/m and damping forces minimized by the operation under high vacuum make the system still susceptible to vibrations. The resonant mode values should be high enough to avoid any interference with frequencies below 100 Hz, which are commonly present in a laboratory environment. Table 3-1 summarises the design requirements collected in the previous paragraphs.

	3D Actuator		**1D Actuator**
	XY Actuation	**Z Actuation**	**X Actuation**
Principle	electrostatic	electrostatic	electrostatic
Structure	comb drive (CD)	parallel plate (PP)	comb drive (CD)
Size	< 1 cm^2		< 1 cm^2
Wafer Layers	Three		Two
Travel Range	5 μm	4 μm	4 μm
Accuracy	100 nm	2 nm	2 nm
Stabilized	100 nm	2 nm	2 nm
Force	1 mN	0.1 N	1 mN
Spring Constant	100 N/m	1 N/m	100 N/m
Cavity Alignment	yes	no	no
Cavity tuning	no	yes	yes
Voltage (DC)	< 100 V	< 100 V	< 100 V
CD Height	< 120 μm	N.A.	< 120 μm
CD Fingers	approx. 300	N.A.	approx. 300
CD Finger Gap Size	< 5 μm	N.A.	< 5 μm
PP gap size	N.A.	21 μm	N.A.
PP size	N.A.	< 0.04 mm^2	N.A.
Resonant Modes	< 100 Hz	< 100 Hz	< 100 Hz

Table 3-1: Design requirements for the 3D and 1D actuator.

Controlling the Actuator

The 1D as well as the 3D actuator are controlled through an external optical read-out setup. This setup as shown in figure 3-4 consists of a laser source, a photodetector and several optical elements such as beam splitters and wave plates. It is used, not only to couple light into the optical cavity with the laser source, but also to uncouple the laser light. The two fibres

required for the 1D and the 3D actuator have two functions. First, the gold or dielectric coated fibres act as a planar mirror in the 3D design or as a concave mirror in the 1D design. Secondly, the laser light interacting with the trapped atom clouds in the optical cavity is coupled back into the fibre and transmitted to the external optical read-out setup.

During the *xy* positioning phase of the 3D actuator, which aligns the two mirrors with the *xy* actuator to each other, laser light from the laser source at a wavelength of $\lambda = 780$ nm is guided through the fibre into the optical cavity. The wavelength of $\lambda = 780$ nm is chosen, because it lies on the D2 transition of ^{87}Rb atoms, which are used in the atom chip experiments [131]. The uncoupled laser beam is then forwarded to a photodetector by passing a polarizing wave plate, followed by a polarizing beam splitter. Since the laser source emits a laser beam of one polarisation, the wave plate and beam splitter can be used to switch the polarizing state and reroute the laser beam on its way back. Finally, the photodetector measures the intensity of the incoming laser beam. A maximum intensity is detected when both mirrors are precisely aligned to each other. This procedure is finished before any atomic clouds are trapped in the optical cavity and any *z* actuation takes place. For the 1D actuator the alignment procedure is not needed, because both cavity mirrors are processed on the same substrate.

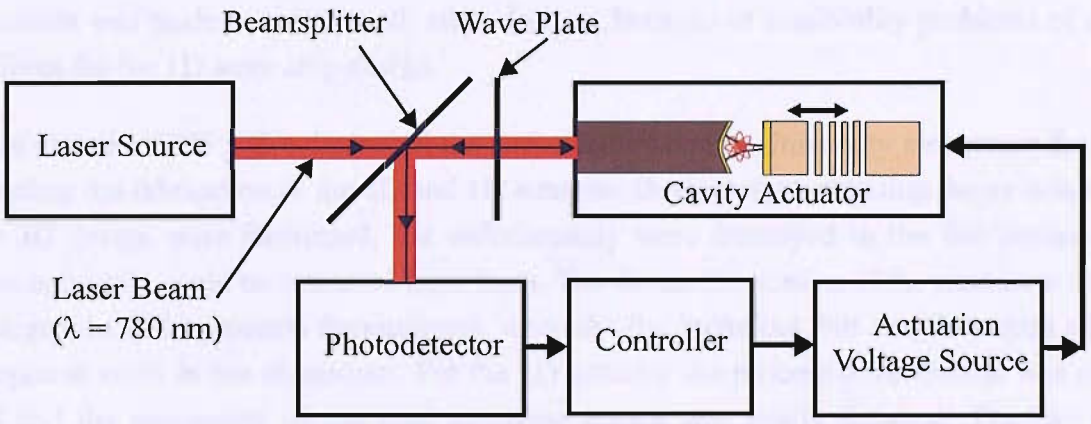

Figure 3-3: Schematic illustration of the feedback system for cavity alignment and tuning of the 1D and 3D actuator. Laser light ($\lambda = 780$ nm) is coupled into the optical cavity, then uncoupled and guided into the photodetector. Any off-resonance changes the light intensity detected by the photo-detector. The output signal of the detector feeds the controller and adjusts the actuation voltage to bring the optical cavity back to resonance.

After loading and trapping the atom clouds in the optical cavity the nanopositioning system represented by the *z* actuator for the 3D design and the *x* actuator for the 1D design is required for tuning the cavity. Both actuators are used to tune the cavity by varying the gap between the two mirrors to achieve resonance. Once the cavity is in resonance, the distance between the two mirrors is critical. Using the feedback system is it possible to link the *z*- or *x*-

actuation with the uncoupled laser light and to stabilize the cavity length. Any offset in the cavity length by more than 2 nm results in an off resonance of the cavity and failure of the atom experiment. It is important that the cavity length is maintained throughout the experiment and stabilized within 2 nm in order to keep the optical cavity in resonance.

3.4 Summary

The concept of two multi layered atom chips are presented. Two atom chip designs are introduced with a three-dimensional (3D) and a one-dimensional (1D) actuator, respectively. Besides actuators the atom chips incorporate additional components such as micro-wires and optical cavity mirrors. The 3D actuator is based on an out-of-plane cavity tuning actuation, whereas the 1D actuator uses in-plane actuation. The one-dimensional actuation of the 1D atom chip design is used to tune the optical cavity. The more complicated 3D actuator uses two degrees of freedom for optical cavity alignment and one degree of freedom for optical cavity tuning. Both actuators can be fabricated by applying a mix of standard and non-standard micromachining processes. The fabrication processes of each atom chip component are compatible to each other making a seamless integration feasible. At the start of the project in 2003 the decision was made to realize both atom designs, because of availability problems of concave fibres for the 1D atom chip design.

In October 2005 a fire destroyed the entire Southampton University cleanroom facility interrupting the fabrication of the 3D and 1D actuator. Devices demonstrating the *xy* actuation of the 3D design were fabricated, but unfortunately were destroyed in the fire before any experimental data could be extracted from them. The device fabrication of the z actuator of the 3D design was still in process development, when the fire broke out, but also destroyed all the development work in the cleanroom. For the 1D actuator the process development was completed and the processing of the final actuation device was nearly finished. The fire also destroyed these devices. As a result of an emergency meeting after the fire between the two research groups of Southampton University and Imperial College of London a contingency plan for this project was established. Part of this contingency plan was to re-run the fabrication of the 3D and 1D actuators with a primary focus on the realization of the one-dimensional actuator and it's in-plane optical tunable micro cavity, because the availability of concave fibre was not a problem any longer.

Chapter 4

Theoretical Analyses

4.1 Introduction

In this chapter the design layouts of the 1D and 3D actuator are presented and an analysis based on the final designs is conducted to predict the physical behaviour of both actuation systems. The analysis is concerned with the x translation of the 1D actuator and the xy and z translation of the 3D actuator. Analytical methods are applied, which are verified by software simulations for each actuation design.

In section 4.2, the design layout of the 1D actuator is described. The design layout is based on the design requirements derived in the previous chapter. An analytical model is applied to the design parameters of the 1D actuator and the translations curve for the in-plane actuation is presented. The lateral instability of the comb drive actuator is evaluated as well as the dynamic response. Finally CoventorWare^{TM} finite element simulations are carried out to verify the analytical results obtained throughout section 4.2.

In section 4.3, the design layout of the 3D actuator is described and the analytical model is outlined. Extracted spring constants are used to obtain the translation curves for the xy and z actuator. Also, the vertical stiffness of the entire structure as well as lateral instability and dynamic response are analysed. Furthermore the results of the software simulations are presented and compared to the analytical calculations.

In section 4.4, the accuracy and stability characteristics of the 1D and 3D actuators are evaluated.

4.2 One-dimensional Actuator (1D)

4.2.1 Design Layout

The one-dimensional actuator is an in-plane actuator, which is used for tuning the optical cavity along the x axis. The design parameters listed in table 4-1 and the design layout as shown in figure 4-1 are based on the design requirement derived in the previous chapter.

Design Parameter	**Value**
Comb fingers N_1	200
Comb finger height h_1 [μm]	120
Comb finger gap g_1 [μm]	5
Beam width w_1 [μm]	5
Beam length l_1 [μm]	400
Comb finger length l_F [μm]	45
Comb finger width w_F [μm]	10
Comb finger overlap δ_0 [μm]	10

Table 4-1: Design parameters for the 1D actuator.

The actuation is achieved with a single comb drive. The comb drive consists of a fixed part and a movable part, which have both a structure height h_1 (see table 4-1). The chosen height can easily fabricated and results in sufficient electrostatic forces required for actuation. The movable structure with N_1 comb fingers is engaged with the set of stationary comb fingers at a gap distance g_1. In order to simplify lithography processing the gap distance g_1 is kept relatively large, well above the lithography resolution limit of 2 μm for this process. The larger gap size decreases the electrostatic forces and is therefore compensated by the high number of comb drive fingers. The movable part of the comb structure encloses a mechanical spring and the vertical planar mirror. The mechanical spring is a double folded suspension flexure with a beam width w_1 at a beam length l_1 providing a low spring constant in x direction, which is suit-

able for low voltage actuation and large deflection behaviour [136].

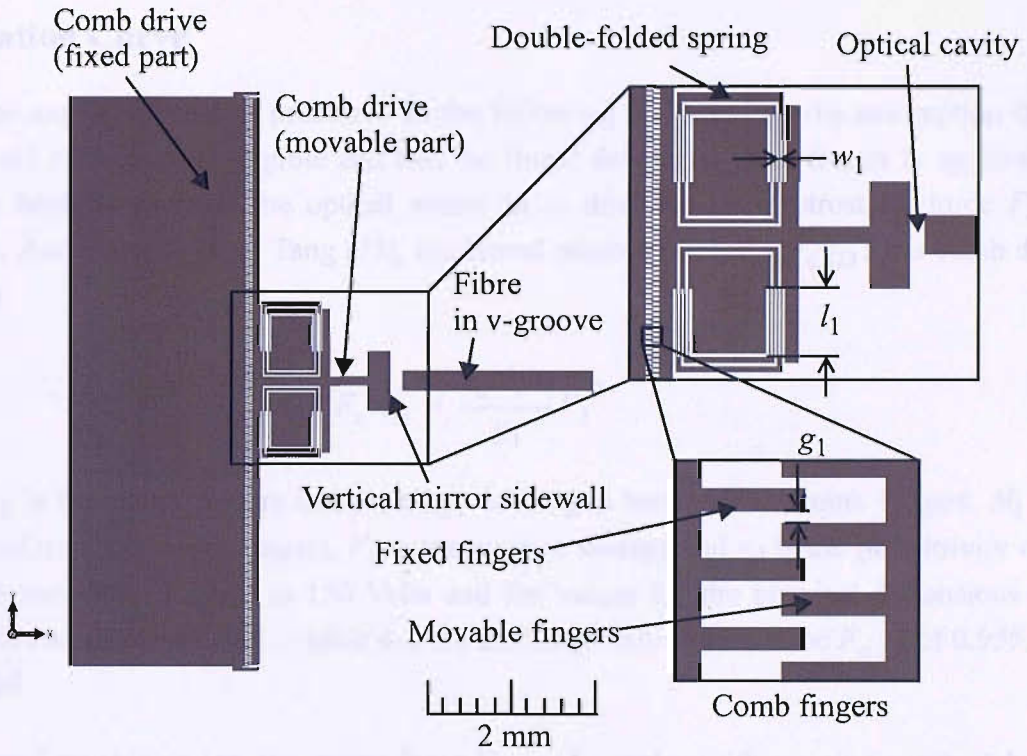

Figure 4-1: The 1D actuator design layout (5 mm by 5 mm) consists of a comb drive. The movable part of the comb drive is suspended by a double folded spring and incorporates the optical planar mirror, which is situated opposite to the v-groove supporting a concave optical fibre.

Opposite to the movable mirror the fibre with the concave tip is mounted in a v-groove by gluing. An additional alignment of the cavity to the optical axis as in the 3D actuator is not required, since the v-groove is fabricated on the same substrate. A misalignment of the v-groove along the y axis is not critical, because the plane mirror surface is fabricated to be much larger than the actual area exposed by the laser light through the optical fibre during illumination. However, important is the angle of incidence of the out coming laser light of the optical fibre. If the angle of incidence is not perpendicular to the plane mirror surface the optical cavity becomes unstable. U-shaped [132],[37] and v-shaped microstructured surfaces have been used in the past for lateral and angular alignment of optical fibre-mirror configurations. In particular silicon wet etched v-grooves provide a good angular alignment below 0.2° [133],[134], which is estimated to be sufficient enough to maintain a stable optical cavity. For this reason the v-groove as a mechanical support structure for the fibre is chosen. The v-groove support also maximizes the stability of the entire fibre structure. Overall the minimum feature size of the actuator is 5 µm making lithography processing and deep dry etching feasible and easy to manage.

4.2.2 Analytical Analyses

Translation Curve

The analytical models presented in the following are based on the assumption that the fringe-field effects are negligible and that the linear deflection-force theory is applicable. In order to laterally position the optical mirror in -x direction an electrostatic force $F_{c,1D}$ is required. According to W.C. Tang [73], the lateral comb drive force $F_{c,1D}$ for a comb drive is given by

$$F_{c,1D} = \frac{\varepsilon_0 N_1 h_1}{g_1} V_1^2 \tag{4.1}$$

where h_1 is the comb fingers thickness, g_1 is the gap between the comb fingers, N_1 is the number of movable comb fingers, V_1 is the applied voltage and ε_0 is the permittivity of air[1]. With the maximum voltage at 150 Volts and the values for the physical dimensions of the comb drive actuator as listed in table 4-1 the maximum achievable force $F_{c,1D}$ of 0.955 mN is calculated.

Based on Hook's law the spring force $F_{s,1D}$ of a spring with a spring constant k_x and a deflection by a distance x is described by

$$F_{s,1D} = k_x \cdot x \tag{4.2}$$

Using equations 4.1 and 4.2, the translation curve for the comb drive actuator is found to be,

$$x(V_1) = \frac{\varepsilon_0 N_1 h_1}{g_1 \cdot k_x} V_1^2 \tag{4.3}$$

where k_x is the spring constant of the double folded spring suspension. Given the physical dimensions of beam width w_1 and beam length l_1 of the double folded spring and under the assumption that all beam elements have a rectangular cross-sections, the moment of inertia for one suspension beam $I_{z,1D}$ can be expressed by [135]:

$$I_{z,1D} = \frac{w_1^3 h_1}{12} \tag{4.4}$$

Thus, the spring constant k_x for the double folded spring suspension of the comb drive structure is given by equation 4.5 [136]

[1]The permittivity of air is approximately equal to that of a vacuum, i.e. 8.854 x 10^{-12} F/m.

$$k_x = \frac{24EI_{z,1D}}{nl_1^3} = \frac{2Ew_1^3 h_1}{nl_1^3} \tag{4.5}$$

where $n = 2$, denoting a double folded system and E is the Young's modulus (169 GPa) for silicon. The calculated value for the spring constant k_x of the double folded spring suspension is 39.61 N/m. Knowing the spring constant k_x of the system the translation curve for the in-plane actuation can be plotted. Figure 4-2 shows the translation curve $x(V_1)$ of the 1D actuator.

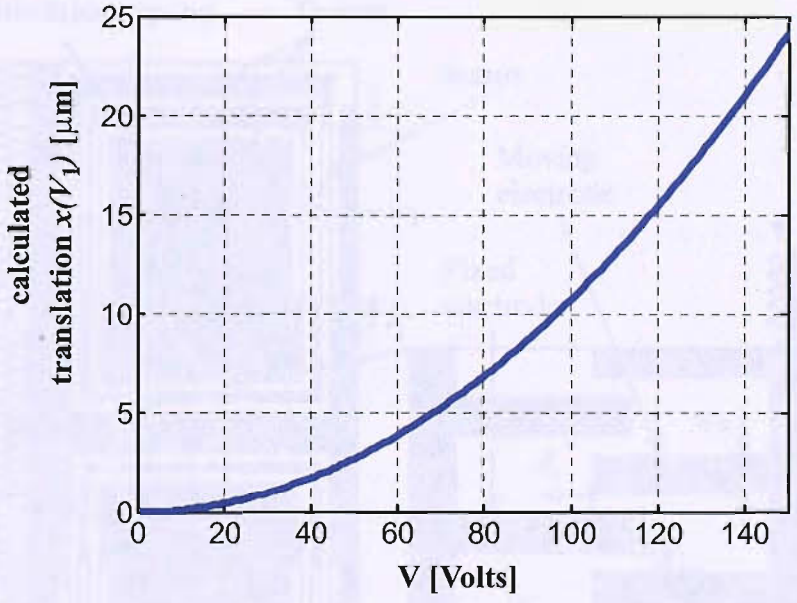

Figure 4-2: Translation curve $x(V_1)$ of the 1D actuator.

An actuation voltage of 137 Volts applied to the comb drive results in a translation of 20 µm of the optical mirror with a force of 0.797 mN. This would be sufficient to tune the cavity over 51 resonance modes at a wavelength of 780 nm.

Parameters	**Eq.**	**Value**
Maximum achievable force $F_{c,1D}$ [mN] at 150 V	4.1	0.955
Moment of inertia for one suspension beam $I_{z,1D}$ [m^4]	4.4	12.5^{-22}
Total spring constant in x direction k_x [N/m]	4.5	39.61
E-static force for the minimum required translation of 4 µm $F_{min,1D}$ [mN]	4.1	0.158
E-static force for the maximum achievable translation of 20 µm $F_{max,1D}$ [mN]	4.1	0.797
Voltage for the minimum required translation of 4 µm $V_{min,1D}$ [V]	4.3	61
Voltage for the maximum achievable translation of 20 µm $V_{max,1D}$ [V]	4.3	137

Table 4-2: Theoretical calculated design parameters of the lateral translation for the 1D actuator.

Lateral Instability

Besides the electrostatic forces along the -x direction, there are also electrostatic forces along the y axis. These lateral forces between the electrode fingers are an important characteristic of comb drive actuators causing a lateral deflection of the movable fingers. This so-called "side instability" limits the actuation range of any comb drive actuator and has to be verified for our proposed one-dimensional design. In order to maintain a stable optical cavity operation it is essential that during the atom experiments no side instability occurs.

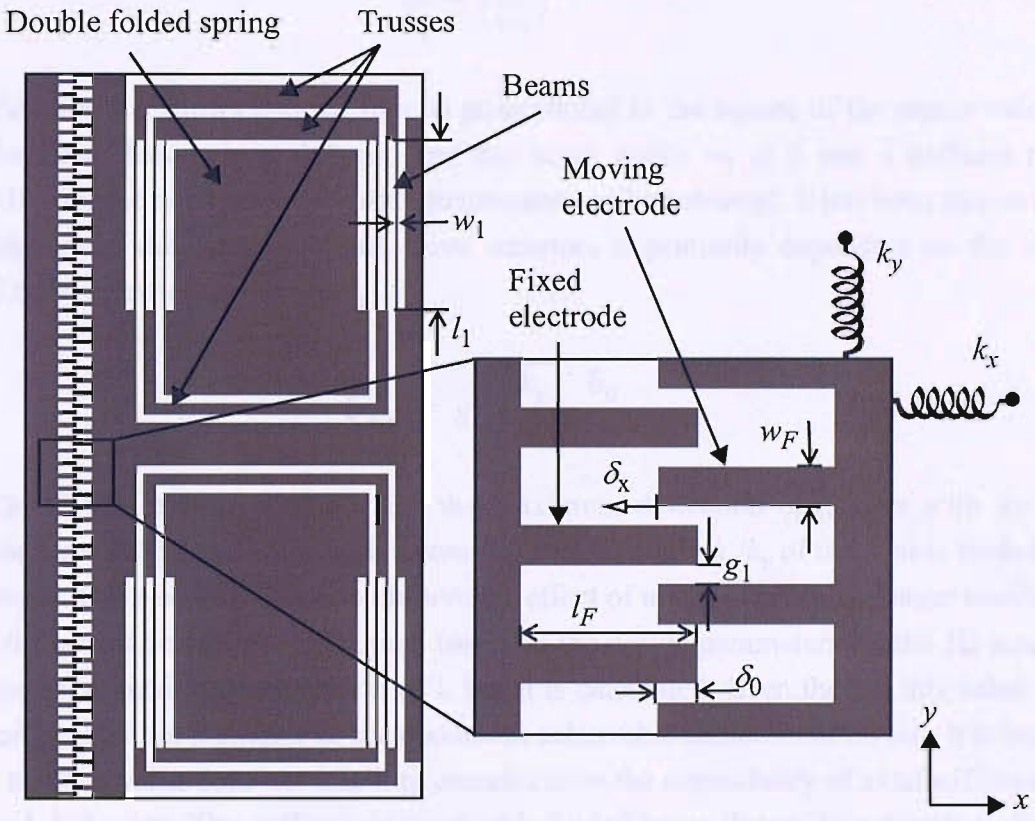

Figure 4-3: Illustration of the double folded spring flexure and comb fingers. The spring suspension consists of 6 rigid trusses and 16 beams, which have a beam width w_1 and a beam length l_1 (see table 4-1). Both moving and fixed comb fingers (electrodes) have a length l_F and a width w_F with an overlap δ_0. The spring constant of the double folded spring is represented by k_x in x direction and k_y in y direction.

The side instability, hence the maximum achievable deflection of the comb drive, is affected by the stiffness ratio of the double folded spring suspension. The spring constant $k_{y,beam}$ along the length of one beam segment of the double folded flexure is given by [135],

$$k_{y,\,beam} = \frac{E w_1 h_1}{l_1}. \tag{4.6}$$

Because of the parallel beam design of the double folded flexure the total spring constant k_y along the y axis can be seen as a sum of the 16 beam springs in parallel,

$$k_y = 16 \cdot k_{y,beam} = 16 \cdot \frac{Ew_1 h_1}{l_1} \quad . \tag{4.7}$$

Combining Equation 4.5 and 4.7 the stiffness ratio is,

$$\frac{k_y}{k_x} = \left(\frac{4l_1}{w_1}\right)^2 . \tag{4.8}$$

Equation 4.8 shows that the ratio is proportional to the square of the aspect ratio l_1/w_1. With the beam length l_1 at 400 μm and the beam width w_1 at 5 μm a stiffness ratio of 1.024×10^5 for the double folded spring suspension can be achieved. It has been shown that the maximum linear deflection of comb drive actuators is primarily dependant on the stiffness ratio of the suspension system [81],

$$\delta_{max} = g_1 \sqrt{\frac{k_y}{2k_x}} - \frac{\delta_0}{2} . \tag{4.9}$$

The above formula suggests that the maximum deflection δ_{max} rises with increasing electrode separation g_1 and also with increasing stiffness ratio k_x/k_y of the double folded spring suspensions. It is also interesting to observe the effect of initial overlap δ_0. Larger overlaps can reduce the largest achievable deflection. Inserting the design parameters for the 1D actuator in Equation 4.9 a maximum translation of 1.1 mm is calculated. Even though this value is very large and well within the range of the maximum achievable actuation of 20 μm, it is important to note that this value does not take into consideration the dependency of axial stiffness on the generated deflection. The stiffness of the double folded beam flexure in y direction decreases with the increase of the displacement δ_x in the x direction. The total spring constant k_y of a double folded beam suspension is composed of two springs in series connection [81]. The first elastic spring constant resulting from Hook's law, i.e., equation 4.7, which is rewritten and calculated here,

$$k'_y = \frac{16Ew_1 h_1}{l_1} = 4.056\times10^6 \text{N/m} \tag{4.10}$$

while the second is a deflection-dependant spring constant, which can be derived as [138],

$$k''_y = \frac{50Eh_1 w_1^3}{\left(\frac{6}{4}\delta_x - 5d\right)^2 l_1} \tag{4.11}$$

where δ_x is the total deflection in x direction and d is the projection of the flexure beams on to the x axis when tilted. Since there is no initial tilt on the flexure beams of the double folded spring suspension present d is zero. Also with $\delta_x = 20$ µm equation 4.11 can be rewritten and the deflection-dependant spring constant can be calculated as,

$$k''_y = \frac{400Eh_1w_1^3}{18\delta_x^2 l_1} = 3.521\times10^5 \text{ N/m} \tag{4.12}$$

As expected the deflection-dependant term is smaller, in fact around the order of 10 smaller than the elastic term of the total spring constant. As mentioned earlier the two springs are in series connection, so that the total stiffness in y direction is,

$$k_y = \frac{k'_y \cdot k''_y}{k'_y + k''_y} \tag{4.13}$$

Inserting the spring constant values from equation 4.10 and 4.12 into equation 4.13 the effective total spring constant at a maximum deflection of 20 µm can be calculated as $k_y = 3.240\times10^5$ N/m. Now we can re-calculate the maximum stable deflection δ_{max} of the comb drive in x direction by applying the total spring constant of Equation 4.13 to Equation 4.9. Thus, the maximum stable displacement δ_{max} including the dependency of axial stiffness on the generated deflection is 315 µm. This value is much larger than the length of each comb finger in our device design making our comb drive actuator, hence the optical cavity, inherently stable.

In the following is an overview of the theoretical calculated design parameters for the lateral instability of the 1D actuator.

Parameters	**Eq.**	**Value**
Spring constant of one beam segment in y direction $k_{y,beam}$ [kN/m]	4.6	253.5
Total spring constant in y direction k_y [MN/m]	4.7	4.1
Stiffness ratio for double folded spring suspension k_y/k_x	4.8	1.024^5
Maximum linear deflection δ_{max} [mm]	4.9	1.1
First elastic spring constant of double folded spring k'_y [N/m]	4.10	4.056^6
Second elastic spring constant of double folded spring k''_y [N/m]	4.11	3.521^5
Total spring constant in y direction $k_{y,d}$ considering axial stiffness upon deflection [N/m]	4.13	3.24^5
Maximum linear deflection $\delta_{max,d}$ considering $k_{y,d}$ [µm]	4.9	315

Table 4-3: Theoretical calculated design parameters for the lateral instability of the 1D actuator.

Dynamic Response

Instability of the optical cavity can also be caused by external vibrations, which are estimated to be in the range of 0 - 100 Hz. When the external vibration frequencies are close to the resonant frequencies of the system it is very likely that the optical cavity goes off resonance and becomes unstable making atom experiments impossible. Therefore it is important to analyse the dynamic response of the one-dimensional actuation structure. Figure 4-4 shows a typical comb drive actuator with a double folded suspension. The actuator has a stationary part and a movable part. The movable part also referred to as shuttle in the following consists of the comb fingers that are connected to the shuttle. Under the assumption that the comb fingers and base plate are rigid the entire shuttle can be seen as a lumped mass. The shuttle is suspended by two double folded springs, each consisting of three rigid trusses and eight beams.

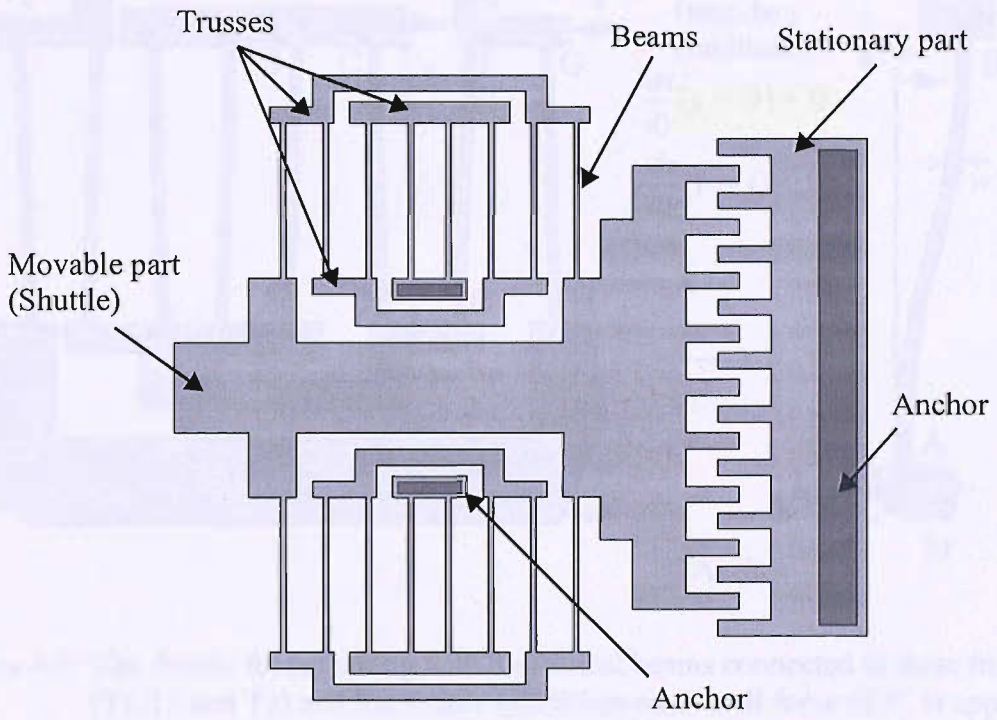

Figure 4-4: Typical comb drive actuator with a double folded spring suspension. The comb fingers of the stationary part are anchored and engage with the movable fingers of the shuttle. The shuttle is suspended by two double folded springs. Each spring consists of eight identical beams, which are attached to an second anchor and three trusses.

In general the resonant frequency of the comb drive can be calculated as,

$$f = \frac{1}{2\pi}\sqrt{\frac{k_x}{M}} \tag{4.14}$$

where k_x is the spring constant in x direction and M is the mass of the movable structure. However, equation 4.14 is a very approximate solution for the resonant frequency. In order to derive a more accurate solution for the resonant frequency the effective mass of the lumped elements such as shuttle, trusses and beams need to be considered. Rayleigh's energy method can be used to find the effective mass of the actuation system [135]:

$$KE_{max} = PE_{max} \tag{4.15}$$

where KE_{max} is the maximum kinetic energy during a vibration cycle, and PE_{max} is the maximum potential energy. First the kinetic energy KE_{max} is evaluated.

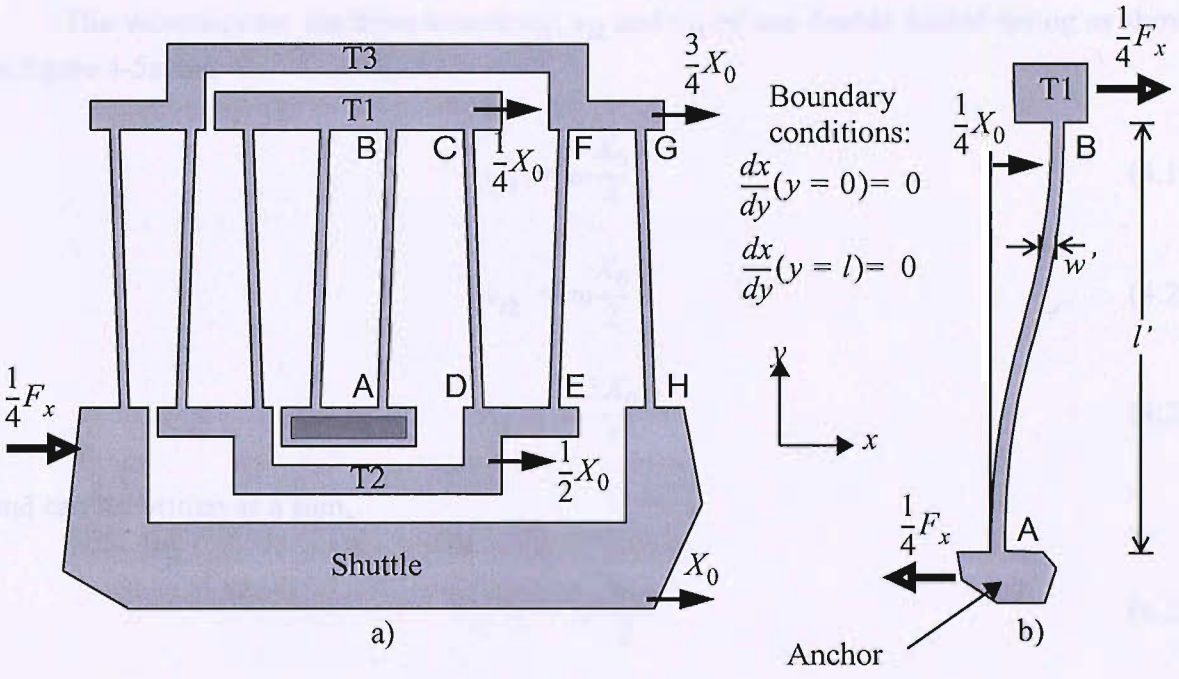

Figure 4-5: The double folded spring with 8 identical beams connected to three trusses (T1,T2 and T3) and the shuttle (a). When an overall force of F_x is applied, each beam experiences a force of $F_x/4$ and is deflected by $X_0/4$.

It is assumed that during the motion, the beams all displace with mode shapes equal to their deflections under static load. Figure 4-5a shows one of the double folded springs and the mode shapes when the resonant shuttle is displaced by X_0 under a force of F_x in the positive x direction. Each of the beams has a length l', width w' and thickness h'. Due to the parallel beam design of the double folded flexure, the analysis can be simplified by considering a beam segment [AB], which is illustrated in figure 4-5b. All the connecting trusses for the eight beam segments are considered rigid, because of the wider design of the trusses. Therefore, as part of the boundary conditions, the slopes at both ends of the beams are identically zero. Also since geometric shortening in the y direction is identical for all 8 beams, there is no induced axial stress as a result of large deflections.

KE reaches its maximum when the structure is at maximum velocity, and is given by,

$$KE_{max} = KE_s + KE_t + KE_b \tag{4.16}$$

$$KE_{max} = \frac{1}{2}v_s^2 M_s + \frac{1}{2}v_t^2 M_t + \frac{1}{2}\int v_b^2 M_b \tag{4.17}$$

where *M's* and *v's* are the masses and maximum velocity, and subscripts *s*, *t* and *b* refer to the shuttle, the sum of the six horizontal trusses and the sum of the sixteen parallel beam segments, respectively. The velocity of the shuttle is,

$$v_s = \omega X_0 \,. \tag{4.18}$$

The velocities for the three trusses v_{t1}, v_{t2} and v_{t3} of one double folded spring as shown in figure 4-5a are,

$$v_{t1} = \omega\frac{X_0}{4} \tag{4.19}$$

$$v_{t2} = \omega\frac{X_0}{2} \tag{4.20}$$

$$v_{t3} = \omega\frac{3X_0}{4} \tag{4.21}$$

and can be written as a sum,

$$v_{t1-3} = \omega\frac{3X_0}{2} \,. \tag{4.22}$$

And so the *KE* for the shuttle and the six trusses are,

$$KE_s = \frac{1}{2}v_s{}^2 M_s = \frac{1}{2}X_0{}^2\omega^2 M_s \tag{4.23}$$

and

$$KE_t = \frac{1}{2}(v_{t1-3})^2 M_t = \frac{9}{8}X_0{}^2\omega^2 M_t \,. \tag{4.24}$$

The velocity profile of the beam segments is proportional to the mode shape at maximum displacement. The mode shape is taken as the static displacement curve under static loading, a common and sufficient assumption given that the beam do not resonate themselves. Each of the 8 pairs of the parallel beams deflect $X_0/4$ and each of them experience a force of $F_x/4$ as shown in figure 4-5b, hence the structural beam deflection equation for the beam segment [AB] is given as [73],

$$x(y) = \frac{F_x}{4(12)E'I'_z}(3l'y^2 - 2y^3) \qquad \text{for } 0 \le y \le l' \tag{4.25}$$

where E' is the Young's modulus of the beam material and I'_z is the moment of inertia of the beam cross section with respect of the z axis. The beam segment [AB] is deflected by $X_0/4$ at point B, so with the boundary condition of $x(l') = X_0/4$ the equation 4.25 can be rewritten as,

$$\frac{X_0}{4} = \frac{F_x l'^3}{48E'I'_z}. \tag{4.26}$$

Substituting equation 4.26 into equation 4.25 the term $F_x/E'I'_z$ is eliminated,

$$x(y) = \frac{X_0}{4}\left[3\left(\frac{y}{l'}\right)^2 - 2\left(\frac{y}{l'}\right)^3\right]. \tag{4.27}$$

Now the velocity profile for segment [AB] can be derived as,

$$v_b(y)\big|_{[AB]} = \frac{X_0}{4}\left[3\left(\frac{y}{l'}\right)^2 - 2\left(\frac{y}{l'}\right)^3\right]\omega \tag{4.28}$$

leading to the KE for [AB] as,

$$KE_{[AB]} = \frac{1}{2}\int v_b^2 dM_{[AB]} \tag{4.29}$$

$$KE_{[AB]} = \frac{1}{2}\int_0^{l'} \frac{X_0^2\omega^2}{16}\left[3\left(\frac{y}{l'}\right)^2 - 2\left(\frac{y}{l'}\right)^3\right]^2 dM_{[AB]} \tag{4.30}$$

$$KE_{[AB]} = \frac{X_0^2\omega^2 M_{[AB]}}{32l'}\int_0^{l'}\left[3\left(\frac{y}{l'}\right)^2 - 2\left(\frac{y}{l'}\right)^3\right]^2 dy \tag{4.31}$$

$$KE_{[AB]} = \frac{13}{1120}X_0^2\omega^2 M_{[AB]} \tag{4.32}$$

where $M_{[AB]}$ is the mass of the segment [AB].

Similarly the $KE_{[CD]}$ is evaluated by first finding the deflection profile,

$$x(y) = \frac{X_0}{4}\left[(-3)\left(\frac{y}{l'}\right)^2 + 2\left(\frac{y}{l'}\right)^3\right] + \frac{X_0}{2} \tag{4.33}$$

then the velocity profile,

$$v_b(y)\big|_{[CD]} = X_0\left[-\frac{3}{4}\left(\frac{y}{l'}\right)^2 + \frac{1}{2}\left(\frac{y}{l'}\right)^3 + \frac{1}{2}\right]\omega \tag{4.34}$$

and finally the kinetic energy KE for the beam segment [CD],

$$KE_{[CD]} = \frac{X_0{}^2\omega^2 M_{[CD]}}{2l'}\int_0^{l'}\left[-\frac{3}{4}\left(\frac{y}{l'}\right)^2 + \frac{1}{2}\left(\frac{y}{l'}\right)^3 + \frac{1}{2}\right]^2 dy \tag{4.35}$$

$$KE_{[CD]} = \frac{83}{1120}X_0{}^2\omega^2 M_{[CD]}\,. \tag{4.36}$$

The kinetic energy $KE_{[EF]}$ for the beam segment [EF] is found to be,

$$x(y) = \frac{X_0}{4}\left[3\left(\frac{y}{l'}\right)^2 - 2\left(\frac{y}{l'}\right)^3\right] + \frac{X_0}{2} \tag{4.37}$$

$$v_b(y)\big|_{[EF]} = \frac{X_0}{4}\left[3\left(\frac{y}{l'}\right)^2 - 2\left(\frac{y}{l'}\right)^3 + 2\right]\omega \tag{4.38}$$

$$KE_{[EF]} = \frac{X_0{}^2\omega^2 M_{[EF]}}{8l'}\int_0^{l'}\left[3\left(\frac{y}{l'}\right)^2 - 2\left(\frac{y}{l'}\right)^3 + 2\right]^2 dy \tag{4.39}$$

$$KE_{[EF]} = \frac{223}{280}X_0{}^2\omega^2 M_{[EF]}\,. \tag{4.40}$$

Also the kinetic energy $KE_{[GH]}$ for the beam segment [GH] can be calculated as,

$$x(y) = \frac{X_0}{4}\left[(-3)\left(\frac{y}{l'}\right)^2 + 2\left(\frac{y}{l'}\right)^3\right] + X_0 \tag{4.41}$$

$$v_b(y)\big|_{[GH]} = X_0\left[-\frac{3}{4}\left(\frac{y}{l'}\right)^2 + \frac{1}{2}\left(\frac{y}{l'}\right)^3 + 1\right]\omega \tag{4.42}$$

$$KE_{[GH]} = \frac{X_0{}^2\omega^2 M_{[GH]}}{2l'}\int_0^{l'}\left[-\frac{3}{4}\left(\frac{y}{l'}\right)^2 + \frac{1}{2}\left(\frac{y}{l'}\right)^3 + 1\right]^2 dy \tag{4.43}$$

$$KE_{[GH]} = \frac{433}{1120}X_0{}^2\omega^2 M_{[GH]}\,. \tag{4.44}$$

Since the total mass of all beams of the two double folded springs is M_b each beam segment is,

$$M_{[AB]} = M_{[CD]} = M_{[EF]} = M_{[GH]} = \frac{1}{16}M_b. \tag{4.45}$$

Therefore,

$$KE_b = 4KE_{[AB]} + 4KE_{[CD]} + 4KE_{[EF]} + 4KE_{[GH]} \tag{4.46}$$

$$KE_b = \frac{13}{4480}X_0{}^2\omega^2M_b + \frac{83}{4480}X_0{}^2\omega^2M_b + \frac{223}{1120}X_0{}^2\omega^2M_b + \frac{433}{4480}X_0{}^2\omega^2M_b \tag{4.47}$$

$$KE_b = \frac{1421}{4480}X_0{}^2\omega^2M_b. \tag{4.48}$$

Collecting the results in equations 4.23, 4.24 and 4.48 and substituting them into equation 4.17 yields

$$KE_{max} = X_0{}^2\omega^2\left(\frac{1}{2}M_s + \frac{9}{8}M_t + \frac{1421}{4480}M_b\right). \tag{4.49}$$

Now the potential energy PE_{max} to achieve maximum deflection is evaluated,

$$PE_{max} = \int_0^{X_0} F_x dx = \int_0^{X_0} k_x x dx = \frac{1}{2}k_x X_0{}^2. \tag{4.50}$$

Finally the resonant frequency can be derived as,

$$KE_{max} = PE_{max} \tag{4.51}$$

$$X_0{}^2\omega^2\left(\frac{1}{2}M_s + \frac{9}{8}M_t + \frac{1421}{4480}M_b\right) = \frac{1}{2}k_x X_0{}^2 \tag{4.52}$$

$$\omega = \sqrt{\frac{k_x}{\left(M_s + \frac{18}{8}M_t + \frac{1421}{2240}M_b\right)}}. \tag{4.53}$$

The denominator on the right-hand side of equation 4.53 can be lumped together as the effective mass of the system,

$$M_{eff} = M_s + \frac{18}{8}M_t + \frac{1421}{2240}M_b \tag{4.54}$$

such that,

$$f_{0,1D} = \frac{1}{2\pi}\sqrt{\frac{k_x}{M_{eff}}} \tag{4.55}$$

where $f_{0,1D}$ is the fundamental resonance frequency. Applying equation 4.55 to the one-dimensional comb drive actuation structure the masses M_s, M_t and M_b are calculated as,

$$M_s = V_s\rho \tag{4.56}$$

$$M_t = V_t\rho \tag{4.57}$$

$$M_b = V_b\rho \tag{4.58}$$

where V_s, V_t and V_b are the volumes occupied by the masses and ρ is the density of silicon. With the values for the volumes and the silicon density the masses are calculated and summarized in table 4-4. With an effective mass M_{eff} and the spring constant k_x the fundamental resonance frequency of the one-dimensional actuator using equation 4.55 is calculated to $f_{0,1D}$ = 1522 Hz. In comparison, the fundamental resonance frequency f_{1D} of the approximate solution from equation 4.14 is calculated at 1728 Hz. In the following the theoretical calculated design parameters for the dynamic response of the 1D actuator is summarized.

Parameters	**Eq.**	**Value**
Density of silicon ρ [kg/μm^3]	-	2.5^{-15}
Volume of shuttle V_s [μm^3]	-	1.344^{8}
Volume of six trusses V_t [μm^3]	-	3.513^{7}
Volume of sixteen beam segments V_b [μm^3]	-	3.84^{6}
Mass of shuttle M_s [kg]	4.56	3.359^{-7}
Mass of six trusses M_t [kg]	4.57	8.782^{-8}
Mass of sixteen beam segments M_b [kg]	4.58	9.6^{-9}
Effective Mass of 1D actuator M_{eff} [kg]	4.54	4.334^{-7}
Total spring constant in x direction k_x [N/m]	4.5	39.61
Fundamental resonance frequency of 1D actuator $f_{0,1D}$ [Hz] (effective mass model)	4.55	1522
Fundamental resonance frequency of 1D actuator f_{1D} [Hz] (approximate solution)	4.1	1728

Table 4-4: Theoretical calculated design parameters for the dynamic frequency response of the 1D actuator.

4.2.3 Simulation

CoventorWare™ software simulations are carried out to confirm the analytical results. CoventorWare™ software is based on the finite element method (FEM) and the boundary ele-

ment method (BEM). A parabolic, manhattan bricks type mesh model is applied. The simulations carried out using this specific mesh model are more time consuming, but deliver more accurate simulation results. Because of the quite large dimensions of the two actuation designs (1D and 3D) the simulations are carried out for each relevant part individually such as comb drive, double-folded spring suspension and center mass actuation. The solid element mesh size of each part is optimized separately and varies to achieve an overall good simulation result considering the size of the part, computing time and simulation outcome. The constant material properties used during the simulations are shown in table 4-5.

	Silicon Substrate
Mass Density [kg/μm^3]	2.5^{-15}
Elastic Modulus [GPa]	169

Table 4-5: Material Properties.

Static Translation Curve

The maximum electrostatic force of the one-dimensional actuator is generated by 200 engaged comb fingers at a maximum available voltage of 150 Volts. Due to the large number of comb fingers and overall size of the structure in combination with the restriction to computation memory, only one pair of the mating comb fingers is electrostatically simulated. In order to obtain the full force of the entire comb drive the force is then multiplied by 200 (the total sum of finger pairs).

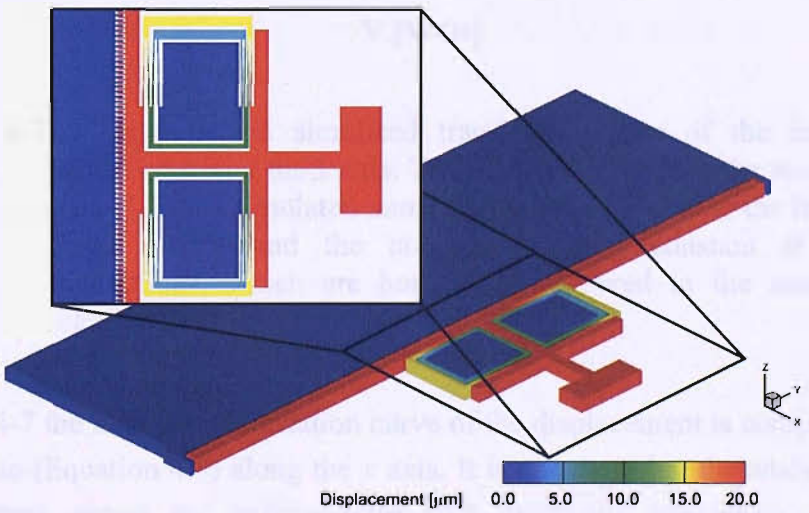

Figure 4-6: Simulated translation of the comb drive structure in *-x* direction of 20 μm at 145 Volts with a generated electrostatic force of 0.745 mN.

With an element mesh size of 1 µm the electrostatic force at the voltage of 150 Volts between one movable comb finger and two anchored fingers is simulated and yields 4.45 µN. Multiplied by the amount of 200 interlocked comb fingers the total electrostatic force $F_{e,1D}$ is found to be 0.890 mN. The simulated total force $F_{e,1D}$ generated by the comb drive at 150 Volts is within 7% of the theoretical value at 0.955 mN. Based on the maximum available electrostatic force $F_{e,1D}$ a displacement of the movable part of the comb drive is simulated and the result is shown in figure 4-6. In order to translate the shuttle up to maximum achievable translation of 20 µm in -x direction a voltage of 145 V is required, which corresponds to a simulated electrostatic force of 0.745 mN.

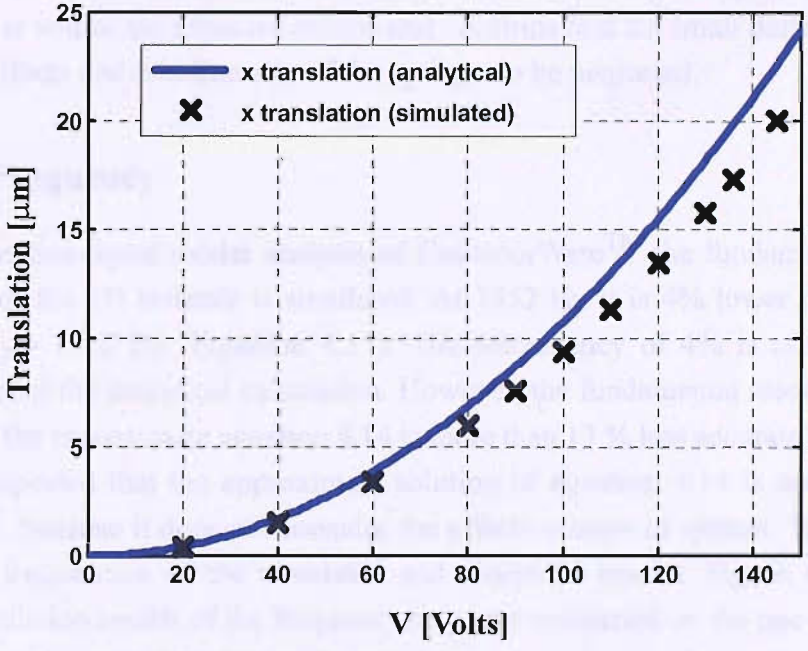

Figure 4-7: Analytical and simulated translation curve of the in-plane actuation along the x axis. The mismatch between the analytical (Eq. 4.3) and simulated translation curve is related to the fringing field effects and the non-linear spring constant at large deflections, which are both not considered in the analytical calculations.

In figure 4-7 the simulated translation curve of the displacement is compared to the analytical translation (Equation 4.3) along the x axis. It is apparent that the analytical and simulated displacement curves are drifting apart with increasing translation. This mismatch between is related to the fringing field effects and the non-linear spring constant at large deflections, which are both not considered in the analytical calculations. In table 4-6 the voltages of the simulated and analytical operating point at 4 µm are compared. Also the simulated and analytical maximum achievable translation is verified.

Parameters	Simulated			Analytical		
	Voltage	Transl.	Force	Voltage	Transl.	Force
Minimum required translation (operating point)	63 V	4 µm	0.153 mN	61 V	4 µm	0.158 mN
Maximum achievable translation	145 V	20 µm	0.745 mN	137 V	20 µm	0.797 mN

Table 4-6: Comparison of the simulated and analytical translation results for the 1D actuator.

At the operating point of 4 µm the simulated voltage is 3 % higher than the analytical result, which is within the expected results and confirms that for small deflections up to 4 µm the fringing effects and non-linearity of the spring can be neglected.

Resonant Frequency

With the non-linear modal analysis of CoventorWare™ the fundamental resonant frequency $f_{s,1D}$ of the 1D actuator is simulated. At 1452 Hz it is 4% lower than the analytical value of $f_{0,1D}$ = 1522 Hz (Equation 4.55). The discrepancy of 4% is caused by the linear approximation of the analytical calculation. However, the fundamental resonant frequency f_{1D} = 1728 Hz of the approximate equation 4.14 is more than 13 % less accurate than the simulated value. It is expected that the approximate solution of equation 4.14 is not as accurate than equation 4.55, because it does not consider the effective mass of system. Table 4-7 compares the resonant frequencies of the simulated and analytical results. Figure 4-8 represents the graphical simulation results of the frequency response conducted on the one-dimensional actuation structure, showing that the fundamental frequency $f_{s,1D}$ is determined by the displacement along the x axis of the trusses and beams from the double folded spring flexure. While the anchors remain at their zero position the shuttle, trusses and beams of the two double folded springs oscillate along the x axis.

Parameter	Simulated	Analytical	
Fundamental resonant frequency	1452 Hz	1522 Hz (Eq. 4.55)	1728 Hz (Eq. 4.14)

Table 4-7: Comparison of the simulated and analytical dynamic frequency response for the 1D actuator.

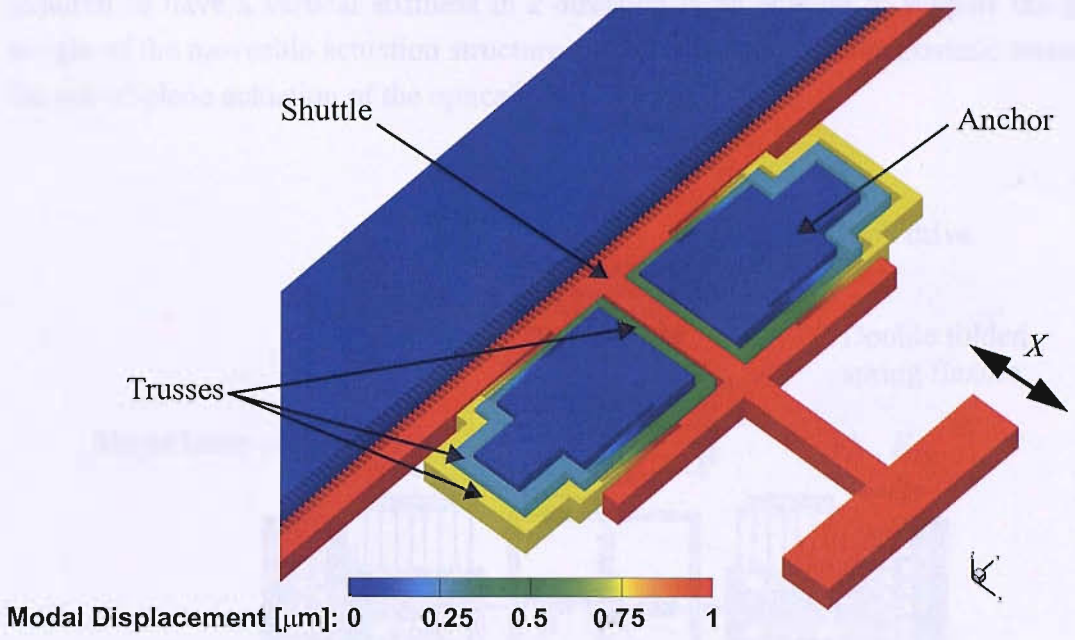

Figure 4-8: Simulated dynamic response of the 1D actuation structure at a fundamental resonant frequency $f_{s,1D}$ of 1452 Hz. While the anchors remain at zero position (blue), the shuttle is oscillating between zero and plus one micron (red) along the x axis.

4.3 Three-dimensional Actuator (3D)

4.3.1 Design Layout

The three-dimensional actuator is an out-of-plane actuator, which is used for the optical cavity alignment in xy direction and the optical cavity tuning in z direction. The actuation in the xy direction is used to compensate any misalignment during the assembling process of the multi-layered wafer stack. The misalignment between both cavity mirrors is caused by the inaccuracy of the bonding equipment and is in the order of five microns. The easiest way to achieve a stroke length of a few microns is through a comb drive. With a setup of four identical comb drives as shown in figure 4-9 it is possible to actuate a center stage in the wafer plane. By using double folded spring flexures for each comb drive spring constants below 50 N/m in the direction of actuation can be achieved. The center stage is connected via four single beam elements functioning as spring suspensions. In this arrangement the center stage can be translated within the wafer plane in $+x$, $-x$, $+y$ and $-y$ direction. The center stage itself incorporates a center mass, which is positioned by four spring suspensions in the middle of the center stage and encloses a microfabricated optical cavity mirror. The four springs attached to the center mass are required to have a low spring constant in z direction in order to actuate the center mass by a parallel plate configuration with low electrostatic forces. This is contrary to the

requirements of the single beam and double folded spring suspensions, because they are required to have a vertical stiffness in z direction large enough to support the gravitational weight of the moveable actuation structure and to withstand the electrostatic forces caused by the out-of-plane actuation of the optical cavity mirror.

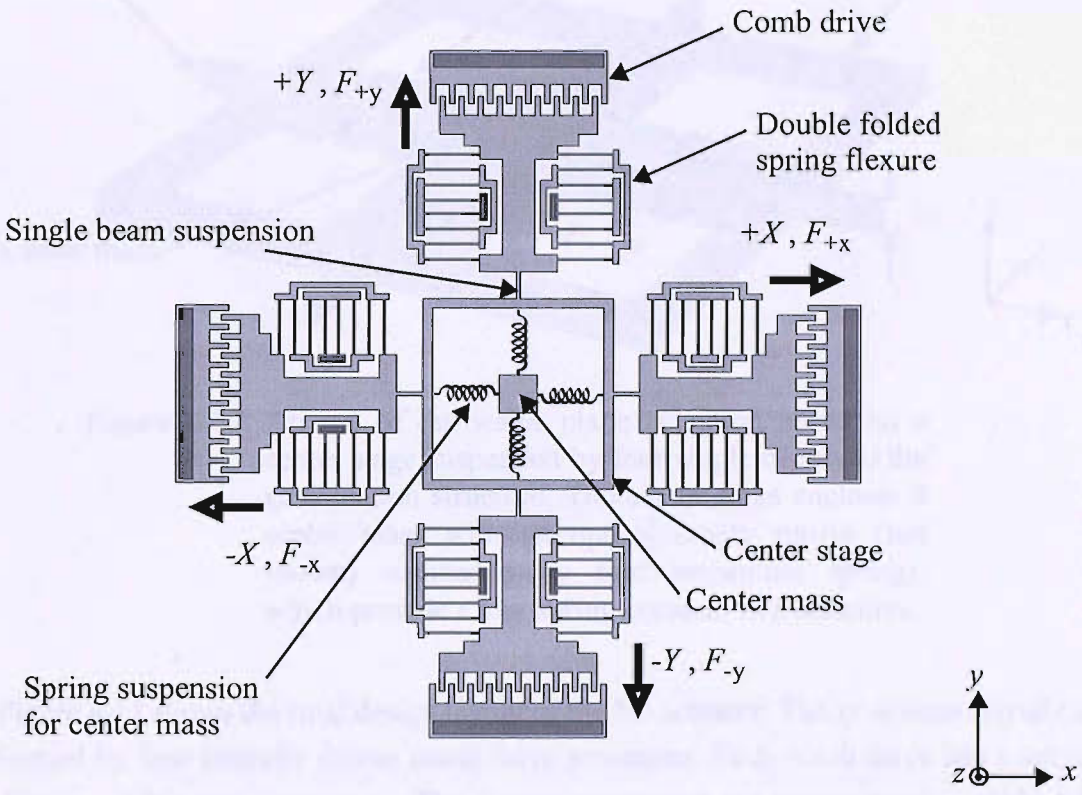

Figure 4-9: A 3D actuator using four identical comb drives suspended by double folded spring flexures for actuating a center stage in the wafer plane (xy direction). The center stage is connected via four single beam suspensions to each comb drive and encloses a suspended center mass with a fabricated optical cavity mirror. The center mass is actuated out of the wafer plane (z direction) by a parallel plate configuration.

The thickness (or height) h_2 of the actuation structures such as comb drives and spring suspensions are of the same thickness as the center stage and the center mass with its spring suspensions, because all of the parts are etched and released simultaneously during one DRIE process. Since the thickness h_2 is directly correlated with the electrostatic force of the comb drives and the spring constants, it is advantageous to enlarge the thickness. However, maximizing the thickness to 120 µm would enlarge the disadvantageous stiffness of the center mass suspension in the z direction. By dividing the thickness in half to h_2 = 60 µm and using a serpentine spring suspension (as shown in figure 4-10) for the center mass a good trade-off is

achieved. The decrease of electrostatic force due to half of the thickness can easily compensated by a large number of comb fingers. The serpentine spring can provide a low spring constant in z direction [136],[137].

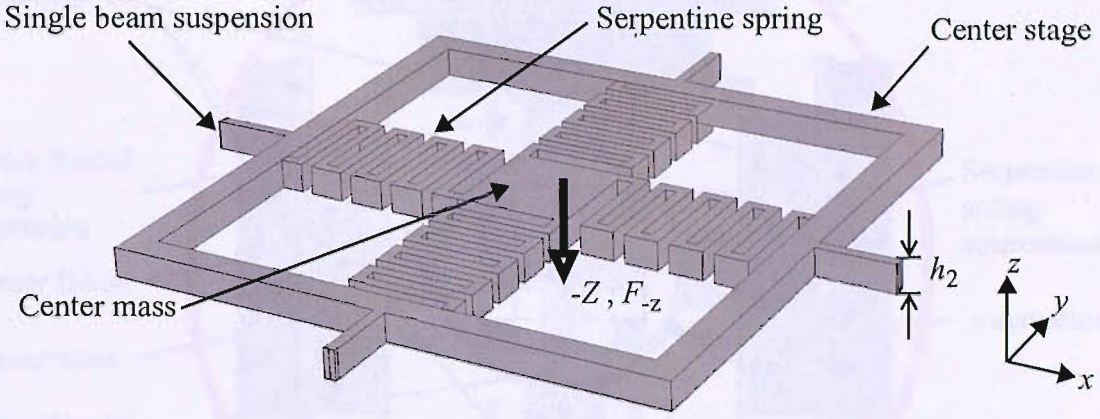

Figure 4-10: An out of the wafer plane actuation based on a center stage suspended by four single beams to the xy actuation structure. The center stage encloses a center mass with an optical cavity mirror (not shown) suspended by four serpentine springs, which provide a low spring constant in z direction.

Figure 4-11 shows the final design layout of the 3D actuator. The xy actuation (red circle) is performed by four laterally driven comb drive structures. Each comb drive has a set of N_2 comb fingers with a gap spacing g_2. The design parameters are summarized in table 4-8 on page 63. With an actuation structure height of h_2 all comb drives are suspended by a set of double-folded spring suspensions, which have a beam width w_2 at a length l_2. Each comb drive is connected by a single beam suspension to a center frame structure. A single beam spring has a length l_3 and a width w_2. The center frame structure encloses a movable mass at the center, which is suspended by four serpentine springs and is actuated in z direction using a parallel plate configuration (green circle). A more detailed three-dimensional drawing of the center frame structure and the parallel plate configuration is shown in figure 4-12. The center mass with the spherical cavity mirror (not shown) is suspended by four serpentine springs. A serpentine spring design is chosen in order to achieve a low spring constant, hence low actuation voltage for the z actuation. The center mass is electrostatically pulled in by applying a voltage between the bottom electrode of the pillar structured center mass and the counter gold electrode (yellow) on the opposite wafer surface. This parallel plate configuration with a gap distance g_3 is used to actuate the cavity mirror along the z axis.

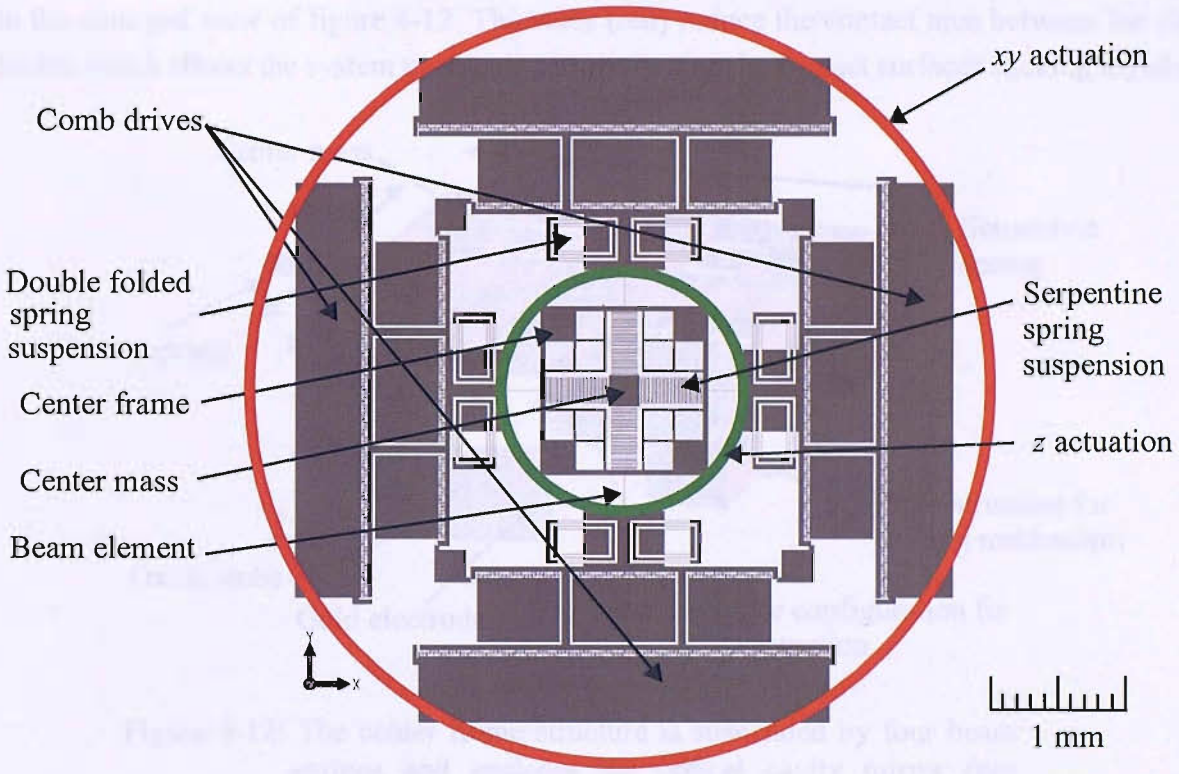

Figure 4-11: The design layout of the 3D 5 x 5 mm actuator includes four individually driven comb drive actuators for *xy* actuation in the wafer plane (red circle). Suspended on double folded spring suspensions each comb drive is attached to the center frame structure by four single beam suspensions. The center frame encloses a center mass with an embedded cavity mirror, which is suspended by four serpentine springs for *z* actuation.

In order to achieve independent actuation between the *xy* and *z* actuation additional parallel plate configurations are incorporated in the center frame structure. In each corner of the frame a pillar structure is located enabling the center frame to be locked once the *xy* optical cavity alignment is carried out. The idea behind this simple but very effective and novel locking mechanism is to anchor the center frame structure to a supporting wafer and thereby improving the stability of the optical cavity against external vibrations. The locking mechanism is based on the electrostatic parallel plate pull-in phenomenon that occurs between the four pillar structures and the embedded opposite facing counter gold electrodes (yellow). The gap spacing of the electrodes is g_4 (see table 4-8 on page 63). At the pull-in voltage the four pillar structures snap towards the bottom electrodes and secure the center frame structure to the substrate. This locks the *xy* actuation stage. The system can be unlocked simply by switching off the applied voltage. In order to avoid a discharge between the two electrodes several silicon

oxide stubs are processed on the bottom surface of the silicon pillars facing the gold electrodes. The oxide stubs are 1 μm in height each with a surface area of 25 μm^2. The principle is shown in the enlarged view of figure 4-12. The stubs (red) reduce the contact area between the electrodes which allows the system to unlock without having the contact surfaces sticking together.

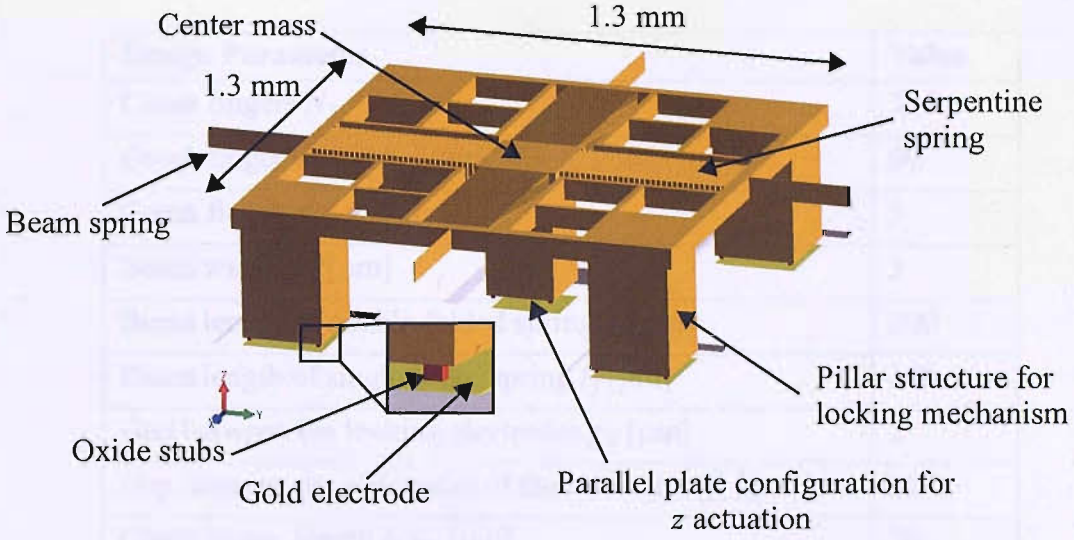

Figure 4-12: The center frame structure is suspended by four beam springs and encloses the optical cavity mirror (not shown) in the center mass. The center mass is suspended by four serpentine springs and is electrostatically actuated towards the bottom gold electrode in -*z* direction. The four pillar structures in each corner of the frame are used to mechanically lock the *xy* alignment actuation, before any cavity tuning takes place. Silicon oxide stubs (red) as seen in the enlarged view avoid stiction of the parallel plate configurations.

4.3.2 Analytical Analyses

With regards to the design layout described in the previous section and the following analytical analyses the design parameters of the 3D actuator are summarized in table 4-8.

Design Parameter	Value
Comb fingers N_2	330
Comb finger height h_2 [μm]	60
Comb finger gap g_2 [μm]	3
Beam width w_2 [μm]	3
Beam length of double folded spring l_2 [μm]	200
Beam length of single beam spring l_3 [μm]	300
Gap between the locking electrodes g_4 [μm]	2
Gap between the electrodes of the z actuator g_3 [μm]	21
Comb finger length $l_{F,3D}$ [μm]	30
Comb finger width $w_{F,3D}$ [μm]	5
Comb finger overlap $\delta_{0,3D}$ [μm]	10
Height of stubs h_s [μm]	1
Surface area of stubs A_s [μm^2]	25
Surface area of z actuation electrode A_z [mm^2]	0.04
Total surface area of locking electrodes A_L [mm^2]	0.221

Table 4-8: Design parameters for the 3D actuator.

XY Actuation

The translation in the wafer plane of the 3D actuator is achieved by four identical comb drives. Each comb drive consists of N_2 comb fingers. The gap g_2 between the comb fingers and the beam width w_2 of the double folded spring suspensions as shown in figure 4-13 are at a length l_2. The four single beams connecting the comb drives with the center frame structure have a length l_3 and at the same width w_2. The height of the entire actuation structure is h_2. With the values for the physical dimensions (table 4-8) and a maximum available voltage V_2 of 150 Volts inserted in equation 4.1 the maximum lateral comb drive force $F_{c,3D}$ of one comb drive actuator is calculated to be 1.314 mN. Since Hook's law can be applied in the same manner as for the 1D actuator the translation function for the comb drive actuator can be expressed as,

$$y(V_2) = \frac{\varepsilon_0 N_2 h_2}{g_2 \cdot k_{tot}} V_2^{\,2} \tag{4.59}$$

where k_{tot} is the sum of the spring constants in the direction of actuation. For example, the comb drive responsible for the actuation in $+y$ direction (as circled green in figure 4-13) is required to overcome the retraction forces of the two pairs of double folded springs along the y axis and the two single beam springs along the x axis (circled red). It is valid to assume, that the two single beam springs are fixed at their ends connecting them with the comb drives, because the spring constants $k_{y,3D}$ for both comb drives is in the order of 10^5 N/m larger than both of the beam springs along the y axis. Hence, the total spring constant $k_{tot,y}$ in $+y$ direction can be derived as followed.

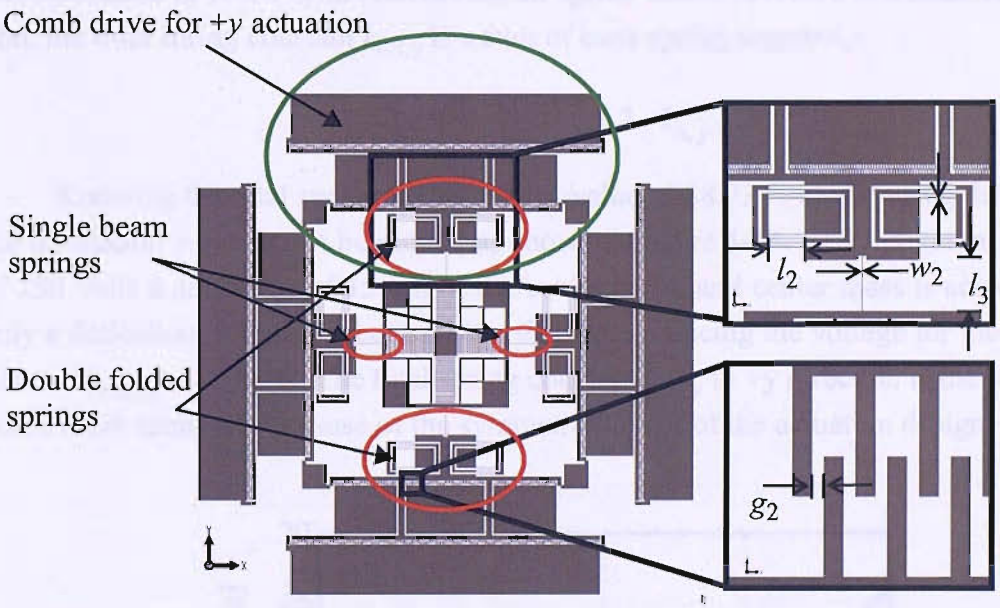

Figure 4-13: Top view of the xy actuator (5 mm x 5 mm) with critical dimensions.

Under the assumption that all beam elements have a rectangular cross-sections, the moments of inertia for the single beams $I_{b,x}$, $I_{b,z}$ and for the double folded suspension beams $I_{s,x}$, $I_{s,z}$ can be expressed by [135]:

$$I_{b,x} = I_{s,x} = \frac{h_2^{\,3} w_2}{12} \tag{4.60}$$

$$I_{b,z} = I_{s,z} = \frac{w_2^{\,3} h_2}{12} \tag{4.61}$$

Thus, the spring constant $k_{s,y}$ for the double folded spring suspension of the comb drive structure along the y axis can be written as,

$$k_{s,y} = \frac{12EI_{s,z}}{l_2^3}. \tag{4.62}$$

The calculated value for equation 4.62 is 34.22 N/m. For a translation of the center frame in the $+y$ axis the force of the $+y$ comb drive has to exceed not only the resistance of the double folded spring system given by $k_{s,y}$ of the $+y$ and the $-y$ comb drive, but also the resistance of the two single beams along the x axis connecting the $-x$ and $+x$ comb drive to the inner frame structure. The spring constant $k_{b,y}$ for a single beam is expressed by [136],

$$k_{b,y} = \frac{12EI_{b,z}}{l_3^3} \tag{4.63}$$

and calculated to 10.14 N/m. Accounting all spring forces involved in a translation in $+y$ direction, the total spring constant $k_{tot,y}$ is a sum of each spring segment,

$$k_{tot,y} = 2 \cdot k_{s,y} + 2 \cdot k_{b,y}. \tag{4.64}$$

Knowing the total spring constant $k_{tot,y}$ value of 88.73 N/m and using the equations 4.59 the translation curve is can be plotted as shown in figure 4-14. At a maximum voltage $V_{max,xy}$ of 150 Volts a deflection of 15 µm of the center frame and center mass is achieved. However, only a deflection of 5 µm is required and therefore reducing the voltage for the in-plane actuation to $V_{min,xy}$ = 80 Volts. The total spring constant $k_{tot,y}$ in +y direction is the same for all four comb drive actuators, because of the symmetric layout of the actuation design.

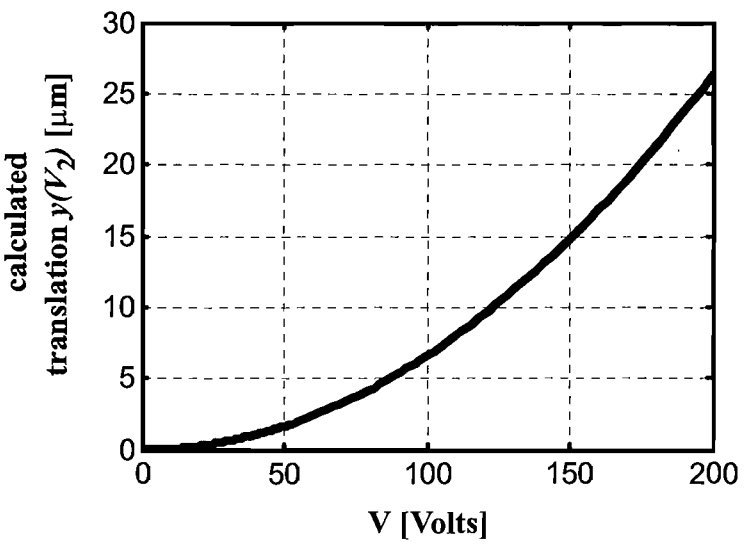

Figure 4-14: The translation curve $y(V_2)$ is identical to for all four comb drives of the actuation system due to the symmetric design layout. At a maximum of 150 Volts a deflection of 15 µm is achieved, however to deflect 5 µm in order to compensate the misalignment during wafer assembly only 80 Volts are required.

Parameters	Eq.	Value
Maximum achievable force $F_{c,3D}$ [mN] at 150 V	4.1	1.314
Moment of inertia for a single beams $I_{b,x}$ in x direction [m^4]	4.60	5.4^{-20}
Moment of inertia for a double folded suspension beam $I_{s,x}$ in x direction [m^4]	4.60	5.4^{-20}
Moment of inertia for a single beams $I_{b,z}$ in z direction [m^4]	4.61	1.35^{-22}
Moment of inertia for a double folded suspension beam $I_{s,z}$ in z direction [m^4]	4.61	1.35^{-22}
Spring constant for the double folded spring suspension $k_{s,y}$ [N/m]	4.62	34.22
Spring constant for a single beam $k_{b,y}$ [N/m]	4.63	10.14
Total spring constant in y direction $k_{tot,y}$ [N/m]	4.64	88.73
Voltage for the minimum required translation of 5 µm $V_{min,xy}$ [V]	4.59	80
Voltage for the maximum achievable translation of 15 µm $V_{max,xy}$ [V]	4.59	150

Table 4-9: Theoretical calculated design parameters of the xy translation for the 3D actuator.

Vertical Stiffness

The movable parts of the xy actuator - the four comb drives and the inner frame structure - are suspended at the anchors of the double folded spring system. This means that the entire mass weight of the movable structure is only supported by those anchors. The gravity force acting on the mass is critical to the system, because any unexpected movement of the actuation structure would result in an unstable optical cavity. The vertical stiffness of the structure specifically the stiffness of the double folded spring suspension and the single beam connections determine any undesired displacement in z direction caused by the force of gravity. In the following the gravitation displacement in z direction is calculated. The spring constants along the z axis is given by [73]

$$k_{s,z} = \frac{12EI_{s,x}}{l_2^3} \tag{4.65}$$

$$k_{b,z} = \frac{12EI_{b,x}}{l_3^3} \tag{4.66}$$

where $k_{s,z}$ is the constant for the double folded spring suspension of one comb drive and $k_{b,z}$ is the spring constant of one single beam. Consequently the total spring constant $k_{tot,z}$ is defined as

$$k_{tot,z} = 4 \cdot k_{s,z} + 4 \cdot k_{b,z} \tag{4.67}$$

$$k_{tot,z} = 4Eh_2{}^3 w_2 \left(\frac{1}{l_2^3} + \frac{1}{l_3^3} \right) \tag{4.68}$$

since four comb drive and four single beams are present. With the physical dimensions inserted in equation 4.68 the total spring constant is calculated to 7.1×10^4 N/m.

The gravitation force F_g is given by

$$F_g = M_2 \cdot g_a \tag{4.69}$$

where g_a is the gravitational acceleration and M_2 is the mass of the movable structure.

Using equations 4.69 and 4.2 the displacement z_1 of the structure in the z direction is expressed by

$$z_1 = \frac{M_2 \cdot g_a}{k_{tot,z}} = \frac{V_3 \cdot \rho \cdot g_a}{k_{tot,z}} \tag{4.70}$$

where V_3 is the volume occupied by the mass M_2 and ρ is the density of silicon. Inserting the values of table 4.10 in equation 4.7 the calculated deflection z_1 of the movable structure in z direction due to its gravitational force is 0.65 nm. With an out of plane displacement of z_1 the stability criteria for the optical cavity at 2 nm is still complied and the effect of gravitational force on the actuation system for the z actuation is negligible.

Parameters	**Eq.**	**Value**
Density of silicon ρ [kg/μm^3]	-	2.5^{-15}
Volume occupied by the mass of movable structure V_3 [μm^3]	-	1.87^8
Mass of the movable structure M_2 [kg]	-	4.68^{-7}
Gravitational acceleration g_a [m/s^2]	-	9.81
Gravitation force F_g [N/m]	4.69	4.58^{-6}
Spring constant for the double folded spring suspension $k_{s,z}$ [kN/m]	4.65	13.69
Spring constant for a single beam $k_{b,z}$ [kN/m]	4.66	4.01
Total spring constant in z direction $k_{tot,z}$ [kN/m]	4.68	7.1
Gravitational deflection z_1 of the movable structure in z direction [nm]	4.7	0.65

Table 4-10: Theoretical calculated design parameters of the vertical stiffness for the 3D actuator.

Z Actuation

The actuation along the z axis of the 3D actuator is achieved by a parallel plate configuration consisting of a fixed bottom gold electrode, which is fabricated on the surface of the supporting substrate, and a movable top electrode. The top electrode is a silicon pillar structure (center mass), which is suspended by four serpentine springs along the x and y axis (as shown in figure 4-15). The cross section A view in figure 4-15 outlines the gap g_3 between both electrodes of the z actuator and the height h_2 of the serpentine springs (see table 4-8). In each corner of the center frame structure are the single pillar structures situated (cross section view B). They are part of the parallel plate configuration, which is used to lock the system. The gap g_4 between the electrodes is 2 µm in order to minimize the pull-in voltage.

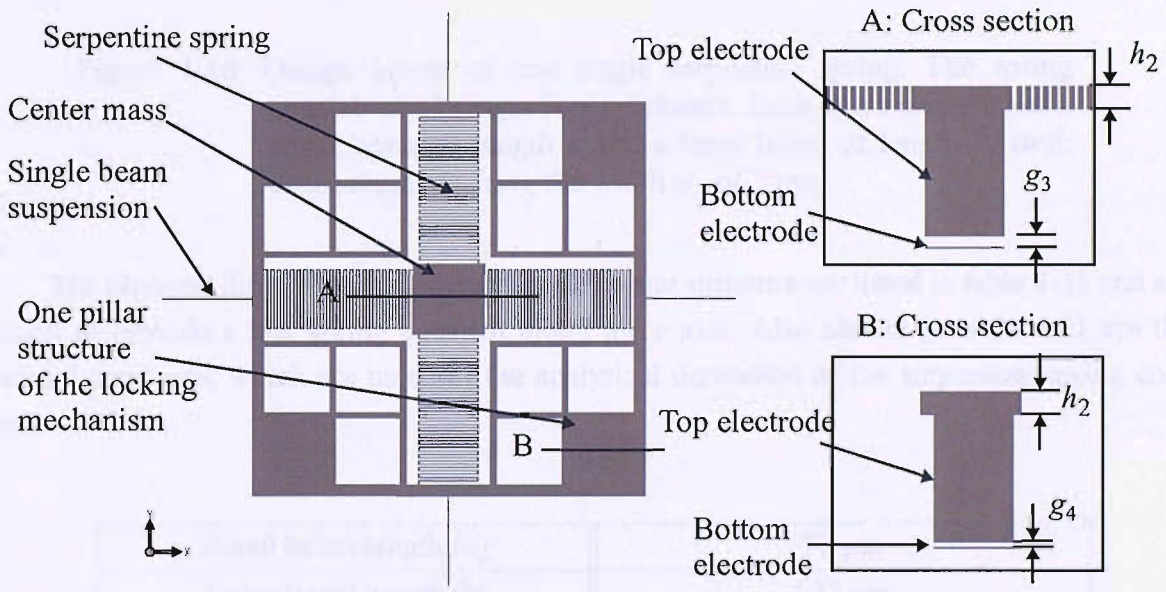

Figure 4-15: Illustration of the center frame structure (1.2 mm x 1.2 mm) detailing the structures of the xy locking mechanism and the structure of the z actuation. Each of the four pillar structures of the locking mechanism (cross section B) has a initial gap distance g_4. The center mass pillar structure has an initial gap distance g_3 (cross section A).

Serpentine Spring Constant

The actuation of the z actuator is dependant on the spring constant in z direction of the serpentine springs. Each of the four serpentine springs has 44 elements (Figure 4-16). A single beam element has a small beam of length a and a large beam of length b. The width w_3 of each beam segment is 3 µm (see enlarged view of figure 4-16).

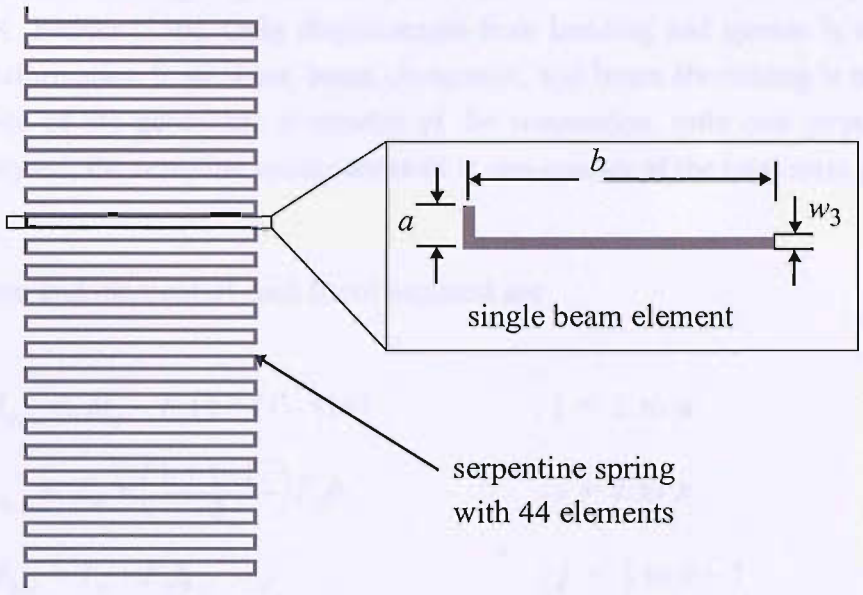

Figure 4-16: Design layout of one single serpentine spring. The spring consists of 44 single beam elements. Each beam element has a small beam of length a and a large beam of length b. Both beam segments have the width w_3 of 3 μm.

The physical dimensions of the serpentine spring structure are listed in table 4-11 and are chosen to provide a low spring constant along the z axis. Also shown in table 4-11 are the material constants, which are used for the analytical derivation of the serpentine spring constant.

Small beam length (a)	11 μm
Large beam length (b)	197 μm
Serpentine spring thickness (h_2)	60 μm
Beam width (both beams) (w_3)	3 μm
Number of beam elements (n)	44
Si Young's modulus (E)	169 GPa
Si Poisson's ratio (ν)	0.3
Shear modulus (G)	$E / (2(1+\nu))$
x axis moment of inertia (I_x)	$w_3 h_2^{\,3} / 12$
z axis moment of inertia (I_z)	$h_2 w_3^{\,3} / 12$
polar moment of inertia (I_p)	$I_x + I_z$
Torsion constant (J)	$0.3225 I_p$ (see [136])

Table 4-11: Physical dimensions and material constants for the serpentine spring.

The derivation of the spring constant k_z in z direction is based on the analytical calculations from G. K. Fedder [136]. Only displacement from bending and torsion is considered in the analysis. Deformation from shear, beam elongation, and beam shortening is neglected. By taking advantage of the geometric symmetry of the suspension, only one serpentine spring needs to be analysed; the resulting spring constant is one-quarter of the total spring constant for the system.

The torsion and moment of each beam segment are

$$M_{a,i} = M_o - F_z[\xi + (i-1)a] \quad ; i = 1 \text{ to } n \tag{4.71}$$

$$T_{a,i} = T_o + \left(\frac{1+(-1)^i}{2}\right)F_z b \quad ; i = 2 \text{ to } n$$

$$M_{b,j} = T_o + F_z \xi \quad ; j = 1 \text{ to } n-1$$

$$T_{b,j} = M_o - jF_z a \quad ; j = 1 \text{ to } n-1$$

where $M_{a,i}$ is the moment and $T_{a,i}$ the torsion of the ith small beam, and $M_{b,j}$ the moment and $T_{b,j}$ the torsion of the jth large beam. Application of the energy method [135] derives the total energy of the serpentine spring as a sum of the strain energy from torsion and moment of each beam segment,

$$U = \sum_{i=1}^{n} \int_0^a \left(\frac{M_{a,i}^2}{2EI_x} + \frac{T_{a,i}^2}{2GJ}\right) d\xi + \sum_{j=1}^{n-1} \int_0^b \left(\frac{M_{b,j}^2}{2EI_x} + \frac{T_{b,j}^2}{2GJ}\right) d\xi \tag{4.72}$$

where n is the number of beam elements, E is the Young's modulus, G is the shear modulus, I_x is the bending moment of inertia for the small and large beams in x axis and J the torsion constant.

Boundary conditions are found from the spring symmetry with the rotation angles, ϕ_0 and ψ_0, constrained to zero by the guided-end condition,

$$\phi_0 = \frac{\partial U}{\partial M_o} = 0 \tag{4.73}$$

$$\psi_0 = \frac{\partial U}{\partial T_o} = 0 \tag{4.74}$$

$$\delta_z = \frac{\partial U}{\partial F_z} \tag{4.75}$$

The application of Castigliano's second theorem - Unit-load method - to equation 4.72 with the guided-end conditions from equations 4.73 and 4.74, provides a solution for the bend-

ing moment M_o and torsion T_o.

$$\phi_0 = \frac{\partial U}{\partial M_o} = \sum_{i=1}^{n} \int_0^a \left(\frac{M_{a,i}}{EI_x} \cdot \frac{\partial M_{a,i}}{\partial M_o} + \frac{T_{a,i}}{GJ} \cdot \frac{\partial T_{a,i}}{\partial M_o} \right) d\xi + \sum_{\cdot\ \cdot\ 1}^{n-1} \int_0^b \left(\frac{M_{b,j}}{EI_x} \cdot \frac{\partial M_{b,j}}{\partial M_o} + \frac{T_{b,j}^2}{GJ} \cdot \frac{\partial T_{b,j}}{\partial M_o} \right) d\xi = 0 \tag{4.76}$$

$$\psi_0 = \frac{\partial U}{\partial T_o} = \sum_{i=1}^{n} \int_0^a \left(\frac{M_{a,i}}{EI_x} \cdot \frac{\partial M_{a,i}}{\partial T_o} + \frac{T_{a,i}}{GJ} \cdot \frac{\partial T_{a,i}}{\partial T_o} \right) d\xi + \sum_{j=1}^{n-1} \int_0^b \left(\frac{M_{b,j}}{EI_x} \cdot \frac{\partial M_{b,j}}{\partial T_o} + \frac{T_{b,j}^2}{GJ} \cdot \frac{\partial T_{b,j}}{\partial T_o} \right) d\xi = 0 \tag{4.77}$$

Substituting equations 4.71 and their first derivative in equations 4.76 and 4.77 results in,

$$\left(\sum_{i=1}^{n} \int_0^a \frac{M_o - F_z(\xi + (i-1)a))}{EI_x} d\xi \right) + \left(\sum_{j=1}^{n-1} \int_0^b \left(\frac{M_o - jF_z a}{GJ} \right) d\xi \right) = 0 \tag{4.78}$$

$$\left(\sum_{i=1}^{n} \int_0^a \frac{T_o + \frac{1}{2}(1 + (-1)^i) F_z \xi)}{GJ} d\xi \right) + \left(\sum_{j=1}^{n-1} \int_0^b \left(\frac{T_o + F_z \xi}{EI_x} \right) d\xi \right) = 0. \tag{4.79}$$

Solving the equations 4.78 and 4.79 we obtain the bending moment M_o and torsion T_o,

$$M_o = \frac{1}{2} F_z n a \tag{4.80}$$

$$T_o = -\frac{F_z b(-a(-1))^{(n+1)} EI_x + 2anEI_x - aEI_x + 2bGJn - 2bGJ}{4(anEI_x + bGJn - bGJ)} \tag{4.81}$$

For n even, equation 4.81 simplifies to,

$$T_o = -\frac{1}{2} F_z b \tag{4.82}$$

Now, the vertical displacement δ_z (Equation 4.75) can be found by solving the last boundary condition

$$\delta_z = \frac{\partial U}{\partial F_z} = \sum_{i=1}^{n} \int_0^a \left(\frac{M_{a,i}}{EI_x} \cdot \frac{\partial M_{a,i}}{\partial F_z} + \frac{T_{a,i}}{GJ} \cdot \frac{\partial T_{a,i}}{\partial F_z} \right) d\xi + \sum_{j=1}^{n-1} \int_0^b \left(\frac{M_{b,j}}{EI_x} \cdot \frac{\partial M_{b,j}}{\partial F_z} + \frac{T_{b,j}^2}{GJ} \cdot \frac{\partial T_{b,j}}{\partial F_z} \right) d\xi \tag{4.83}$$

Substituting for M_o and T_o in equations 4.71, equation 4.83 becomes

$$\delta_z = \left(\sum_{i=1}^{n} \int_0^a \left(\frac{\left(\frac{1}{2}F_z na - F_z(\xi + (i-1)a)\right)\left(\frac{1}{2}na - \xi - a(i-1)\right)}{EI_x} + \right. \right. \tag{4.84}$$

$$\left. \left. \frac{\left(-\frac{1}{2}F_z b + \frac{1}{2}(1+(-1)^i)F_z b\right)\left(-\frac{1}{2}b + \frac{1}{2}(1+(-1)^i)b\right)}{GJ} \right) d\xi \right) + \left(\right.$$

$$\left. \sum_{j=1}^{n-1} \int_0^b \frac{\left(-F_z b\frac{1}{2} + F_z\xi\right)\left(-\frac{1}{2}b + \xi\right)}{EI_x} + \frac{\left(\frac{1}{2}F_z na - jF_z a\right)\left(\frac{1}{2}na - ja\right)}{GJ} d\xi \right)$$

Solving equation 4.84 the vertical displacement δ_z is a function dependant on F_z,

$$\delta_z(F_z) = \frac{F_z(a^3GJn^3 + 3anb^2EI_x + b^3nGJ + n^3a^2bEI_x + 2na^2bEI_x - b^3GJ - 3n^2a^2bEI_x)}{12 \cdot EI_x GJ} \tag{4.85}$$

whereas G, J, n, a, b, E, I_x are constants defined by the geometry and material constants of the serpentine spring as listed in table 4-11. Finally, the total spring constant for the system is given by

$$k_{m,z} = 4F_z/\delta_z. \tag{4.86}$$

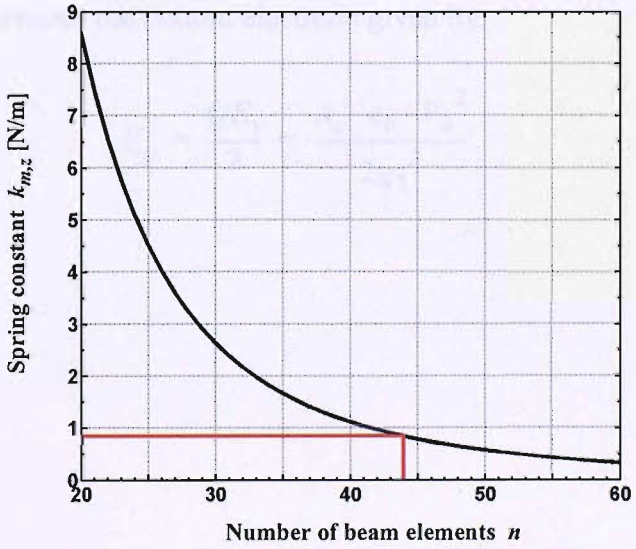

Figure 4-17: Serpentine spring constant $k_{m,z}$ vs. number of beam elements n (for even n).

Figure 4-17 displays the equation 4.86 as function $k_{m,z}$ over n (for even n). The serpentine spring constant $k_{m,z}$ for the system is outlined in figure 4-17 (red) and is calculated to be 0.835 N/m for the geometry with 44 beam elements.

Actuation Forces

The parallel plate electrostatic z actuator is based on a voltage controlled capacitor model (as shown in figure 4-18). The charge on the capacitor is

$$Q = V_4 \cdot C = \frac{V_4 A_z \varepsilon_0}{g_3} \tag{4.87}$$

where V_4 is the applied voltage, C is the capacity, A_z is the area of one capacitor plate, g_3 is the initial gap distance, and ε_0 is the permittivity of air.

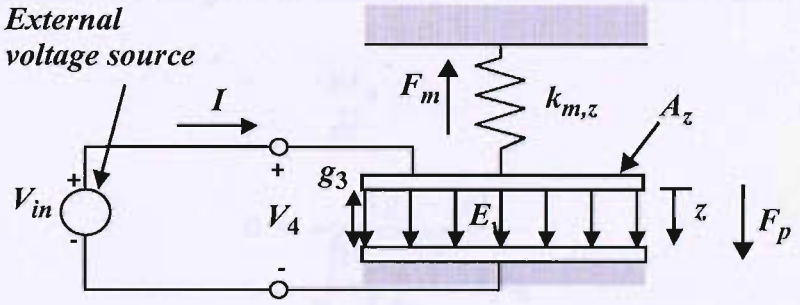

Figure 4-18: Model of the electrostatic z actuator with voltage control.

The electric field E_v between the parallel plates creates an electrostatic force F_p pulling the upper electrode towards the bottom electrode given by,

$$F_p = \frac{QE_v}{2} = \frac{A_z \cdot \varepsilon_0 \cdot V_4^{\,2}}{2g_3^{\,2}}. \tag{4.88}$$

Translation Curve for z Actuation

In the state of equilibrium between both electrodes the electrostatic force F_p is equal to the mechanical spring force F_m expressed by,

$$F_p = F_m. \tag{4.89}$$

$$\frac{A_z \cdot \varepsilon_0 \cdot V_4^2}{2(g_3 - z)^2} = k_{m,z} \cdot z \tag{4.90}$$

Solving Equation 4.90 with respect to the voltage V_4 leads to the expression

$$V_4 = \sqrt{\frac{z \cdot 2k_{m,z}}{A_z \varepsilon_0}}(g_3 - z). \tag{4.91}$$

From equation 4.91 the point of instability for the system can be derived

$$\frac{dV_4}{dz} = 0 \tag{4.92}$$

$$0 = \frac{k(g_3 - 3z)}{\sqrt{\frac{2k_{m,z} \cdot z}{A_z \varepsilon_0}} \cdot A_z \varepsilon_0} \tag{4.93}$$

Solving equation 4.93 with respect to z leads to the expression

$$z = \frac{1}{3} g_3 \tag{4.94}$$

Inserting the values $A_z = 0.04$ mm^2, $g_3 = 21$ µm, $k_{m,z} = 0.835$ N/m for the actuator equation 4.91 is plotted in figure 4-19. At an actuated distance z beyond the 1/3 of the initial gap distance g_3 (blue line) the system becomes unstable (upper branch of graph) and the pull-in phenomenon becomes effective, which then means that the maximum actuation is limited to 7 µm.

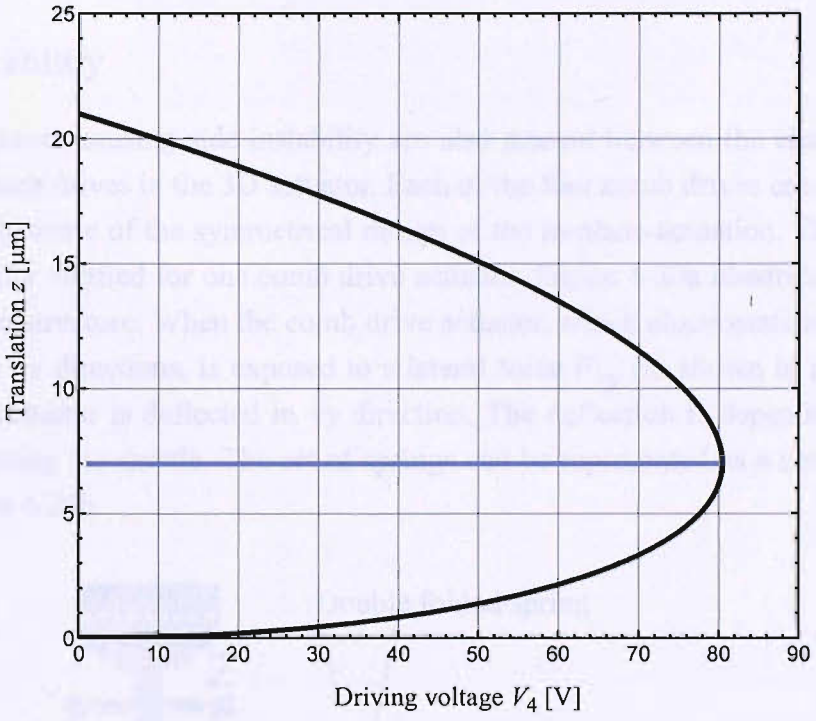

Figure 4-19: Graph showing z translation of the z actuator as a function of driving voltage V_4. There are two equilibrium deflections for each value of the voltage. The solutions corresponding to the lower branch of the graph are stable, whereas the upper branch is unstable.

The dc pull-in voltage $V_{z,pi}$ of 80.45 V can be calculated from Equation 4.91 for $z = g_3/3$,

$$V_{z,pi} = \sqrt{\frac{g_3 \cdot 2k_{m,z}}{3A_z\varepsilon_0}\left(g_3 - \frac{g_3}{3}\right)} = \sqrt{\frac{8g_3^3 \cdot k_{m,z}}{27A_z\varepsilon_0}} \tag{4.95}$$

Pull-in Voltage of the Locking Mechanism

The parallel plate configuration of the locking mechanism has a total electrode area A_L of 0.221 mm^2. This is the sum of the four pillar electrode structures (as detailed in the cross section B of figure 4-3) with an individual electrode area of 235 µm by 235 µm. The center frame, which incorporated the locking mechanism, is suspended by four single beams (as shown in figure 4-15) to the each of the four comb drives. A single beams has a vertical spring constant of 4056 N/m (Equation 4.67), hence the total effective spring constant $k_{b,z,tot}$ in z direction is 16224 N/m. Using the value for $k_{b,z,tot}$, g_4 and A_L (see table 4-8) in Equation 4.92, we obtain a pull-in voltage for the locking mechanism $V_{L,pi}$ of 140 V.

The calculated pull-in voltages for the z actuation and the locking mechanism are in agreement with the design requirements of the limited maximum voltage at 150 Volts.

Lateral Instability

Lateral forces causing side instability are also present between the electrode fingers of the actuated comb drives in the 3D actuator. Each of the four comb drives encounters the same lateral forces, because of the symmetrical design of the in-plane actuation. Therefore the side instability is only verified for one comb drive actuator. Figure 4-20a illustrates each spring of the xy actuation structure. When the comb drive actuator, which electrostatically translates the center stage in $+x$ directions, is exposed to a lateral force F_{+y} (as shown in figure 4-20a) the shuttle of the actuator is deflected in $+y$ direction. The deflection is dependant on the set of springs suspending the shuttle. The set of springs can be represented as a series of springs as shown in figure 4-20b.

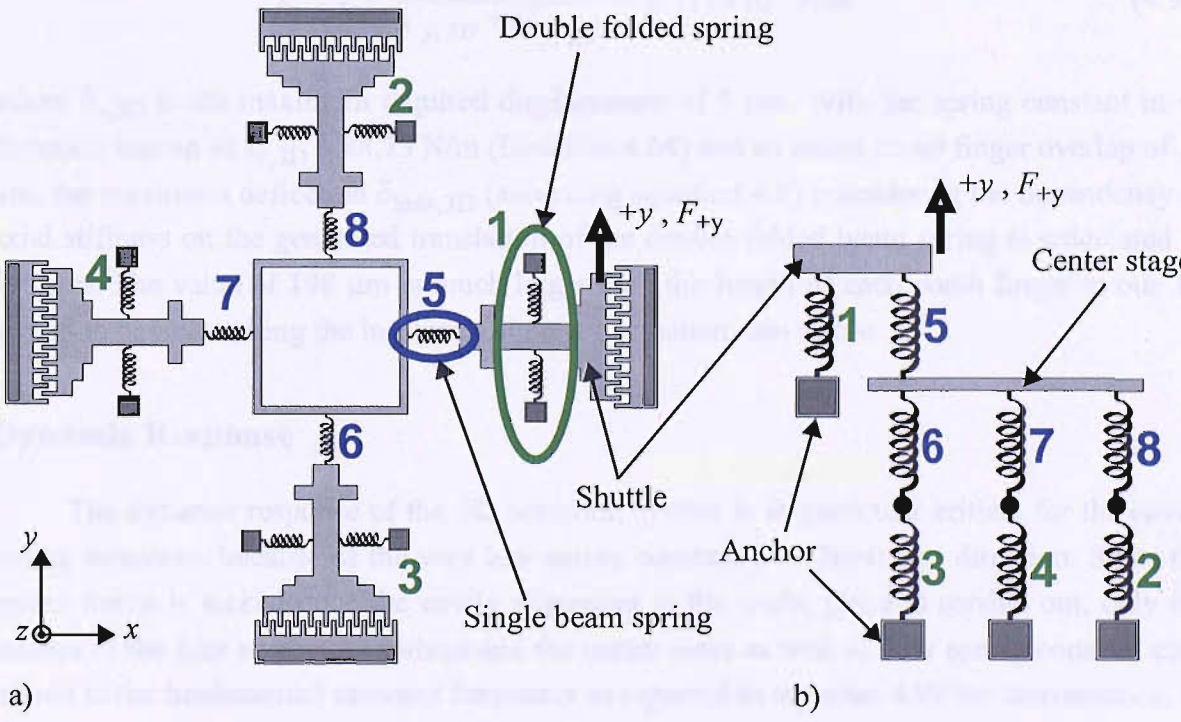

Figure 4-20: Spring setup for the in-plane actuation (a), where members 1-4 (green) denote the double folded spring suspensions of the comb drive actuators and 5-8 (blue) denote the single beam springs. The system can be seen as a series of springs (b) upon impact of side instability forces F_{+y} along the $+y$ axis.

Since the springs numbered 6,7,8 and 2,3,4 in figure 4-20b are in series connection to spring 5, the overall spring constant for the set of springs 2-8 is less than the spring constant for the single beam spring 5. Knowing that the spring constant for the beam spring 5 is 10.14 N/m (Equation 4.63) and taking into account that the double folded spring 1 is in parallel connec-

tion, the entire spring constant for the side instability is a sum of the spring constants from spring 1 and 5. Also considering that the spring constant for the double folded spring is in the order of 10^5 N/m as calculated for the 1D actuator (see page 45) and therefore significantly higher, it is valid to assume that the entire spring constant for side instability in $+y$ direction is dominated by the value of the double folded spring constant (1). The spring constant $k_{y,3D}$ of the double folded spring 1 including the deflection-dependant term is calculated from equations 4.10. to 4.13 and are repeated here for convenience,

$$k'_{y,3D} = \frac{16Ew_2h_2}{l_2} = 2.434\times10^6 \text{ N/m} \tag{4.96}$$

$$k''_{y,3D} = \frac{400Eh_2w_2^3}{18\delta_{x,3D}^2 l_2} = 1.217\times10^6 \text{ N/m} \tag{4.97}$$

$$k_{y,3D} = \frac{k'_{y,3D}\cdot k''_{y,3D}}{k'_{y,3D}+k''_{y,3D}} = 8.113\times10^5 \text{ N/m} \tag{4.98}$$

where $\delta_{x,3D}$ is the maximum required displacement of 5 µm. With the spring constant in $+x$ direction known as $k_{x,3D}$ = 88.73 N/m (Equation 4.64) and an initial comb finger overlap of 10 µm, the maximum deflection $\delta_{max,3D}$ (according equation 4.9) considering the dependency of axial stiffness on the generated translation of the double folded beam spring is calculated as 198 µm. The value of 198 µm is much larger than the length of each comb finger in our 3D actuation device making the in-plane alignment actuation also stable.

Dynamic Response

The dynamic response of the 3D actuation system is in particular critical for the cavity tuning actuation, because of the very low spring constant (< 1 N/m) in z direction. Since the center frame is locked once the cavity alignment in the wafer plane is carried out, only the masses of the four serpentine springs and the center mass as well as their spring constant contribute to the fundamental resonant frequency as repeated in equation 4.99 for convenience,

$$f_{3D} = \frac{1}{2\pi}\sqrt{\frac{k_{m,z}}{M_{eff}}} \tag{4.99}$$

where M_{eff} is effective mass including the center mass and spring masses. Due to the design of the z actuation structure, in particular the dimensions of the actuated center mass, it is valid to assume that the effective mass M_{eff} is dominated by the center mass, which is with 4.064×10^{-8} kg much higher compared to the effective masses of the four serpentine springs. Therefore the fundamental resonance frequency f_{3D} can be calculated from equation 4.99 as 721 Hz using only the center mass without considering the effective spring masses. The simulation results for the resonant frequency of the z actuator as shown in the following section

confirms a mismatch of less than 3% between the simulated and analytical results neglecting the effective spring masses.

Parameters	**Eq.**	**Value**
Serpentine spring constant $k_{m,z}$ [N/m]	4.86	0.835
Pull-in voltage $V_{z,pi}$ for the z actuation [V]	4.92	80.45
Pull-in voltage $V_{L,pi}$ for the locking mechanism [V]	4.92	140
First elastic spring constant of double folded spring $k'_{y,3D}$ [N/m]	4.93	2.434^{6}
Second elastic spring constant of double folded spring $k''_{y,3D}$ [N/m]	4.94	1.217^{6}
Total spring constant in y direction $k_{y,3D}$ considering axial stiffness upon deflection [N/m]	4.95	8.113^{5}
Maximum linear deflection $\delta_{max,3D}$ [µm]	4.9	198
Effective Mass of 3D actuator M_{eff} [kg]	-	4.064^{-8}
Fundamental resonance frequency of 3D actuator f_{3D} [Hz]	4.96	721

Table 4-12: Theoretical calculated design parameters for the 3D actuator with regards to the z actuation, locking mechanism, lateral instability and dynamic frequency response.

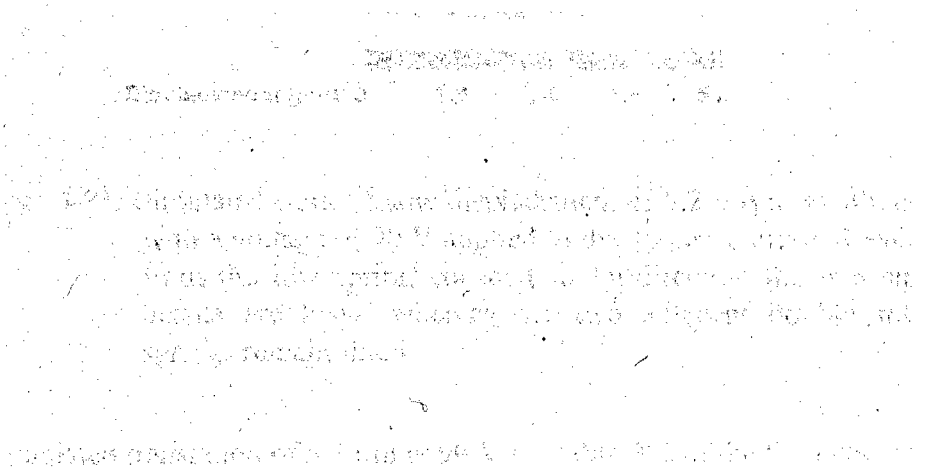

4.3.3 Simulation

In order to verify the analytical calculations of the 3D actuator CoventorWare^{TM} software is used again to carry out the simulations.

Static Translation Curve

One pair of the 330 engaged comb fingers from each of the four comb drives generates a simulated electrostatic force $F_{e,3D}$ of 3.675 µN at 150 Volts. Multiplied by 330 interlocked comb fingers the total force is 1.213 mN, which is within 8% of the theoretical value. The in-plane actuation is only required to translate the center frame structure by ±5 µm in the wafer plane, because of the alignment compensation. Hence, the required actuation voltage decreases. Figure 4-21 shows the simulation results of the comb drive actuation in +*y* direction, when a voltage of 90 V is applied to the +*y* comb drive.

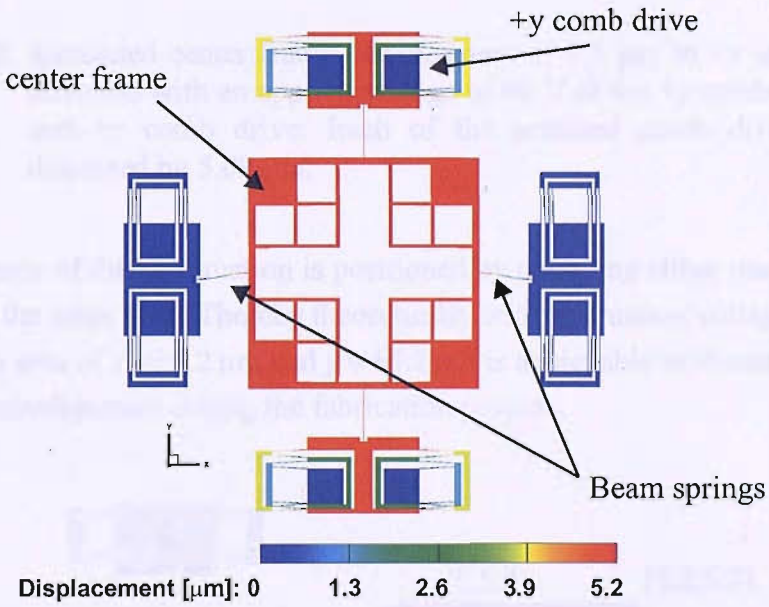

Figure 4-21: Simulated center frame displacement of 5.2 µm in +*y* direction with a voltage of 90 V applied to the +*y* comb drive. Resulting from the low spring constant in +*y* direction the two single beams are bend, whereas the two adjacent double folded springs remain fixed.

The simulated translation of 5.2 µm at 90 V is within 3% of the theoretical value at 5.33 µm and fulfils the design requirement of a 5 µm alignment compensation. Also a combined actuation using two comb drive segments at the same time is simulated. Figure 4-22 shows the results for a maximum radial translation of 7.1 µm at 90 V in the +*y* and the +*x* direction.

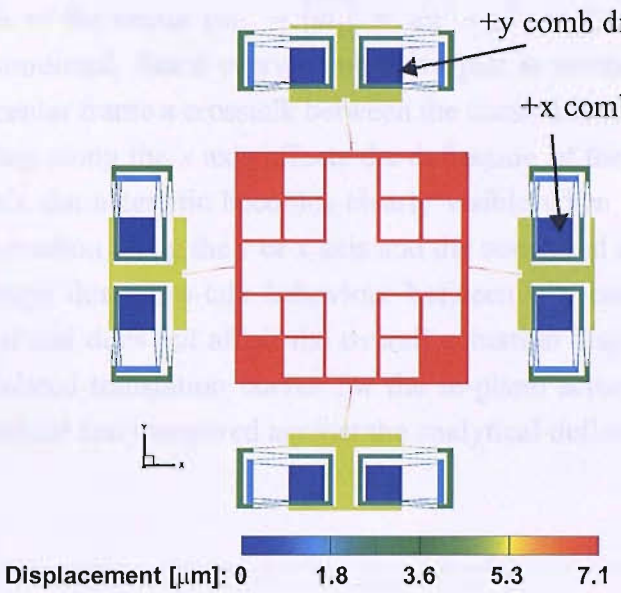

Figure 4-22: Simulated center frame displacement of 7.1 μm in $+y$ and $+x$ direction with an applied voltage of 90 V at the $+y$ comb drive and $+x$ comb drive. Each of the actuated comb drives is displaced by 5.09 μm.

The center frame of the xy actuation is positioned by operating either one comb drive or two comb drives at the same time. Thereby theoretically with a actuation voltage of 90 volts, a maximum actuation area of $x = \pm 5.2$ μm and $y = \pm 5.2$ μm is achievable as shown in figure 4-23 compensating any misalignment during the fabrication process.

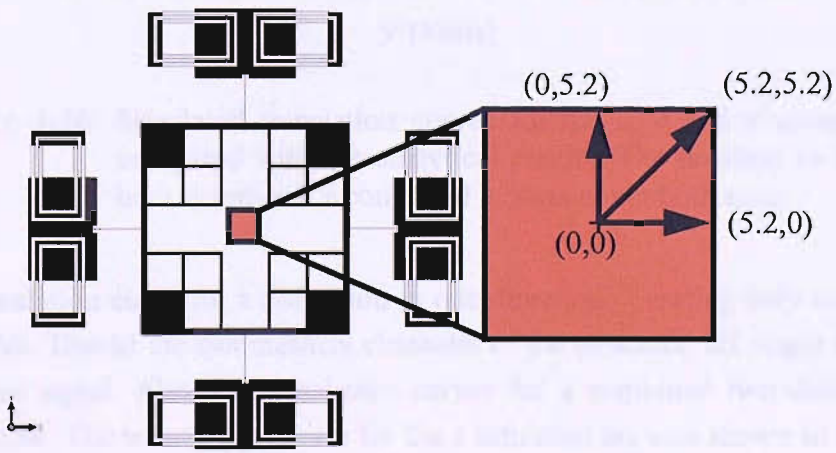

Figure 4-23: Actuation area covered by the two-dimensional in-plane actuator.

However, the software simulation uncovers that the maximum travel range does not match the magnitude of the vector ($m_1 = \left|\overrightarrow{m_1}\right| = \sqrt{x^2 + y^2}$) at 7.35 µm. Instead, a displacement of 7.1 µm is simulated. Since every comb drive pair is mechanically connected by the single beams to the center frame a crosstalk between the comb drives is expected. For example, the comb drive pulling along the x axis affects the deflection of the other comb drive pulling along the y axis. This characteristic becomes clearly visible when comparing the translation curves for a single actuation along the y or x axis and the combined actuation (as shown in figure 4-24). Even though this cross-talk behaviour between two comb drive actuators is not desired, it is minimal and does not affect the overall actuation displacement considerably. In figure 4-24 the simulated translation curves for the in-plane actuation and the out-of-plane actuation are summarized and compared against the analytical deflection curves.

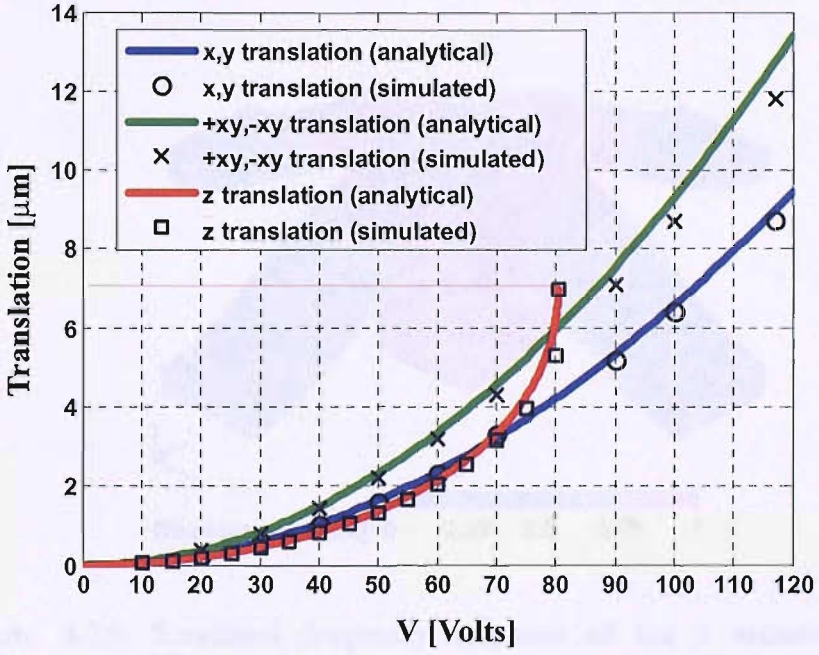

Figure 4-24: Simulated translation curves for the x, y and z actuation is compared with the analytical results. The notation xy is used here to indicate a combined motion along both axes.

The translation curve for a deflection in one direction operating only one comb drive is outlined in blue. Due to the symmetrical character of the structure, all single direction deflection curves are equal. Also the translation curves for a combined two direction deflection (green) are equal. The translation curves for the z actuation are also shown in figure 4-24. The simulation yields a maximum deflection of 7 µm at the pull-in voltage of 82.2 V which is within 2% of the analytical calculated pull-in voltage of 80.45 V. At the operating point of 4 µm the actuation voltage is simulated at 75 V, which is compared to the analytical value at 73.8 V within 1.7%.

The translation ranges for in-plane alignment and out-of-plane cavity tuning are all in agreement with the analytical results. It is important to notice that the simulated maximum deflections are boundary conditions and differ from the operating points at 4 µm for the *z* actuation and 5 µm for the *xy* actuation.

Resonant Frequency

The simulation of the frequency response of the 3D actuator is only applied to the center frame structure. With the locking mechanism in place only the elements (e.g. serpentine springs and center mass) for the *z* actuation are influenced by external vibrations. Figure 4-25 illustrates the simulated frequency response of the *z* actuator. The serpentine springs and their ends coloured in blue are fixed to the center frame allowing the center mass (red) to oscillate along the *z* axis at a frequency of 724 Hz.

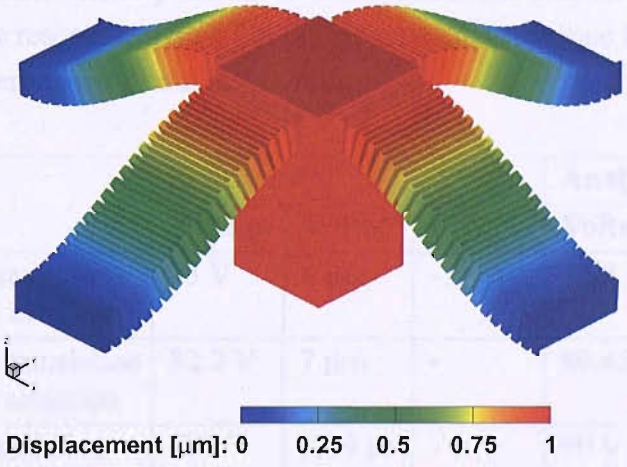

Figure 4-25: Simulated frequency response of the *z* actuation. At a fundamental resonance frequency of 724 Hz the center mass (red) oscillates along the *z* axis suspended by the four serpentine springs, which are fixed to the center frame structure at their blue ends.

As mentioned earlier the analytical calculated fundamental resonant frequency with 721 Hz is a very close match with the simulated value of 724 Hz. The analytical and simulated frequency are within 3%. Therefore, equation 4.97 can be used and the spring masses of the system can be neglected. A summary of the simulated and analytical results is listed in the table 4-13 on page 83.

4.4 Accuracy and Stability of the Actuators

The planar fibre mirror in the 3D actuation structure and the planar side wall mirror of the 1D actuator form a resonator with the spherical mirror (3D) and the concave fibre mirror (1D) respectively. Laser light with a wavelength of 780 nm is coupled into the resonator resulting the cavity to become resonant when scanning over the actuation range between 0-20 μm. From scanning over the entire actuation range the dependence of reflected power versus the actuator position can be observed and resonant modes linked to the cavity position can be identified as sharp dips (fringes) in the reflected intensity. In order to keep the cavity in one of these resonant modes the movable mirror is fixed and stabilized in one mode position - the resonant cavity is locked. In the atom chip experiment atoms are guided into the resonator. Their presence in the locked cavity changes the resonance properties of the cavity in such a way [139] that for example single atoms can be detected passing through the cavity system. It is of highest importance that during the experiments the cavity is precisely locked and stabilised within a few nanometers of the resonant mode position. It is also essential that the positioning system is capable of actuating the resonator with 2 nm to fine tune the resonance fringes in order to conduct the atom chip experiment without difficulties.

Parameters	**Simulated**			**Analytical**		
	Voltage	**Transl.**	**Freq.**	**Voltage**	**Transl.**	**Freq.**
Minimum required translation (operating point) for *z* actuation	75 V	4 μm	-	73.8 V	4 μm	-
Maximum achievable translation (pull-in voltage) for *z* actuation	82.2 V	7 μm	-	80.45 V	7 μm	-
Minimum required translation (operating point) for *xy* actuation	90 V	5.09 μm	-	90 V	5.2 μm	-
Fundamental resonant frequency	-	-	724 Hz	-	-	721 Hz

Table 4-13: Comparison of the simulated and analytical results of the *xy* actuation, *z* actuation and dynamic frequency response for the 3D actuator.

The accuracy of motion and stabilization within 2 nm are key requirements for a successful atom chip experiment. Besides the 'side instability' of the comb drive actuators, there are several other factors that can induce instability to the actuation system. For example the noise of the output signal of the actuation voltage source is critical. If the noise of the output voltage is large enough the stability as well as the positioning accuracy of the actuator, hence the optical cavity, is affected negatively. General available DC Voltage Supplies have a voltage noise (rms) of around 1-5 mV. Since the operation voltage of the actuator is directly related with the translation of the actuator, the impact of noise from the operation voltage to the actuation accuracy and stability can be evaluated by looking at the translation function of the actuator. With respect to the comb drive actuator of the 1D design the motion accuracy of in-plane actuation

is strongly dependent on the gradient of the first derivation of the translation function (Equation 4.3) and is given by

$$\frac{d}{dV_1} \cdot y(V_1) = \frac{d}{dV_1} \cdot \left(\frac{\varepsilon_0 N_1 h_1}{g_1 \cdot k_x}\right) V_1^2 = 2 \cdot m \cdot V_1 \tag{4.100}$$

where m is the gradient. Due to the quadratic character of the translation function, the accuracy is defined by the gradient m of the equation 4.100. However, the linear approximation of equation 4.100 is only valid for small ΔV_1. Increasing the driving voltage V_1 at 61 V of around 5 mV results in the motion of 0.6 nm at the operating point of 4 µm. A voltage source with a maximum noise of 5 mV has an analytical resolution within the stability and accuracy requirements of the experimental setup. The voltage stability hence accuracy of actuation can be further increased by additional electronics such as a close loop feedback system.

Especially the change of temperature during the experiments can destabilize the optical cavity system. For example a thermal drift of the voltage source generated by an external rise of ambient temperature in the laboratory can cause a drift in the actuation voltage, which inevidently leads to the loss of the resonant mode of the cavity. One counter measure is a closed loop feedback system, which eliminates any thermal voltage drift of the DC source. However, it is anticipated that throughout the experiments the ambient temperature will not change more than one degree Celsius, so the effect of thermal drift caused by the internal heating of the voltage source is expected to be insignificant.

The atom chip experiment takes place in a high vacuum chamber with a pressure of 10^{-11} mbar at a room temperature of around 20 degree Celsius. Since the vacuum chamber has no specific cooling equipment the actual atom chip and its actuation structure is exposed to the temperature changes within the laboratory and the vacuum chamber. Extrinsic heat caused by the change of ambient temperature around and within the vacuum chamber can cause the actuation structure to expand or contract due to the thermal expansion coefficient of crystalline silicon. If in a worst case scenario the air temperature in the vacuum chamber changes by plus one degree Celsius, the movable silicon structure of the 1D actuator which encloses the plane mirror elongates along the optical axis of the micro cavity due the thermal expansion. Figure 4-26 illustrates the silicon structure before any temperature change ($\Delta T = 0$) at an initial length L_i and after a one degree Celsius increase of temperature ($\Delta T = 1°C$) resulting in a final length L_f.

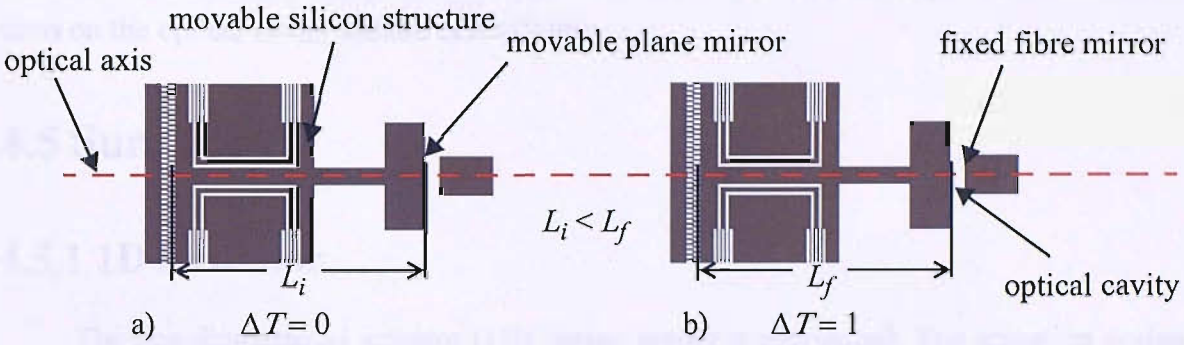

Figure 4-26: Thermal expansion of the movable structure along the optical axis before a change of temperature (a) and after a change of temperature (b). The initial length L_i increases due to thermal expansion according equation 4.101 to a final length L_f.

For solid materials the thermal expansion can be calculated as,

$$L_f = L_i(1 + \alpha \cdot \Delta T) \tag{4.101}$$

where L_i is the initial length of the solid material before the change of temperature, L_f is the final length recorded after the change of temperature, ΔT is the difference of the temperature and α is the coefficient of thermal expansion. With a temperature change ΔT of one degree Celsius, a thermal expansion coefficient α of $3\times10^{-6}\,K^{-1}$ for crystalline silicon at 20 degree Celsius and an initial structure length L_i of 1650 µm the final length L_f is calculated to 1650.010 µm. Although the overall thermal expansion is 10 nm the elongation at each end of the silicon structure is only 5 nm. But even with a thermal mirror movement of 5 nm the optical cavity becomes off-resonant. In comparison to the 3D actuator the thermal expansion of the mirror structure with an initial length of 380 µm is calculated to 0.6 nm, which is below the required actuation resolution of 2 nm. Therefore an increase of temperature by 1°C does not affect the resonant cavity of the three-dimensional actuation structure. For the 1D actuator the thermal expansion is with 5 nm much larger and is expected to change the resonant mode of the optical cavity throughout the experiments. One way to avoid any significant thermal expansion is to heat up or cool down the vacuum chamber and stabilize the chamber temperature within 0.1 degree Celsius.

Besides extrinsic heat there is also intrinsic heat. However, the intrinsic heat of the actuators caused by the power dissipation of the driving voltage for the comb drives is negligible. Since the current flow of comb drive actuators is small the power dissipation is low, hence no significant heat is generated in the silicon structure that can cause an expansion large enough to show a negative effect on the cavity system. The accuracy of the motion and the stabilisation of the actuated optical micro cavity is also constrained by external noises such as vibrations. It is estimated that within the laboratory vibrations between 0-100 Hz are present. With analytical calculated resonant frequencies above 724 Hz (3D) and 1452 Hz (1D) and the usage of

anti-vibration tables, which filter out frequencies below 100 Hz, the impact of external vibrations on the optical cavity system is negligible.

4.5 Summary

4.5.1 1D Actuator

The one-dimensional actuator (1D) design layout is introduced. The actuation design is theoretically analysed by deriving the translation curve for the 1D actuator, which is verified by simulations. The 1D actuator translates a plane micro mirror up to 20 μm at a simulated maximum voltage of 145 Volts using a comb drive actuation structure with 200 comb fingers, which have a gap spacing of 5 μm and a height of 120 μm. Since stability and translation accuracy of the optical cavity is a key requirement, the lateral instability of the comb drive actuation structure is evaluated. Also the fundamental resonance frequency of the system is analysed. Both dynamic response and lateral instability of the 1D actuator are found to be not critical. The fundamental resonance frequency is calculated at 1452 Hz, which is well beyond the critical range of external vibrations between 0 - 100 Hz. The impact of heat on the actuation device is calculated as well. The analytical results show that the thermal heat expansion of the actuation device is critical and can cause the optical cavity to become instable. Adequate cooling or heating of the vacuum chamber temperature is necessary. It is also found that the required analytical resolution of 2 nm of the actuator can be achieved with a 5 mV stabilized voltage source.

4.5.2 3D Actuator

The three-dimensional actuator (3D) design layout is introduced. The design incorporates a two-dimensional *xy* comb drive actuator in the wafer plane, which is used for cavity alignment with a maximum translation of 15 μm at 150 Volts. The comb drive actuation structure consists of 330 comb fingers, which have a gap spacing of 3 μm and a height of 60 μm. The translation curve for the *xy* actuation is derived and verified with simulations. The design also includes an out-of-plane parallel plate *z* actuator, which is responsible for the optical cavity actuation. The z actuator includes a serpentine spring system, of which the spring constant is analytically derived. With a total spring constant as low as 0.835 N/m the optical cavity actuation is analytically calculated and simulated with maximum translation of 7 μm at 80 Volts. The 3D actuator also incorporates a locking mechanism, which allows the *xy* actuation structure to be locked before the *z* actuation of the optical cavity takes place. The locking mechanism is based on a parallel plate configuration and is able to lock the *xy* actuator at a 140 Volts. For the 3D actuator the same stability and accuracy requirements are in place. The lateral instability of the comb drive actuator and the dynamic response with a simulated fundamental resonance frequency of 724 Hz is also not critical.

Chapter 5

Fabrication

5.1 Introduction

In this chapter, the fabrication of the one-dimensional actuator (1D) and the three-dimensional actuator (3D) is outlined. The actuation devices are fabricated by applying standard bulk micromachining processes as well as non-standard fabrication techniques. Both, standard and non-standard processes, have been developed and are described in detail. The presented fabrication process for both actuators is focused on a seamless fabrication solution to realize a single atom chip including wires, optical cavity and actuator.

In section 5.2 the fabrication process of the 1D actuation device is outlined. The fabrication of the 1D actuator is based on a silicon on glass substrate (SOG), using wet and dry etching techniques as well as thin film deposition techniques.

Section 5.3 describes the fabrication process of the 3D actuation device. The more complicated three-dimensional actuation structure is also based on a SOG substrate, however the final atom chip design includes an additional third silicon wafer, which is attached to the SOG substrate by applying a bonding process.

5.2 1D Actuator

The one-dimensional actuator is fabricated along with micro mirrors, micro wires and an optical fibre in order to create a single atom chip with an optical tunable cavity. In particular the fabrication of the planar mirror, which is actuated by the electrostatic comb drive, and the integration of the optical fibre with its concave fibre mirror is difficult. A stable optical cavity requires both cavity mirrors, the planar mirror and the concave fibre mirror, to be aligned accurately to each other. Between the two cavity mirrors, which are situated in the *xy* plane of the wafer surface, several misalignment errors can occur. A good alignment is present when both mirrors are aligned to the optical axis of the micro cavity (green) as illustrated in figure 5-1. Figure 5-1 shows a misalignment of the two mirrors along the *y* axis (a) and along the *z* axis (b). Since the tuning of the optical cavity takes place along the *x* axis (yellow) no alignment in this direction is necessary. Additional misalignment can also take place in the *xy* plane and *xz* plane, when the mirrors are tilted with respect to the optical axis as shown in (c) and (d) of figure 5-1.

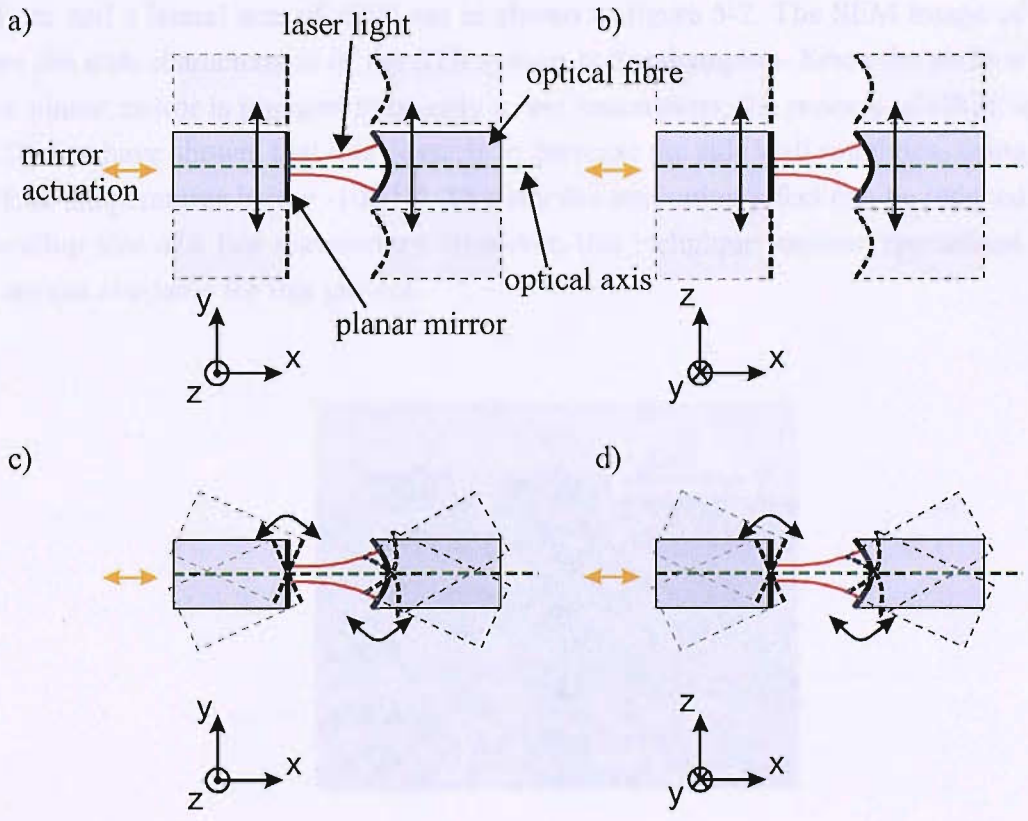

Figure 5-1: Potential misalignment errors between planar mirror and concave mirror (a-d). Displacement of planar mirror and concave mirror in *y* direction (a) and *z* direction (b). Misalignment due to tilt of planar mirror or optical fibre in *xy* plane (c) and *xz* plane (d).

The misalignment between the two mirrors in *y* direction (5-1a) as well as in *z* direction (5-1b) is eliminated by a large planar mirror surface area of 400 μm^2. By enlarging the physical dimensions of the planar mirror a misalignment as shown in 5-1a and 5-1b is not critical any more, because the mirror surface is much larger than the actual spot size of 25 μm^2 created by the laser light (red) coming out of the fibre. In order to minimize an angular tilt of the optical fibre mirror as shown in 5-1c and 5-1d a v-groove is introduced. The v-groove is perpendicular to the planar mirror surface and lies within the optical axis of the cavity system. The v-groove acts as a mechanical supporting structure, which fixes the fibre in its position and minimizes not only the angular tilt but also the displacement of the fibre with respect to the optical axis in *y* and *z* direction. The angular tilt of the planar mirror in the *xy* plane (5-1c) is controlled by the lithography and the angular tilt in the *zx* plane is eliminated by processing a perfectly vertical side wall mirror.

Vertical side walls in silicon wafers can be created by deep reactive ion etching (DRIE), however the side walls obtained are not smooth due to the nature of the process. Deep dry etching machines as well as the available STS ASE system use the Bosch process for deep etching. Unfortunately, the Bosch process forms scallops on the side wall, which have a vertical size of <0.7 μm and a lateral size of <300 nm as shown in figure 5-2. The SEM image of figure 5-2 shows the etch characteristic of the STS system at Southampton. Since the surface roughness of the planar mirror is required to be only a few nanometers, the process of DRIE is not suitable. Studies have shown, that it is possible to decrease the side wall roughness using cryogenic DRIE at temperatures below -100 °C. Thereby the scalloping effect can be reduced to a vertical scallop size of a few nanometers. However, this technique requires specialised machines, that are not available for this project.

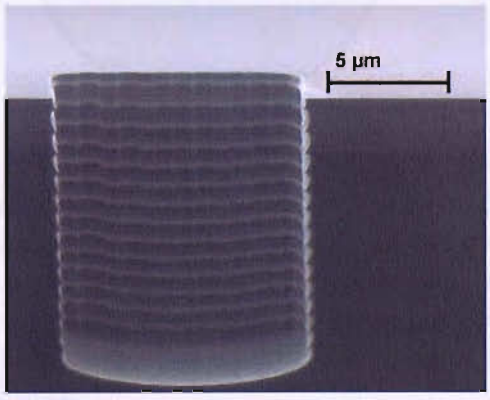

Figure 5-2: SEM image of etch pattern after deep dry etching with the available STS ASE system. During the etching process scallops are formed on the vertical side walls. The scallops have a vertical size of 0.7 μm and a lateral size of <300 nm.

Another way to create a vertical side wall is by using a wet etch process. It is known, that vertical silicon side wall microstructures with high aspect ratios can be fabricated by using silicon wafers with a specific orientation [124]. For example, a (110) silicon wafer has one of its (111) planes perpendicular to its surface. Due to the crystallographic orientation of the (110) silicon wafer and the high selectivity between (111) and (110) planes when anisotropically etched in a potassium hydroxide solution (KOH), side walls can be created, which are not only perfectly vertical, but also atomically smooth [125],[126].

In order to avoid a misalignment of the optical cavity system it is important that the v-groove and the optical fibre is situated perpendicular to the planar mirror side wall. Figure 5-3 shows a representation of a (110) silicon wafer used for processing. The flat of the wafer indicates the orientation of the (111) planes, the vertical side walls respectively, on the (110) surface plane. The vertical side walls are located in parallel to the wafer flat (profile view A). According to the crystallographic orientation of the (110) silicon wafer, it is possible to create v-grooves formed by another group of two crossing (111) planes, but the v-grooves would be located at a 35 degree angle to the wafer flat as shown in the profile view B of figure 5-3 [140]. This v-groove is not perpendicular to the (111) planes and therefore not suitable as a fibre support.

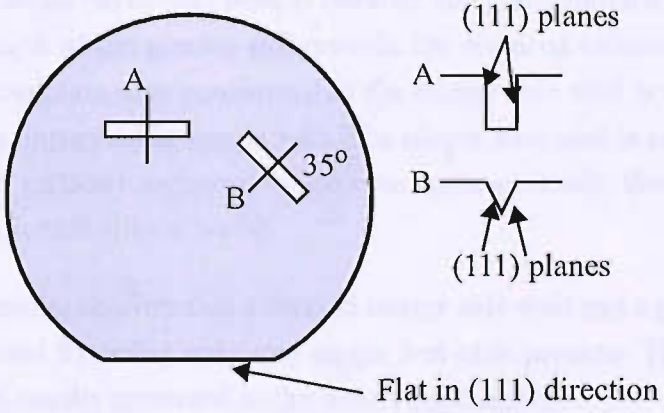

Figure 5-3: Schematic view of two etch patterns on a (110) oriented silicon wafer. Etch pattern A is in parallel to the (111) planes of the wafer flat and creates vertical side walls. Etch pattern B forms a v-groove, but at an undesired 35 degree angle to the wafer flat and therefore not suitable to hold the optical fibre.

In order to find out if a v-shaped groove in the pre-defined location perpendicular to the vertical mirror side wall can be fabricated an etch simulation is carried out. The Coventor^{TM} software simulation package, which has been used to simulated the translation behaviour of the actuation designs in chapter 4, includes also an etch simulator. The software module called 3DEtch from Coventor^{TM} is used to verify the feasibility of fabricating the v-groove and verti-

cal mirror side wall by applying only one wet etch process. The advantage of conducting the computer simulation is to avoid a costly and lengthy fabrication process. The etch simulator is capable of wet etching a mask pattern anisotropically into a (110) oriented silicon wafer. The wet etch simulation is carried out in a concentrated KOH solution with a weight concentration of wt40% and a bath temperature of 70 °C. The KOH concentration and temperature is chosen, because it reflects the condition of the available etch bath setup at Southampton. The simulation is performed according the simulation log-file illustrated in appendix A-1. During the simulation the mask of the one-dimensional actuator as shown in appendix A-2 is aligned to the (111) planes of the (110) oriented silicon wafer and etched 180 μm deep into the wafer surface. Since the v-groove structure crosses a variety of crystallographic planes throughout the wet etching process the side walls of the groove are not expected to be perfectly v-shaped and are predicted to be rough. The images of figure 5-4 represent the simulated etching results showing the complete actuation structure including one large anchor for the stationary part of the comb drive, two small anchors for the movable part of the comb drive, the mirror structure and v-groove. As outlined in red in figure 5-4a the wet etched v-groove is in fact perpendicular to the mirror side wall. Additionally the etch simulation reveals that only a partly v-shaped groove can be created as shown in the cross-sectional view of figure 5-4b. The groove is v-shaped at the bottom with vertical side walls at the top. Even though the resulting groove is only partly v-shaped and its side walls are rough the overall roughness along the entire v-groove is not critical, because when the optical fibre is lowered and glued into the v-groove the side walls along the entire length of the groove still provide the required mechanical support and fixation. The wet etch simulation also confirms that the mirror side wall is vertical with respect to the wafer surface as illustrated in figure 5-4c. The mirror side wall is not only vertical but also indicates a smooth surface roughness, which is in agreement with the alignment to the (111) planes of the (110) oriented silicon wafer.

Overall the simulation results confirm that a vertical mirror side wall and a perpendicular situated v-groove can be created by using only one single wet etch process. This is also in agreement with the fabrication results presented in the following chapters.

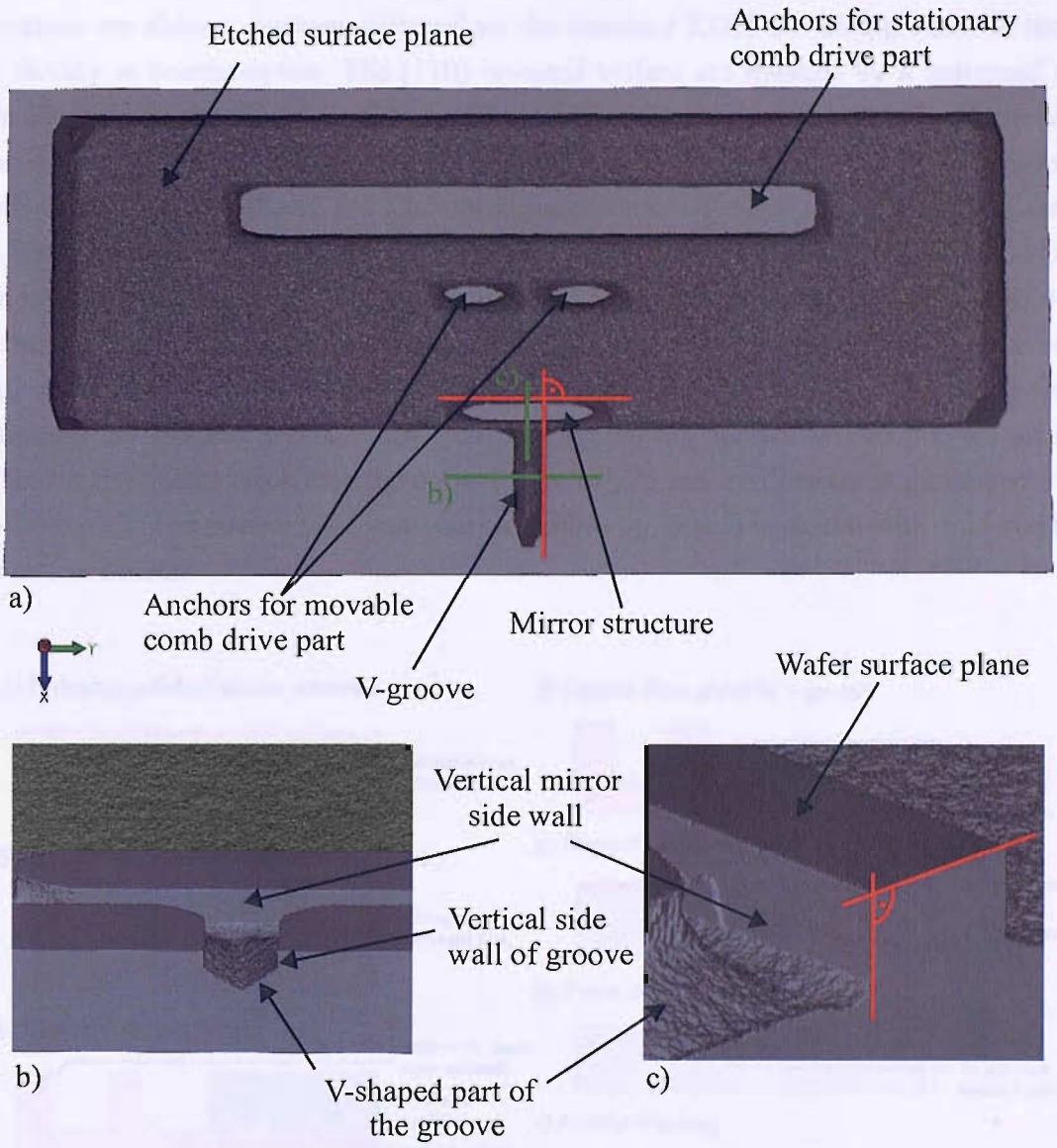

Figure 5-4: Simulation result of an anisotropic wet etch forming comb drive anchors, mirror structure and v-groove on a (110) oriented silicon wafer. The v-groove is located perpendicular to the mirror structure (a). The cross-section of the groove (b) reveals a partly v-shaped groove with side walls of high surface roughness. The rough side wall surfaces however do not affect the mechanical fibre support and fibre alignment. Additionally the mirror side wall is vertical with respect to the wafer surface and smooth according the alignment to the (111) planes (c).

5.2.1 Fabrication Process

The 1D actuator is fabricated on a (110) oriented double-polished 300 µm thick 4 inch silicon wafer. The fabrication process of the one-dimensional actuator including the micro optical cavity is diagrammatically illustrated in figure 5-5. The silicon wafer is anisotropically wet etched in a potassium hydroxide solution (KOH). The solution has a kalium weight con-

centration of wt40% and the bath temperature is regulated at 70 °C. The concentration and temperature are chosen, because they reflect the standard KOH wet etch process in the clean room facility at Southampton. The (110) oriented wafers are masked by a patterned silicon nitride layer of 50 nm thickness (b). A 180 µm deep anisotropic wet etch forms the vertical mirror side wall and the anchors for the actuation structure (c). Apart from the atomically smooth vertical side wall and the anchors an additional v-groove is wet etched at the same time. The fabrication is followed by an e-beam evaporation, which coats the vertical side wall with a layer of gold forming a planar mirror with a low surface roughness (d). The gold layers from the top and bottom surfaces are removed by a subsequent ion beam milling process leaving only gold on the vertical side walls behind (e). Removing the gold layer especially from the top surfaces is essential, because any gold left on the top surface would prevent an anodic bond. In the next fabrication step the optical fibre of 125 µm in diameter is glued down inside the v-groove (f). The optical fibre has a concave fibre tip, which is coated with gold and is used as a concave mirror.

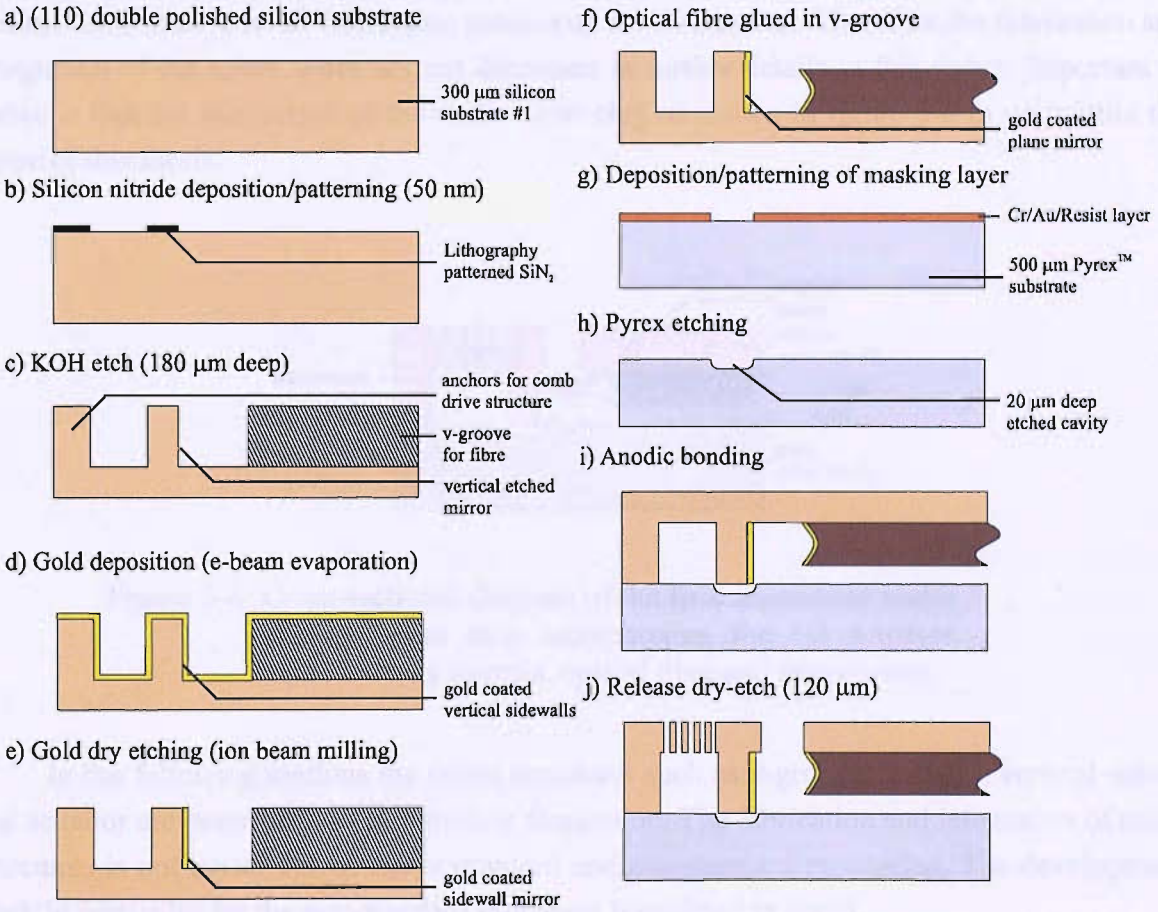

Figure 5-5: Overview of the fabrication process of the 1D actuator and optical cavity system.

After the silicon wafer processing a second Pyrex™ wafer is processed. The Pyrex™ wafer is patterned by depositing and masking a layer of Cr/Au and resist (g). A cavity with a depth of 20 μm is then wet etched in a buffered-HF solution using the patterned and 500 μm thick Pyrex™ wafer (h). As mentioned above an anodic bonding process is used to attach the two wafer substrates chemically to each other (i). Before the actual bonding process begins the cavity of the Pyrex™ wafer is aligned directly underneath the movable part of the actuation structure ensuring that the planar mirror is free to be actuated. In a final fabrication step a 120 μm deep dry-etch process on the front of the SOG substrate is carried out to release the comb drive actuator (j).

A final cross-sectional diagram of the assembled multi-layered atom chip is shown in figure 5-6. Atoms are trapped in the optical cavity of which the vertical planar mirror is actuated by the comb drive actuator. Figure 5-6 shows also the integrated miro wires. The gold wires are fabricated on the substrate surface of the Pyrex™ wafer and magnetically guide the atoms into the optical cavity. The fabrication of the micro wires is already established by other members of the Southampton research group [121],[122]. This process can easily be adapted and included in the overall fabrication process of the 1D actuator. Therefore the fabrication and integration of the micro wires are not discussed in further details in this thesis. Important to notice is that the fabrication of the entire atom chip as shown in figure 5-6 in not within the scope of this thesis.

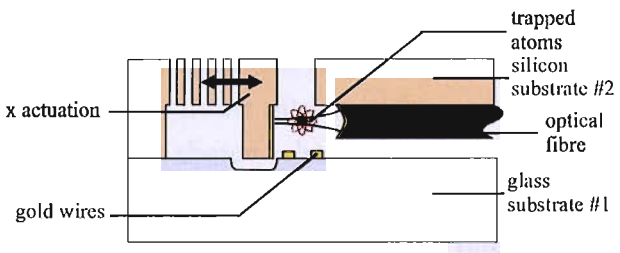

Figure 5-6: Cross-sectional diagram of the final assembled multi-layered atom chip incorporating the 1D actuator, optical cavity mirrors, optical fibre and micro wires.

In the following sections the micro structures such as v-groove, anchors, vertical mirror and actuator are described in detail in their fabrication. The fabrication and integration of those structures is not trivial and involves standard and non-standard processing. The development work in particular for the non-standard processes is outlined in detail.

5.2.2 V-groove

The v-groove for the optical fibre support and the vertical mirror side wall are etched simultaneously in the KOH solution. The wet etch process is applied to (110) oriented silicon

wafers with a flat identifying the (111) planes cutting through the (110) surface plane that form an angle of 90°. The silicon wafers have a thickness of 300 µm and are double polished, because both side are used throughout the processing.

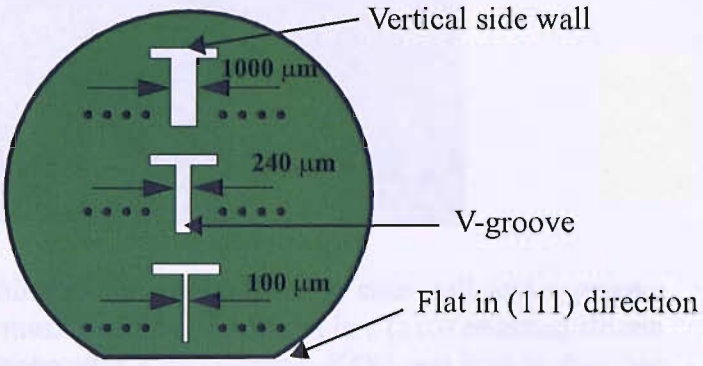

Figure 5-7: A silicon wafer with a flat identifying the (111) planes, which have an angle of 90° to the (110) surface plane. The substrate is masked with a patterned silicon nitride layer (green). The pattern enclosed three types of different sized T structures. The T structure have horizontal openings, which are aligned in parallel to the wafer flat and form the vertical side walls during the KOH wet etch. The vertical T bars represent the v-grooves opening with a width of 100, 240 and 1000 µm.

In order to verify the simulation result of figure 5-4 a (110) oriented silicon wafer is prepared by growing a 50 nm thick silicon nitride (Si_3N_4) layer in a low pressure chemical vapour deposition (LPCVD) process. The silicon nitride is then patterned with a lithography mask, which is aligned to the wafer flat as shown schematically in figure 5-7. The mask pattern consists of T structures each enclosing a vertical side wall in the horizontal bar and a v-groove in the vertical bar perpendicular to it. The v-grooves have an initial mask opening of 100 µm, 240 µm and 1000 µm (see figure 5-7). Silicon nitride is chosen as a masking layer, because the etch rate in KOH is negligible compared to silicon. Therefore very thin layers of silicon nitride can be used. The silicon nitride mask is also easy to strip after the KOH wet etch process by using either an orthophosphoric wet etch solution or a silicon nitride dry etch process, which are both available processes in the clean room facility at Southampton. The KOH wet etching result is illustrated in figure 5-8 and shows the vertical side wall and the adjacent v-groove with an initial opening of 240 µm after a four hour and forty minutes etch process. When comparing the simulation results in figure 5-4 with the real etching results in figure 5-8, it becomes clear that the resulting v-groove side walls are rougher than initially simulated. Only a limited v-groove sidewall roughness is tolerable, because with increasing roughness less resting points for the optical fibre are provided. If there are not enough resting points the v-groove is not able to fulfil its required function. However, this is not of any concern after evaluating the etching results, because the overall roughness along the entire v-groove still provides the required mechanical support and fixation for the optical fibre.

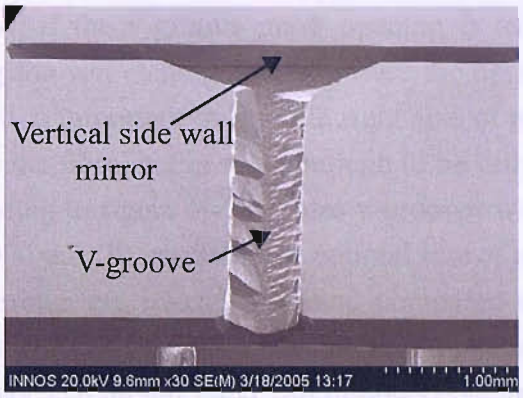

Figure 5-8: KOH wet etching of the vertical mirror side wall and v-groove with an initial mask opening of 240 μm in a (110) oriented silicon wafer. SEM image after a 280 minutes KOH wet etch is showing the v-groove, which is a suitable mechanical support structure for the optical fibre and the vertical side wall, which is still suitable as a planar mirror. Even though the side wall surfaces are very rough.

In addition there are two more requirements that the v-groove must meet. First, the v-groove must have the right size to fit the optical fibre with a 125 μm diameter. This can be achieved by choosing the right initial mask opening in the silicon nitride layer at the beginning of the KOH wet etch process. Secondly, the v-groove must posses two anchor points in order to provide adequate fixation and support. The required two anchor points are only present if the v-groove is fully developed as it is schematically illustrated in figure 5-9a. In comparison a not fully etched v-groove is shown in figure 5-9b, which increases the risk of misalignment of the optical fibre, because the fibre would be free to move on the bottom plane of the v-groove during the gluing process.

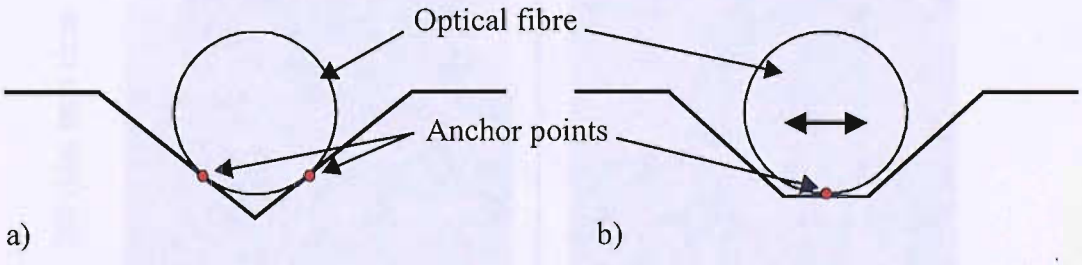

Figure 5-9: Schematic drawing of the optical fibre in the v-groove with two anchor points in a fully etched v-groove (a) providing adequate fixation and support, compared to an optical fibre in a not fully etched v-groove (b) with only one anchor point causing misalignment during the gluing process of the fibre.

If the initial mask opening is too small the optical fibre does not fit in the fully etched v-groove. On the other hand, if the v-groove mask opening is too big the v-groove cannot develop completely during the wet etching and can cause the optical fibre to misalign in the gluing process. Therefore it is important to find the right size of mask opening, where the v-groove is big enough to fit the fibre, but is small enough to be fully etched. The silicon wafer that has been etched according to figure 5-7 includes v-grooves with different mask openings of 100 µm, 240 µm and 1000 µm. To establish the optimal size of mask opening the cross sections of the different openings are investigated and compared using SEM images of the grooves. The v-grooves shown in figure 5-10 have an initial opening of 100 µm and 240 µm and have been wet etched for 120 minutes and 280 minutes reaching an etch depth of 120 µm and 260 µm respectively. The v-groove with an initial opening of 1000 µm is not shown, because even after an etching depth of more than 260 µm the v-groove is not fully developed and therefore not suitable as a fibre support. The fact that an KOH etch depth of 180 µm is required in order to achieve a comb drive actuator thickness of 120 µm rules out the v-groove with an 1000 µm initial opening as well. The SEM images of figure 5-10 show, that after an etch time of 120 minutes both v-grooves, 100 µm (a) and 240 µm (b), are not fully etched. After an etch time of 280 minutes the v-groove with the 100 µm opening is fully etched, but the v-groove with the 240 µm opening has still not developed completely.

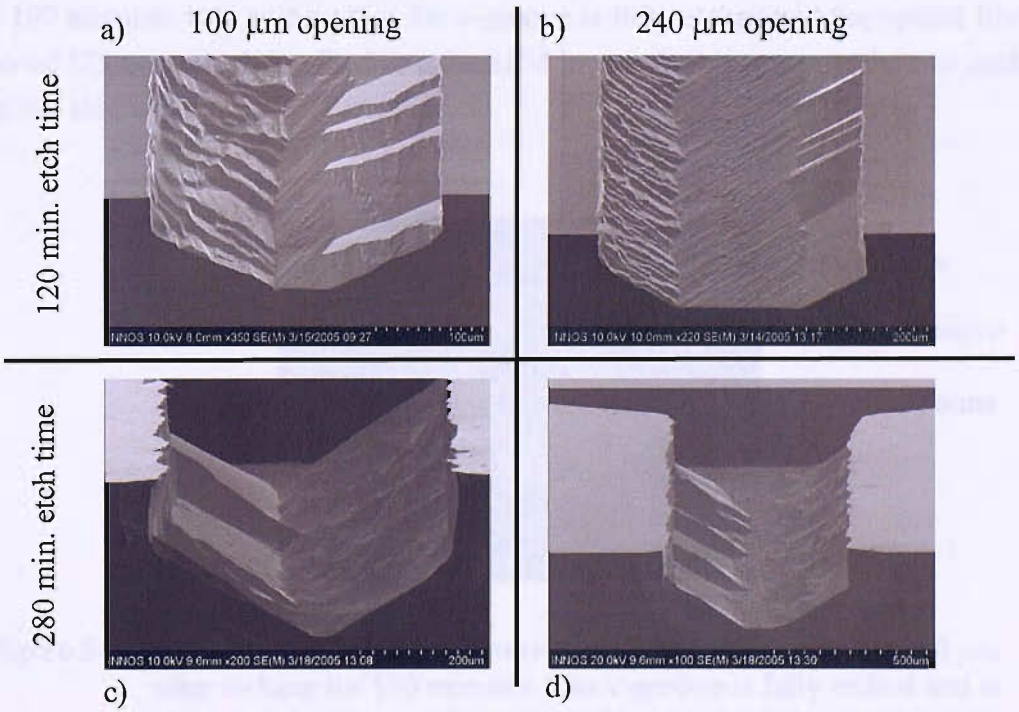

Figure 5-10: SEM images show v-grooves with 100 µm and 240 µm initial opening after etched in KOH for 120 and 280 minutes. After 120 min. the v-grooves are not fully etched (a,b). After 280 min. the 100 µm sizes v-groove is fully etched (c), but the 240 µm v-groove is still not fully developed (d).

Measuring the etch depth at different etch times in a variety of v-grooves with different openings the overall etch rate is averaged to 0.96 μm/min. according to table 5-1. Since the etch depth is set to 180 μm a total KOH wet etch time of 189 minutes is required.

V-groove Opening [μm]	Etch Time [min.]	Etch Depth [μm]	Etch Rate [μm/min]
100	120	120	1
100	120	115	0.96
100	160	150	0.94
100	280	250	0.90
240	160	147	0.92
240	280	263	0.94
1000	180	175	0.97
1000	180	174	0.96
		Averaged Etch Rate	**0.96**

Table 5-1: Measured average etch rate of a (110) silicon wafer in KOH (70°C/wt40%).

Figure 5-11 shows the etch result of a v-groove with a 100 μm opening after an KOH wet etch of 190 minutes. It is evident that the v-groove is fully etched and the optical fibre with a diameter of 125 μm, which is edited into the SEM image, is able to rest at the two anchor point (red) on the side walls.

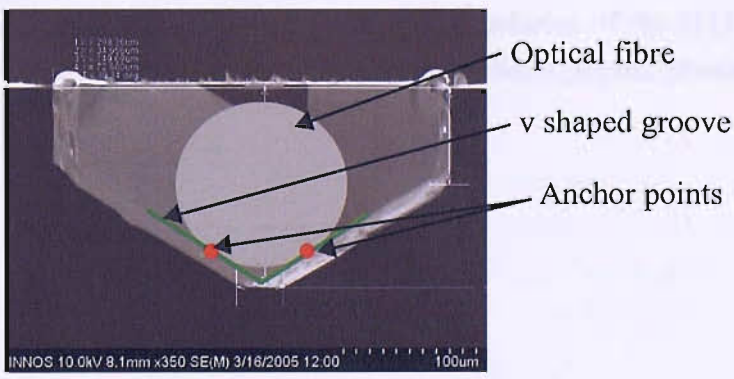

Figure 5-11: KOH etch result for a v-groove with an initial opening of 100 μm after etching for 190 minutes. The v-groove is fully etched and is able to fit an optical fibre with a diameter of 125 μm. The fully etched v-groove (green) provides two anchor points (red) for the fibre.

Important to note is that the v-groove is also enlarging laterally during the wet etch process. For example, an initial opening of 100 μm or 240 μm is doubling in size after an etch time

of only 120 minutes as shown in figure 5-10. Therefore even a v-groove with an initial mask opening of 100 μm is large enough to fit the 125 μm optical fibre after the wet etch process is completed.

5.2.3 Anchors for the comb drive actuator

In addition to the side wall and v-groove other micro structures need to be formed during the KOH wet etch process. These structures are part of the comb drive actuator and function as anchors and attach the comb drive structure to the supporting Pyrex™ substrate. The comb drive actuator requires one anchor, which fixes the stationary comb fingers to the underlying Pyrex™ substrate and another pair of anchors, on which the spring and the movable comb fingers of the actuator are suspended. A simple way of etching the required anchors is by patterning rectangles in the silicon nitride mask, which turn into rectangular pillar structures throughout the etching process. But there is one problem. Due to the orientation of the wafer surface is it not possible to create a rectangular pillar structure without major under etching of the masking pattern. Figure 5-12 shows again the simulation result of the KOH wet etch conducted earlier. However, this time the focus is on the etched anchors of the actuation structure identifying the impact of undercutting on the rectangular shaped anchor structures during the wet etch process. The image of figure 5-12a shows one large anchor, which supports the fixed part of the comb drive actuator, two small anchors attached to the spring of the actuation structure and one middle sized anchor, which is used for the movable planar mirror. In figure 5-12b an enlarged image of one of the two spring anchors is shown in detail. The red rectangular plane represents the surface area of the silicon nitride mask. It becomes clear that throughout the etching process a significant under etching along the y direction occurs. In x direction no undercutting occurs because the vertical side walls form the boundaries of the (111) planes. The under etching is caused by the adjoining and fast etching crystallographic planes at each end of the rectangular pattern.

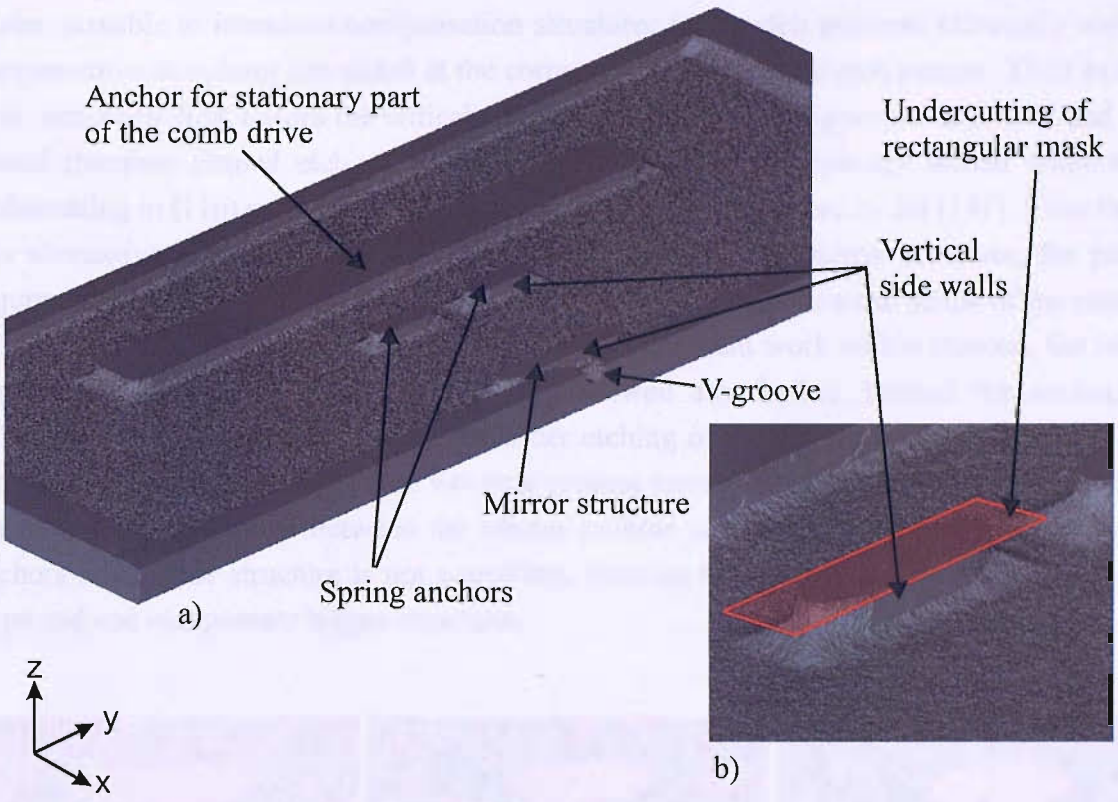

Figure 5-12: A KOH wet etch simulation of the vertical mirror side wall, v-groove and anchors in a (110) oriented silicon wafer. The large anchor represents the stationary part of the comb drive actuator. The middle sized anchor represents the mirror structure and the two smaller anchors suspend the spring and the movable actuation part (a). The enlarged image (b) from one of the smaller anchors shows the undercutting of the rectangular masking pattern along the *y* direction.

The undercutting of the masking nitride layer becomes critical when the dimensions of the anchors are too small. Having a too small sized anchor structure from the start the under etching can be so severe that the anchor disappears or gets so small, that the remaining surface area is not large enough to form a chemical bond during the anodic bonding process. It is estimated that a minimum bonding surface area of 100 μm by 100 μm is needed to make a strong chemical bond between the Pyrex™ and silicon wafer. Not only the size of the anchors of the actuator is important, but also the size of the anchor for the mirror structure. Figure 5-13 shows the example of the undercutting of the mirror structure. The set of microscope images are taken during the KOH wet etch after 90 minutes (a), 150 minutes (b) and 190 minutes (c,d). From an initial anchor size of 1 mm in length and 150 μm in width the anchor reduces its length to 1/3 after an etching time of 190 minutes (c). The SEM image (d) illustrates a more detailed view of the undercutting result after 190 minutes etch time on the initial 1 mm large mirror structure, which is outlined by the red rectangle. The disadvantageous under etching is also present for the rest of the rectangular anchors of the actuator and needs to be considered.

Besides enlarging the anchors and mirror structure in order to avoid bonding problems it is also possible to introduce compensation structures to the etch patterns. Generally wet etch compensation structures are added at the corners of an anisotropic etch pattern. Their purpose is to etch away first, before the critical etch pattern is attacked. Appropriately sized and positioned rhombus shaped etch patterns can be precisely anisotropically etched without any undercutting in (110) oriented silicon wafers as previously presented by Jia [141]. Even though this alternative method is suitable to etch the anchors and the mirror structure, the process requires a fair amount of development work in finding the right size and shape of the compensation structures. To keep processing costs and development work within reasons, the idea of applying compensation structures was not followed any further. Instead the anchors are enlarged in size taking into account the under etching of the rectangular etch patterns. Their sizes are increased so that after the wet etch process enough structural surface area remains to get a strong anodic bond between the silicon anchors and the Pyrex™ wafer. Enlarging the anchors and mirror structure is not a problem, because the overall size of the 1D actuator is large and can compensate bigger structures.

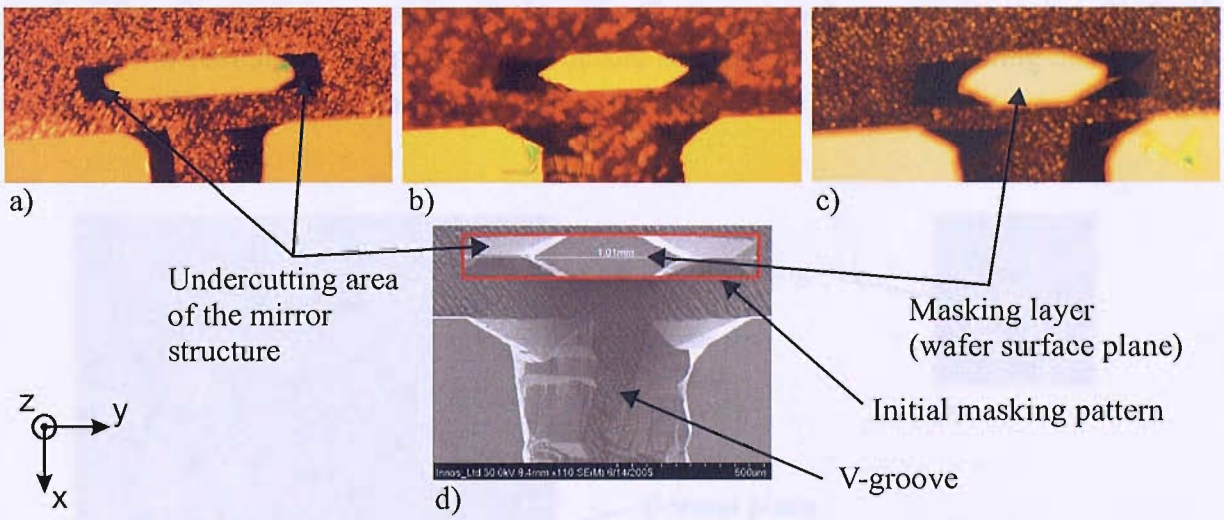

Figure 5-13: Microscope images of the KOH wet etch result of the mirror structure with an initial length of 1 mm and a width of 150 µm after 90 min. (a), 150 min. (b) and 190 min. (c). With a longer etch time the length of the mirror structure reduces to 1/3 of the initial length along the *y* axis. The SEM image shows a detailed view of the microscope image (c) with the initial rectangular silicon nitride mask pattern (red).

As a result of the undesired under etching of the rectangular mask patterns the anchors are resized accordingly. In the final design layout (see appendix I-2) of the 1D actuator the anchors are dimensioned as follows. The large anchor is chosen at a length of 5.7 mm and a width of 300 µm. This large size is possible, because of the size of the stationary comb drive part enclosing a large amount comb fingers. Hence, the undercutting of this anchor is not critical. The middle sized anchor for the mirror is 1300 µm in length and 200 µm in width. Even

with final length of 430 μm (1/3 of the initial length) after wet etching the mirror plane is large enough to cover the full width of the v-groove and fibre. For the mirror structure the bonding criteria does not apply, because the mirror is movable and is not anchored to the underlying Pyrex™ substrate. The two smaller spring anchors are 700 μm in length and 200 μm in width. Reducing also to 1/3 after the KOH wet etch a length of 230 μm remains, which is double the estimated size required for a strong bond.

5.2.4 Vertical side wall for the planar mirror

One of the key requirements of the planar mirror is a mirror side wall, which is perfectly vertical. A perfectly vertical side wall can be achieved by aligning the (110) oriented wafer to the (111) planes, which cut through the (110) surface at a 90° angle. A further key requirement is a very smooth mirror surface. But since the mirror side wall is formed by the bounding (111) planes their surfaces are atomically smooth. Of critical importance however is the precise alignment during the lithography process. If the alignment is very accurate (~0.1°) atomically smooth walls with a surface roughness of a few nanometers can be achieved. On the other hand, if the silicon nitride mask is misaligned with respect to the wafer flat during the mask exposure undercutting of the masking area occurs and surface steps form during the wet etching process. An example of a bad alignment is shown in figure 5-14.

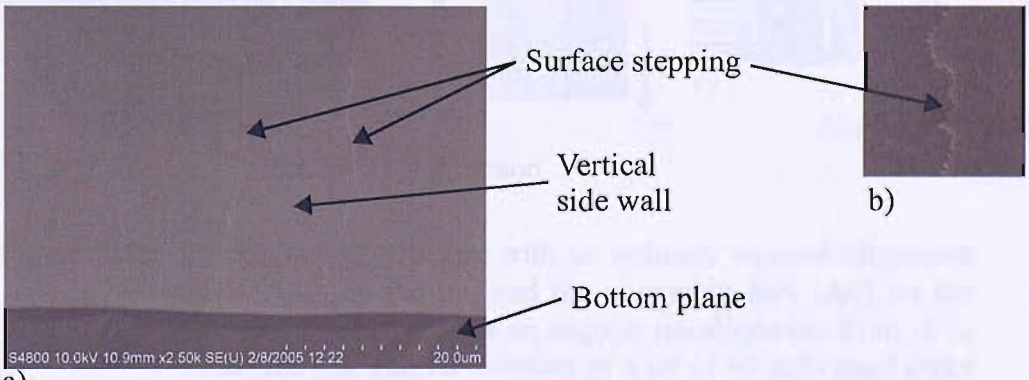

Figure 5-14: SEM image of a vertical etched side wall with a bad mask alignment causing stepping along the walls (a). The enlarged image (b) shows one individual step in detail.

The side walls are still perfectly vertical, but the wall is covered with surface steps. The degree of misalignment can be determined by the amount of surface steps on the side wall. The less accurate the alignment the more surface steps are present. Disadvantageous is when the surface stepping occurs within the area of the mirror where the laser light is reflected, because the stepping results in an increase in surface roughness, which negatively affects the optical properties of the cavity system.

Generally the flats of silicon wafers are only accurate within an angle of two degrees. Thus aligning the silicon nitride mask with the wafer flat would not be accurate enough. Even if the wafer flats were 100% aligned it would be very difficult to align the alignment marks of the lithography mask with the edge of the wafer, where the flat is located. In 1996 Vangbo et. al. [127] reported on a precise mask alignment to the crystallographic orientation of silicon wafers using wet anisotropic etching. They introduced a design tool, which can be used to detect the crystallographic orientation with the highest precision possible. The design tool is an alignment fork that, when etched briefly, can be used to determine the misalignment of the mask used. It also includes alignment marks for aligning a subsequent mask with the correct crystallographic direction. Using this method it is possible to find the (111) vertical planes on the (110) oriented silicon wafer within an accuracy of 0.1° and to create atomically smooth mirror side walls. The method takes advantage of the symmetric under etching behaviour around the (111) direction. The alignment structure is shown in figure 5-15.

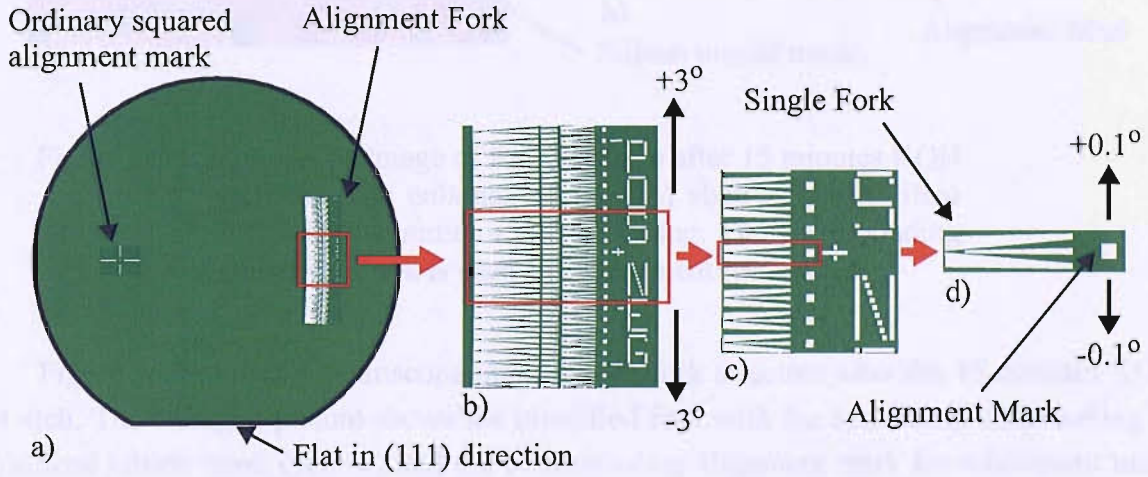

Figure 5-15: The alignment structure with an ordinary squared alignment mark (AM) on the left and the alignment fork (AF) on the right (a). The AF detects an angular misalignment from -3 to +3 degree (b). The AF consists of a set of 60 individual forks (c), which are repeated with an increment of 0.1°. Each fork has an additional AM for subsequent re-alignment (d) [127].

The alignment structure encloses an ordinary squared alignment mark on the left side of the lithography mask and the alignment fork structure on the right side (5-15a). The alignment fork structure consists of a set of forks. The forks are repeated with an angular increment of 0.1° and each fork has an alignment mark for subsequent re-alignment (5-15d). The total number of 60 forks cover an angular misalignment of +3 and -3 degree (5-15b). After a KOH wet etch for around 15 minutes the fork showing a symmetric under etching of the silicon nitride mask (green) identifies the (111) planes with a precision of 0.1°. Then the alignment mark of the identified fork is used for aligning the subsequent lithography mask, which

encloses the anchor structures, mirror structure and v-groove. The alignment process starts with covering the 50 nm LPCVD silicon nitride layer on the (110) silicon wafer with a 1.1 µm thick resist (SPRT-510). The resist is exposed with the mask of the fork structure. After the development of the resist and a hardbake for 30 minutes at 140 °C the Vangbo fork structure is opened in a silicon nitride dry etch process. Then a 15 minutes KOH etch is performed and the (111) planes are identified.

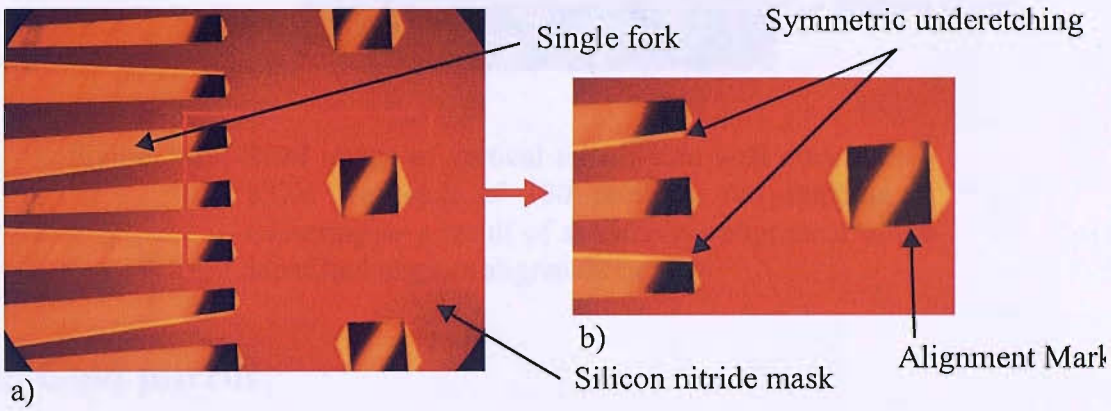

Figure 5-16: Microscope image of fork structure after 15 minutes KOH etch (a). The enlarged picture (b) shows the identified fork with a symmetric under etching. The corresponding alignment mark is used for subsequent re-alignment.

Figure 5-16 shows a microscope image of the fork structure after the 15 minutes KOH wet etch. The enlarged picture shows the identified fork with the symmetric undercutting of the silicon nitride mask (yellow) and the corresponding alignment mark for subsequent mask alignment. The subsequent mask encloses the anchors, v-groove and mirror structure, which is applied to the silicon wafer from figure 5-16. Then the second KOH wet etch is performed in order to etch the vertical mirror side wall. The result is shown in the SEM image of figure 5-17. The alignment is successful, because no stepping on the side wall is present.

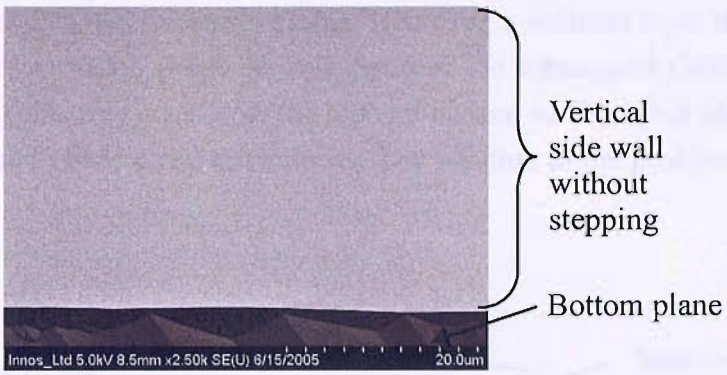

Figure 5-17: SEM image of vertical mirror side wall after a final KOH wet etch of 190 minutes. No stepping is occurring as a result of an accurate alignment to the identified angular alignment mark.

5.2.5 Gold mirror

The quality factor Q of the optical cavity is mainly dependant on the reflectivity of the gold mirrors [142]. Light scattering from a rough surface of the gold coated vertical side wall mirror and the concave fibre mirror should be minimised in order to obtain a high reflectivity. It is estimated that the concave fibre mirror has a RMS surface roughness of a few nanometers. The very low surface roughness of the planar mirror is achieved by applying a micromachining process to the KOH wet etched vertical silicon side wall. The process involves the deposition of a reflective layer of gold on the atomically smooth vertical silicon surface. Due to the skin depth of the laser light at a wavelength of 780 nm in gold the thickness of the reflective gold layer is required to be as thick as 60 nm. Since the adhesion of gold on silicon is poor, a 20 nm thin adhesion layer of chrome is deposited before the gold layer is applied. The Cr/Au layer is deposited by an e-beam evaporation method. In a subsequent process the Cr/Au layer is removed from the top and bottom surfaces, but leaving a reflective Cr/Au layer on the mirror side wall. Initially, it was planned using a wet etch process to remove the Cr/Au layer, but the process had to be adjusted accordingly as explained in the following.

In the evaporation process an electron beam (e-beam) is focused in the vacuum chamber of the machine onto a boat filled with the material to be deposited as shown in figure 5-18. The e-beam evaporates the solid material inside the boat. The location where the e-beam hits the material represents the point source of evaporation with a radial flux characteristic. Above the point source the processing wafers are placed. In a normal machine setup the wafer substrates are rotated during the evaporation process as shown in figure 5-18a. This way multiple wafers can be processed at the same time and a good uniform and homogeneous layer deposition over the entire wafer surface can be achieved. Using this setup the thickness of the Cr/Au layer is constant over the entire wafer, independent on the topology of the wafer surface. The deposi-

tion rate on vertical side walls is equal to the deposition rate on the wafer surface as well as on the bottom planes of the deep etched micro structures. However, a uniform layer thickness of Cr/Au over the entire wafer substrate is not desired, because the subsequent Cr/Au wet etch would not only remove the reflective layer from the top and bottom surfaces, but also from the vertical mirror side wall due to their equal thicknesses. The solution to the problem is a static angle e-beam evaporation.

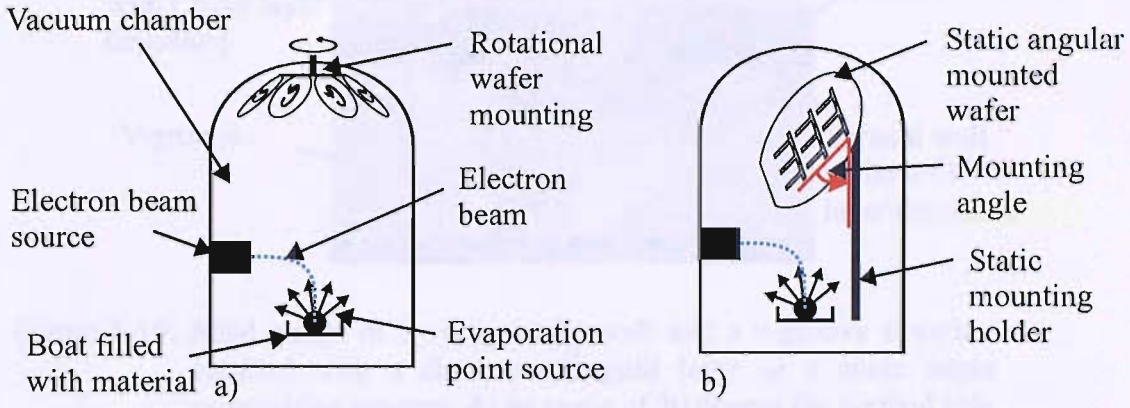

Figure 5-18: Schematic machine setup for e-beam evaporation (not to scale). An electron beam evaporates the desired material out of a boat. The evaporation point source has a radial flux, which provides a uniform and homogeneous layer deposition when the wafers are rotated during the deposition (a). In a static angle evaporation (b) the wafer is fixed throughout the evaporation process and mounted at an angle (red) much closer to the evaporation source.

In a static angle e-beam evaporation the wafer substrate is not rotated but static throughout the evaporation process. A special designed static wafer holder is used allowing only one wafer to be processed at a time, but at any desired angle as shown in figure 5-18b. Depending on the angle used during the evaporation the deposition rates on the vertical side wall and top surface can be varied. Choosing an angle smaller than 45 degree, the deposition rate on the vertical side walls is higher than on the top and bottom surfaces. With a thicker layer of Cr/Au on the vertical mirror side wall and a thinner layer on the top and the bottom surface the isotropic wet etch process can now be applied successfully clearing the top and bottom surface from Cr/Au with a reflecting layer of Cr/Au remaining on the vertical mirror side wall. Figure 5-19 shows a SEM image of a static angle evaporated mirror side wall, which has been evaporated with a 20 nm thick layer of chrome and a 100 nm thick layer of gold at an angle of 20 degree. With the wafer flat mounted towards the evaporation source (as previously shown in figure 5-18b) the mirror side wall structures are exposed to the flux of evaporation. Figure 5-19 also illustrates that the mirror side wall has a shadowed area with no gold deposition. The silicon wafer is mounted at a static angle. As a result the bottom part of the mirror side wall is

obstructed by the opposite side wall and no deposition takes place in this region. The shadowing effect is not present in the active area of the mirror, which is located in front of the v-groove, because the v-groove is an open structure without obstructing the path of the evaporation flux.

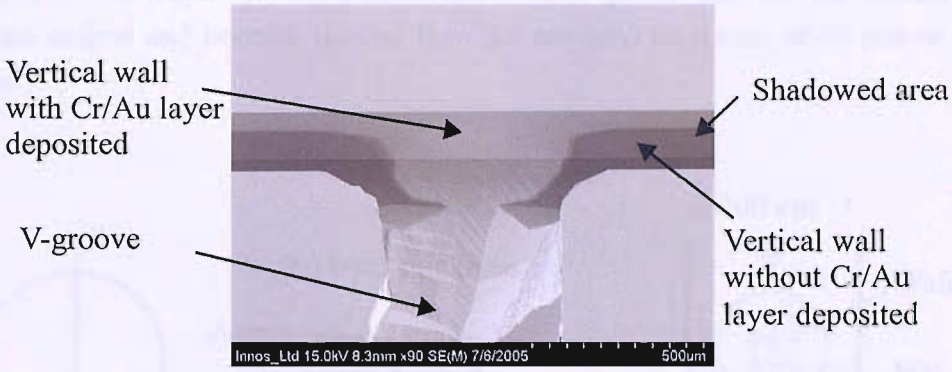

Figure 5-19: SEM image of a vertical side wall and a v-groove structure covered with a chrome and gold layer in a static angle evaporation process. At an angle of 20 degree the vertical side wall opposite to the mirror side wall obstructs the path of the evaporation flux resulting in a shadowed area where no deposition takes place.

The gold and chrome layer are chemically wet etched, using first a gold etchant solution followed by a chrome etchant solution. The Cr/Au covered wafer is fully immersed in a glass beaker of gold etchant and afterwards in a second beaker with the chrome solution. The silicon wafer is kept in the gold etchant for 45 seconds. After approximately 35 seconds the visible yellow shining gold layer on the top surface slowly fades away turning from a yellow gold colour into a dark brown chrome colour. At this point the gold is completely etched away on the top and bottom surfaces, but only partly etched on the vertical mirror side wall. Then the chrome layer is removed by dipping the silicon wafer in the chrome etchant for around 10 seconds. Now both metal layers are removed from the top surface. The wafer is now ready for the anodic bonding process.

During the gold wet etch it is noticed that the gold layer is not fading away uniformly at the same time over the entire wafer surface. This indicates that the deposited gold layer varies in thickness. In fact the gold layer is removed more slowly at the edge of the wafer flat than on the opposite edge on the wafer. This is caused by a difference in the deposition rate of the static angle evaporated silicon wafer depending on the distance between the wafer surface and the evaporation source. The fixed wafer in the static evaporation method is much closer to the point source compared to the rotational method, therefore the flux per square centimetre varies significantly. Since the wafer is oriented with the flat towards the evaporation source (see figure 5-18b) micro structures located around the wafer flat are exposed to a higher deposition

rate than structures further away on the other edge of the wafer. Figure 5-20a illustrates the change of gold thickness with respect to the wafer flat after the static evaporation process. The different Cr/Au thicknesses are also present on the mirror side walls. This means when the silicon wafer is completely immersed in the gold etchant the mirror side walls located further away from the wafer flat are experiencing a significant over etch compared to the structures located closer to the wafer flat. As a result the thinner gold layers on the vertical side wall structures are etched and become thinner than the required thickness of 60 nm or even etch away entirely.

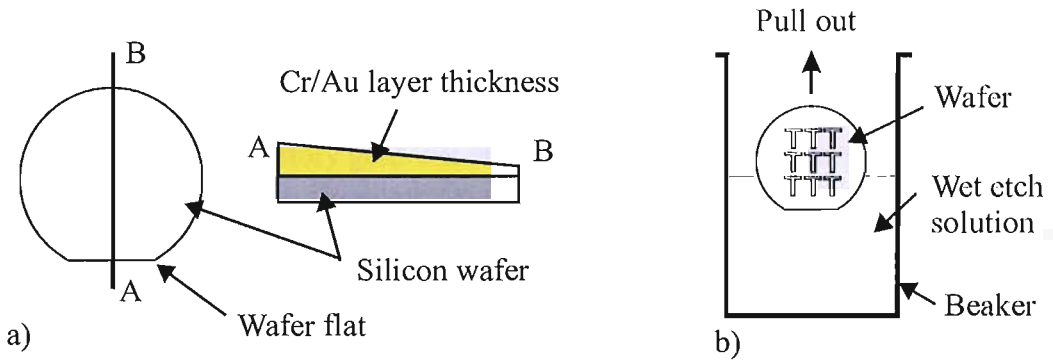

Figure 5-20: The wafer surfaces and deep etched micro structures close to the wafer flat experience a higher deposition rate than further away located features (a). The profile view from A to B illustrates the difference in the Cr/Au layer thickness across the wafer. Also a schematic drawing of the pull out procedure is shown (b). Pulling out the wafer in steps or very slowly the over etching of thinner covered mirror surfaces can be avoided.

There are two solutions to the problem. First, at the beginning of the gold and chrome etch the entire wafer is immersed in the solution, but then as the gold surface gets thinner and starts to fade away in colour the wafer is partly pull out of the solution. By slowly pulling out the gold evaporated silicon wafer the thinner deposited gold layers located away from the wafer flat are not immersed in the wet etch solution any more, whereas the micro mirrors close to the wafer flat are still immersed and continue to be etched. Figure 5-20b illustrates the pull out procedure for the gold etched silicon wafer. A major disadvantages of this procedure is that the process is not very controllable and repeatable, due to the fact that pulling out the wafer in stages or very slowly requires a very steady hand. Also disadvantageous is that certain mirror structures, even though they are not immersed in the solution any more continue to etch, because of gold etchant adhering to corners and around the edges of the micro structures due to surface attraction forces. Figure 5-21 shows a SEM image of a gold etched mirror side wall after applying the described pull out procedure. The mirror surface coverage with gold is not satisfactory. The gold is etched unevenly and etched away completely at the top of the side wall near the wafer surface. Also patches of gold are visible at the bottom plane of the mirror

structure. These remaining and unwanted gold patches will act as a masking layer when the bottom plane is etched through during the final DRIE release etch.

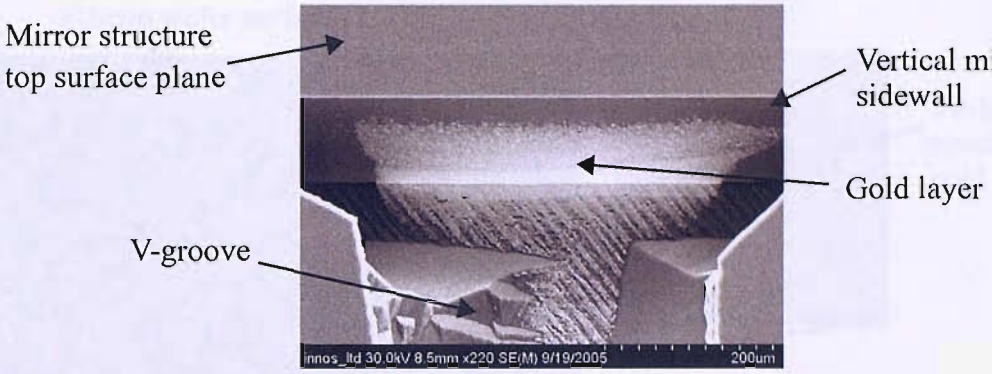

Figure 5-21: Unsatisfactory gold wet etch result after applying the pull out procedure. Gold layer is etched away at the top of the mirror side wall. Also undesired gold patches at the bottom plane remain leading to masking during the final DRIE release etch.

Another way to avoid the wet etch problem, is to deposit a thicker layer of gold and thereby compensating the over etch of the mirror structures with the thinner gold layer. A fully immersed wet etch could then be applied, without worrying about etching the gold mirror away. The disadvantage of this process is that a gold layer is required which is twice or even three times thicker than the initial thickness of 100 nm. As a result of a longer deposition time the surface roughness of the gold layer increases because of kinetic roughening [143]. Hence, a small increase in surface roughness will induce a large loss in the cavity finesse [39]. Finally, depending on the location of the mirror structure on the wafer substrate the difference in gold thickness after wet etching would also vary quite significantly.

Instead of using the problematic isotropic wet etch process to remove the Cr/Au layer an alternative process is investigated. In this process the metal layer is removed by applying an anisotropic ion beam milling process. During the ion beam milling ions are accelerated, physically bombarding the wafer surface. The accelerated ions hit the gold surface and remove the gold layer from the wafer surface. Since the trajectory of the ions is perpendicular to the wafer surface the ion beam milling (IBM) process is anisotropic. The IBM process is therefore very suitable for removing selectively the gold from the top and bottom wafer surfaces. After the gold layer is removed by the IBM process the chrome layer can then be removed by a wet etch. Wet etching and over etching the chrome layer is not critical because the chrome is protected during the chrome etch by the covering gold layer on the mirror side wall. Figure 5-22a shows a SEM image of a mirror side wall, which is covered with a layer of Cr/Au that has been ion beam milled to remove the gold layer from the top and bottom surfaces. The wafer is also wet etched to remove the chrome layer from the top surfaces in order to prepare the wafer for the

bonding process. In the enlarged SEM image (figure 5-22b) the grain structure of the gold layer is visible.

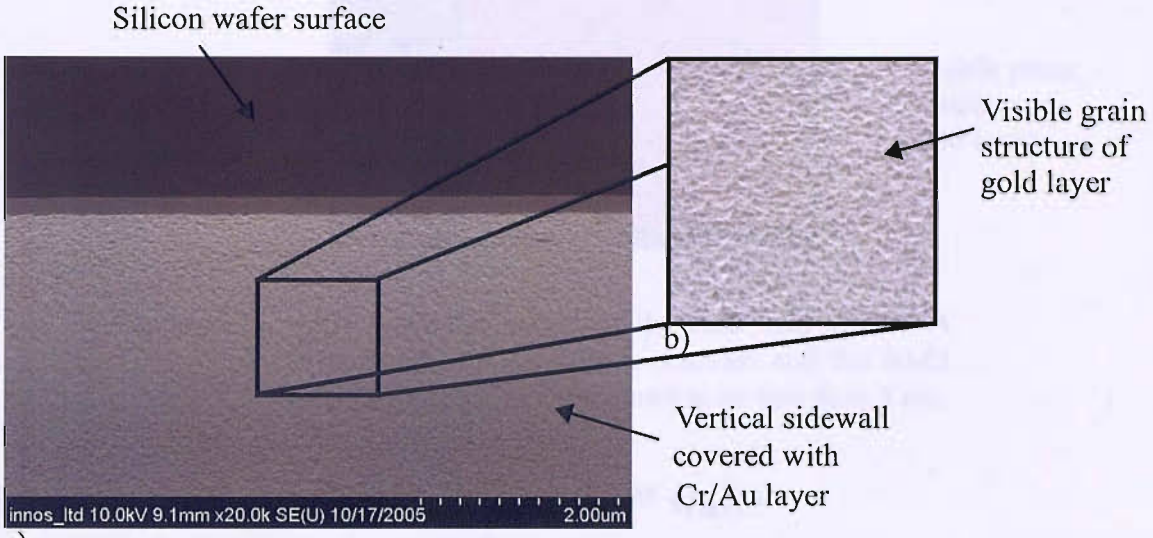

Figure 5-22: SEM images of the fabrication result after processing the gold side wall mirror. The vertical side wall with the remaining gold layer and the underneath lying chrome layer (a), the visible grain structure of the evaporated gold layer (b)

On the gold coated mirror side wall an atomic force microscope (AFM) measurement is performed. In order to measure the gold layer on the vertical side wall a test wafer is specially prepared. The preparation included the separation of a small piece from the vertical side wall structure on the test wafer. Breaking the test wafer exactly near the vertical side wall turned out to be much more difficult than anticipated. However, after several attempts a small piece of gold coated side wall is extracted and after mounting it horizontally on the AFM stage the measurement is carried out. The AFM measurement result is shown in figure 5-23. Scanning a surface area of 7.4 μm^2 the RMS surface roughness is measured to be less than 3 nm. It is estimated that a cavity mirror surface roughness of 3 nm is sufficient to achieve single atom detection within the optical system [37].

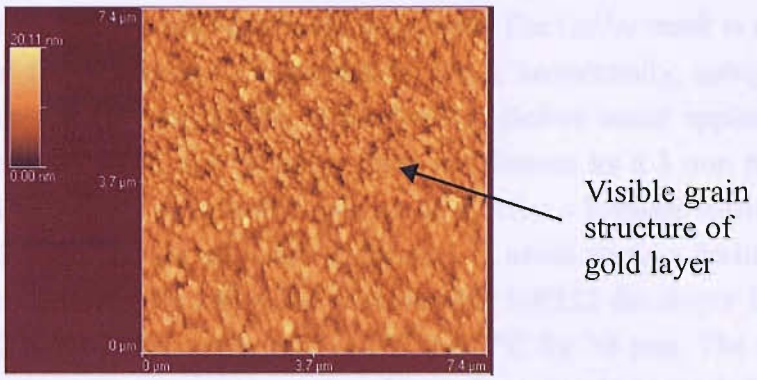

Figure 5-23: AFM scanning image of the side wall mirror. A surface area of 7.4 μm^2 is scanned and the RMS surface roughness is measured to be less than 3 nm.

5.2.6 Actuation cavity in the Pyrex™ wafer

In order to actuate the planar mirror it is necessary that the mirror structure is free to move. This can be achieved by etching a cavity into the Pyrex™ substrate. With a cavity or gap spacing of 20 µm between the top surface of the mirror structure and the underneath positioned etch cavity in the Pyrex™ substrate the anodic bonding process is interrupted. Other structures such as the anchors of the comb drive actuator on the silicon wafer, which are in direct contact with the Pyrex™ surface, form a chemical strong bond. Borosilicate glass such as Pyrex™ is the most widely used glass substrates in MEMS, not only because it can be anodically bonded to a silicon wafer without difficulty, but also because is can easily be micro structured using a variety of glass micromachining technologies such as chemical wet etching [144] or deep reactive ion etching (DRIE) [145]. Both technologies are available in the clean room at Southampton. Chemical wet etching using various concentrations of hydrofluoric acid (HF) are a very common method for shallow etching [146], deep etching [147] and through etching of glass wafers [148], because the etching rate is fast and a large quantity of glass wafers can be processed simultaneously. The choice of mask for glass etching in HF depends on the etch depth and HF concentration, but normally photoresist or a combination of a thin Cr/Au layer and photoresist are used. An alternative method of etching a glass substrate is by deep reactive ion etching (DRIE) using SF_6 plasma [149]. Although DRIE is a suitable alternative to wet etching the overall etch rate of 0.5 µm/min is low and time consuming compared to the fast etch rate of 8 µm/min using concentrated HF. Also the fact that the metal ions in the Pyrex™ substrate will contaminate the etching facility makes this process less suitable.

In order to wet etch the 20 µm deep cavity in the Pyrex™ wafer a photoresist on top of a Cr/Au layer is used in a 48%HF 2:1 H_2O wet etch solution at room temperature. According to Minquang [150] this HF concentration achieves an etch rate of 3.5 µm/min. The front side of the Pyrex™ wafer is evaporated with a 40 nm layer of chrome and 400 nm layer of gold. The

Cr layer functions as the adhesion layer because the Au layer is difficult to adhere directly onto the Pyrex™ substrate. The Au layer is used as the etching mask. The Cr/Au mask is etched by wet etching in Au etchant for 3 min and Cr etchant for 10 s, sequentially, using Shipley SPRT220-7 positive photoresist (11 µm) as the etching mask. Before resist application the Pyrex™ wafer is dehydrated at 140 °C for 30 min, which is followed by a 3 min primer for resist adhesion purposes. The resist is spun at 890 rpm for 60 s. After a hotplate softbake at 90 °C for 1 min the wafer is left for 15 min at room temperature to avoid stiction during contact exposure. The wafer is then exposed for 240 s and developed in MF322 developer for 2 min. Before etching, the SPRT220-7 photoresist is hard baked at 80 °C for 30 min. The thickness after hardbake is about 10 µm. The photoresist is not only used as an etching mask for the Cr/Au wet etch, but also as an etching mask for the subsequent HF Pyrex™ wet etch. The backside of the Pyrex™ wafer is not protected during the HF etching process, because it is not used throughout the processing. After wet etching for 6 min the photoresist and underneath lying Cr/Au layer are still intact and no damage is visible under the microscope. The cavity is measured with a depth of 21 µm. After the cavity etching the resist and Cr/Au layer are stripped off the Pyrex™ wafer surface. The resist is stripped in a fuming nitric acid (FNA) solution for 10 min. The Cr and Au layer is stripped using the Cr and Au etchant.

In a subsequent process a second Cr/Au layer is applied on the cavity side of the Pyrex™ wafer. The microscope image of the Pyrex™ cavity and the second metal layer is shown in figure 5-24a. The image was taken from the backside of the Pyrex™ wafer after the substrate was anodically bonded onto the processed silicon wafer.

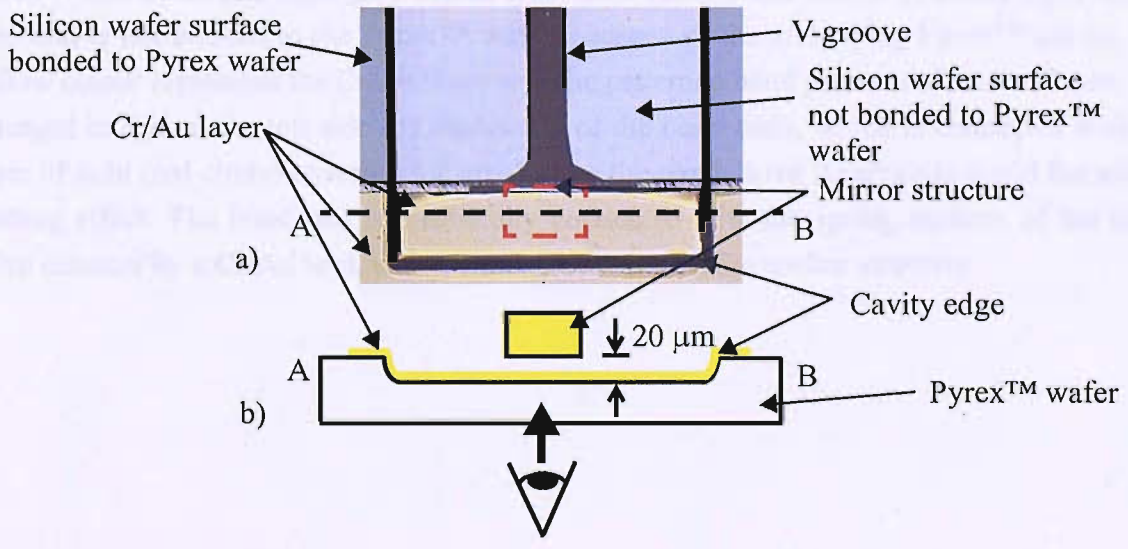

Figure 5-24: Microscope image of the wet etched Pyrex™ cavity from the backside of the Pyrex™ wafer after it is bonded to the silicon wafer (a). The mirror structure is located in the cavity etched area and is not bonded to the Pyrex™ substrate. The profile view across the cavity shows the position of the mirror structure 20 µm above the cavity bottom surface, which is covered with a second Cr/Au layer.

The Pyrex™ cavity is positioned underneath the mirror structure during the bonding alignment, so that during the actual bonding process the mirror structure is not bonded and remains free. The view of the mirror structure (red square) is obstructed by the Cr/Au layer in the microscope image. The schematic wet etch profile of the Pyrex™ cavity is illustrated in figure 5-24b.

The second Cr/Au layer with a thickness of 60 nm of chrome and 1300 nm of gold are required for two reasons. First, the metal layer is patterned to form bond pads. The bond pads are electrical contacts, which are wire bonded to the outer packaging, in order to apply the driving voltage to the actuation device. Second, the Cr/Au layer prevents the so-called micro-loading effect during the DRIE process to release the comb drive actuator at the end of the fabrication of the SOG process [151]. During deep dry etching of electrostatic force sensors or actuators with comb drive structures narrow trenches etch more slowly than wide trenches. As a result of this etching behaviour an over etch is necessary for releasing the silicon comb drive structure on a SOG substrate. During the over etching the silicon facing the glass substrate is damaged by ion bombardment, which is a critical problem for reliability of the devices especially in automotive applications. A metal layer patterned onto the glass substrate and electrically connected with the silicon during the dry etch process resolves this problem. The metal layer avoids the charge accumulation at the glass surface, which is the origin of ion bombardment of the silicon structures facing the glass substrate. Figure 5-25a shows a collage of two microscope images of the 1D actuation structure looking from back onto the Pyrex™ wafer after the anodic bonding process of the patterned silicon and Pyrex™ wafer. The grey colour in the image (a) represents areas where the silicon structures such as anchors are bonded to the Pyrex™ substrate. The light grey colour near the v-groove and mirror structure represent an area that is not bonded to the Pyrex™ wafer, because of the underlying Pyrex™ cavity. The yellow colour represents the Cr/Au layer with the patterned bond pads and electrical leads. The enlarged image on the left side (b) shows one of the bond pads, which is connected with the layer of gold (red circle) covering the area below the comb drive structure to avoid the micro-loading effect. The bond pad is electrically connected with the spring anchors of the comb drive actuator by a Cr/Au lead, which extends underneath the anchor structure.

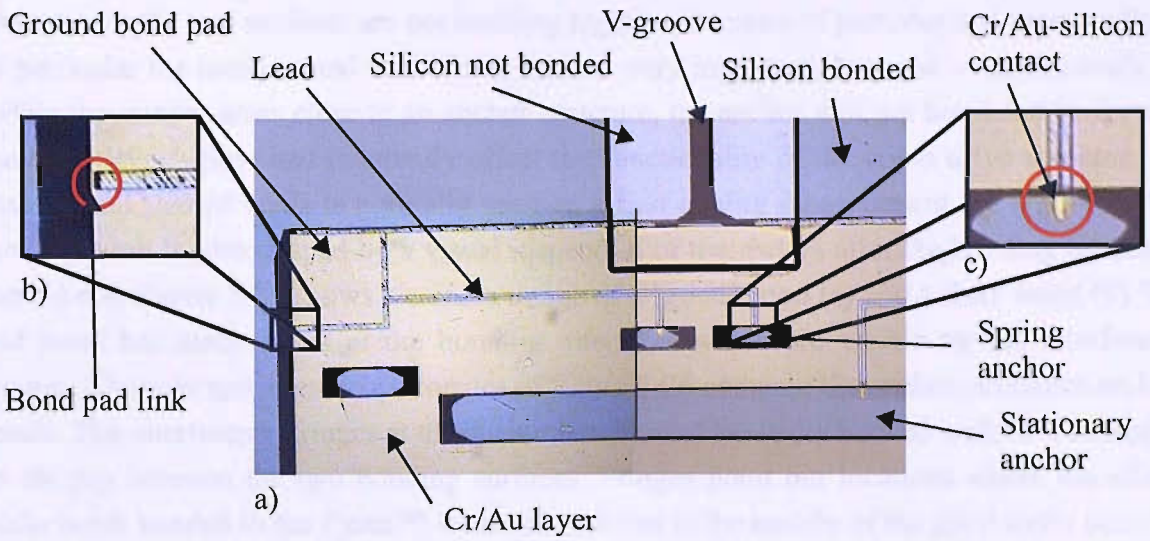

Figure 5-25: Microscope image of the 1D actuation structure taken from the back of the Pyrex™ wafer after the anodic bonding process of the patterned silicon and Pyrex™ wafer (a). The Pyrex™ wafer has a patterned Cr/Au layer, which is connected to the silicon wafer to avoid the micro-loading effect during the DRIE release etch. The metal pattern includes two bond pads. A ground pad, which is connected via a lead with the spring anchors and a voltage pad (not shown) to apply the actuation voltage. The leads extend underneath the anchor structures forming an electrical contact after bonding (c). The bond pad link (b) is removed during the final sawing process to disconnect the two bond pad contacts.

The enlarged image on the right side (c) shows the lead extension being pressed in between the silicon and Pyrex™ surfaces (red circle) after bonding. Actuating the comb drive requires two electrical contacts, one ground contact and one contact to apply the actuation voltage. The ground is connected to the bond pad shown in figure 5-25a, the driving voltage is connected to the second bond pad on the right side of figure 5-25a (not shown). The second bond pad is connected via a lead with the large stationary anchor. Important to notice is that after the deep dry etching the bond pads need to be disconnected from each other. This is achieved by precisely sawing through the bond pad link after fabrication, when the devices are cut to fit the packaging.

5.2.7 Anodic Bonding

The silicon wafer and Pyrex™ wafer are attached to each other by applying an anodic bonding process. The process chemically bonds the two interfacing surfaces of the silicon wafer and glass wafer permanently together. Before the bonding process can start both wafer surfaces are cleaned in a FNA solution for 10 min to assure that surfaces are clean and free

from any particles. Contaminated surfaces can lead to voids during the bonding. Voids are areas where the two surfaces are not bonding together, because of particles that separate them. In particular the location and size of the voids is very important, because when the voids are within the critical areas close to an anchor structure, the anchor will not bond and be fixed to the Pyrex™ substrate and inherently affect the functionality of the comb drive actuator. The amount and size of voids is normally used as a first quality measurement for a good or bad bond and can be determined by a visual inspection of the wafers after the bonding process is carried out. Figure 5-26 shows a camera image of a 'good' bond (a) and a 'bad' bond (b). The bad bond has many voids at the bonding interface, which are visible by the interference fringes. The enlarged microscope images of figure 5-26 compare the anchor structures on both bonds. The interference fringes at the anchor structure of the badly bonded wafer are caused by an air gap between the two bonding surfaces. Fringes point out locations where the silicon wafer is not bonded to the Pyrex™ wafer. The circles in the middle of the good wafer bond are not at the bonding interface on the front side of the Pyrex™ wafer. The circles are on the back side of the Pyrex™ wafer and therefore not critical to the process.

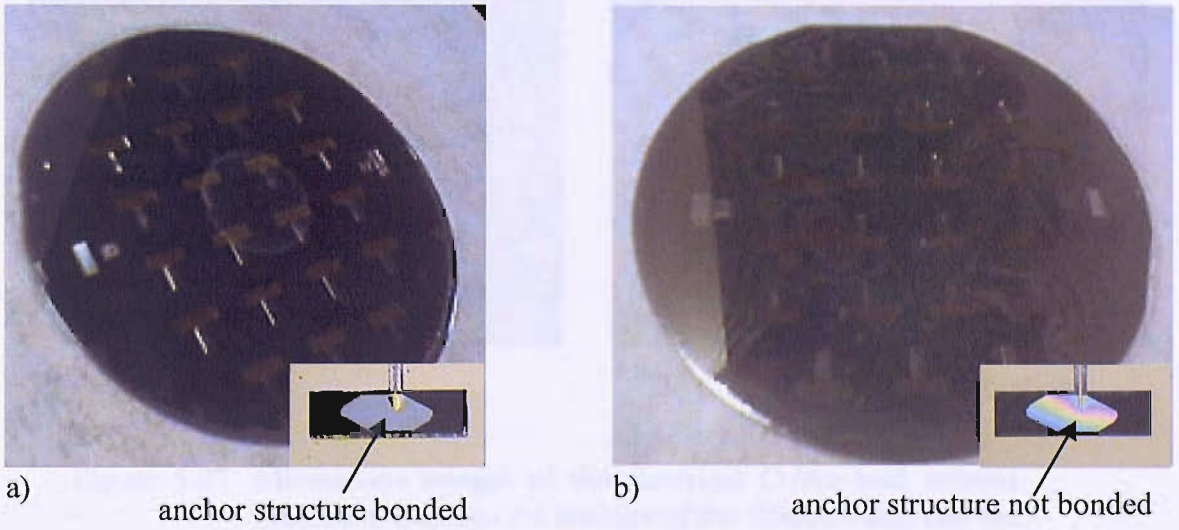

Figure 5-26: Photograph images to two silicon-Pyrex™ wafer bonds. Left side (a) represents a good bond, right side (b) a bad bond. The bad bond is covered with interference fringes from voids, where particles are trapped in between the interfacing bonding surfaces. Fringes point out locations where the wafer surfaces are not bonded to each other. The enlarged images compare the anchor structure in a bonded location (a) and a not bonded location (b).

The wafers are bonded on an EVG 620 bonder. Prior to bonding the wafers are aligned to each other. A precise alignment is critical. Not only the electrical leads need to be aligned underneath the anchor structures, but also the anchor structures themselves need to be aligned to the opening in the Cr/Au layer as illustrated in the enlarged images of figure 5-25. After

alignment the bonding process is started. The bonding chamber is pumped down to a pressure of 10^{-5} torr. The wafers are then pressed together with a force of 400 N and bonded for 15 min with an applied voltage of 900 V and a temperature of 310 °C. Generally bonding temperatures are about 400 °C, but during the first bonds it is found that a temperature beyond 310 °C cause the chrome layer to diffuse into the gold layer and visa versa. Diffusion increases the resistivity of the electrical contact forming a 'bad' electrical contact with regards to the electronics for the actuation. Figure 5-27 shows the images of two anchor structures that have been bonded at 310 °C (a) and 380 °C (b). The lead extension bonded beyond the critical temperature of 310 °C shows first signs of deterioration of the Cr/Au layer, which is pressed between the silicon anchor and the Pyrex™ surface, whereas the Cr/Au layer bonded at 310 °C does not show any visible change. As a result of these findings the temperatures of all subsequent bonded wafers are kept at 310 °C in order to maintain a 'good' electrical contact.

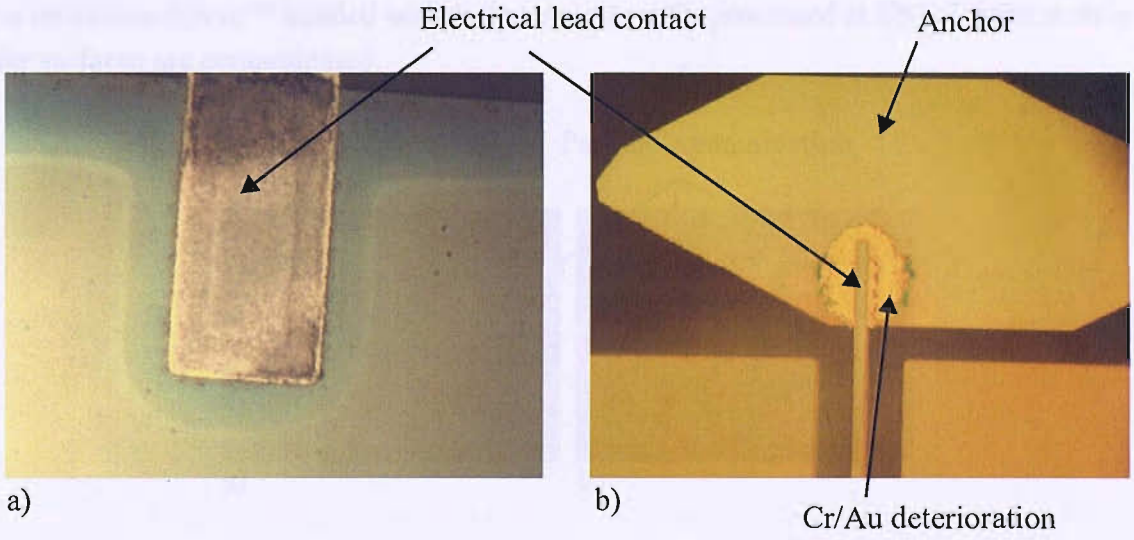

Figure 5-27: Microscope images of the electrical Cr/Au lead contact bonded in between the anchors of the silicon wafer and the Pyrex™ wafer. At the critical bonding temperature of 310 °C no diffusion of the Cr and Au occurs (a), but beyond the critical temperature at around 380 °C the Cr/Au deteriorates due to the diffusion of both metals. Diffusion causes an increase in resistivity of the electrical contact.

5.2.8 Comb drive actuator

After the bonding process a deep reactive ion etch (DRIE) is applied releasing the comb drive actuator. The masking layer for the comb drive actuator is a positive photoresist. The photoresist (SPRT220-7) is spun on the back side of the bonded silicon wafer with a thickness of 7 µm. After spinning a hotplate softbake at 90 °C for 1 min is done. Then the wafer is left for 15 min at room temperature to avoid stiction during contact exposure. After exposed for

180 s with the comb drive mask pattern, the wafer is developed in MF322 developer for 2 min. Finally a hardbake at 80 °C for 30 min is applied hardening the resist in order to withstand the DRIE process.

At this point of processing all the wafers were destroyed in the university clean room fire. After the fire the wafer processing was outsourced to Standford University in the USA (SNF). A repeat of the process was started at SNF in May 2006. In the beginning the process was estimated to be finished in a six months period. However, transferring the process was much more difficult than initially anticipated and even now in October 2007 the processing has not been completed at SNF. Transferring the process on paper is easy and straight forward, but repeating the process in real life with different machines in a different clean room is very difficult and time consuming. Especially if you are not on site, and communication is mainly limited to telephone conversations and emails and third parties are involved for processes such as anodic bonding and DRIE. The pictures of figure 5-28 show microscope images of the resist layer on silicon-Pyrex™ bonded wafers that are currently processed at SNF. Unfortunately the wafer surfaces are contaminated.

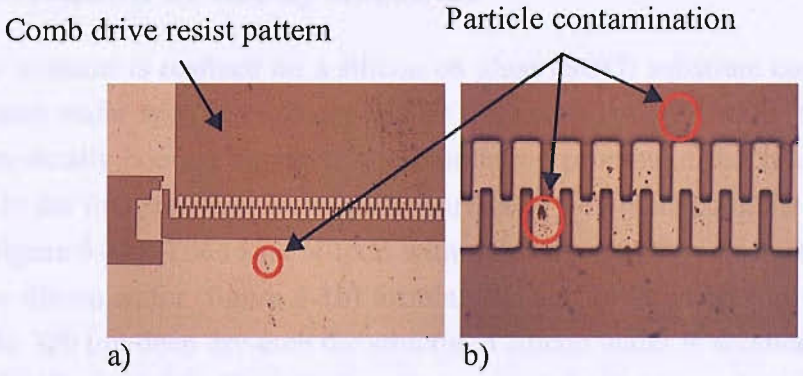

Figure 5-28: Microscope images of patterned photoresist layer on the bonded silicon-Pyrex™ wafers processed at SNF. Wafer surfaces are contaminated with particles. Particle contaminations are present on the entire wafer surface (a). The detailed image (b) indicates that the particle contamination occurred before resist deposition and patterning, because the particles are located underneath the resist. Unfortunately all the wafers need rework.

The overall cleanliness of the wafer surface is bad, indicated by the dark spots in figure 5-28a-b. The particle contamination is present underneath the resist pattern, which indicates that the wafer surface was not clean before applying the resist. Unfortunately all SNF wafers require rework, because masking particles in the resist pattern in particular in between the comb fingers will cause the fingers to stick together after DRIE. The actuator will not work eventually. This is just one example, which under normal conditioned should not have happened. But reworking and making compromises throughout the remote processing at SNF is essential in order to recover what was lost in the fire.

5.3 3D Actuator

The 3D actuator is more complicated than the 1D actuator in its structural design as well as in its fabrication. Due to the complexity of the three-dimensional actuated optical cavity system the fabrication is split into three processing stages. The first stage involves the fabrication of the two-dimensional actuator, which is required for the cavity alignment in the wafer plane. In a second stage the out-of-plane actuator for tuning the optical cavity in *z* direction is fabricated. In the final processing stage both, the *xy* actuator and the *z* actuator, are combined into one single three-dimensional actuation system. The fabrication processes in the following sections represent only the fabrication work of stages one and two, because towards the end of the fabrication of the first two stages the university fire destroyed all the devices and wafers, which had been fabricated up to this point. After the fire the fabrication was focused on the 1D actuator due to the time and resource constraints on the project. The fabrication of the 3D actuator was not repeated and stopped after the fire.

5.3.1 Fabrication of the xy actuator

The *xy* actuator is realized on a silicon on glass (SOG) substrate consisting of a double polished silicon wafer with a thickness of 380 µm and a Pyrex™ wafer (500 µm thickness), which are anodically bonded together. The fabrication process of the *xy* actuator is shown in figure 5-28. In the first step the silicon wafer surface is patterned using the positive photoresist SPR220-7 (figure 5-1a). The resist is spun with a thickness of 10 µm in order to etch 320 µm deep into the silicon wafer (figure 5-1b) forming the anchor structures for the actuation structure. After the 320 µm deep dry-etch the structured silicon wafer is anodically bonded onto the Pyrex™ wafer (figure 5-1d). Once the bonding is carried out a second deep dry-etch of 60 µm is performed using the masking resist SPRT518 with a thickness of 2.2 µm to release the actuation structure (figure 5-1e). In order to align the structures from the first DRIE on the back with respect to structures on the front for the second DRIE additional alignment marks for double-sided alignment are implemented in the lithography masks. Figure 5-28 does not show the alignment marks as they are located at the edge of the wafer some distance away from the actuation device.

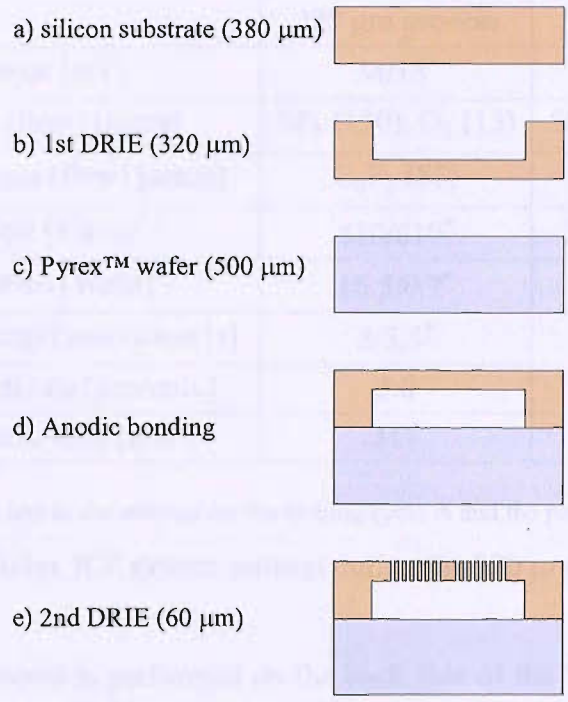

Figure 5-29: Fabrication process of the *xy* actuator.

320 μm deep dry-etch (1st DRIE)

The quality, reproducibility and reliability of the *xy* actuator is strongly dependent on the fabrication results of the two deep reactive ion etching (DRIE) processes. They define the geometry and shape of the various parts of the actuator such as anchors, spring suspensions and comb fingers. An important aspect during the deep reactive ion etching is the evolving form and profile of the various parts of the actuator. The shape, roughness and verticality, especially of the anchors at the end of first dry-etch and the spring suspension and comb drive fingers after the second dry-etch are critical for the functionality of the actuation structure. Therefore, a DRIE process is carried out on a test structure. The test structure is based on the process listing and mask layout outlined in the appendix C.1.1 and C.1.2. The test structure consists of trenches, squares and an initial design of an actuation structure, which include several comb drive designs. The dry etch machine parameters for both, the first and second dry-etching process are detailed in table 5-1. Important to notice is, that the figures in table 5-1 are optimized parameters providing good etch results in terms of shape, roughness and verticality for the deep dry etch process. The optimized parameters are based on a standard etch recipe provided by the machine manufacturer.

	320 μm process	60 μm process
Pressure [mT]	34/18*	34/18*
Etch gas (flow) [sccm]	SF_6 (130), O_2 (13)	SF_6 (130), O_2 (13)
Passivation gas (flow) [sccm]	C_4F_8 (85)	C_4F_8 (85)
RF Coil [Watts]	810/610*	810/610*
RF Platten [Watts]	16.5/0.7*	16.5/0.7*
Time of Etching/Passivation [s]	8/5.5*	8/5.5*
Average etch rate [μm/min.]	3.0	3.0
Total process time [min.]	117	46

*whereas A/B refers to the settings for the etching cycle A and the passivation cycle B.

Table 5-1: Multiplex ICP system settings during the 320 μm and 60 μm etch.

The first DRIE process is performed on the back side of the 380 μm thick silicon substrate by applying a positive 10 μm thick photoresist (SPR220-7). The lithography steps to apply the resist are equal to the 1D actuator application. Since throughout the dry etching process not only the silicon is attacked and etched away but also the photoresist, a relatively thick photoresist layer of 10 μm is chosen. By choosing a thick layer of resist a total depth of 320 μm in the silicon wafer can be achieved as illustrated in figure 5-30. Figure 5-30 shows the etching results of a 320 μm deep dry etched silicon wafer on a set of anchors from the test structure after the resist layer was stripped. It is noticeable that the surface roughness on the planar side walls of the anchors increases with the etch depth as shown in the enlarged image of a stationary comb drive anchor in figure 5-30b. The side wall roughening is not of any concern, because the anchors are only used as a support structure for the comb drive actuator. The optimized etching parameters from table 5-1 are not perfect, especially for a 320 μm deep etch. A lateral overetch at the anchor structures is present. The lateral overetch increases with the etch depth of the anchor and is in particular critical for the spring anchors (figure 5-30c) which in the test structure are 50 by 50 μm in size. The lateral overetch causes the anchors to become thinner throughout the etching process. When they become too thin at the bottom the anchors brake off during the etching process. Figure 5-30a shows four spring anchors broken lying on the bottom surface plane. In comparison the figure 5-30c shows two spring anchors of which one is still intact and standing, whereas the anchor in the front is broken. In order to prevent the breaking of the anchors as a result of the lateral overetch the anchors are increased in their size. In the final mask design for the 320 μm deep etch the minimum anchor size area is increased to 150 by 150 μm.

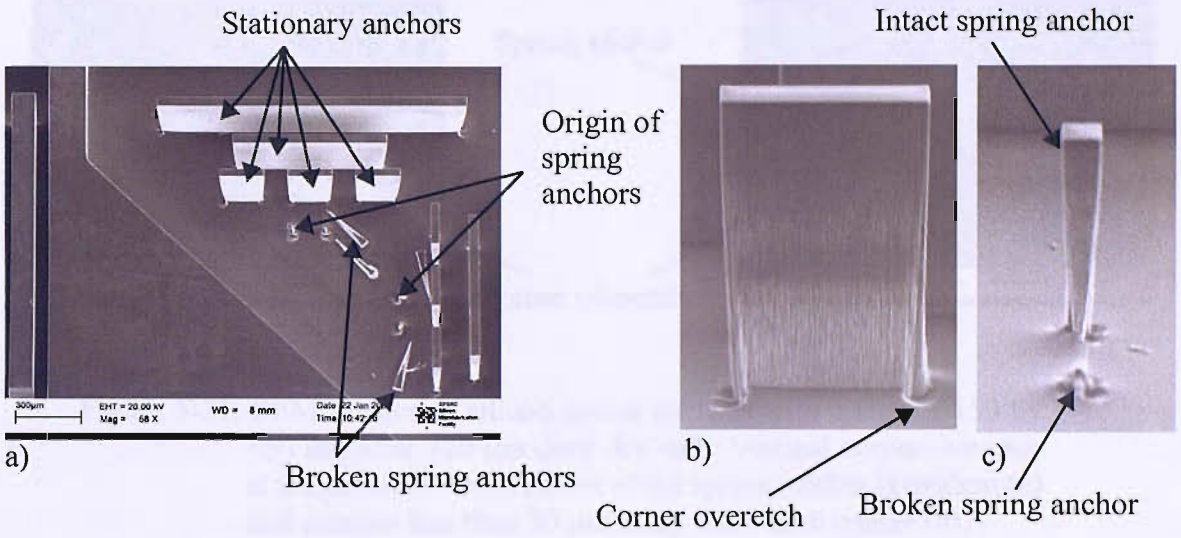

Figure 5-30: A 320 μm deep dry-etch of a test structure on the back-side of a double polished silicon wafer. Deep etched stationary anchors are intact, but spring anchors are broken (a) due to a later overetch. All anchors show side wall roughening and corner overetch at the bottom of the anchor structure (b). One spring anchor is intact and one anchor is broken (c).

Besides the lateral overetch there is also a vertical overetch at the bottom of each anchor corner evident.The corner overetch is visible at the bottom each anchor structure by a circular etch pattern in the bottom surface plane. The disadvantageous effect of the vertical overetch causes a deformation at the foundation of the rigid anchor posts resulting in an irregularity of the attached suspension beams in the 60 μm actuation layer. The rectangular shape of the beam structures becomes distorted and the actuation becomes less controllable and less predictable. It is measured that the corner overetch extends not more than 30 μm away from the initial size of the anchors as shown in figure 5-31. This means, that in the mask design for the 60 μm comb drive actuation structure a 30 μm overlap is to be added to the initial anchor size in order to avoid for example a deformation of the critical suspension beams. The overlap of 30 μm is also included for the stationary anchors.

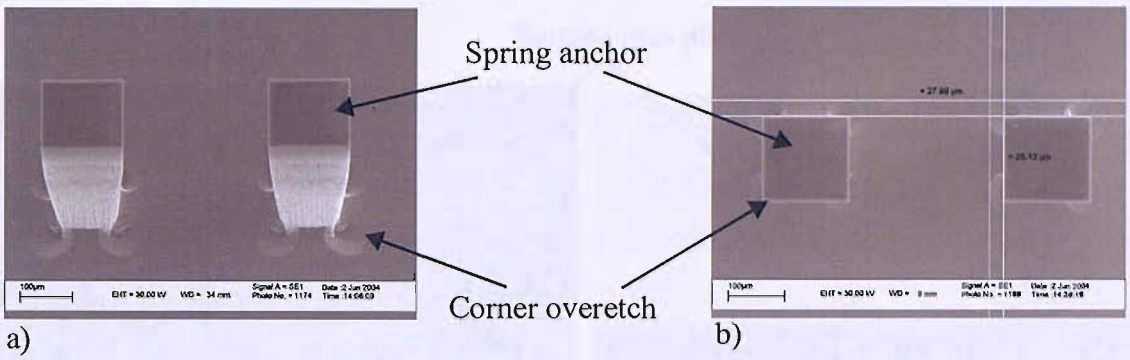

Figure 5-31: SEM images of silicon spring anchors with a size of 150 by 150 μm after 320 μm deep dry etch. Vertical corner overetch at the bottom of each corner of the spring anchor is evident (a) and extends less than 30 μm away from each corner (b).

In general, the etch rate of a DRIE process depends mainly on three factors. First, the opening of the etch structure. Smaller mask openings are etched with a slower etch rate than larger openings. This is in particular important for the 60 μm deep etch of the comb fingers. The comb fingers of the 3D actuator with a feature size of 3 μm are the smallest openings. They etch significantly slower than the rest of the comb drive structures. This etching behaviour also applies to the 320 μm deep etch of the silicon anchors of the actuation structure. Depending on the size of the anchors and their distance between each other uneven etch rates can occur. An investigation is carried out to ensure that the bottom etch plane is etched at a constant etch rate to achieve a uniform and even etch plane. It is found that with a mask opening bigger than 300 μm the etch rate becomes constant. For detailed results see appendix C.1.3. Second, the etch rate is typically 5% faster in the center of the wafer than at the edges. Finally the etch rate depends on the etching gases and concentrations. Considering all three factors the anchor structures of the 320 μm deep etch are situated more than 400 μm apart from each other and the actuation devices are placed as close as possible to the center point of the silicon wafer using the etch conditions from table 5-1. Figure 5-32 shows an SEM image of the anchor structures using the final mask design after it is etched 320 μm deep into the silicon wafer. A set of four groups of pillar structures are illustrated representing the anchor structures of the four comb drive actuators for the *xy* actuation. The anchors are located 400 μm apart from each other with a minimum size of 150 by 150 μm. The deep etched surface plane obtained is not only uniform and even over the entire area of the actuation device, but also possesses a smooth surface roughness as illustrated in the cross sectional image (b) of the figure 5-32.

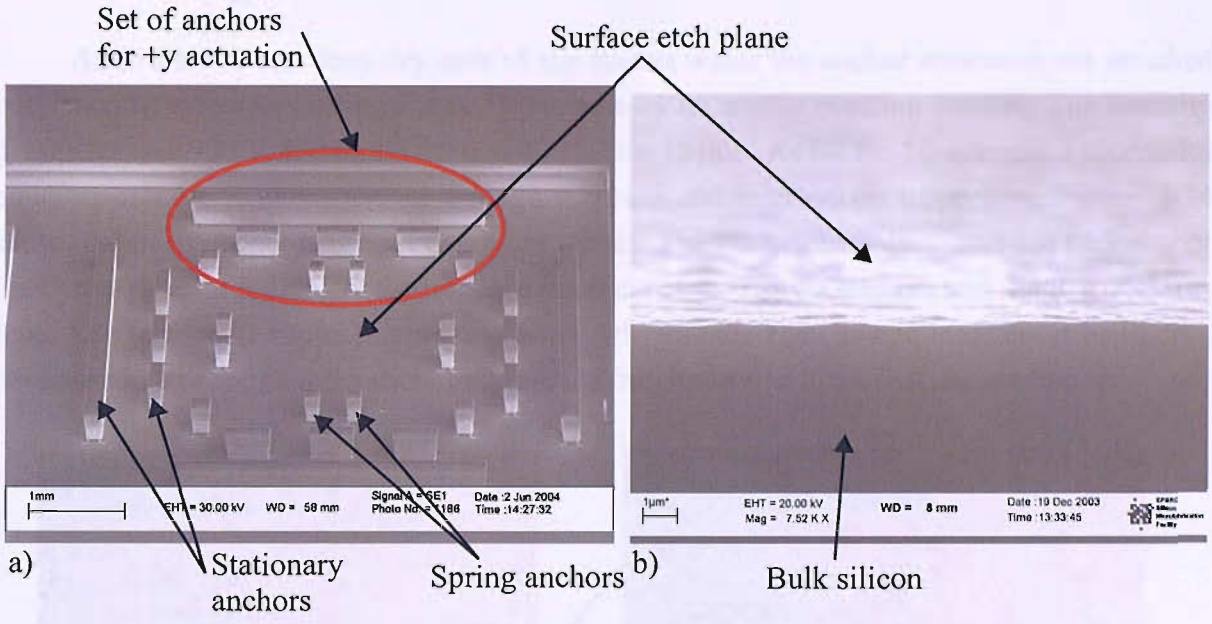

Figure 5-32: A 320 µm deep etch of the final *xy* actuator including four groups of anchor structures for each direction of actuation (a). Each group contains of four rectangular stationary anchors and two squared spring anchors. The cross sectional view of the 320 µm etched surface plane (b) illustrates the uniform and smooth surface roughness.

On the etched surface plane of figure 5-32b an AFM measurement is carried out. An area of 50 μm^2 is measured with a RMS surface roughness of 26 nm as shown in the AFM scanning image of figure 5-33. Since the etched surface plane defines the shape of the comb drive structure within the 60 µm silicon layer and determines the actuation characteristics of the 3D actuator respectively a uniform and smooth surface is advantageous. Both, SEM and AFM images confirm that a deep dry etch process is satisfactory in particular with regards to uniformity and surface roughness of the etched surface plane.

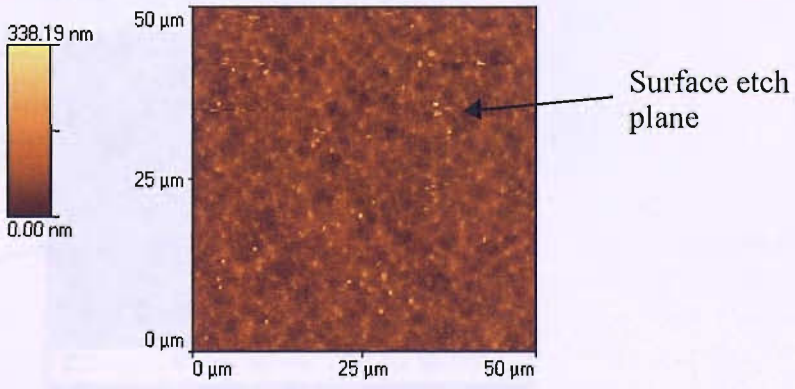

Figure 5-33: AFM measurement of the 320 µm deep etched surface plane of the *xy* actuator. An area of 50 μm^2 is measured with a RMS surface roughness of 26 nm.

Anodic bonding

After the 320 µm deep dry etch of the silicon wafer the anchor structures are attached permanently to the supporting Pyrex™ substrate by an anodic bonding process. The bonding parameters are 900 V, 400 N, 10^{-5} torr at 400 °C for 15 min. As for the 1D actuator a successful bonding process is characterised through a visual and microscope inspection. Figure 5-34 shows the microscope images of two bond results. The images are taken from the backside of the Pyrex™ wafer looking at the bonding interface of the silicon anchors and the Pyrex™ surface. The left image represents a good bond, whereas the right image indicates a bad bond, because some of the anchors show interference fringes around areas that are not bonded.

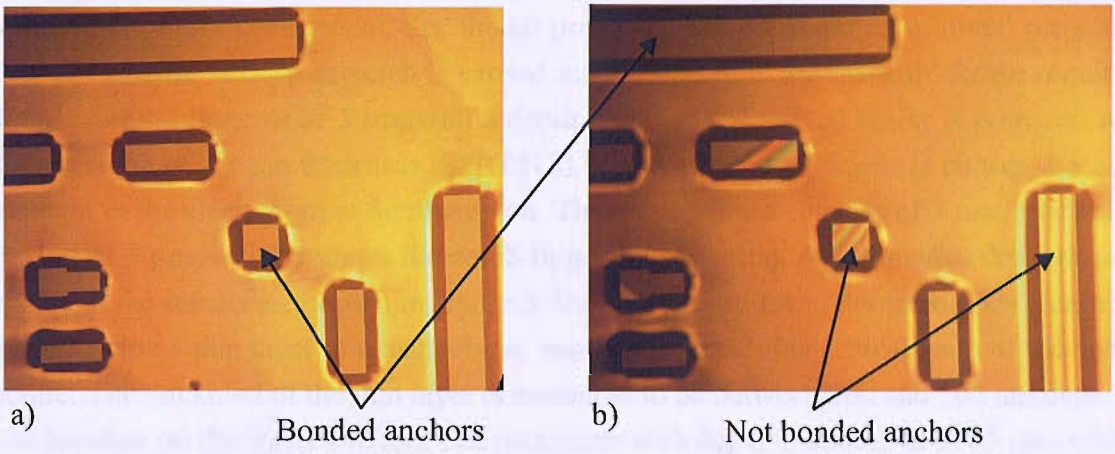

Figure 5-34: Anodic bonding result of a 'good' bonded silicon-Pyrex™ wafer (a) and a 'bad' bond (b). The anchor structures of the 'bad' bond show interference fringes, areas that have not bonded.

In figure 5-35 a SEM image of a cross section of the anodically bonded silicon-Pyrex™ wafer is shown. The image shows a stationary anchor structure, which is bonded to the Pyrex™ wafer. The anchor was etched 320 µm deep leaving a 60 µm layer of silicon for the actuation structure.

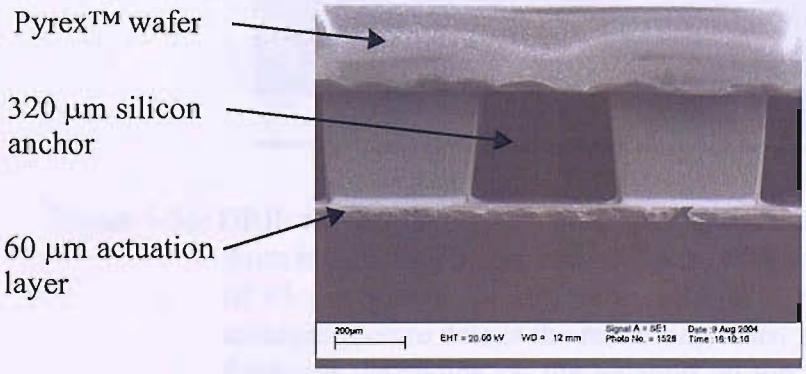

Figure 5-35: Cross section of a 320 µm deep etched silicon wafer bonded onto a Pyrex™ wafer.

60 μm deep dry-etch (2nd DRIE)

The second 60 μm deep dry etch is performed on the front side of the silicon-Pyrex™ bonded substrate. The etching process releases the comb drive structure, which has a minimal feature size of 3 μm. With comb finger openings as small as 3 μm the etch rate of the comb fingers is much smaller compared to larger openings such as the spring beams. In order to release the comb fingers an overetch is required. Once the large features are etched through the etching process continues until the smallest features are released. The additional time of overetch needs to be taken into account when choosing the appropriate thickness of the masking resist layer. In photolithography processing the masking resist layer thickness is normally kept smaller than the minimum feature size required in order to avoid resolution problems during exposure and resist development. For the 60 μm deep etch the required minimal resist thickness is not known. A deep dry etch is carried out to determine the resist thickness required to etch the minimal features of 3 μm with a depth of 60 μm. A silicon wafer is prepared with a patterned resist of 2.2 μm thickness (SPRT518). The resist and thickness is chosen, because it is standard in the clean room at Southampton. The mask pattern consists of 3 μm trenches with a spacing of 3 μm, which reflects the comb finger size opening. A 46 minutes dry etch is performed and the results are shown in figure 5-36. After 46 minutes, the maximum etch time is reached leaving a thin layer of resist behind, enough to protect the critical parts of the actuator structure. The thickness of the thin layer is measured to be between 300 and 500 nm depending on the location on the wafer surface. The maximum etch depth is measured at 85 μm, which is deep enough to etch through the 60 μm silicon layer of the actuator structure.

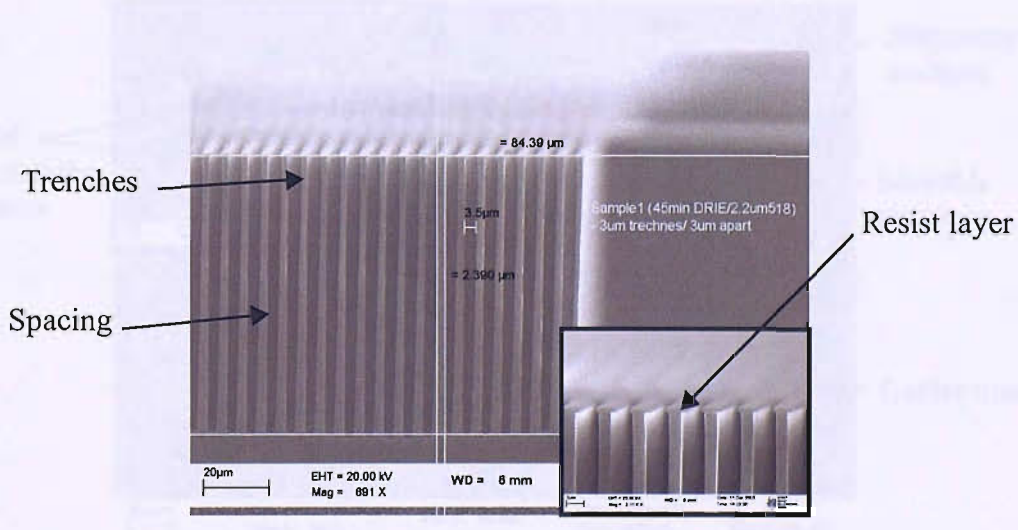

Figure 5-36: DRIE for 46 min on the test structure. The test structure encloses 3 μm trenches with a spacing of 3 μm, which reach an etch depth of 85 μm with a 2.2 μm photoresist as a masking layer. The enlarged picture details the remaining resist with 300 to 500 nm thickness depending on the location on the wafer. The 2.2 μm photoresist is thick enough to etch and release the 60 μm actuation structure.

In addition, figure 5-36 shows a very good side wall verticality of the 3 μm trenches, which represent the comb fingers of the comb drive actuator. However, the images reveal a discrepancy between the initial design and the actual outcome of the microstructures after dry etching. The initial gap spacing between the trenches in the test structure is specified in the design with 3 μm, but due to the undercut during the etching process a broadening of the gap occurs, which results in a final gap size of around 3.5 μm after processing. This inevitable broadening effect is related to the Bosch process that is used for the deep reactive ion etching process. The undercut for the etching apparatus is specified by the manufacturer with 250 nm. This is in agreement with the etch results presented in figure 5-36. The undercut of the 3 μm masked resist layer on top of the trenches, the comb fingers respectively, is clearly visible in the enlarged image of figure 5-36. The deflection y is inversely proportional to the gap size g meaning the enlarged gap between two adjacent comb fingers can be compensated either by increasing the driving voltage or by obtaining the same electrostatic force in adding more comb fingers to the structure. This way the full working envelope can still be achieved.

As mentioned earlier the test structure also encloses comb drive structures, which are shown in figure 5-37. The images are taken from the same wafer, which is shown in figure 5-36. In the first instance the SEM image shows nothing out of the ordinary, but when focusing on the beams of the springs and the beams of the center mass it is evident, that the vertical side walls of the beam structures, which are widely exposed to the etching plasma, are destroyed as the result of lateral underetching.

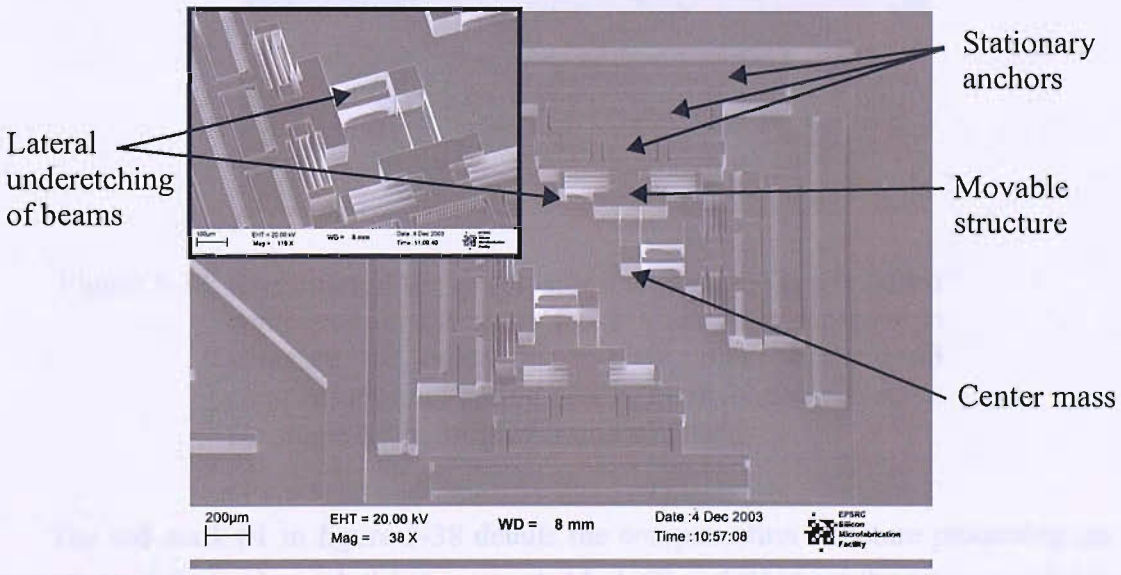

Figure 5-37: SEM images of 46 min deep dry etch on a comb drive structure. Enlarged image shows side wall overetching on beam structures with an initial width of 3 μm.

The underetching is so severe that beams with an initial width of 3 µm are almost entirely etched away as shown in the enlarged image of figure 5-37. The remaining shape of the beams is a distortion of the theoretical rectangular cross section, which makes the actuator unreliable and unpredictable in its motion. The beams are also most likely not able to support the weight of the actuation structure. Although the DRIE Bosch process has a highly anisotropic etching character structures exposed to large etching areas are etched horizontally during the etching and passivation cycles more than structures in confined areas. This is a result of the mobility of the etching gases, which is higher than in smaller and confined areas such as comb fingers. Since on the same wafer the trench structures have a very good vertical etch profile the decision is made not to attempt to evade the horizontal etch behaviour by a time consuming process development effort. Instead the lateral underetching on small features located within large etching areas is minimized by adding compensation structures near the critical parts such as the beams. Figure 5-38 outlines a re-design of the two-dimensional actuator highlighting the added compensation structures marked in red.

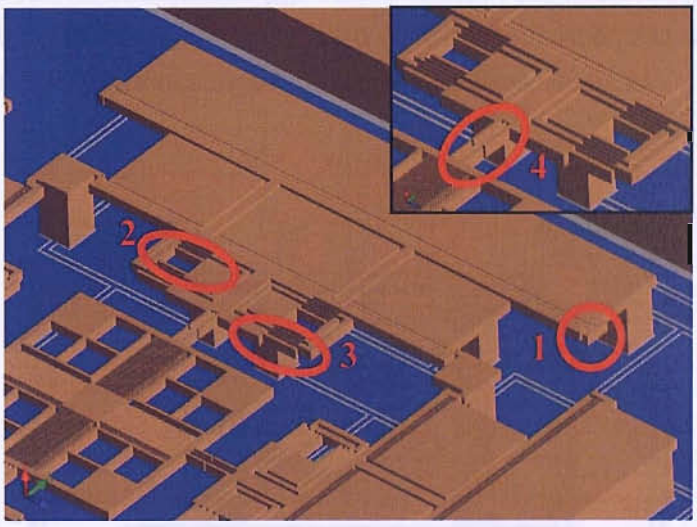

Figure 5-38: Re-design of the *xy* actuator including the newly added compensation structures (red). Mark #1 compensation structure for outer finger plate, mark #2 and #3 compensation for spring beams, mark #4 compensation for single beam of inner frame structure.

The red mark #1 in figure 5-38 details the compensation structure protecting the outer finger plate of the each comb drive segment. Mark #2 and #3 show the compensations avoiding any structural damage to the double-folded beam suspension. Finally mark #4 outlines the compensation for the single beam connection between the comb drive and the inner frame structure.

The final fabricated *xy* actuator applies two lithography masks, KB24M-AA for the 320 µm deep dry etch and KB24M-AB for the 60 µm release etch. Both masks and the correspond-

ing process listing of the fabrication is presented in appendix C.2. In figure 5-39a the complete *xy* actuation structure is shown including the center frame structure and the four comb drive actuators used for cavity alignment in the wafer plane. The enlarged smaller images detail the critical actuation parts of the *xy* actuator: the single beam connecting the center frame structure to the comb drive actuator (b), the spring suspension (c), the beams of the spring suspension (d), the anchors with the attached stationary comb fingers (e), the interlocked comb fingers (f-g). All actuation parts are etched successfully. In particular the compensation structures surrounding the single beam (b) effectively prevent the lateral underetching of the rectangular beams. The beams of the spring suspension are also well protected by the compensation structures (c,d). All the beams are intact and fully functional. The profile view of figure 5-39e shows the 60 μm comb drive structure on top of the 320 μm stationary anchors, which themselves are bonded to the underlying Pyrex™ substrate. The anchors and comb drive structures are well defined in their shape during the deep dry etch processes and in agreement with the design layout. The compensation structures at the outer finger plates (g) of each anchor structure are also providing adequate protection. The comb fingers are very well formed vertically (g) as well as in their lateral dimensions (g). The spacing of the comb drive fingers however is 3.5 μm instead of 3.0 μm as initially designed because of the Bosch process used. At this point of the project the university fire destroyed all the *xy* actuation devices.

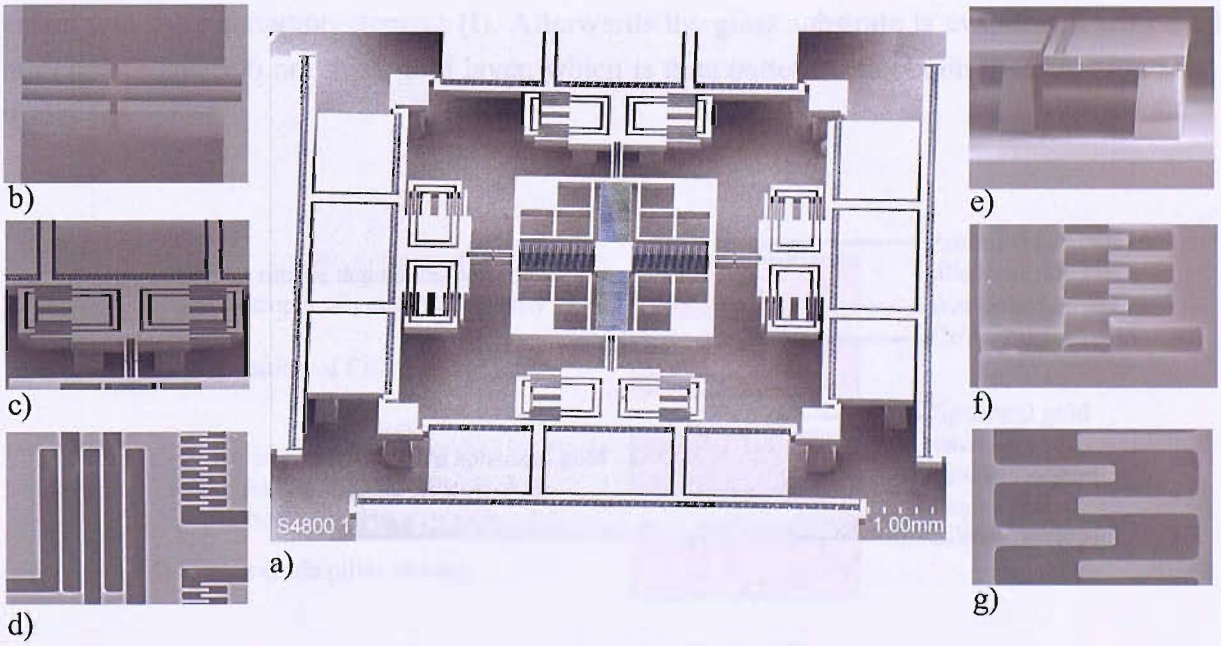

Figure 5-39: SEM images of the fabrication results of the final *xy* actuator (a). The compensation structures successfully protect the critical actuation parts such as single beams (b), spring suspensions (c), spring beams (d) and outer fingers plates (e,f). All beams and comb fingers are intact and fully functional.

5.3.2 Fabrication of the z actuator

The *z* actuator is realised by a simpler fabrication process. Instead of fabricating the entire three-dimensional actuator only the inner frame structure is fabricated, which encloses the *z* actuation and the locking mechanism, without the attaching comb drive actuators for cavity alignment (see chapter 4.31, figure 4-13). The fabrication process of the *z* actuator is presented in figure 5-40. Starting with a 380 µm thick silicon substrate, the optical concave cavity mirror is fabricated on the front side. The silicon substrate is protected by a 180 nm patterned silicon nitride layer and isotropically wet etched to form a spherical cavity (a) The front surface of the silicon substrate is evaporated with a layer of 60 nm chrome and 400 nm of gold (b) and patterned by a Cr/Au wet etch to form the high reflective cavity mirror (c). Then a 1 µm thick PECVD silicon oxide is deposited on the back side of the silicon wafer (c). The oxide layer is then patterned creating small stubs (d). The stubs are squared pillars with a size of 5 µm positioned within the inner frame structure to avoid stiction of the actuation electrodes. Afterwards a 320 µm deep dry-etch is carried out forming the anchor structure of the *z* actuator (e). In a parallel process the glass substrate is prepared. As described in chapter 4.1 the *z* actuation of the *xyz* actuation is achieved by locking the inner frame structure to the surface of the Pyrex™ wafer and electrostatic displacement of the mass in the center of the inner frame structure, which is suspended on four serpentine springs. First, the glass structure is isotropically etched 2.5 µm and 21 µm deep to create a surface plane for the electrodes of the locking mechanism and the *z* actuation element (f). Afterwards the glass substrate is evaporated with a 60 nm chrome and 500 nm thick gold layer, which is then patterned to obtain the actuation electrodes (g).

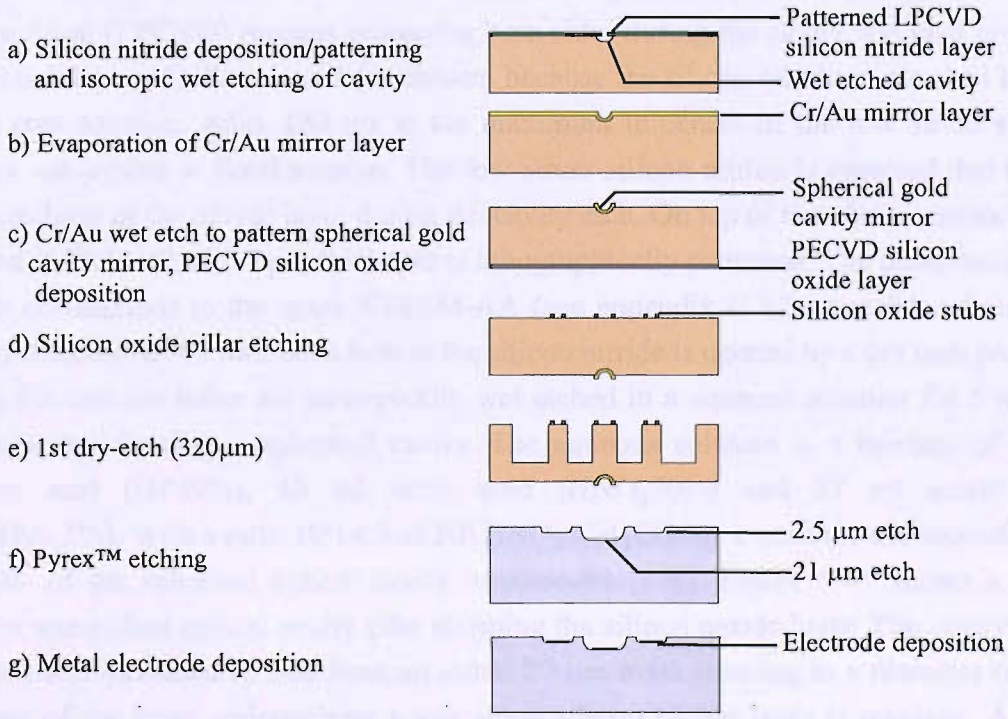

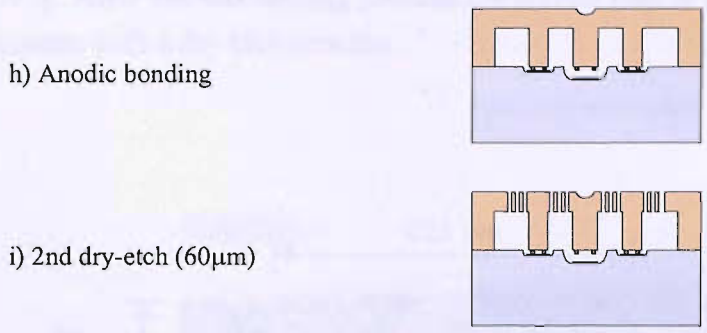

Figure 5-40: The fabrication process of the *z* actuator. The *z* actuator does not include the comb drive actuators for the cavity alignment in the wafer plane, which simplifies the fabrication process.

Finally the silicon and the glass wafer are anodically bonded (h) and the second 60 μm dry etch is performed releasing the actuation structure (i). For the entire fabrication process five masking layers are required. Both process listing and mask layouts are detailed in appendix C.3.

Optical cavity mirror

The optical cavity mirror is processed on the front side of the silicon substrate. Before the actual wet etch is applied the wafer surfaces on the front and the back are covered with a 180 nm layer of silicon nitride. The silicon nitride is deposited by a low pressure chemical vapour deposition (LPCVD) process protecting both sides during the cavity wet etch process. A relative thick layer of silicon nitride is chosen, because the silicon nitride is attacked by the cavity wet etch solution. Also, 180 nm is the maximum thickness of the low stress silicon nitride layer achievable at Southampton. The low stress silicon nitride is required due to the large underetching of the nitride layer during the cavity etch. On top of the silicon nitride layer a photoresist (SPRT518) of 1.7 μm thickness is lithographically patterned. The photoresist pattern, which corresponds to the mask KB86M-AA (see appendix C.3.2), consists of circular holes with a diameter of 80 μm. Each hole in the silicon nitride is opened by a dry etch process. Afterwards the circular holes are isotropically wet etched in a aqueous solution for 5 min at room temperature forming a spherical cavity. The aqueous solution is a mixture of 30ml hydrofluoric acid (HF49%), 43 ml nitric acid ($HNO_3$70%) and 27 ml acetic acid (CH_3COOH99.5%). With a ratio 10:14:9 of HF:HNO_3:CH_3COOH a uniform and smooth etch characteristic of the spherical optical cavity is achieved [120]. Figure 5-41 shows a SEM image of the wet etched optical cavity after stripping the silicon nitride layer. The cavity is 35 μm deep and and increased in size from an initial 80 μm mask opening to a diameter of 125 μm. Because of the large underetching a low stress silicon nitride layer is required. A high

stressed nitride layer would deform throughout the etching process and change the etching profile of the cavity. After the wet etching process the silicon nitride is stripped on both sides of the wafer substrate with a dry etch process.

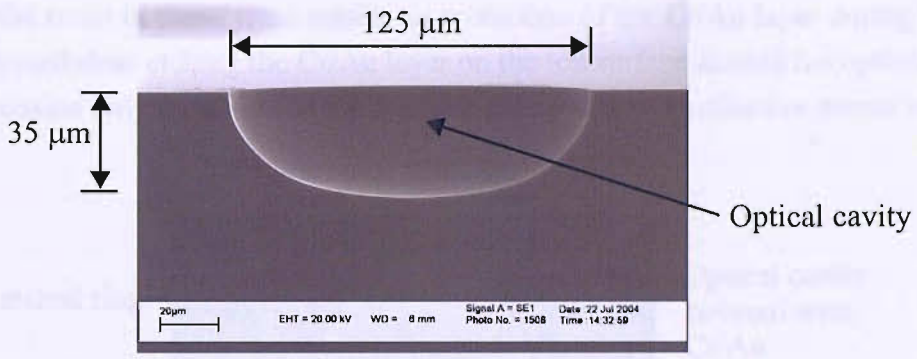

Figure 5-41: SEM image of the optical cavity after wet etched in a HNA mixture with a ratio 10:14:9 of HF:HNO_3:CH_3COOH for 5 min at room temperature. The concave profile of the optical cavity is 35 µm deep with a circular opening and 125 µm in diameter.

In the following the optical cavity is evaporated with a layer of chrome (60 nm) and a layer of gold (400 nm) transforming the optical cavity into a concave optical mirror. During the evaporation process the entire wafer surface is covered with the chrome and gold. While the reflective metal layer is only required in the area of the optical cavity, other areas on the wafer surface demand to be free from any metal, mainly because metal acts a masking material during DRIE processes making a release etch of the actuation structure impossible. The Cr/Au layer is not only functioning as a reflective mirror, but is also used to create alignment marks on the front side of the silicon substrate. The alignment marks are required for the double sided alignment when the back side of the substrate is lithographically patterned and prepared for the 320 µm deep dry etch.

For patterning the Cr/Au layer the photoresist Shipley S1818 is spun on top of the Cr/Au layer with a thickness of 2.2 µm and exposed with the mask pattern according the mask KB86M-AB in appendix C.3.2. The positive photoresist S1818 is used because it is suitable for wet etching metals. It is sufficient adherent and withstands a Cr/Au wet etch. When spinning the positive resist it is important that the 35 µm deep cavity is fully covered with resist, because only areas that are exposed during the lithography will uncover the Cr/Au layer after resist development. In particular covering the bottom of the optical cavity it is critical. The photoresist S1818 is very liquid compared to other resists such as SPRT518/510, which are also standardized at Southampton and are more viscous. This characteristic of the Shipley S1818 photoresist is advantageous. The SEM image in figure 5-42 taken after the Cr/Au wet

etch reveals are ring of etched Cr/Au at the periphery of the cavity. Nevertheless inside the optical cavity a layer of Cr/Au is visible. When spinning a resist over a wafer surface with a topology, in this case deep etched cavities, the resist layer is always thicker at the edges of the cavity structure. This effect is similar to the edge bead of a planar wafer coated with resist from spinning. This thicker layer of resist is very likely to stick to the lithography mask during the contact exposure, when the mask and the wafer surface are in physical contact with each other. The peeling of the resist in these areas means no protection of the Cr/Au layer during the wet etch process. Nevertheless etching the Cr/Au layer on the top surface around the optical cavity is not critical, because only the inside of the concave cavity acts as a reflective mirror surface.

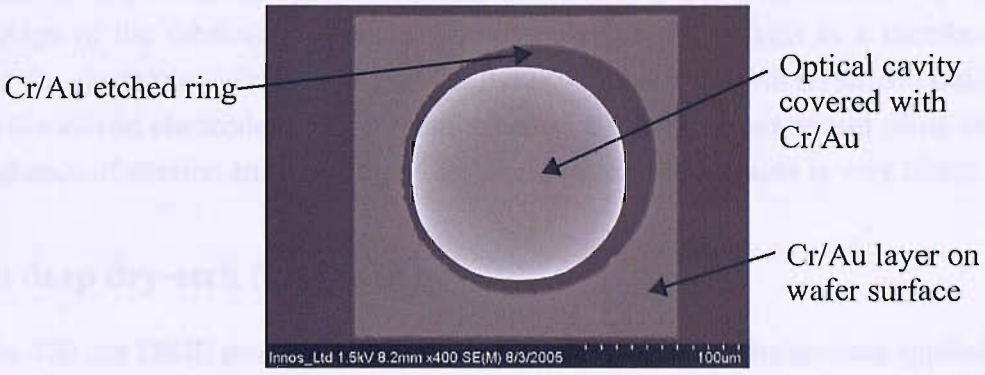

Figure 5-42: SEM image of the optical cavity after evaporating a layer of chrome (60 nm) and gold (400 nm) and subsequent wet etching to remove the metal layer from the wafer surface. A ring area is visible where Cr/Au is etched away. The thicker resist ring around the cavity surface is sticking to the lithography mask and is peeling off during contact exposure leaving a ring of Cr/Au to be etched.

Silicon oxide stubs

The silicon oxide stubs are very important micro structures and essential for the functionality of the *xyz* actuator. As illustrated in chapter 4.3.1 figure 4-12 the oxide stubs are processed on the four silicon pillar structures, which are used for locking and unlocking the *xy* actuation stage. An additional set of oxide stubs are processed on the actuated center mass of the *z* actuator. Both, the four pillar structures of the locking mechanism and the actuated center mass structure have each a set of five oxide stubs on their electrode surface. Each oxide stub is 1 μm in height with a surface area of 25 μm^2. The surface area is kept small in order to prevent a permanent stiction, when they come into contact with the opposing metal electrodes on the Pyrex™ during operation of the locking mechanism as well as the *z* actuation. The silicon oxide stubs are also non-conductive preventing a possible discharge between the electrodes during contact.

The back side of the silicon wafer is deposited with a 1 μm thick layer of silicon oxide using a PECVD process. On the silicon oxide layer a 2.2 μm thick SPRT518 resist layer is spun and patterned. During the lithography exposure the mask KB86M-AC (see appendix C.3.2) is aligned to the front Cr/Au alignment marks of the silicon substrate. The double sided alignment procedure positions the silicon oxide stubs on the back side with respect to the optical cavity on the front side of the substrate. The 5 μm^2 surface area of the silicon oxide stubs is also small enough to prevent stiction not only during operation of the *xyz* actuator but also during the anodic bonding process. When the bonding voltage of 900 Volts is applied between the two wafer substrates the 320 μm tall silicon electrode structures are pulled towards the metal electrodes of the Pyrex™ wafer due to the electrostatic forces. The anchor structures are attached to the 60 μm silicon layer of the silicon substrate, which is not released by etching yet. At this stage of the fabrication process the 60 μm silicon layer acts as a membrane and is pulled by the electrostatic forces towards the Pyrex™ substrate. With no silicon oxide stubs in between the silicon electrodes and the metal electrodes the structures would come into contact and the chance of stiction and bonding of the planar electrode surfaces is very likely.

320 μm deep dry-etch (1st DRIE)

The 320 μm DRIE process for the *z* actuator is identical to the process applied to the *xy* actuator. The process flow including processing parameters and mask layout (KB86M-D) are detailed in the appendix C.3. Because the silicon oxide stubs are only 1 μm in height a good coverage with the much thicker SPR220-7 photoresist of 10 μm is achieved without difficulty and deep dry etching up to 320 μm is straightforward. Unfortunately, just before the DRIE could be carried out the university fire destroyed all the device wafers.

Pyrex™ cavity etching

The processing of the Pyrex™ wafer is done in parallel to the processing of the silicon wafer. Before the Pyrex™ substrate is bonded to the structured silicon wafer the metal electrodes on the Pyrex™ surface are processed. The Pyrex™ substrate is electrically non conductive so the metal electrodes can directly be created on the Pyrex™ surface without an isolation layer. As illustrated in the design layout of the *xyz* actuator in chapter 4.3.1 two groups of electrodes on the Pyrex™ substrate are defined. One group of four electrodes, which is used for the locking mechanism of the center frame structure and another group consisting only of one single electrode, which is used for the cavity actuation. The four locking electrodes require a distance of the 2 μm to the opposite facing silicon anchor electrodes. Including the height of the silicon oxide stubs the distance between the oxide stubs and the metal electrodes is only 0.5 μm. The single electrode for the cavity actuation however requires a much larger distance of 21 μm to the opposite facing center mass electrode. One way to realize the two groups of electrodes is by creating two surface planes within the Pyrex™ substrate, one plane at a depth of 2.5 μm enclosing the four locking electrodes and one plane at a depth of 21 μm holding the

single actuation electrode. The two surface planes are fabricated by applying two subsequent wet etch processes. One wet etch process etching the 2.5 μm surface plane, the other wet etching the 21 μm plane.

There are two difficulties involved in wet etching the two surface planes. First, processing the 21 μm deep surface area for the single metal electrode within the 2.5 μm deep surface area for the center frame structure. Secondly, the metal electrodes require electrical contacts which are realized by electrical leads extending out of the 21 μm deep etched cavity to a wire bond pad area. Both, etching the two topologies - one deeper and within the other - and processing the electrical leads guiding out of the cavities is challenging, in particular spinning and patterning the resist layer inside the cavity areas is not trivial. A schematic drawing of the metal electrodes on the wet etched Pyrex™ substrate is illustrated in figure 5-43. The sketch shows the four locking electrodes, the single actuation electrode and the electrical leads with the wire bond pads. For the metal electrodes a 60 nm layer of Cr and 500 nm layer of Au is chosen, which can easily deposited by an e-beam evaporation process. The total electrode thickness is 560 nm (60 nm Cr/500 nm Au) and requires a cavity depth of 2.5 μm in order to achieve the designed separation of 2 μm between the top silicon electrode and the bottom metal electrode.

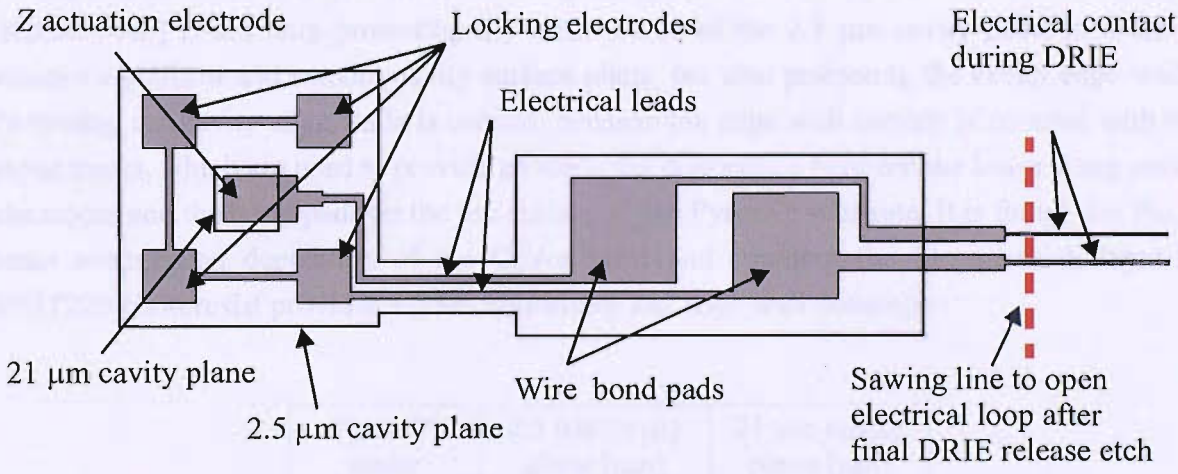

Figure 5-43: Schematic layout of the patterned Pyrex™ wafer after cavity etching and metal electrode processing. On the left side of the layout is the actual center frame actuation structure (not visible) enclosing the four metal locking electrodes and the actuation electrode. In the middle of the device layout two metal wire bond pads are processed, which are used to electrically connect the four metal electrodes of the locking mechanism and the actuation electrode. The electrical leads are extending towards the left of the device and attach all five metal electrodes to the silicon wafer after bonding in order to avoid the micro loading effect. After DRIE the electrical loop is opened by sawing through the electrical leads (red line).

Figure 5-43 also shows a pair of lead extensions on the right. They provide an electrical contact during the final deep dry etch to avoid the micro loading effect. The red line in figure 5-43 indicates the sawing line, where the electrical loop is opened after the release etch. Once the electrical leads are separated the electrical voltages for operating the locking mechanism and the cavity actuation can be applied.

First, the 2.5 μm deep cavity area is wet etched. Because the etch depth is only 2.5 μm the masking layer (KB86M-AE) for the Pyrex™ wet etch consists only of a 2.2 μm layer of photoresist S1818. Spinning the resist on the planar wafer surface and exposing during the lithography process is a standard procedure and unproblematic. Once the resist is spun and patterned, the Pyrex™ wafer is wet etched for 1 min in a diluted HF solution at room temperature. Two parts of concentrated HF solution (48%) is diluted with one and a half part of H_2O to achieve a reduced etch rate of 2.5 μm/min [150]. The 2.5 μm wet etch is carried out before the 21 μm wet etch, because resist spinning and patterning in a 2.5 μm deep surface area is less difficult than processing resist over a 21 μm deep cavity during the lithography. After the first wet etch the resist is stripped off the Pyrex™ surface and the masking layer for the second 21 μm deep wet etch process is prepared. The masking layer consists of a Cr/Au/resist (40nm/ 400nm/11μm) layer combination as used for the *z* actuator. The application and layer thicknesses of the chrome, gold and resist layers are identical to the processing of the Pyrex™ wafer for the *z* actuator. It is important that during the 21 μm wet etch process the masking layer (KB86M-AF) is not only protecting the surface area of the 2.5 μm cavity plane in order to achieve a uniform and smooth cavity surface plane, but also protecting the cavity edge walls. Protecting the cavity edge walls is critical, because the edge wall surface is covered with the metal tracks, which are used to provide an electrical connection between the lower lying cavity electrodes and the bond pads on the top surface of the Pyrex™ substrate. It is found that the e-beam evaporation deposition of the Cr/Au layer and spinning the 11 μm thick layer of SPRT220 photoresist provides a good uniformity and edge wall coverage.

Pyrex™ wafer	2.5 μm cavity plane [μm]	21 μm cavity plane [μm]
1	2.4	19
2	2.6	21
3	2.5	20
4	2.7	22
5	2.5	21
6	2.4	21

Table 5-1: Depth measurement result of the two cavity planes after wet etching in a diluted HF solution with a ratio 2:1.5 of HF:H_2O for 1 min (2.5 μm cavity) and 8.5 min (21 μm cavity).

Applying the 11 μm thick resist layer is advantageous, because it is much higher than the 2.5 μm deep cavity and therefore covers the 2.5 μm deep etched cavity during the resist spinning process in a smooth and uniform fashion. Once the masking layer is processed the second wet etch process is applied with the same diluted HF solution. With an etch rate of 2.5 μm/min the etch time is set to 8 minutes and 30 seconds achieving a maximum etch depth of around 21 μm. After completion of the both wet etch processes the etch depth on a set of six processing wafers is measured. The measurement results are presented in table 5-1. The etching results of both wet processes are very encouraging. The etch depths for the first 2.5 μm cavity wet etch are measured between 2.4 and 2.7 μm. This is a good etching result, because an average etch depth of 2.5 μm is achieved. The results are also in agreement with the estimated etch rate of 2.5 μm/min. The depth measurements of the second 21 μm cavity etch are also positive.

All the wafers are wet etched individually by immersing one at a time horizontally in a teflon beaker, that holds only one single wafer. This setup is used in order to reduce the volume of chemicals required to conduct the wet etch process. A plastic tweezer is used to place the substrate in the beaker and subsequently remove it from the beaker after the etch time of 1 min or 8.5 min. During the etching process each wafer is agitated. The described etching process is a very manual process, which is time critical. In particular the agitation during each etching cycle and the removal with the tweezer is estimated to be the reason for the difference in the etch depth achieved for each wet etched wafer. Nevertheless, the overall variation from the required 2.5 μm and 21 μm etch depth is acceptable and within the process control limits causing no major interference with the design objectives.

Metal electrode deposition

After the successful wet etch process of the Pyrex™ wafer, the 2.5 μm and 21 μm cavity planes are deposited with a 60 nm layer of Cr and 500 nm layer of Au by applying a gold evaporation process. At this stage one of gold covered Pyrex™ wafer is inspected with the SEM to evaluate the etch uniformity and cavity edge profile of the 2.5 μm and 21 μm cavity planes after the wet etching process. Figure 5-44a is a perpendicular view of the top surface of the gold covered Pyrex™ wafer showing the larger 2.5 μm cavity plane with the embedded 21 μm cavity plane. Both cavity planes are uniformly etched and the edge side wall especially of the 21 μm cavity indicates a flat and positive etching profile, which is also illustrated in the profile view of figure 5-44b. The flatness of the edge is a result of the isotropic and large lateral etching behaviour of the HF wet etch solution [147]. This flat edge profile is especially advantageous for the subsequent resist pattering and Cr/Au wet etch forming the metal electrodes of the locking mechanism and *z* actuator.

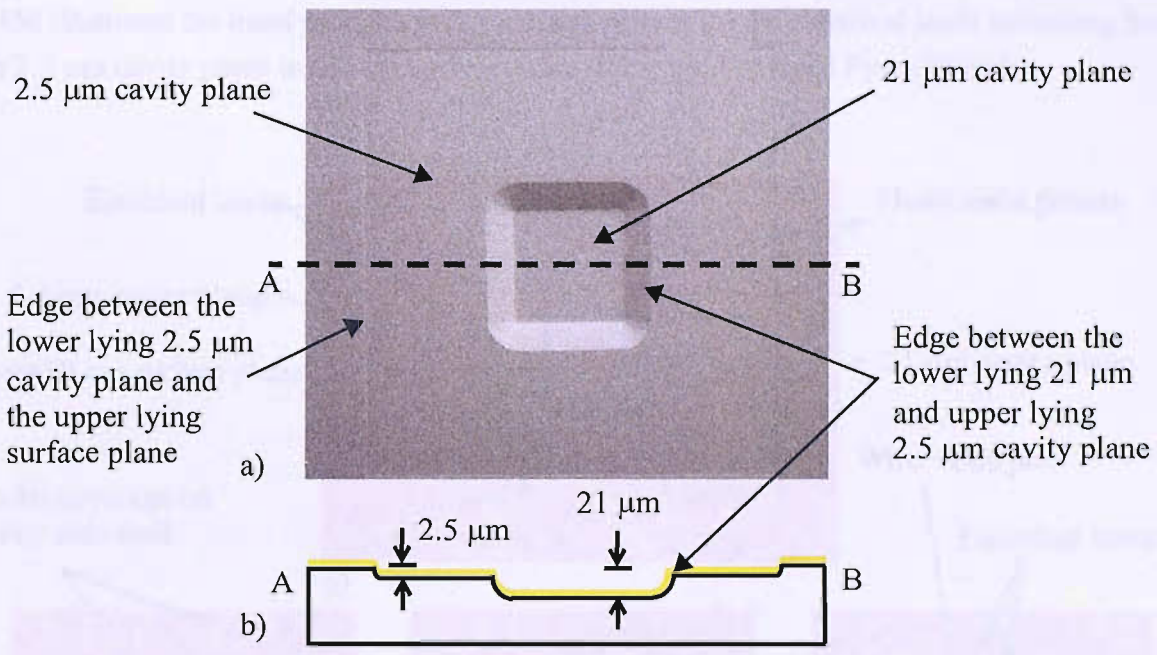

Figure 5-44: SEM image of the wet etched Pyrex™ cavities after Cr/Au evaporation. Both, the 2.5 µm and 21 µm cavity show uniform etched surface planes (a). The image also indicates that a flat positive etch profile of the 21 µm cavity edge is achieved, which is a result of the isotropic and large lateral etching behaviour. The profile view across the cavity (b) - not to scale - illustrates the obtained positive profile characteristic of both cavity edges.

For patterning the Cr/Au layer the photoresist Shipley S1818 with a thickness of 2.2 µm is spun on top of the Cr/Au layer and exposed with the mask KB86M-AG. When spinning the positive resist it is important that not only the bottom plane, but also the side wall edges of the 21 µm deep cavity are fully covered with resist. The resist must cover the bottom plane uniformly, because it defines the metal electrode of the *z* actuator. The side walls must also be covered, because one side is used for the metal track patterning, which electrically connects the lower lying metal electrode to the upper lying metal bond pad area.

The photoresist S1818 is used, because it delivers a good resist coverage of deep cavities as shown previously for the optical cavity mirror. It is found that the resist coverage is more uniform at the flat side wall of the 21 µm cavity edge in comparison to the much steeper side wall of the circular cavity mirror. Figure 5-45 shows several microscope images of the Cr/Au layer on the Pyrex™ wafer with the patterned S1818 photoresist on top. Figure 5-45a captures the area of the four metal electrodes for the locking mechanism within the 2.5 µm cavity plane and the center electrode for the *z* actuation within the 21 µm cavity plane, which are visualized by the patterned resist. The enlarged images, 5-45b and 5-45c, detail the good resist coverage on the side wall of the 21 µm cavity edge. The resist not only covers the side wall itself very

uniformly, but also the 21 μm deep bottom plane as well as the 2.5 μm deep top plane. Figure 5-45d illustrates the bond pad area with the resist pattern for the electrical leads extending from the 2.5 μm cavity plane to the top surface plane of the gold covered Pyrex™ wafer.

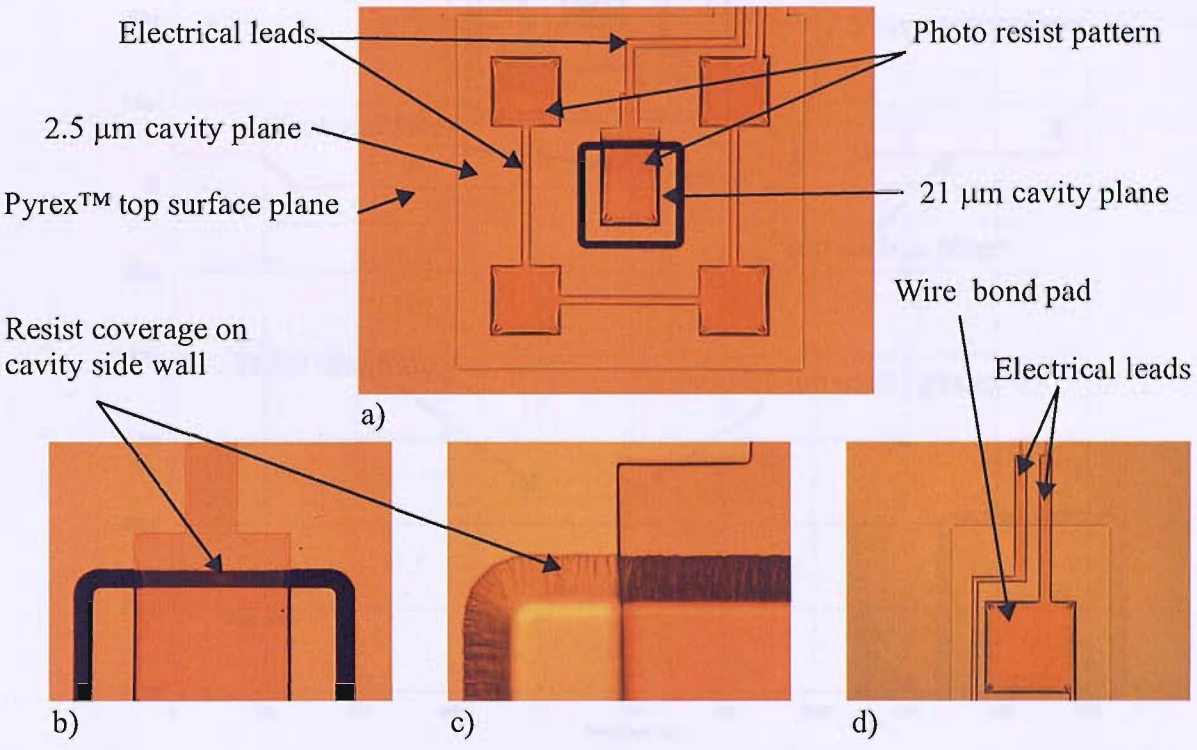

Figure 5-45: Microscope images of the Pyrex™ wafer before the metal electrode wet etching. The Pyrex™ is covered with a layer of Cr/Au and a patterned resist layer of S1818 (2.2 μm). The resist defines the four metal electrodes of the locking mechanism and the single electrode of the *z* actuator (a) including the electrical leads. The enlarged images detail the uniform resist coverage of the metal electrode inside the 21 μm cavity plane and on the cavity edge side wall (b,c). Also good resist coverage of the bond pads and electrical leads extending from the 2.5 μm cavity plane onto the top surface plane is shown (d).

After wet etching the Cr/Au layer on the Pyrex™ substrate the topology measurement of the cavities and the embedded metal electrodes is carried out. The result of the measurement in figure 5-46 shows the profile view (from point A to point B) of the 2.5 μm and 21 μm cavity including the single metal electrode of the *z* actuator and the electrical leads connecting the four metal eletrodes of the locking mechanism. The profile is obtained using a stylus profiler (KLA Tencor P16). The metal electrode in the deep cavity is situated 21 μm away from the top surface plane or the opposite silicon electrode of the center mass respectively. Also shown are the electrical leads for the locking electrodes within the 2.5 μm cavity plane. They are etched and well defined by the metal layer.

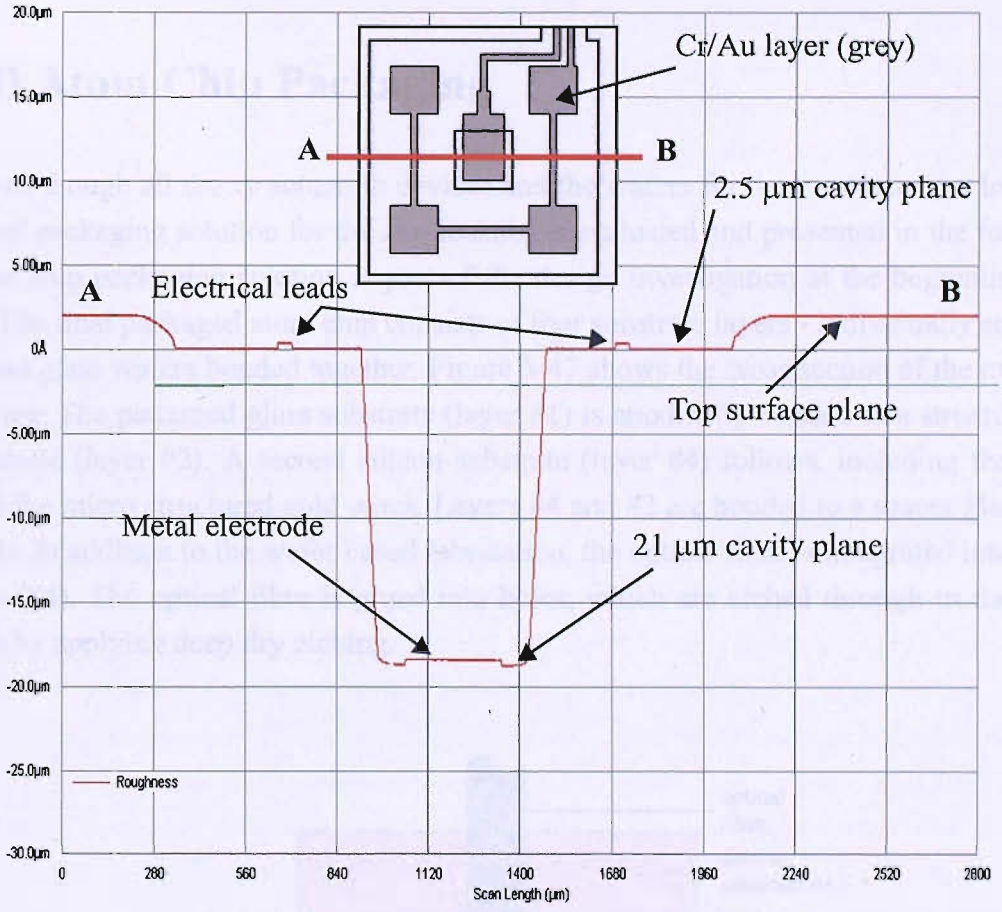

Figure 5-46: Profile measurement of the 2.5 µm and 21 µm cavity planes showing the electrical leads in the shallow cavity and the single metal electrode in the deep cavity.

With the patterning of the metal layer on the substrate surface, the structured Pyrex™ wafer is ready for the anodic bonding process.

Anodic bonding

The anodic bonding process attaches the 320 µm etched silicon wafer to the cavity etched Pyrex™ wafer. Unfortunately the bonding process is not carried out because at the time when both silicon and Pyrex™ wafers were prepared for bonding the university fire destroyed all the substrates.

60 µm deep dry-etch (2nd DRIE)

The second deep dry etch of the bonded silicon-Pyrex™ wafer is a subsequent fabrication step of the anodic bonding process. However, the second DRIE process cannot be carried out, because the wafers were lost in the fire. Therefore no fabrication results for the anodic

bonding process and the DRIE process are presented.

5.4 3D Atom Chip Packaging

Even though all the *xy* actuation devices and the wafers for the *z* actuator are lost in the fire a final packaging solution for the *xyz* actuator is evaluated and presented in the following. The atom chip packaging solution is part of the design investigation at the beginning of the project. The final packaged atom chip consists of four substrate layers - individually structured silicon and glass wafers bonded together. Figure 5-47 shows the cross section of the multi-layered device. The patterned glass substrate (layer #1) is anodically bonded to a structured silicon substrate (layer #2). A second silicon substrate (layer #4) follows, including the optical fibre and the micro structured gold wires. Layers #4 and #2 are bonded to a spacer glass wafer (layer #3). In addition to the wafer based fabrication, the optical fibre is integrated into the top substrate (#4). The optical fibre is glued into holes, which are etched through in the silicon substrate by applying deep dry etching.

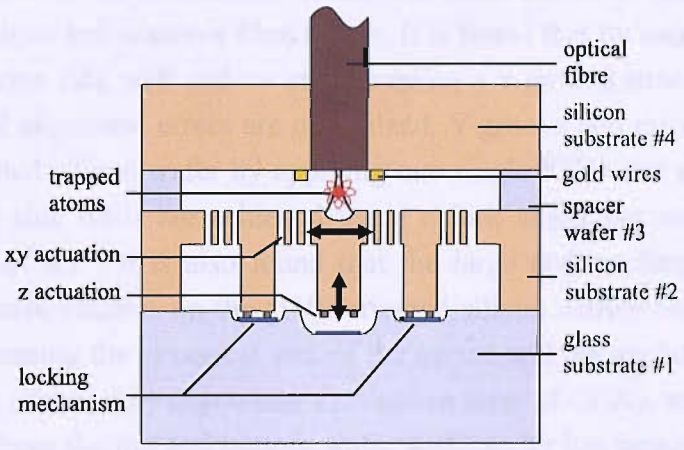

Figure 5-47: Schematic overview of the multi-layered three-dimensional atom chip actuator.

Important to notice is that the fabrication of the entire atom chip as shown in figure 5-47 in not within the scope of this thesis.

5.5 Conclusions

During the fabrication process of the *xy* actuator several fabrication issues are addressed. It is found that a 10 μm resist layer of SPRT-220 is thick enough to withstand a 320 μm deep dry-etch. Fairly good anchor profiles are created, however overetching in the corners of the anchor structures at their foundation occurs. With a large enough offset between the 60 μm and

320 μm structures this overetch has no disadvantageous affect on the actual actuation device. Also not critical is the side wall roughness of the anchors, since they do not play any active part in the actuation. It is also found that a uniform surface is achieved by placing anchors more than 300 μm apart from each other and that the surface roughness, which was measured to be 26 nm, in the 320 μm etched surface plane is smooth and in agreement with the design objectives. For the 60 μm deep dry-etch a minimum resist thickness of SPRT-518 2.2 μm is needed. A good side wall verticality is achieved during the release etch. The inevitable broadening effect as a results of the 60 μm deep reactive ion etching process is found to be 250 nm. It is possible to compensate the enlarged finger gap by increasing the driving voltage or by obtaining the same electrostatic force in adding more comb fingers to each comb drive segment. Due to unexpected side wall overetching of the critical beam structures various compensation elements are required. They maintain the functionality of the releasing actuation structure. The fabrication of the *xy* actuator is completed, however all the fabricated devices were lost in the university fire.

The fabrication of the one-dimensional *z* actuator requires a less complicated manufacturing process as the *xyz* actuator, which is owed to the accessibility of the concave optical fibre. A critical aspect in the fabrication of the one-dimensional actuator is the alignment between the plane mirror and concave fibre mirror. It is found that by increasing the reflective area of the plane mirror side wall and by implementing a v-groove structure for the concave fibre mirror potential alignment errors are minimized. V-groove and mirror structure are created in a (110) oriented silicon wafer by applying one single KOH wet etch process. Atomically smooth mirror side walls are achieved using a fork alignment structure with a mask alignment accuracy of 0.1^{o}. It is also found that the large underetching of the rectangular anchor and mirror mask patterns on the (110) oriented silicon wafers can easily be compensated by simply increasing the structural size of the mirror and the anchors. A mirror surface roughness of 3 nm is achieved by depositing a reflective layer of Cr/Au, which is removed in a subsequent process from the top and bottom wafer surfaces by ion beam milling (IBM). The IBM process is used instead of an isotropic wet etch process leaving only a reflective layer of Cr/Au at the mirror side wall behind.

Chapter 6

Characterization tests

6.1 Introduction

Towards the end of the project the university fire destroyed not only the devices of the *xy* actuator but also all the processing wafer for the *z* actuator and 1D actuator. Since no functional devices are available no characterization test on the final fabricated actuators is carried out. However, after fabricating the planar mirror of the 1D actuator an optical measurement has been conducted to characterize the quality of the planar mirror surface. The results are presented in section 6.2.

6.2 1D Actuator

The functional one-dimensional comb drive actuator is not realized. Therefore, no experimental data of the actuated micro cavity is obtained. Only an optical characterization of the optical planar mirror is carried out. The optical measurements are conducted in the laboratory of our collaboration partner at Imperial College London with the help of Michael Trupke and are detailed in the following section.

6.2.1 Optical measurements

The optical analysis is performed using a fibre with a planar coating, with a reflectivity of 99%. The coating is applied using a transfer procedure in which a section of coating from a donor surface [152] is attached to the cleaved tip of the fibre using index-matching epoxy glue. The fibre is then lowered into the v-groove to form a resonator with the vertical side wall. To test the properties of this resonator, the silicon chip is mounted onto a macroscopic piezoelectric actuation stage and translated over a small range, while the fibre remained stationary. Laser light with a wavelength of 780 nm is coupled into the fibre and the dependence of reflected

power versus actuator position is observed. The resulting curve for an average cavity length of 2 μm is shown in figure 6-1. The sharp dips (fringes) in reflected intensity occur when the cavity becomes resonant with the laser light.

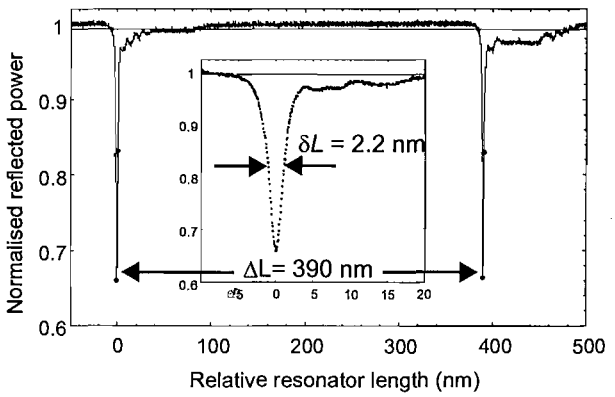

Figure 6-1: Normalised reflected power of the plane-plane resonator versus resonator length at an average cavity length of 2 μm.

The finesse F of the optical cavity is obtained by the ratio of ΔL (the distance between two fringes) to the full width at half maximum (FWHM) δL of the resonances. This ratio is related to the effective reflectivities of the resonator mirrors given by the relationship [142],

$$F = \frac{\pi \sqrt[4]{\rho_1 \rho_2}}{1 - \sqrt{\rho_1 \rho_2}} \approx \frac{\Delta L}{\delta L} \tag{6.1}$$

where ρ_1 is the reflectivity of the planar side wall mirror, ρ_2 the reflectivity of the concave fibre mirror. For the plane-plane resonator tested at a resonator length of 2 μm the distance ΔL between two fringes and the FWHM δL of the resonances are measured at 390 nm and 2.2 nm respectively resulting in a finesse $F = 179$.

Using this procedure, the finesse at cavity lengths L in the range of 2 μm to 30 μm in steps of 2 μm is measured and plotted in figure 6-2. The finesse decreases with resonator length because of the nature of this resonator geometry, which does not restrain the light in directions perpendicular to its optical axis. It is observed that the finesse of the resonator is highly dependent not only on its angular alignment, which is comprehensible given its geometry, but also on the location on the gold mirror at which the resonator is formed. This may be due to post-manufacturing contamination with dust or humidity.

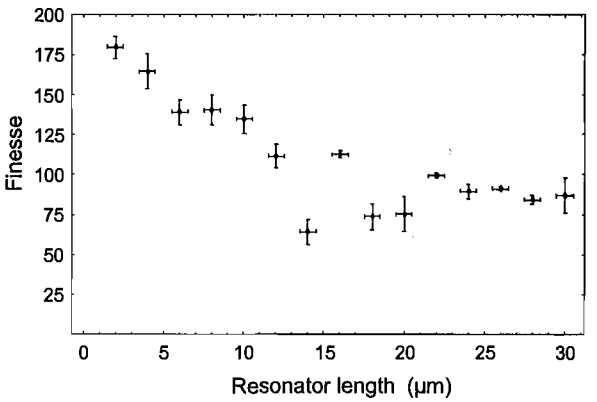

Figure 6-2: Finesse of the plane-plane resonator versus resonator length, with statistical errors for the finesse values from a set of five measurements at each resonator length and the estimated uncertainty of the resonator length.

Overall the finesse of the plane-plane resonator remains higher than 100 for resonator lengths of up to 12 µm, and higher than 50 in the entire range of this experiment as can be seen in figure 6-2. From the finesse the quality factor is derived [142],

$$Q = \frac{2LF}{\lambda}. \tag{6.2}$$

The highest measured quality factor Q for this resonator is 1.34×10^4 at a resonator length of 30 µm. These results are encouraging for two reasons. Firstly, the plane-plane resonator tested is already of sufficient quality for applications such as the detection of single atoms [7],[39]. Furthermore, it is anticipated that even higher finesse values for the case of a concave fibre-mirror can be achieved. The latter will also restrain the perpendicular components of the cavity mode and therefore provide a smaller mode volume, which is advantageous for our applications.

6.3 3D Actuator

Since the farbication of the *xy* actuator was not repeated after the university fire no actuation experiments for a cavity alignment are presented. Also the fabrication of the *z* actuator is not completed so no experimental data of the cavity actuation are presented.

Chapter 7

Conclusion and Suggestions for Further Work

7.1 Conclusion

Atom Chips are microfabricated structures with integrated optical elements such as atom traps, guides, beam splitters and mirrors. These optical elements are surface structures, that are realized by applying micro fabrication techniques. In order to exchange quantum information between atoms and photons optical cavity systems are required. Such optical cavity systems using actuated optical mirrors have been developed on atom chip surfaces. However, up to now only macroscopic optical cavities have been demonstrated, where macroscopic mirrors are actuated in the wafer plane by large piezoelectric stage actuators on top of micro structured wafer surfaces. The integration of a micro actuator together with a set of micro mirrors to create a tunable optical micro cavity using M(O)EMS fabrication techniques is still one goal that has not been achieved yet. To fulfil this goal a tunable optical micro cavity on an atom chip is developed.

The development of the actuated optical micro cavity on the atom chip involves two actuation design concepts, a three-dimensional actuator (3D) for cavity actuation out of the wafer plane and a one-dimensional (1D) actuator for actuation in the wafer plane. Both cavity actuation designs are based on a multi-layered atom chip, which also integrates micro wire structures for atom guiding and trapping. The actuation of the cavity system for both, 3D and 1D, actuators is achieved by electrostatic actuators, which is the most feasible solution in comparison to magnetic and thermal actuation and with regards to integration, fabrication, development and available processes. Magnetic actuators are not suitable, because the magnetic fields required will interfere with the magnetic atom guiding fields. Thermal actuators are also not suitable, because the heat dissipation during the thermal expansion of the actuator will

interrupt the guiding and trapping of the atoms.

The 1D actuator incorporates a one-dimensional electrostatic comb drive actuator, which actuates a planar mirror in the wafer plane along the x axis. The 1D actuator is theoretically analysed by deriving the translation curve for the mirror actuation. The results of the analysis are in good agreement with the simulation results. The 1D actuator translates the micro mirror up to 20 μm at a simulated maximum voltage of 145 Volts. Since stability and translation accuracy of the optical cavity is a key requirement, the lateral instability of the comb drive actuation structure is evaluated. Also the fundamental resonance frequency of the system is analysed. Both dynamic response and lateral instability of the 1D actuator are found to be not critical. The fundamental resonance frequency is calculated at 1452 Hz, which is well beyond the critical range of external vibrations between 0 - 100 Hz. The impact of heat on the actuation device is calculated as well. The analytical results show that the thermal heat expansion as a result of an ambient temperature change of 1°C is critical and can cause the optical cavity to become instable. Adequate cooling or heating of the vacuum chamber temperature is necessary. It is also found that the required analytical resolution of 2 nm of the actuator can be achieved with a 5 mV stabilized voltage source.

The 3D actuator incorporates a two-dimensional xy electrostatic comb drive actuator in the wafer plane, which is required to compensate the misalignment of the two optical mirrors during the fabrication process and an out-of-plane electrostatic parallel plate z actuator for the optical cavity actuation. The optical cavity mirrors consist of a fixed planar fibre mirror and movable concave mirror, which is integrated in the z actuator. The calculated translation curve for the xy actuation is calculated and simulated with a maximum translation of 15 μm at 150 Volts. However, to deflect 5 μm and to compensate the misalignment only 80 Volts are required. For the z actuation of the concave mirror a serpentine spring system is chosen in order to reduce the actuation voltage. The spring constant is analytically derived and calculated as low as 0.835 N/m simulating a maximum required translation of 7 μm at 80 Volts. The 3D actuator also incorporates a locking mechanism, which allows the xy actuation structure to be locked before the z actuation of the optical cavity takes place. The locking mechanism is based on a parallel plate configuration and is able to lock the xy actuator at a 140 Volts. For the 3D actuator the same stability and accuracy requirements are in place. The lateral instability of the comb drive actuator is not critical, because the stability limit calculated with a value of 198 μm is much larger than the length of each comb finger. The dynamic response of the z actuator with a simulated fundamental resonance frequency of 724 Hz is also not critical. The thermal heat expansion of the 3D actuator is also found to be not critical, because 1°C temperature change only results in a thermal expansion of the mirror structure of 0.6 nm, which is below the required actuation resolution of 2 nm.

In order to fabricate the 1D and 3D actuator, a number of non-standard fabrication processes had to be developed. A critical aspect in the fabrication of the one-dimensional actuator is the alignment between the planar mirror and concave fibre mirror as well as the fabrication

of a very smooth planar mirror surface. A process was developed to achieve an atomically smooth mirror surface. It was found that by increasing the reflective area of the planar mirror structure and by implementing a v-groove structure for the concave fibre mirror potential alignment errors are minimized. V-groove and mirror structure are created in a (110) oriented silicon wafer by applying a single KOH wet etch process. Atomically smooth mirror side walls are achieved using a fork alignment structure with a mask alignment accuracy of 0.1^{o}. The undesired large underetching of the rectangular anchor and mirror mask pattern on the (110) oriented silicon wafers during the wet etch process is compensated by increasing the structural size of the mirrors and the anchors avoiding a time consuming development effort finding suitable wet etch compensation structures. In order to achieve a high reflective planar mirror a 20 nm chrome and 100 nm gold layer is angle evaporated on the atomically smooth vertical silicon mirror side wall. The deposited Cr/Au mirror layer is measured with RMS surface roughness of 3 nm. During the evaporation process the reflective layer is not only deposited on the mirror side wall but also on the top and the bottom wafer surfaces. Different approaches have been investigated to selectively remove the Cr/Au layer from the top and bottom wafer surface including KOH wet etching and ion beam milling (IBM). The isotropic wet process is dismissed because of increasing surface roughness and non uniform thickness layers over the wafer surface as well as the planar mirror side wall during the wet etch procedure. Instead the anisotropic IBM process is applied leaving only a reflective layer of Cr/Au at the mirror side wall behind. The optical characterization of the gold coated planar mirror is performed using a fibre with a planar coating, with a reflectivity of 99%. It is found that the highest measured quality factor Q for this planar-planar mirror cavity is 13400 at a cavity length of 30 μm, which is already of sufficient quality for applications such as detection of single atoms. It is anticipated that even higher quality values can be achieved with a concave fibre-mirror configuration.

The batch fabrication process of the 1D actuator is based on a 300 μm silicon substrate, which is after wet etching 180 μm deep v-groove and mirror structures bonded to a Pyrex™ substrate. The Pyrex™ substrate is wet etched in the area where the movable mirror is located. When the Pyrex™ substrate is anodically bonded to the silicon substrate the mirror remains free to move. Lastly, after bonding the comb drive actuator is released by a 120 μm deep dry-etch with a resist pattern masking the actuation part of the comb drive structure.

The fabrication of the three-dimensional actuator involves also a combination of wet etch and dry-etch processes. The actuation structures of the *xy* and *z* actuator are fabricated using dry etch processes. It is found that a 10 μm resist layer of SPRT-220 is thick enough to withstand the first 320 μm deep dry-etch forming the anchor structures for the 3D actuator. Fairly good anchor profiles are created, however overetching in the corners of the anchor structures at their foundation occurs. With a large enough offset between the 60 μm and 320 μm structures this overetch has no disadvantageous affect on the actual actuation device. Also the increased side wall roughness of the deep etched anchors is not of concern, since they do not play any active part in the actuation. It is also found that a uniform surface is achieved by

placing anchors more than 300 μm apart from each other and that the surface roughness, which was measured to be 26 nm, in the 320 μm etched surface plane is smooth and in agreement with the design objectives. For the 60 μm deep dry-etch a minimum thickness of 2.2 μm SPRT-518 resist is needed. Vertical side walls are achieved during the release etch forming the comb drive fingers of the actuator. The inevitable broadening effect as a results of the 60 μm deep reactive ion etching process is found to be 250 nm. It is possible to compensate the enlarged finger gap by increasing the driving voltage or by obtaining the same electrostatic force in adding more comb fingers to each comb drive segment. Due to unexpected side wall overetching of the actuation structures various compensation elements are added to the mask pattern. They protect several critical beam structures, which are essential to maintain the functionality of the releasing actuation structure.

The batch fabrication process of the 3D actuator is based on a 380 μm silicon substrate, which is after patterning 320 μm deep anchor structures bonded to a structured Pyrex™ substrate. The Pyrex™ substrate is structured with metal electrodes, which lock the *xy* actuator and operate the *z* actuator. Since the metal electrodes of the locking mechanism require a distance of 2.5 μm to the opposite silicon electrodes and the electrode of the *z* actuator a distance of 21 μm, a process is developed to etch two topologies and pattern the embedded electrodes. When wet etching the 2.5 μm cavity in HF a photoresist protection is sufficient, but for wet etching the 21 μm cavity in HF a metal-resist layer is required. By applying and patterning a 2.2 μm S1818 photoresist a uniform and good side wall resist coverage is achieved. This way the electrical leads extending from the 2.5 μm and 21 μm deep cavities onto the top wafer surface are wet etched without difficulties.

Using the above processes and designs it is shown that actuated micro optical cavities on atom chips can be realized by applying M(O)EMS fabrication techniques.

7.2 Suggestion for Further Work

As a result of the cleanroom fire in October 2005 at the University of Southampton only theoretical calculations and simulations of the 3D and 1D actuator designs have been presented and initial fabrication results are reported. Reproducing what was lost in the fire turned out to be much more difficult than initially anticipated and has not been completed up to this point. Nevertheless, all the fabrication results until the fire incidence have been presented in detail and are already very promising and encouraging.

7.2.1 1D Actuator

In the first instance the fabrication of the 1D actuator is to be completed. There are several wafers requiring the application of the last masking pattern. This masking pattern defines the comb drive structures of the actuation structure after the final release etch. Furthermore, the

silicon-Pyrex™ wafer sandwich is sawn into a number of actuation devices. In a final fabrication step the optical fibre is introduced into the v-groove with the concave fibre mirror glued in proximity of the planar mirror side wall. Quantitative measurements on a number of working devices should be carried out, including high vacuum measurements in a SEM of the static deflection and the lateral resonances. After the functionality of the actuator is established optical cavity measurements are conducted evaluating the quality factor and tunability of the cavity system.

Secondly, the 1D actuator is to be incorporated into the proposed atom chip design. Micro wires are integrated along with the 1D actuator to form an atom chip, which is capable of not only guiding and trapping atoms, but also detecting single atoms.

7.2.2 3D Actuator

Since both, the *xy* actuator and *z* actuator of the 3D actuation design were not refabricated after the fire, it is recommended to repeat the fabrication of both actuators. Upon completion the static deflection of *xy* actuator is measured. Also the locking mechanism and the cavity actuation of the *z* actuator is measured. Once the functionality of the *xy* and *z* actuator is verified a *xyz* actuator is designed and fabricated. The *xyz* actuator is integrated in the proposed multi-layered single atom chip design.

7.2.3 Atom Chip

After the realization of the two atom chip designs and demonstration that with current micro machining technology is it possible to detect single atoms a further improvement of the atom chip can be addressed. It would be advantageous to eliminate the optical fibre in the cavity system of the atom chip and replace it with an integrated optical wave guide. Using an integrated optical wave guide in particular for the 1D actuator would eliminate any alignment errors between the cavity mirrors, because the wave guides can be fabricated directly on the wafer surface of the actuation structure by applying deposition and lithography processing.

Besides having only one actuated cavity system on the atom chip it is also beneficial to create an entire array of actuated cavity systems on the atom chip surface. Then the quantum information could be exchanged between individual atoms in different cavity systems.

Appendix H

Coventor Etch Simulation

In this appendix, the Coventor log-file is listed for the wet etch simulation described in chapter 5. The Coventor log-file includes a list of commands based on the python scripting language and is read into the Coventor 3DEtch software (A.1). The wet etch simulation uses the mask layout of the 1D actuator, which is presented in section A.2.

H.1 Wet Etch Log-File

```
#============================================================
#! python
# -*- coding: utf-8 -*-
# Copyright (c) 2005, Coventor, Inc. All rights reserved.
# "Do a single wet etch simulation with a top mask"
#============================================================
# The following lines are needed in every application script
import sys
import etch3dx
from etch3dApp import EtchApp
from masks import *
#from skirtedWafer import *
#============================================================
# The following lines set all input values for the application
voxelsPerMicron = 0.5                #voxels per micron
waferThickness = 300.                #thickness in microns
#waferType = etch3dx.Wafer100   #right side is a pre-defined constant
waferType = etch3dx.Wafer110_Flat111_Left  #alternate version of preceding line - waferType
etch3dx.Wafer110_Flat110
waferMaterialID = 1                  #material index in the range [1,255]
maskAngle = 90                       #angle between primary flat & mask x-axis (degrees)
maskFile  = "110_small"              #name of GDS mask file, excluding .gds extension
topMask = "L4D0"                     #an arbitrary name for the top mask
topMaskIndex = 4                     #the index of the top mask in maskFile.gds
reverseTopMaskPolarity = False   #True or False
bottomMask = None                    #an arbitrary name for the bottom mask
bottomMaskIndex = 1                  #uncomment this line if maskFile.gds contains a bottom mask
```

```
                                # and specify the layer index
reverseBotMaskPolarity = False   #True or False
boundsScaleFactor = 1.1          #amount to scale outer bounds of masks
concentration = 0.7              #concentration parameter (must be > 0.0 and <= 1.0) Simple KOH
solution (without additives) 70degC at a concentration of around 33%. Etchant 40% KOH 60 degC is
0.69
temperature = 343                #temperature of bath
numFrames = 350                  # z=190um;
interactive = False              #set to false to run in batch mode
#================================================================
# The following lines are a minimal Python script.
# Construct the application ('app' is an arbitrary name)
app = EtchApp( voxelsPerMicron )
# Process masks
masks = Masks( maskFile )
masks.readMaskLayer( topMaskIndex, topMask )
#masks.readMaskLayer( bottomMaskIndex, bottomMask )
# USER: read additional mask layers here
#The next function call has optional arguments after the first argument
app.setMasks( masks, \
        topMaskName=topMask,\
        reverseTopPolarity=reverseTopMaskPolarity,\
        bottomMaskName=bottomMask,\
        reverseBottomPolarity=reverseBotMaskPolarity,\
        boundsScaling=boundsScaleFactor )
# The next line is essential and must occur after calling setMasks()
wafer = app.getWafer( waferThickness, waferMaterialID=waferMaterialID )
app.setExtractSurfaces( True ) #change argument to False if you don't want to view in Zsplat
app.extractSurfaces( "blank_wafer" )
# USER: add wafer preprocessing here
# define mask orientation with respect to wafer
etchsim = app.getEtchSim()
angle,xax,yax,zax = etch3dx.getWaferRotation( waferType, maskAngle )
etchsim.setWaferRotation(angle,xax,yax,zax)
# construct RPF
rpf = etch3dx.RPF_Cinterp( concentration )
#rpf.setParameterA(2,1,1.2)
#rpf.setParameterB(3,1,7.0)
etchsim.setRPF( waferMaterialID, rpf )
etchsim.setTemperature( temperature )
# run the etch3D simulation
if interactive:
etchsim.visualize()
else:
etchsim.etch( numFrames)
# USER: add wafer postprocessing here
# extract iso-surfaces for visualization in zsplat
app.extractSurfaces( "after_etch3d" )
app.done( interactive)
#================================================================
```

H.2 Mask Layout

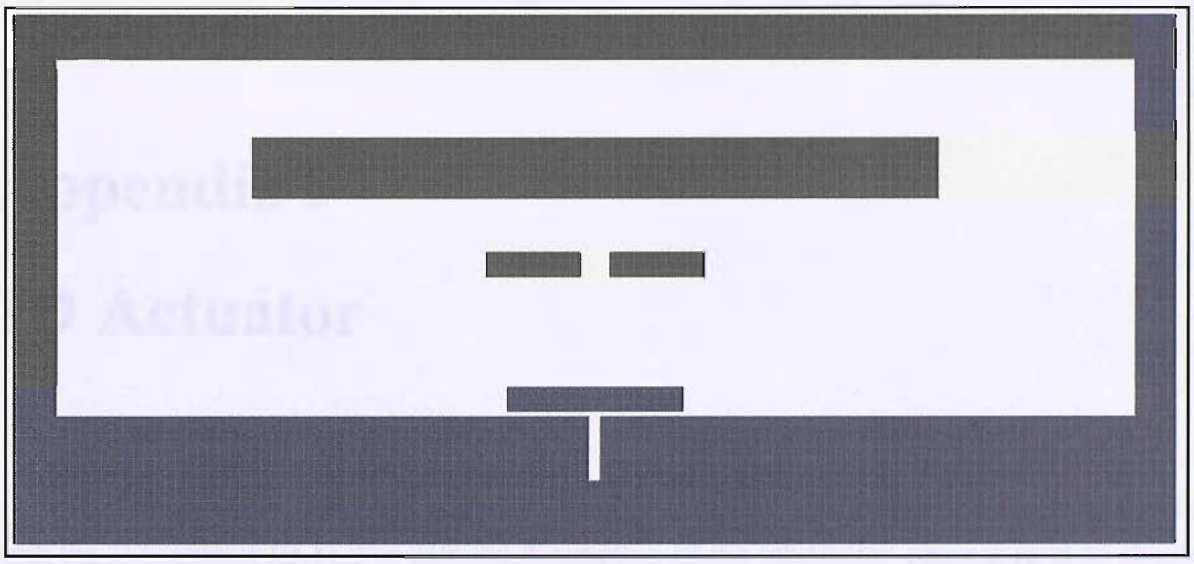

Figure H-1: Mask layout used for the KOH wet etch simulation on the one-dimensional actuation design.

Appendix I

1D Actuator

In this appendix, the LMS process listing is given for the fabrication batch associated with the 1D actuator (B.1). For detailed description of the fabrication process refer to chapter 5. LMS is a library system which allows to create a fabrication batch file from a large variety of standard and nonstandard process steps. This appendix also includes the mask layouts for the device fabrication of the 1D actuator (B.2). The mask layouts were created in Tanner EDA L-Edit version 11 [153].

I.1 LMS Process Listing

The LMS-file for the fabrication batch of the one-dimensional actuator is listed. Chapter 5.2 describes the fabrication batch in detail.

Batch K4041s - <110> 1D Actuator

1	x	P-EM	E-BEAM Mask/Reticle Writing
2	x	G-S12	Title Page: 5x 4inch silicon wafers 300mm, 5x 4 inch pyrex wafers 500mm
3	x	G-1P	Lithography Notes
4	x	G-1	Notebook page
5	x	G-1	Preparation of the 5x pyrex wafers (WA#1-5) before bonding to silicon wafers
6	x	W-C3X	Fuming Nitric Acid clean, wafers with GOLD
7	x	F7-0	Furnace 7: Load in N2: Loading horizontally, 400°C, 60 min., N2
8	x	W-C3X	Fuming Nitric Acid clean, wafers with GOLD
9	x	X-0	General inspection stage: Microscope only
10	x	G-1	Cavity etch in pyrex wafers
11	x	ME-CRAU0	Evaporate Chrome-Gold: 40nmCr/400nmAu
12	x	W-C3X	Fuming Nitric Acid clean, wafers with GOLD
13	x	P-G0X	Photolith mask KB90M_AC, DField: nom. 11μm resist of SPRT220
14	x	X-0	General inspection stage
15	x	P-RHBX	Hardbake (for wafers with GOLD) - 80°C/30min.
16	x	X-0	General inspection stage

17	x	WM-0X	Wafers with GOLD: wet etch 400nm Au layer (approx. 3 min./check every 30 sec. though) - Au etchant - WA #1-5 !!! overetch to be minimized, cause of small gold features !!!
18	x	WM-0X	Wafers with GOLD: wet etch 40nm Cr layer (approx. 10 sec.) - Cr etchant - WA #1-5 !!! overetch to be minimized, cause of small Cr features !!!
19	x	X-0	General inspection stage: Microscope only
20	x	WH-0X	Wafers with GOLD: HF 48% 2parts / H_2O 1 part (3.5µm/min) etch for 6 min. - no agitation -
21	x	P-RSXR	esist strip (for wafers with GOLD)
22	x	W-C3X	Fuming Nitric Acid clean, wafers with GOLD
23	x	WM-0X	Wafers with GOLD: strip etch 400nm Au layer - WA #1-5
24	x	WM-0X	Wafers with GOLD: strip etch 40nm Cr layer - WA #1-5
25	x	W-C3X	Fuming Nitric Acid clean, wafers with GOLD
26	x	X-0	General inspection stage: Microscope only
27	x	G-1	Putting Cr/Au bond pattern on pyrex wafers
28	x	ME-CRAU0	Evaporate Chrome-Gold: 60nm Cr/1300nm Au
29	x	W-C3X	Fuming Nitric Acid clean, wafers with GOLD
30	x	P-G0X	Photolith mask KB90M_AE, LField: nom. 11µm resist of SPRT220 (for metal wet etch)
31	x	X-0	General inspection stage
32	x	P-RHBX	Hardbake (for wafers with GOLD) - 90°C/30min.
33	x	WM-0X	Wafers with GOLD: wet etch 1300nm Au layer (approx. 6 min./check every 30 sec. though) - Au etchant - WA #1-5
34	x	WM-0X	Wafers with GOLD: wet etch 60nm Cr layer (approx. 20 sec.) - Cr etchant - WA #1-5
35	x	P-RSX	Resist strip (for wafers with GOLD)
36	x	W-C3X	Fuming Nitric Acid clean, wafers with GOLD
37	x	X-0	General inspection stage: Microscope only
38	x	G-1	Preparation of the 5x silicon wafers (WA#6-10) before bonding to pyrex wafers
39	x	LN-0	Deposit LPCVD 50nm Si3N4 !!! without pad oxide !!! on both sides
40	x	W-C2	Fuming Nitric acid clean, 2nd pot only
41	x	P-G1	Photolith mask KB90M AA, DField on fronts: nom.1.1µm resist
42	x	P-RHBD	Hardbake for dry etch (30min at 140C)
43	x	P-RG	Spin resist on edges
44	x	P-RHBD	Bake resist on edges
45	x	D-N1E	Etch Si3N4. Anisot. L/F EBMF/OPTICAL resist OPT80+ CHF3+Ar50nm Si3N4 etch + short overetch - Opening Vangbo Structure
46	x	P-RS	Resist strip (FN strip)
47	x	W-C2	Fuming Nitric acid clean, 2nd pot only
48	x	X-0	General inspection stage: Microscope only
49	x	WS-3	Etch silicon in standard KOH - 15 min. etch for precise alignement fork structure in order to identify [111] planes
50	x	W-C1	RCA clean
51	x	W-C2	Fuming Nitric acid clean, 2nd pot only
52	x	P-G1	Photolith mask KB90M AB, LField on fronts: nom. 1.1µm resist
53	x	P-RHBD	Hardbake for dry etch
54	x	P-RG	Spin resist on edges
55	x	P-RHBD	Bake resist on edges
56	x	D-N1E	Etch Si3N4. Anisot. L/F EBMF/OPTICAL resist OPT80+ CHF3+Ar50nm Si3N4 etch + short overetch - Opening Design Structure
57	x	P-RS	Resist strip (FN strip)
58	x	W-C2	Fuming Nitric acid clean, 2nd pot only

59	x	WS-3	Etch silicon in standard KOH 189min (approx. 180μm deep) WA#6-10
60	x	W-C1	RCA clean
61	x	W-C2	Fuming Nitric acid clean, 2nd pot only
62	x	WN-1	Strip/Wet etch Si3N4, Orthophosphoric acid 160degC. WA#6-10
63	x	W-C1	RCA clean
64	x	ME-CRAU0	Evaporate Chrome-Gold: 20deg static evaporation, 20nmCr/100nmAu
65	x	B-0	Ion-Beam Mill: Etch Au and stop etch some where into the Cr. Remaining Cr to be removed using wet etch.
66	x	WM-0	Wet etch Cr til clear using Cr etch. Minimise over etch
67	x	W-C3X	Fuming Nitric Acid clean, wafers with GOLD
68	x	G-1	Notebook page: Annealing step prevents gold to deteriorate during the bonding procedure
69	x	F7-0	Furnace 7: Load in N2: Loading horizontally, 400 °C, 60 min., N2
70	x	G-1	Bonding of silicon wafers to pyrex wafers (alignment bonding on EVG)
71	x	WH-D1X	Dip etch silicon wafers with GOLD. Dip etch, 20:1 BHF 25°C. Until just hydrophobic
72	x	S-AB	Anodic Bonding (400 N, 900 V, 310 °C, 15 min)
73	x	W-C3X	Fuming Nitric Acid clean, wafers with GOLD
74	x	X-0	General inspection stage: Microscope only
75	x	P-G0X	Photolith mask KB90M_AD, LField: SPRT518 2.2μm (for dry etch), double side alignment with EVG
76	x	X-0	General inspection stage
77	x	P-RHBX	Hardbake for dry-etch (for wafers with GOLD)
78	x	DS-S0X	ASE Deep Silicon Etch 120μm (no backing wafer required), depth:120 μm into silicon to release comb drive structure (overetch time rquired) - Au Contaminated - all 5 Wafers pairs
79	x	P-0X	Apply drops of resist on mirror wall and delimiters only (for wafers with GOLD)
80	x	P-RHBX	Hardbake (for wafers with GOLD) - only at room temperature for one day
81	x	S-SX	Sawing. Specify details. GOLD CONTAMINATED: sawing all five wafers (approx. 10 cuts each wafer) into chips size
82	x	W-0X	RCA clean of chips in wetroom in IMTEC bath

I.2 Mask Layouts

The mask layout files created in Tanner EDA L-edit version 11 consist of cells and layers. The actuation designs are saved as different cells. A cell can include another cell as an instance. The highest cell, called "topcell", shows the distribution of the designs across the wafer surface. Each device fabrication batch uses a number of masking layers, which are exposed onto the wafer surface during lithography processing. The fabrication of 1D actuator requires a set of five masks, which correspond to five masking layers in the L-edit layout file as shown in table B.2. Since capturing significant information on a screen shot is difficult an enlarged figure of the actuation device is presented in section B.2.1-5.

Mask Number	Layer Number	Masking Layer
KB90M	AA	Vangbo Mask
KB90M	AB	Anchors and Mirror Mask
KB90M	AC	Pyrex™ Cavity Mask
KB90M	AD	Comb Drive Mask
KB90M	AE	Pyrex™ Bond Pad Mask

Table 9-1: Five lithography masks are used for fabricating the one-dimensional actuator.

I.2.1 Vangbo Mask (KB90M-AA)

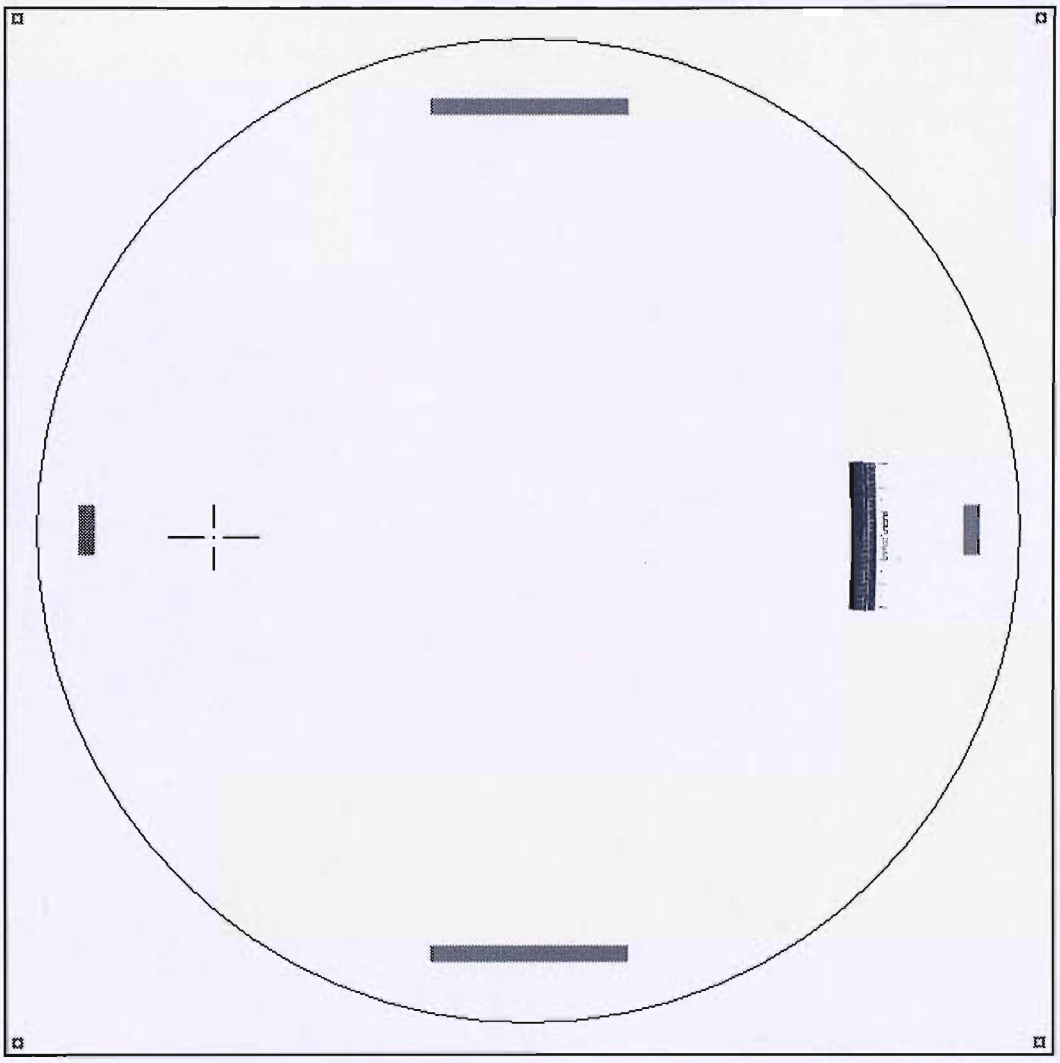

Figure I-1: Mask layout KB90M-AA of the 1D actuator with the vangbo structure.

I.2.2 Anchor and Mirror Mask (KB90M-AB)

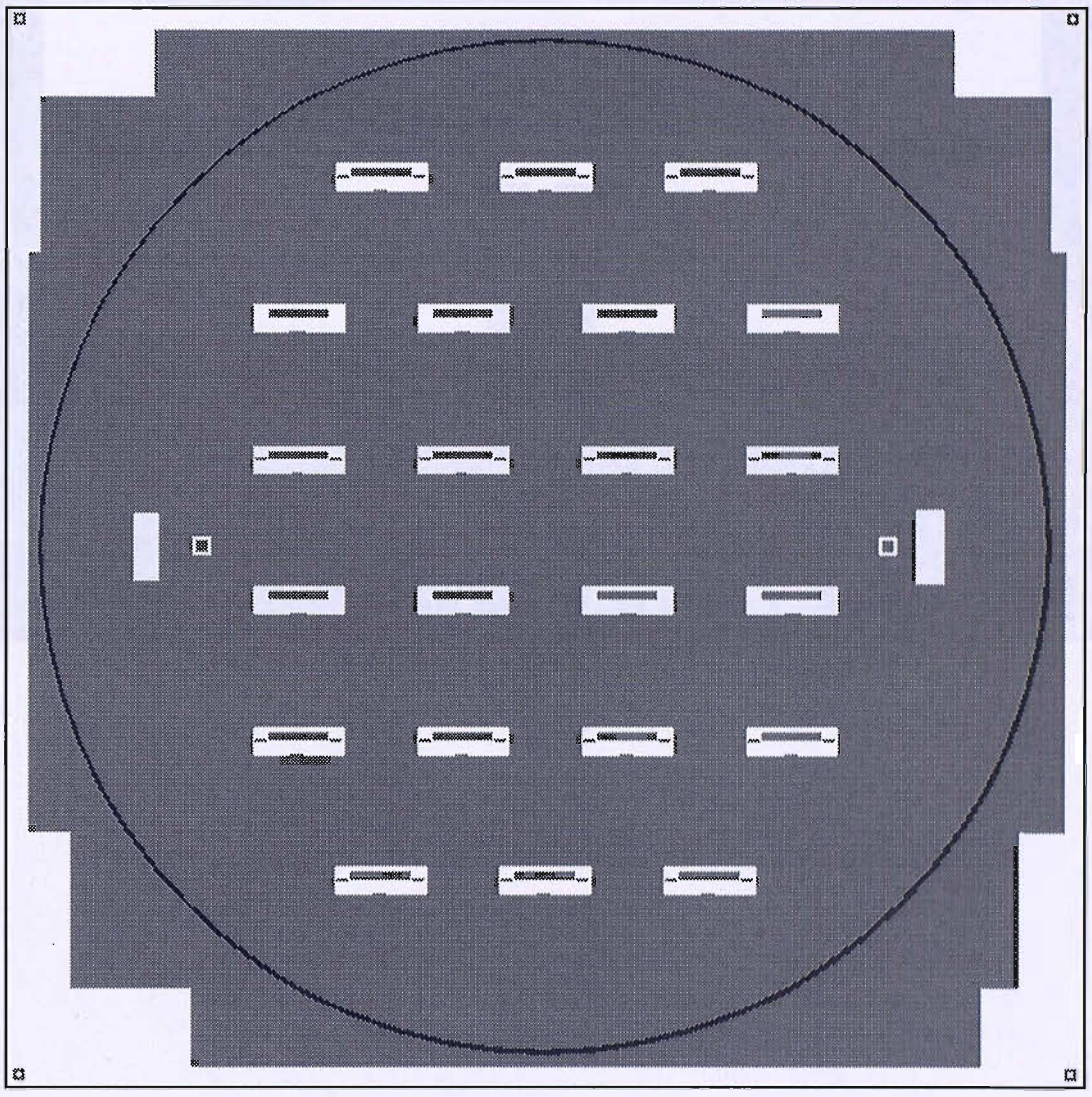

Figure I-2: The mask layout KB90M-AB of the 1D actuator with anchor and mirror structures.

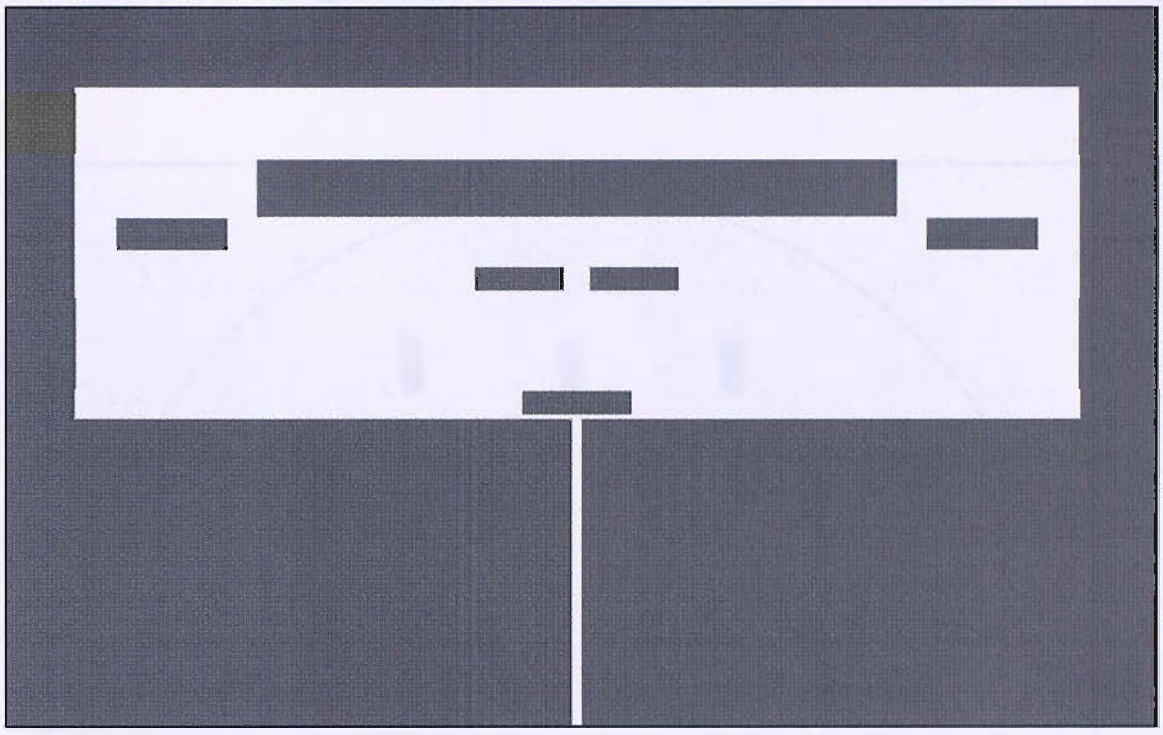

Figure I-3: One single actuation device depicted and enlarged from figure B-2.

I.2.3 Pyrex™ Cavity Mask (KB90M-AC)

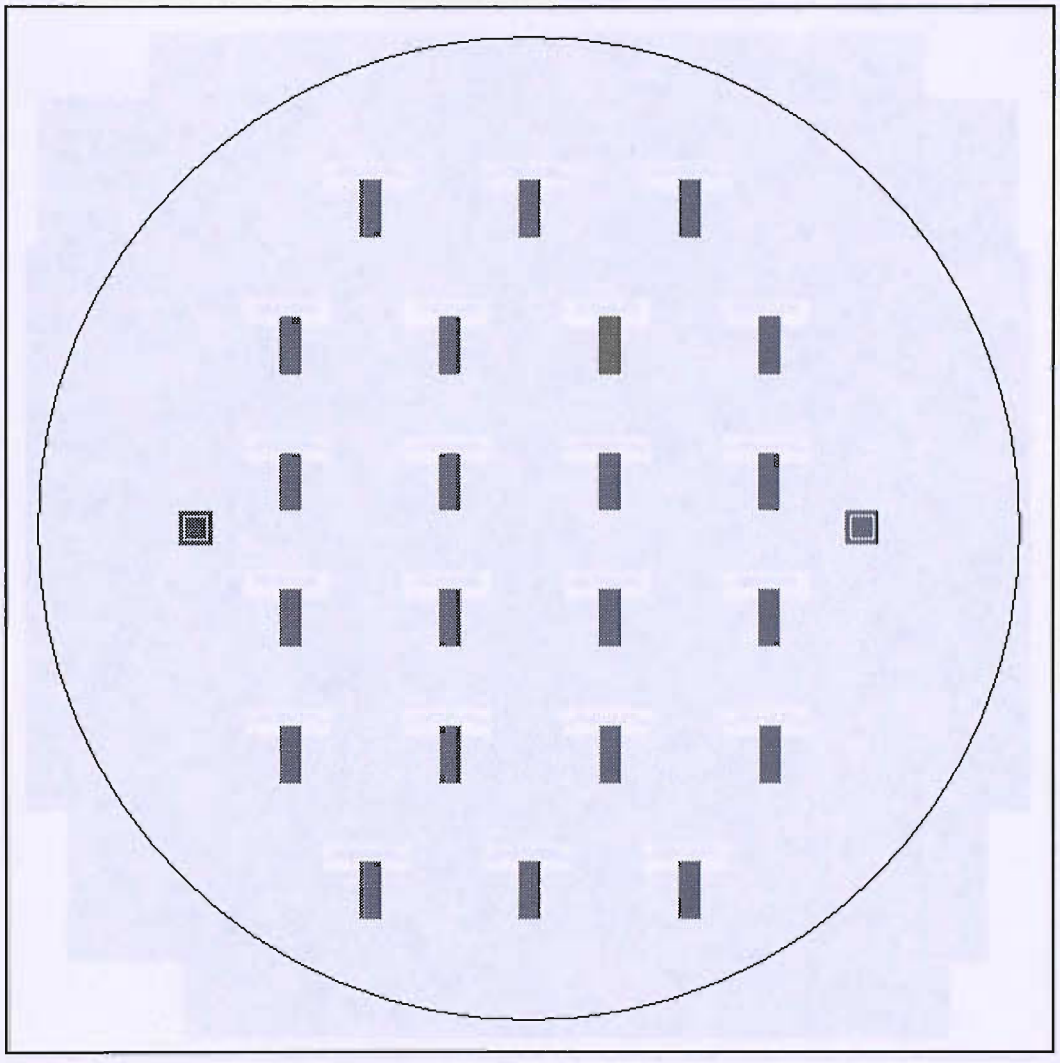

Figure I-4: The mask layout KB90M-AC of the 1D actuator with cavity structures.

I.2.4 Comb Drive Mask (KB90M-AD)

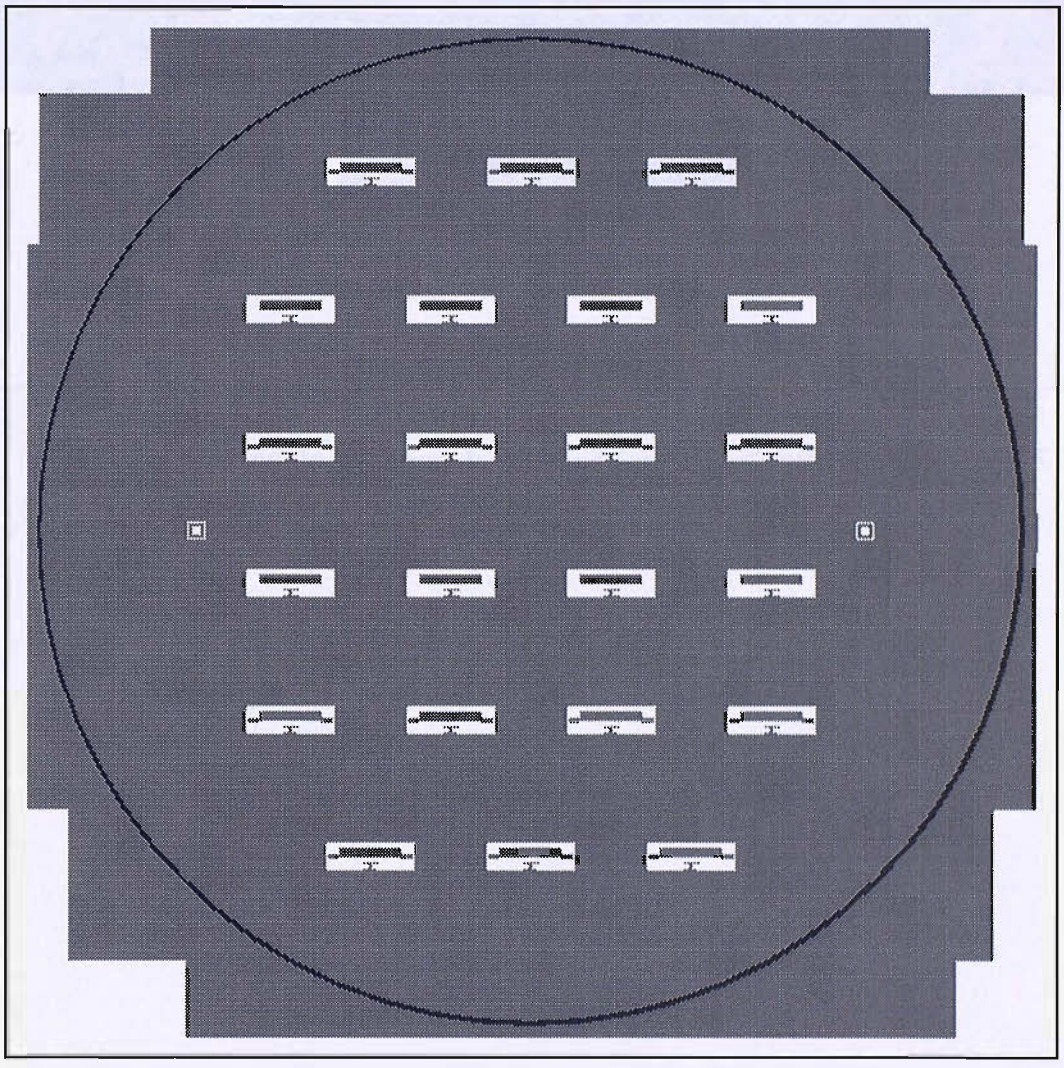

Figure I-5: The mask layout KB90M-AD of the 1D actuator with comb drive structures.

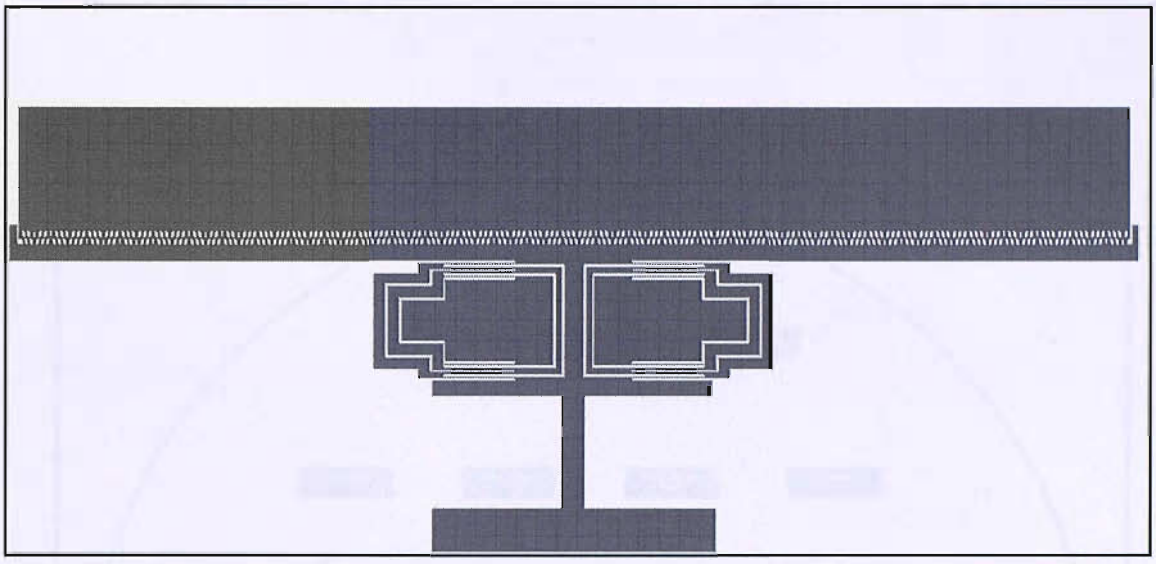

Figure I-6: One single actuation device depicted and enlarged from figure B-5.

I.2.5 Pyrex™ Bond Pad Mask (KB90M-AE)

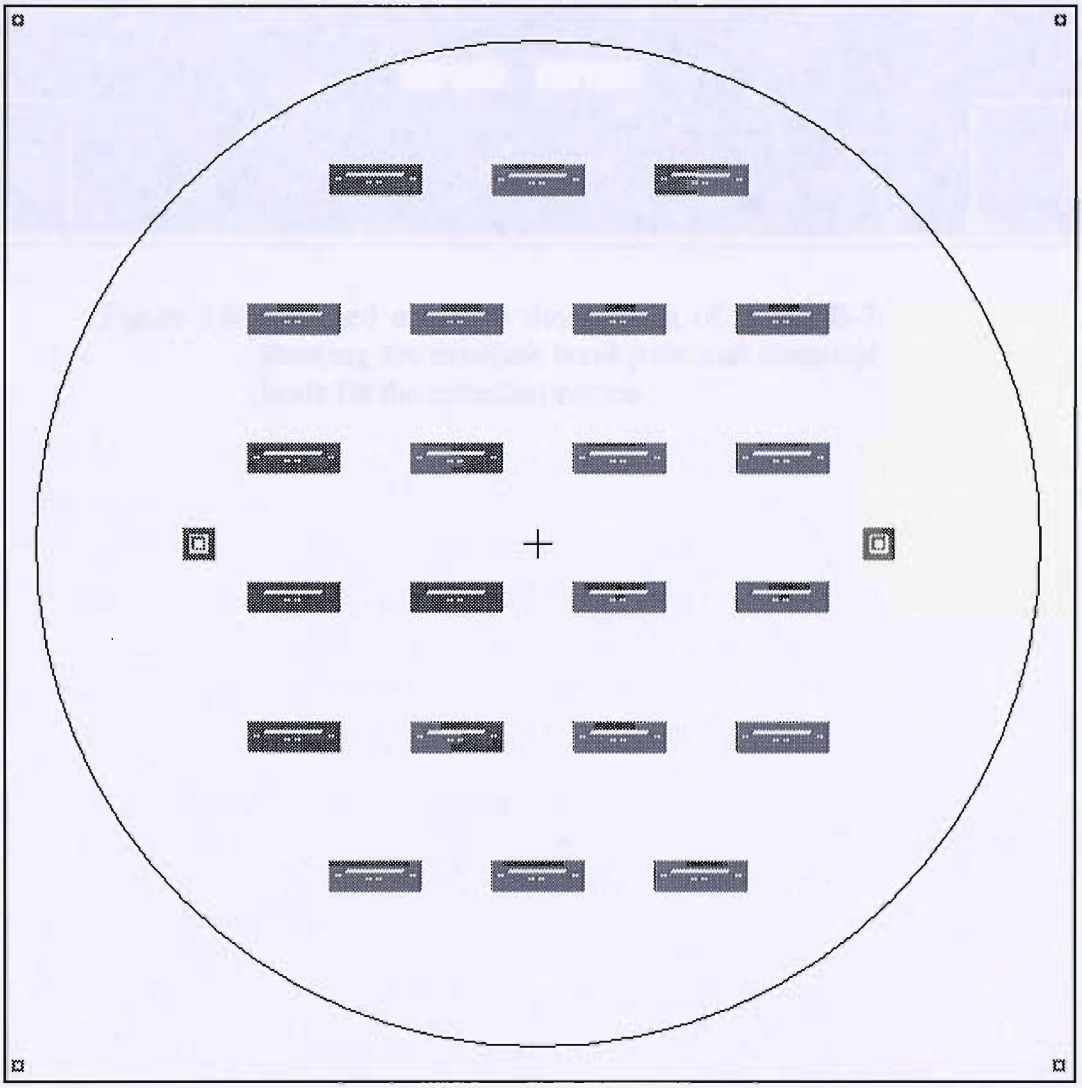

Figure I-7: The mask layout KB90M-AE of the 1D actuator with the bond pad areas and gold layer to avoid micro loading effect.

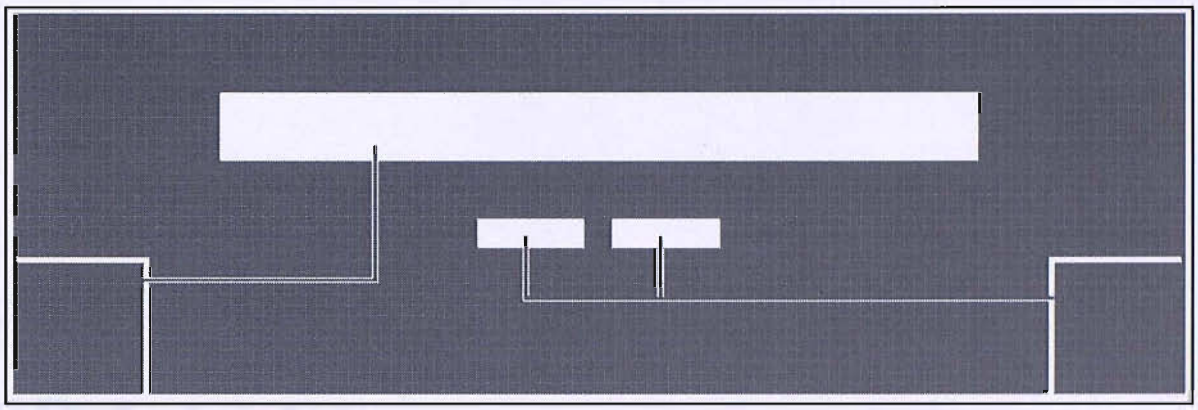

Figure I-8: Enlarged actuation device area of figure B-7 showing the masking bond pads and electrical leads for the actuation device.

Appendix J

3D Actuator

In this appendix, the LMS process listings and mask layouts are given for the fabrication batches associated with the 3D actuator. For detailed description of the fabrication process refer to chapter 5.3. In section C.1 the process listing and mask layout for the development batch is presented. Section C.1.3 details the results of the etch rate dependancy on different mask openings. Section C.2 and C.3 illustrate the LMS process listings and mask layouts for the device fabrication batches of the *xy* actuator and the *z* actuator respectively.

J.1 Process Development Batch

J.1.1 LMS Process Listing

The LMS-file for the development batch of the three-dimensional actuator is listed. Chapter 5.3.1 describes the fabrication batch in detail.

Batch K2604s	- Development Batch for 3D Actuator	
1	P-EM	E-BEAM Mask/Reticle Writing
2	G-S12	Title Page: 6 wafers (W1-6), MATERIAL:4", P-type, thin 380µm, double polished, 2 pyrex wafers (500µm, W7/8) for Anodic Bonding
3	W-C2	Fuming Nitric acid clean, 2nd pot only (W1-6)
4	P-G2	Photolith mask KB06MTS, Front, Light Field: nom. 2.2µm resist (for dry-etch of 60µm Si) SPRT518
5	P-RHBD	Hardbake of SPRT518 for dry etch on W1/W2
6	D-0	Dry etch: STS ASE, etch depth: 60µm, with approx. 2µm/min etch rate -> t1= 30min on W1/W2, side: front
7	P-G0	Photolith mask KB06MTS,SPR220-7, Light Field: nom. 10µm resist (for dry-etch of 320µm Si) of W3-6
8	P-RHBD	Hardbake of SPR220-7 for dry etch on W3-6
9	D-0	Dry etch: STS ASE, etch depth: 320µm, with approx. 2µm/min etch rate -> t2= 160min on W3-6, side: back

10	P-RS	Resist strip on W1-6
11	W-C2	Fuming Nitric acid clean, 2nd pot only (W1-6)
12	G-3	Special Instructions: Cleaving of W1/W2 for SEM inspection by engineer
13	X-0SEM	inspection after cleaving W1/W2
14	G-3	Special Instructions: Sawing of W3/W4 for AFM inspection (approx. 3 cuts each wafer)
15	X-0AFM	inspection after sawing W3/W4
16	G-3	Special Instruction: Anodic Bonding (EVG) of W5 to W7 and W6 to W8, 900 V, 400 N, 10^{-5} torr at 400 °C for 15min.
17	W-C3X	Fuming Nitric Acid clean, wafers with GOLD
18	X-0	Visual Inspection by Microscope of 2 wafer sandwich W5/W7 and W6/W8
19	X-0SEM	inspection of W5/7 and W6/8
20	G-3	Special Instructions: Sawing of W5/7 or W6/8 for SEM inspection (approx. 3 cuts each wafer)
21	X-0SEM	inspection again, but only W5/7 or W6/8 to characterize bonding after sawing

J.1.2 Mask Layout (KB06M)

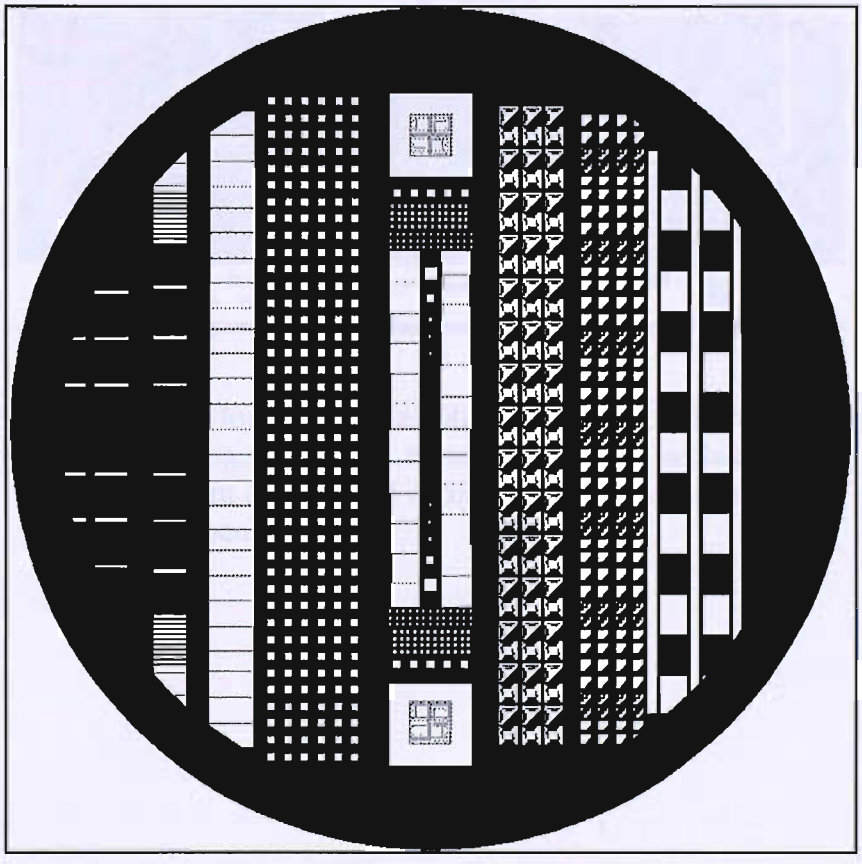

Figure J-1: Development batch process mask layout (KB06M).

The test structure consist of trenches, pillars, squares and initial actuation designs of different widths and varying. Trenches, pillars and squares vary in size and have different distances between them.

J.1.3 Etch rate dependancy on the mask opening

The following two pictures compare the etch depths after a 45 min dry-etch. The SEM images capture different sized square openings. The etch depths vary dependant on the intial size of the square opening. Figure C-2 shows a slight increase of around 13 µm in etch depth for an opening of 250 µm compared to a 300 µm opening. Only for openings larger than 300 µm the etch rate becomes constant (figure C-3). Both 300 µm and 400 µm openings measure with 133 µm the same etch depth.

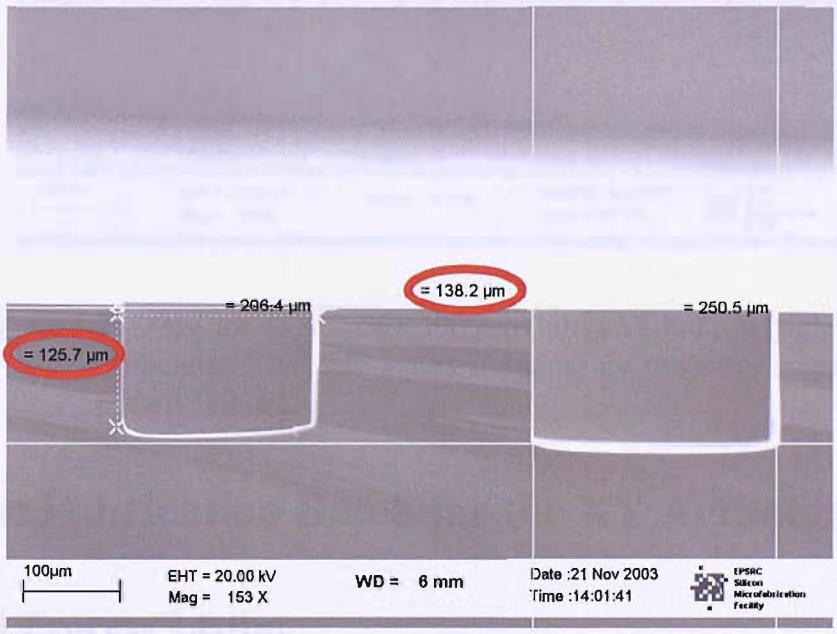

Figure J-2: DRIE for 45 min of a 200 µm (left) and 250 µm (right) opening. The depth measurement (red circled) of the 250 µm opening is 13 µm deeper compared to the 200 µm opening.

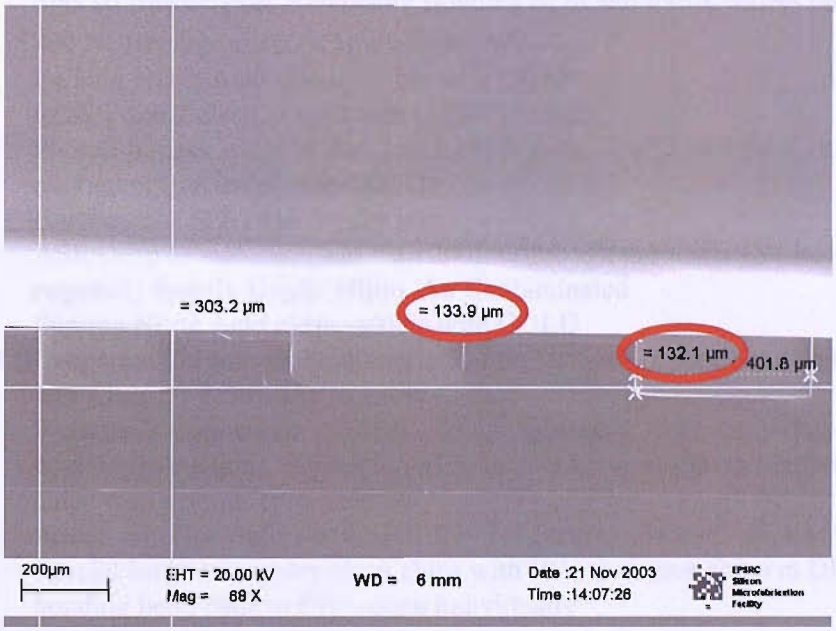

Figure J-3: DRIE for 45 min of a 300 µm (left) and 400 µm (right) opening. The etch depths are equal for openings larger than 300 µm.

J.2 Device Fabrication Batch for the XY Actuator

J.2.1 LMS Process Listing

The LMS-file for the device fabrication batch of the *xy* actuator is listed. Chapter 5.3.1 describes the fabrication batch in detail.

Batch K4052s - Device Fabrication Batch for xy actuator

1	P-EM	E-BEAM Mask/Reticle Writing
2	G-S12	Title Page: 12 wafers (W1-12), MATERIAL:4", P-type, thin 380µm, double polished W1-6, Pyrex wafers (500µm, W7-12)
3	G-1	Preparation of 6 Pyrex Wafers for bonding
4	W-C3	Fuming Nitric acid clean, wafers with GOLD (W7-12)
5	F7-0	Furnace 8: Load in N2: Loading horizontal, 400°C, 30min., N2
6	W-C3	Fuming Nitric acid clean, wafers with GOLD (W7-12)
7	G-1	Silicon Wafer processing W1-6
8	W-C2	Fuming Nitric acid clean, 2nd pot only
9	P-G0	Photolith mask KB24M-AA, Front, Light Field: nom. 10µm resist SPR220-7 Dry-etch of 320µm Si - BACK of Wafer)
10	D-0	ASE Deep Silicon Etch > 200µm/through the wafer (Backing wafer required) Specify Depth: 320µm, Au Contaminated, W1-6
11	X-0	General inspection stage - SEM and Microscope
12	P-RS	Resist strip (for wafers with GOLD)

13	W-C3	Fuming Nitric Acid clean, wafers with GOLD
14	G-3	Special Instructions: Anodically Bonding of Si and Pyrex wafers on EVG: 900 V, 400 N, 10^{-5} torr at 400 °C for 15min., W7-12
15	W-C3	Fuming Nitric Acid clean, wafers with GOLD
16	W-0X	RCA 1 and 2 clean in gold area in IMTEC Bath
18	P-G0	Photolith mask KB24M-AB, Light Field: nom. SPRT518 2.2μm, double sided alignment (for wafer with GOLD)
19	P-RHBD	Hardbake of SPRT518 for dry etch
20	D-0	ASE Deep Silicon Etch less than 200μm/through the wafer (No backing wafer required) Specify Depth: 60μm, Au Contaminated
21	W-C3	Fuming Nitric Acid clean, wafers with GOLD
22	ME-CRAU0	Evaporate Chrome-Gold: 40nmCr/500nmAu to make wire bond pad, static evaporation - flux perpendicular to wafer surface
23	P-RF	Front resist application (S1818) - do not spin resist, only apply drops on structures
24	G-3	Special Instructions: Separation of Actuators by up wafer and individually clean chips with acetone (pre-clean)
25	P-RS	Resist strip (for wafers with GOLD) - FN Strip (individual chips in beaker)
26	G-3	Special Instructions: dry clean chips with IPA, then glue chips in DIP and finally bonding bond pads to DIP - done individually

J.2.2 Mask Layouts

The device fabrication of the *xy* actuator requires a set of two masks, KB24M-AA and KB24M-AB. Both mask layouts are presented in the following and include enlarged figures of the actuation device.

Anchor Mask (KB24M-AA)

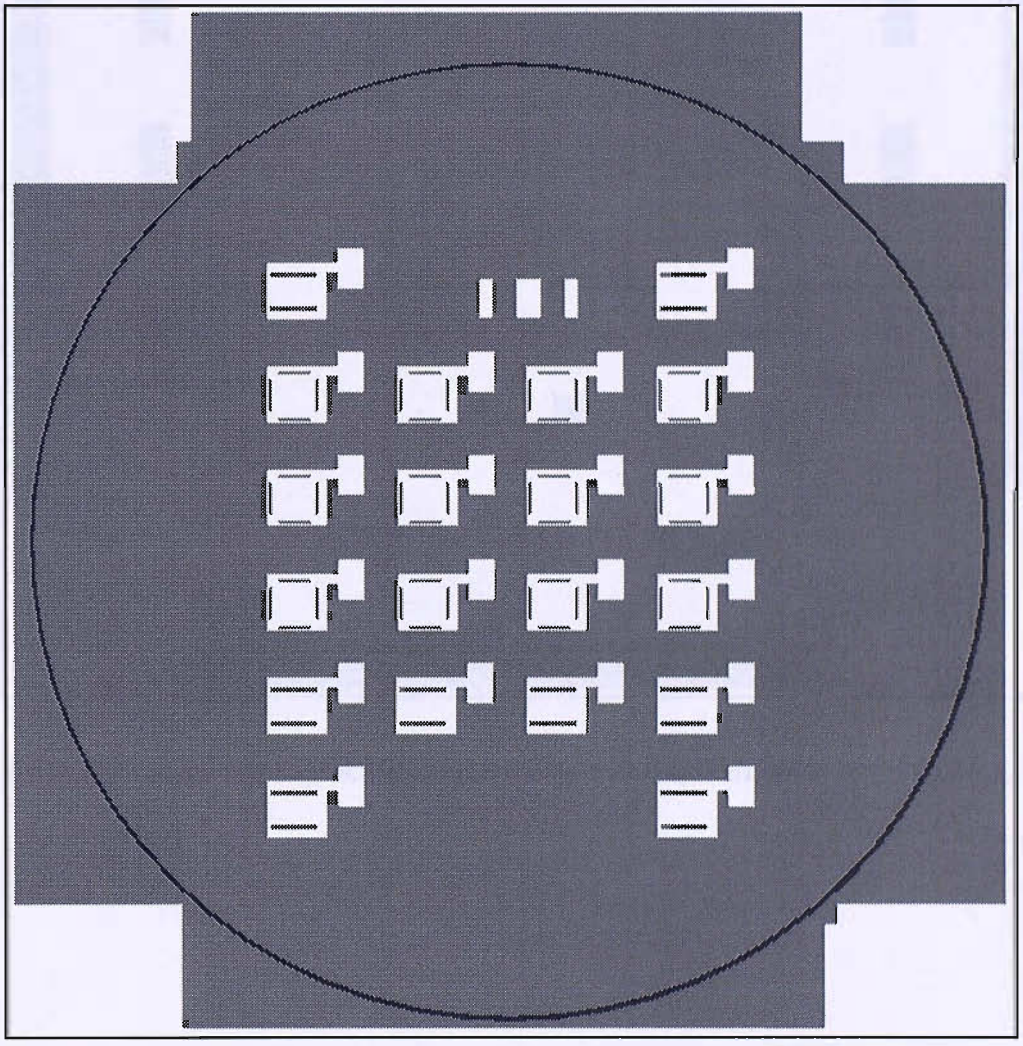

Figure J-4: The mask layout KB24M-AA of the *xy* actuator with the anchor structures (3D actuator).

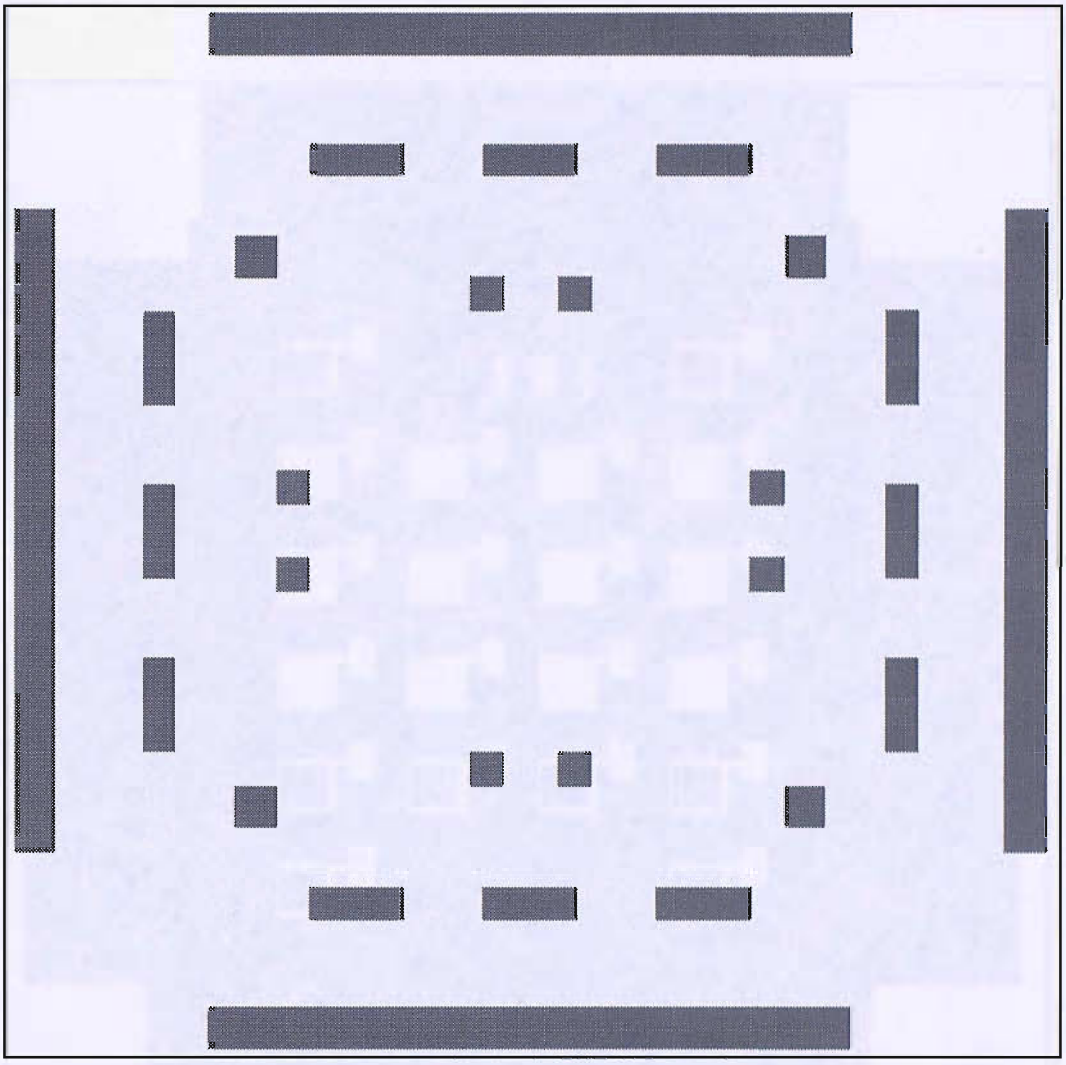

Figure J-5: One single *xy* actuation device depicted and enlarged from figure C-4.

Comb Drive Mask (KB24M-AB)

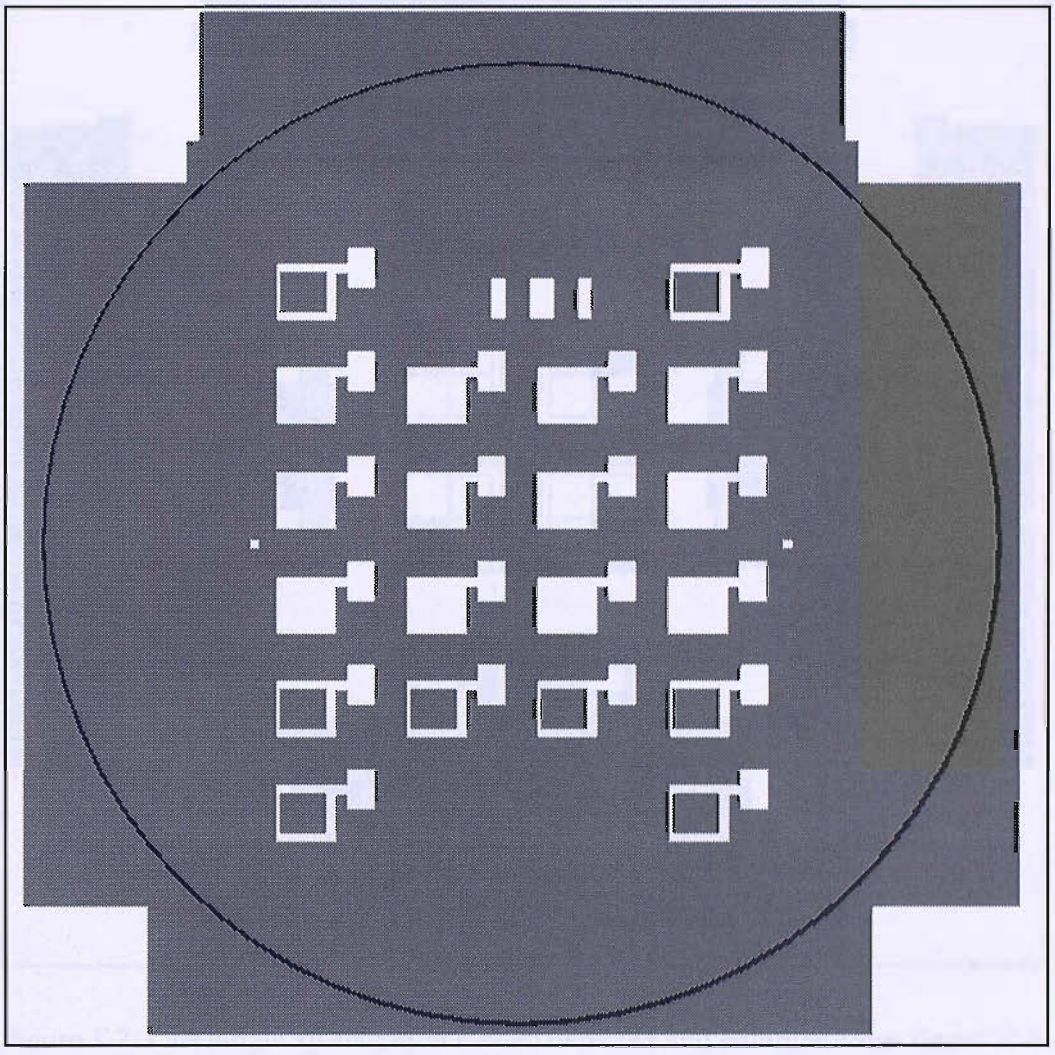

Figure J-6: The mask layout KB24M-AB of the *xy* actuator with the comb drive structures (3D actuator).

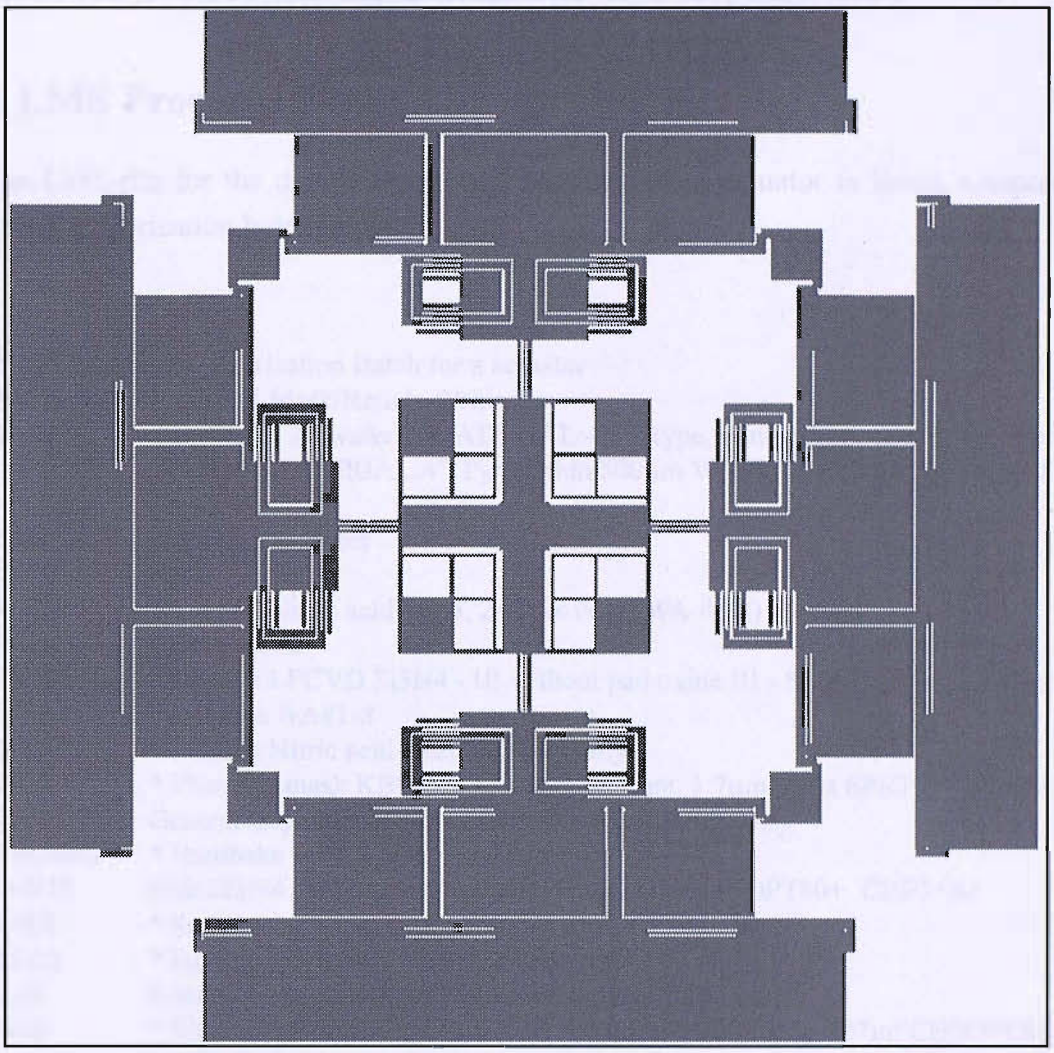

Figure J-7: One single *xy* actuation device depicted and enlarged from figure C-6.

J.3 Device Fabrication Batch for the Z Actuator

J.3.1 LMS Process Listing

The LMS-file for the device fabrication batch of the *z* actuator is listed. Chapter 5.3.2 describes the fabrication batch in detail.

Batch K2937s - Device Fabrication Batch for z actuator

1	P-EM	E-BEAM Mask/Reticle Writing
2	G-S12	Title Page: 26 wafers, MATERIAL:4", P-type, thin 380µm, double polished - WA#1-8, MATERIAL:4", Pyrex, thin 500µm WA#9-18 +8 backing wafers for stages 39,41-47
3	G-1P	Lithography Notes
4	G-1	Notebook page
5	W-C2	* Fuming Nitric acid clean, 2nd pot only (WA #1-8)
6	W-C1	* RCA clean
7	LN-0	* Deposit LPCVD Si3N4 - !!! without pad oxide !!! - Specify process: 180nm on both sides WA#1-8
8	W-C2	* Fuming Nitric acid clean, 2nd pot only
9	P-G1	* Photolith mask KB86M- AA, DField: nom. 1.7µm resist SPRT518 STANDARD
10	X-G	General inspection stage - Microscope Inspection only
11	P-RHBD	* Hardbake for dry etch
12	D-N1F	Etch Si3N4. Anisot. D/F EBMF/OPTICAL resist OPT80+ CHF3+Ar
13	P-RS	* Resist strip
14	W-C2	* Fuming Nitric acid clean, 2nd pot only
15	X-0	General inspection stage - microscope inspection only
16	W-0	* Wet etch of Si in 30ml HF(49%) + 43ml HNO3 (70%) + 27ml CH3COOH (standard) in Telfon beaker for 5min. on shaking table - WA#1-8 - etch depth approx. 100µm
17	W-C2	* Fuming Nitric acid clean, 2nd pot only
18	D-N1F	Strip Etch Si3N4. Anisot. D/F EBMF/OPTICAL resist OPT80+ CHF3+Ar
19	X-0	General inspection stage - microscope inspection and SEM
20	W-C2	* Fuming Nitric acid clean, 2nd pot only
21	ME-CRAU0	Evaporate Chrome-Gold: Cr/60nm and Au/400nm
22	W-C3X	* Fuming Nitric Acid clean, wafers with GOLD
23	P-G0X	* Photolith mask KB86M- AB, LField: nom. 2.2µm resist S1818 (for metal wet-etch) - !!! Top Gold Side Only !!! - Resist coverage of entire cavity is not important - Alignment: Chrom square (AB) positioned over cavity whole
24	X-G	General inspection stage - Microscope Inspection only - GOLD CONTAMINATED
25	P-RHBX	* Hardbake for wet etch Au/Cr
26	WM-0X	400nm Au layer (approx. 2 min./ check every 30 sec. though), Au etchant - WA#1-8
27	WM-0X	60nm Cr layer (approx. 30 sec./ check every 10 sec. though), Cr etchant - WA#1-8
28	P-RSX	* Resist strip (for wafers with GOLD)
29	W-C3X	* Fuming Nitric Acid clean, wafers with GOLD
30	X-0	General inspection stage - microscope inspection and SEM Check front cavity and cleaniness of back side in order to deposit SiO2 1µm
31	LD-0X	+ General PECVD deposition; SiO2 deposition only on back side, thickness 1µm !!! Attention: Gold pattern on front to be facing down - be very careful placing wafer down on platter (avoiding scratches in gold pattern) !!!

32	P-G0X	* Photolith mask KB86M- AC, LField: DoubleSided, Alignment - nom. 2.2μm SPRT 518 resist (for dry-etch) !!! - front gold AM aligned to back SiO2 AM - !!!
33	X-0	General inspection stage - microscope inspection only
34	P-RHBX	* Hardbake for SiO2 dry-etch
35	D-O1X	+ Etch SiO2 Anisot. - Au CONTAM - PT RIE80 - CHF dry etch 1 μm stubs - approx. 50min. process time !!! Attention: Gold pattern on front to be facing down - be very careful placing wafer down on platter (avoiding scratches in gold patter)
36	D-A2X	Dry Resist Strip (use P-RS if possible) SRS GOLD ASHER !!! 5 min. only - check gold cavity afterwards !!!
37	P-RSX	* Resist strip (for wafers with GOLD)
38	W-C3X	* Fuming Nitric Acid clean, wafers with GOLD
39	X-0	General inspection stage - microscope inspection only (both gold cavity and stubs) - GOLD CONTAMINATED -
40	P-G0X	* Photolith mask KB86M- AD, LField: SiO2 alignment marks used for single sided alignment- nom. 10μm resist of SPR220 (for 320μm Si ASE DRIE) - on the Back of the wafer
41	X-0	General inspection stage - microscope inspection only -GOLD CONTAMINATED-
42	P-RHBX	* Hardbake for ASE DRIE - horizontal
43	DS-D0X	ASE Deep Silicon Etch > 200μm/through the wafer (Backing wafer required) Specify Depth: 320 μm Au Contam - WA#1-8
44	D-A2X	Dry Resist Strip (use P-RS if possible) SRS GOLD ASHER !!! 5 min. only (from Gareth) - check gold cavity afterwards !!!
45	P-RSX	* FN Resist strip (for wafers with GOLD) WA#1-8
46	W-C3X	* Fuming Nitric Acid clean, wafers with GOLD WA#1-8
47	X-0	General inspection stage - microscope inspection on both sides (cavity and stubs) - WA#1-8 - GOLD CONTAMINATED -
48	W-C3X	* Fuming Nitric Acid clean, wafers with GOLD - WA#9-18 - PYREX Wafers
49	F7-0	* Furnace 7: Load in N2: Loading horizontal, 400°C, 30min., N2 - COULD BE GOLD CONTAMINATED -
50	W-C3X	* Fuming Nitric Acid clean, wafers with GOLD - WA#9-16
51	G-1	*Notebook page: Wafer #9-16 - wafers for 2.5μm (1st stage) and 21μm (2 stage) pyrex etch
52	G-1	*Notebook page: Wafer #9-16 - processing wafers (1nd stage)
53	W-C3X	* Fuming Nitric Acid clean, wafers with GOLD
54	P-G0X	* Photolith mask KB86M- AE, DF Field: S1818 2.2μm (for 2.5 μm Pyrex etch)
55	P-RHBX	* Hardbake for 2.5μm wet etch of Pyrex
56	X-0	General inspection stage - try to measure resist thickness on one wafer again with Nanospec and check under microscope - GOLD CONTAMINATED -
57	WH-0X	+ Blank stage sheet: HF:H_2O 2:1.5 (etchrate approx. 2.5μm/min.), etch down to 2.5μm into Pyrex - gentle agitation in beaker - etch back of Pyrex wafer is not a problem
58	P-RSX	* FN Resist strip (for wafers with GOLD)
59	W-C3X	* Fuming Nitric Acid clean, wafers with GOLD
60	G-1	*Notebook page: Wafer #9-16 - wafers for 21μm (2 stage) pyrex etch
61	G-1	*Notebook page: Wafer #9-16 - both processing and development wafers (2nd stage)
62	ME-CRAU0	Evaporate Chrome-Gold: Cr 40nm / Au 400nm - WA#9-16
63	W-C3X	* Fuming Nitric Acid clean, wafers with GOLD
64	P-G0X	* Photolith mask KB86M-AF, DField: nom.11μm resist of SPR220 (for metal wet-etch)

65	P-RHBX	* Hardbake for 21μm wet etch of Pyrex
66	WM-0X	400nm Au layer (approx. 2 min./ check every 30 sec.) - Au etchant - WA#9-16
67	WM-0X	40nm Cr layer (approx. 30 sec./ check every 10 sec.) - Cr etchant - WA#9-16
68	WH-0X	+ Blank stage sheet: HF (48%) 2 parts / H_2O 1.5 part (2.5μm/min) etch for 8.5 min. - gentle agitation -
67	X-0	General inspection stage - check under microscope edges from 2.5μm to 21μm cavities - GOLD CONTAMINATED -
68	P-RSX	* FN Resist strip (for wafers with GOLD)
69	W-C3X	* Fuming Nitric Acid clean, wafers with GOLD
70	G-1	*Notebook page: Wafer #9-16 - wafers applied with gold electrode in 21μm and 2.5μm cavities on processing wafers
71	ME-CRAU0	Evaporate Chrome-Gold: Cr 60nm / Au 500nm - WA#9-16
72	W-C3X	* Fuming Nitric Acid clean, wafers with GOLD
73	P-G0X	* Photolith mask KB86M-AG, LF Field: nom. 2.2μm resist of S1818 (for metal wet-etch)
74	P-RHBX	* Hardbake for wet etch of Au/Cr
75	X-0	General inspection stage: check resist coverage where the gold edges are - GOLD CONTAMINATED -
76	WM-0X	500nm Au layer (approx. 2 min./ check every 30 sec.) - Au etchant - WA#9-16
77	WM-0X	60nm Cr layer (approx. 30 sec./ check every 10 sec.) - Cr etchant - WA#9-16
78	X-0	General inspection stage: check if gold leads go beyond/out of the cavities - GOLD CONTAMINATED -
79	P-RSX	* FN Resist strip (for wafers with GOLD)
80	W-C3X	* Fuming Nitric Acid clean, wafers with GOLD
81	G-1	*Notebook page: Both following stages help to prevent to gold deteriorate during the bonding procedure
82	F7-0	* Furnace 7: Load in N2: Loading horizontal, 400°C, 60min., N2 GOLD CONTAMINATED
83	WH-D1X	Dip etch oxide, Wafers with GOLD. Dip etch, 20:1 BHF 25°C. Until just hydrophobic !!! check stubs again !!!
84	G-3	* Special Instructions: Anodically Bonding of silicon WA#1-8 and pyrex WA#9-16, EVG bonding
85	W-C3X	* Fuming Nitric Acid clean, wafers with GOLD 8 wafer sandwiches
86	D-A2X	Dry Resist Strip (use P-RS if possible) SRS GOLD ASHER !!! 5 min. only - check gold cavity afterwards !!!
87	W-C3X	* Fuming Nitric Acid clean, wafers with GOLD - 8 wafer sandwiches
88	P-G0X	* Photolith mask KB86M - AH, LF Field: nom. 2.2μm SPRT518 resist, Single Sided Alignment to front gold alignment mark (for dry 2nd DRIE in STS ASE)
89	X-0	General inspection stage - microscope inspection - GOLD CONTAMINATED -
90	P-RHBX	* Hardbake for SPRT518 2.2μm, 120min. at 140°C
91	X-0	General inspection stage - microscope inspection - GOLD CONTAMINATED -
92	DS-S0X	ASE Deep Silicon Etch Less than 200μm (No backing wafer required) Specify Depth: 60μm into silicon to release structure (overetch time required)
93	X-0	General inspection stage - microscope inspection - GOLD CONTAMINATED -
94	W-C3X	* Fuming Nitric Acid clean, wafers with GOLD
95	X-0	General inspection stage - microscope inspection and SEM only on one wafer - GOLD CONTAMINATED -
96	P-RGX	* Spin resist: Frontspin resist (to cover/protect structure during sawing) (for wafers with GOLD)
97	G-3	* Special Instructions: backing on hotplate to dry resist, afterwards sawing into chip size
98	W-C3X	* Fuming Nitric Acid clean, wafers with GOLD of individual chips
99	G-3	* Special Instructions: dry cleaning and mounting in DIP

J.3.2 Mask Layouts

The device fabrication of the *z* actuator requires a set of eight masks, which are listed in th table 3-1. All mask layouts are presented in the following and include enlarged figures of the actuation device.

Mask Number	Layer Number	Masking Layer
KB86M	AA	Cavity Mirror Mask
KB86M	AB	Gold Mirror Mask
KB86M	AC	Silicon Oxide Stubs Mask
KB86M	AD	Anchor Mask
KB86M	AE	Shallow Pyrex™ Cavity Mask
KB86M	AF	Deep Pyrex™ Cavity Mask
KB86M	AG	Metal Electrode Mask
KB86M	AH	Spring Mask

Table 10-1: Eight lithography masks are used for fabricating the *z* actuator of the 3D actuator.

Cavity Mirror Mask (KB86M-AA)

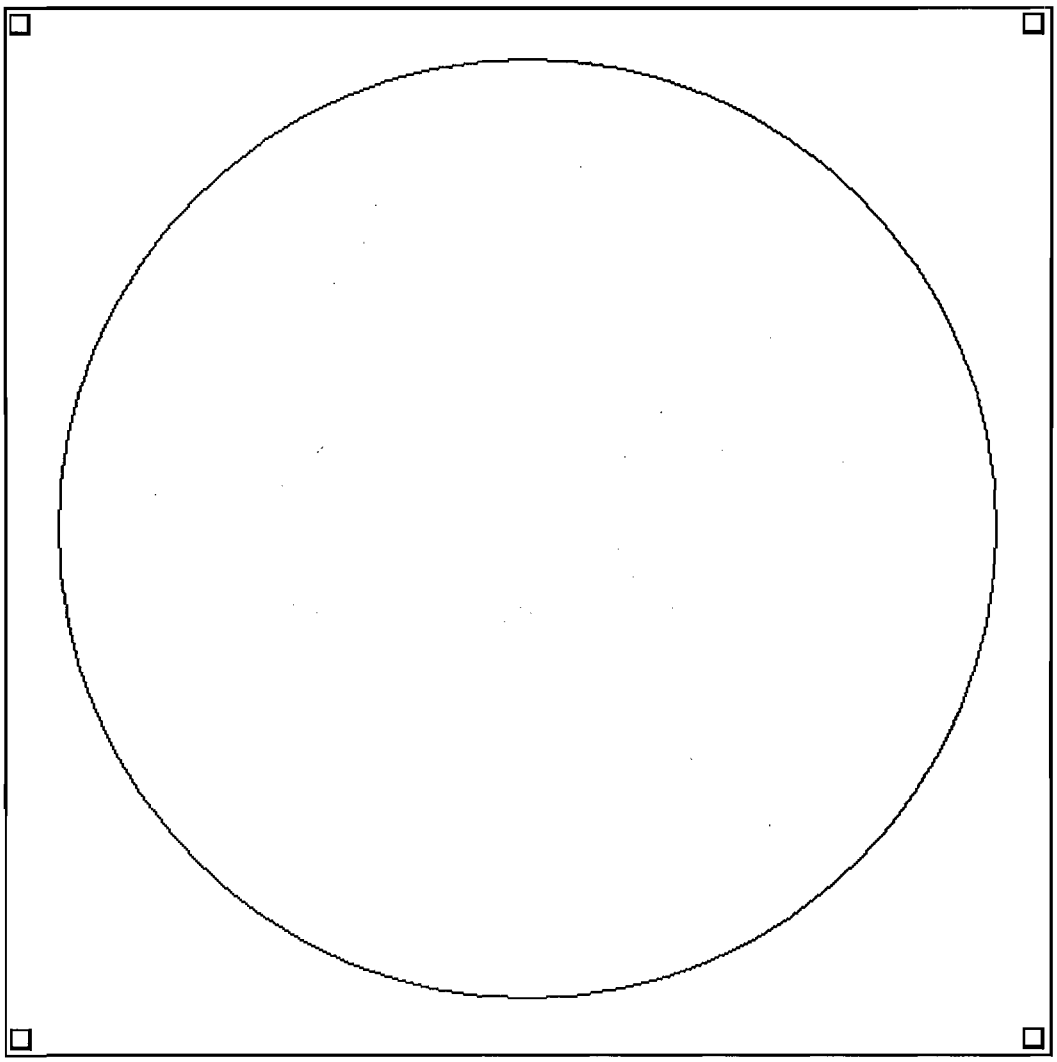

Figure J-8: The mask layout KB86M-AA of the *z* actuator with the cavity mirror structures (3D actuator). At this scale the structures are not visible.

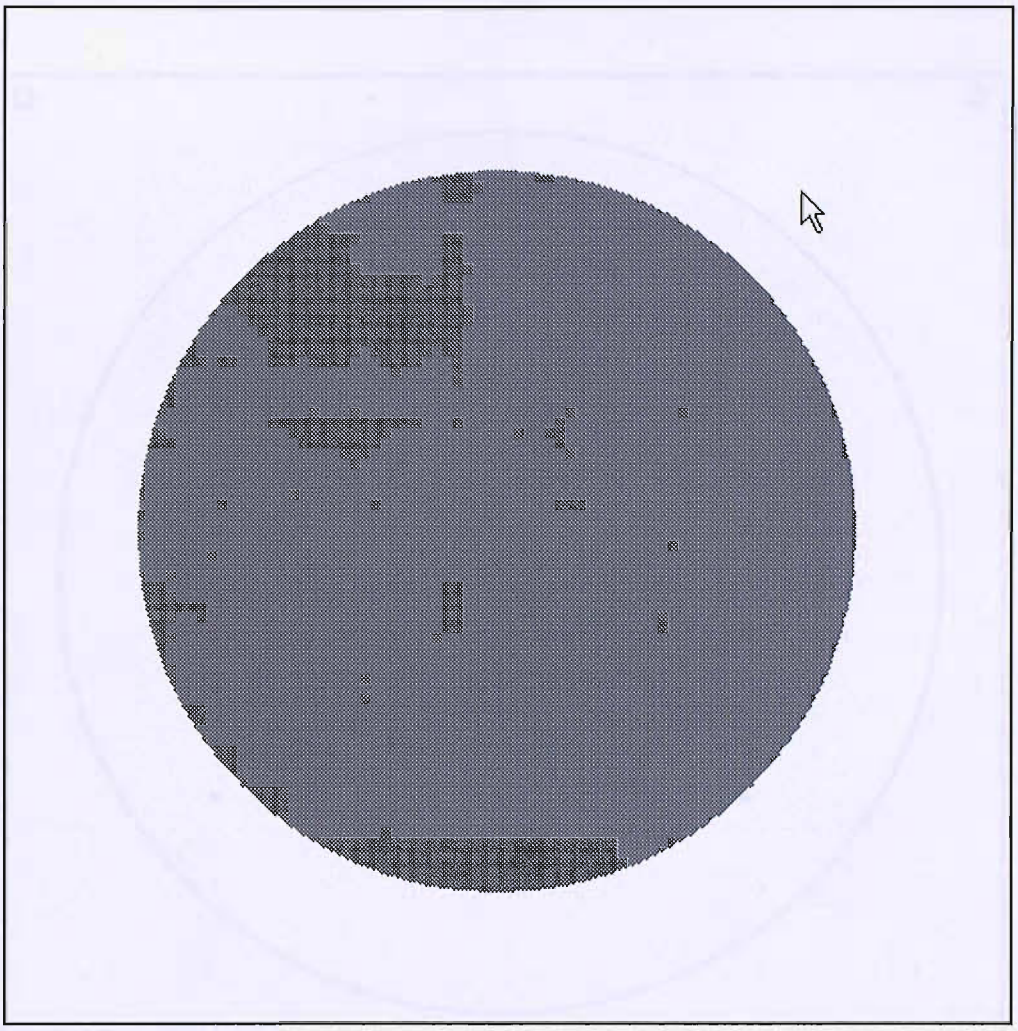

Figure J-9: Enlarged circular cavity mirror from figure C-8.

Gold Mirror Mask (KB86M-AB)

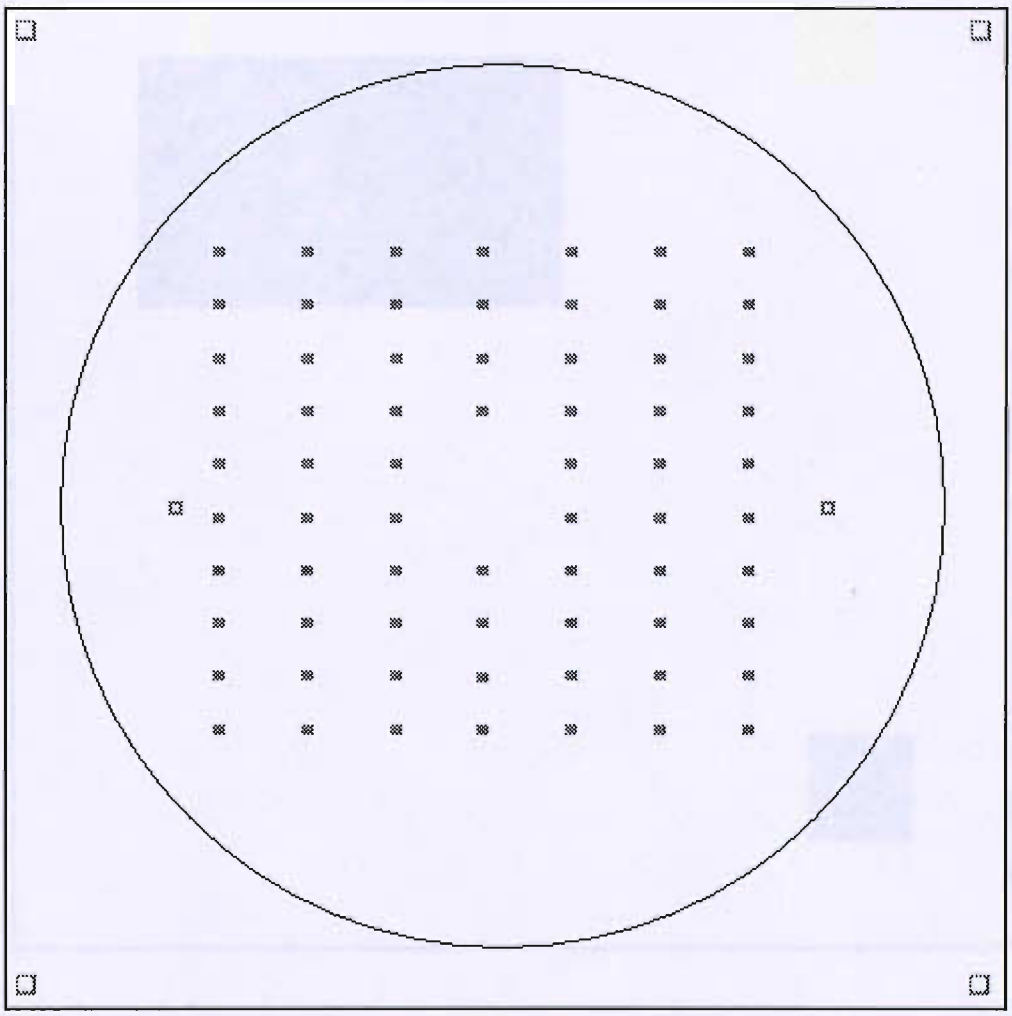

Figure J-10: The mask layout KB86M-AB of the *z* actuator with the gold mirror and bond pad structures (3D actuator).

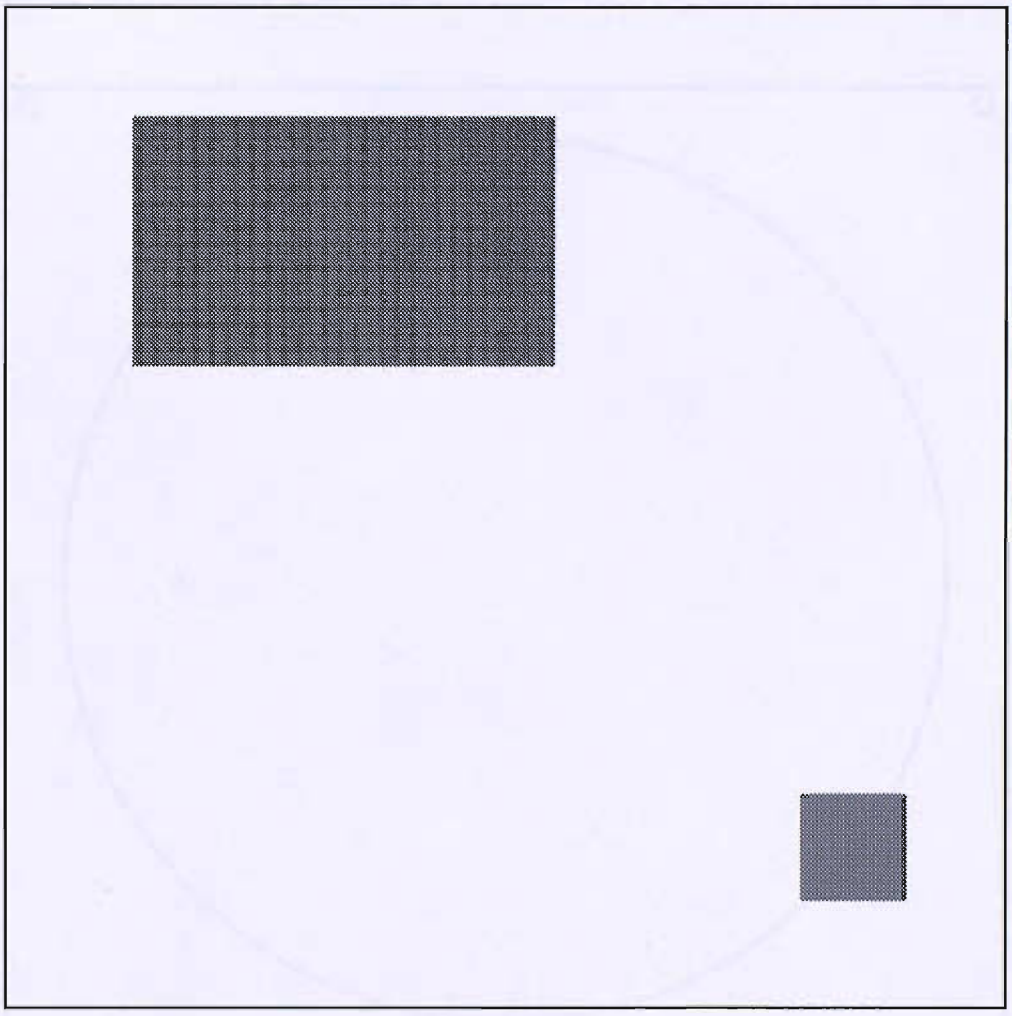

Figure J-11: The bond pad area (upper left corner) and the mirror structure (lower right corner) for one single actuator enlarged from figure C-10.

Silicon Oxide Stubs Mask (KB86M-AC)

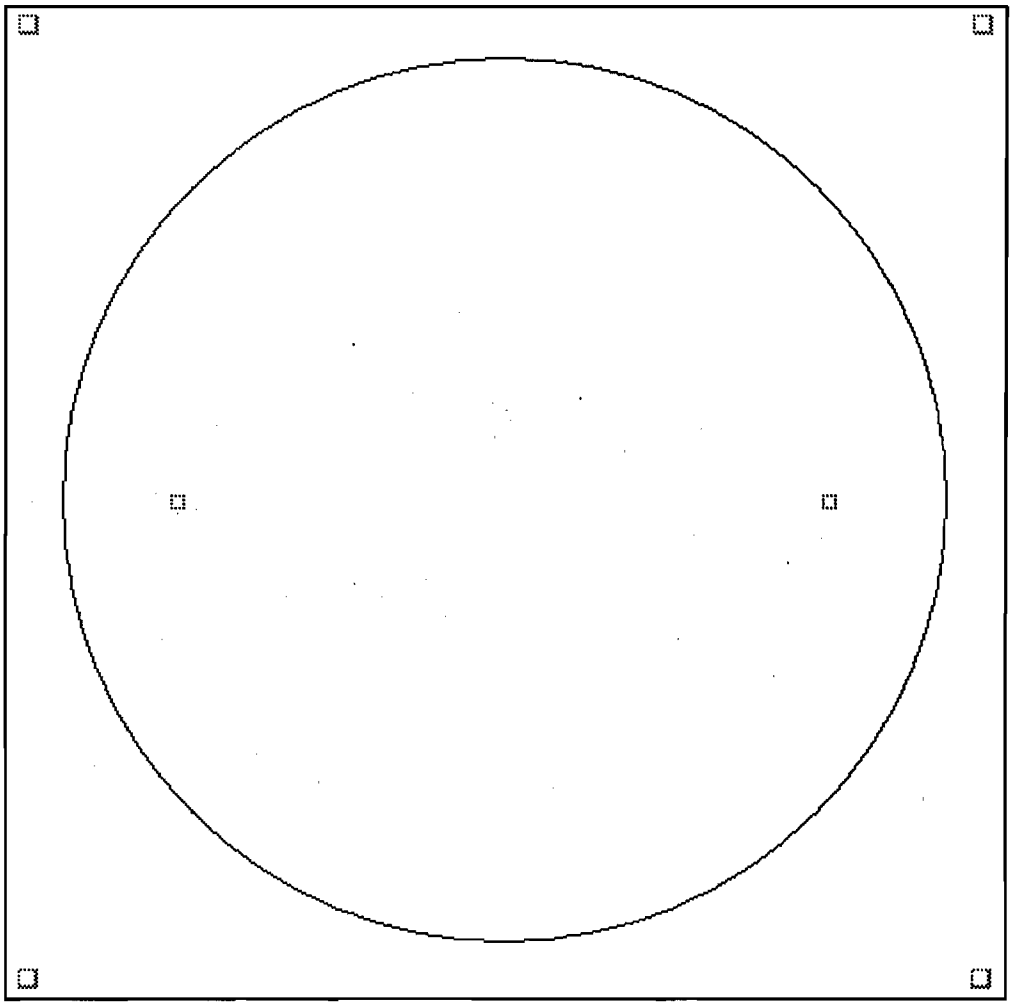

Figure J-12: The mask layout KB86M-AC of the *z* actuator with the silicon oxide stubs structures (3D actuator). At this scale the structures are not visible.

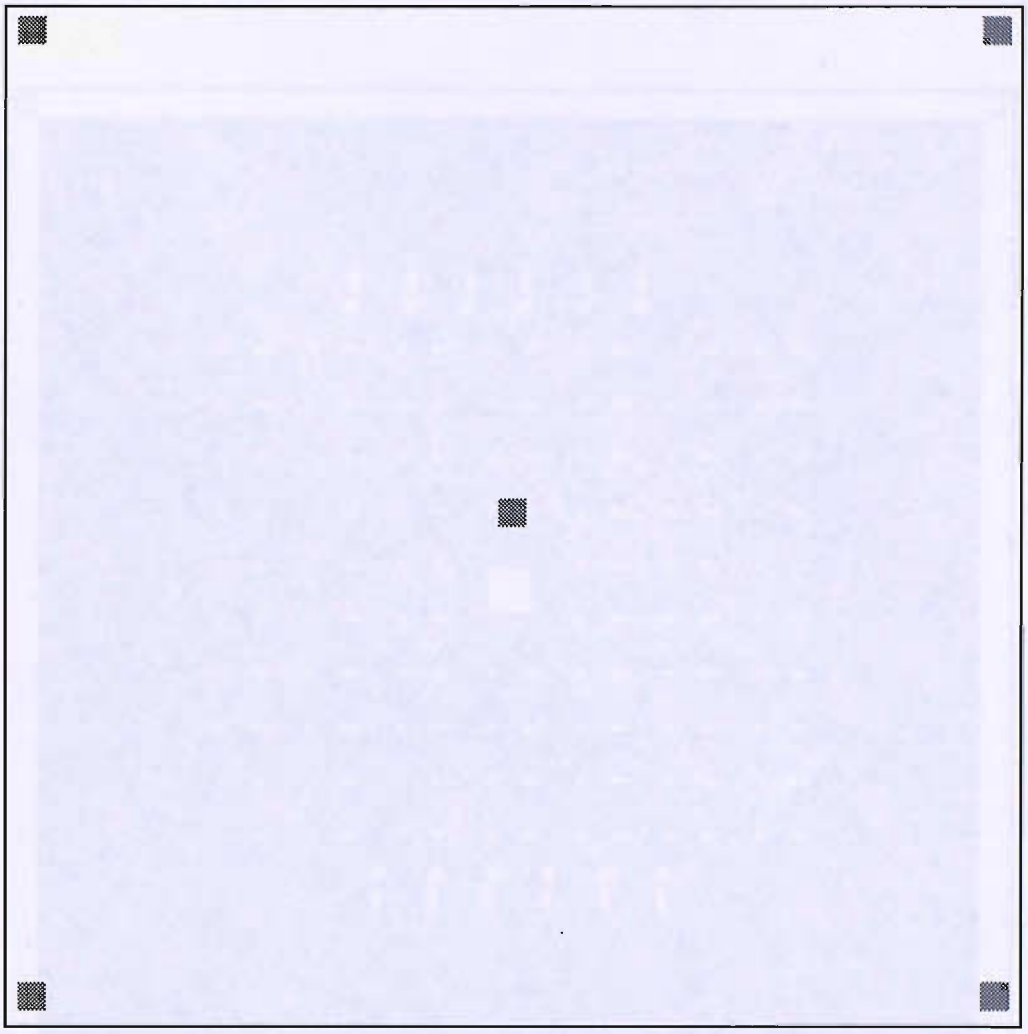

Figure J-13: Silicon oxide stubs of actuation electrode from one single *z* actuation device depicted and enlarged from figure C-12.

Anchor Mask (KB86M-AD)

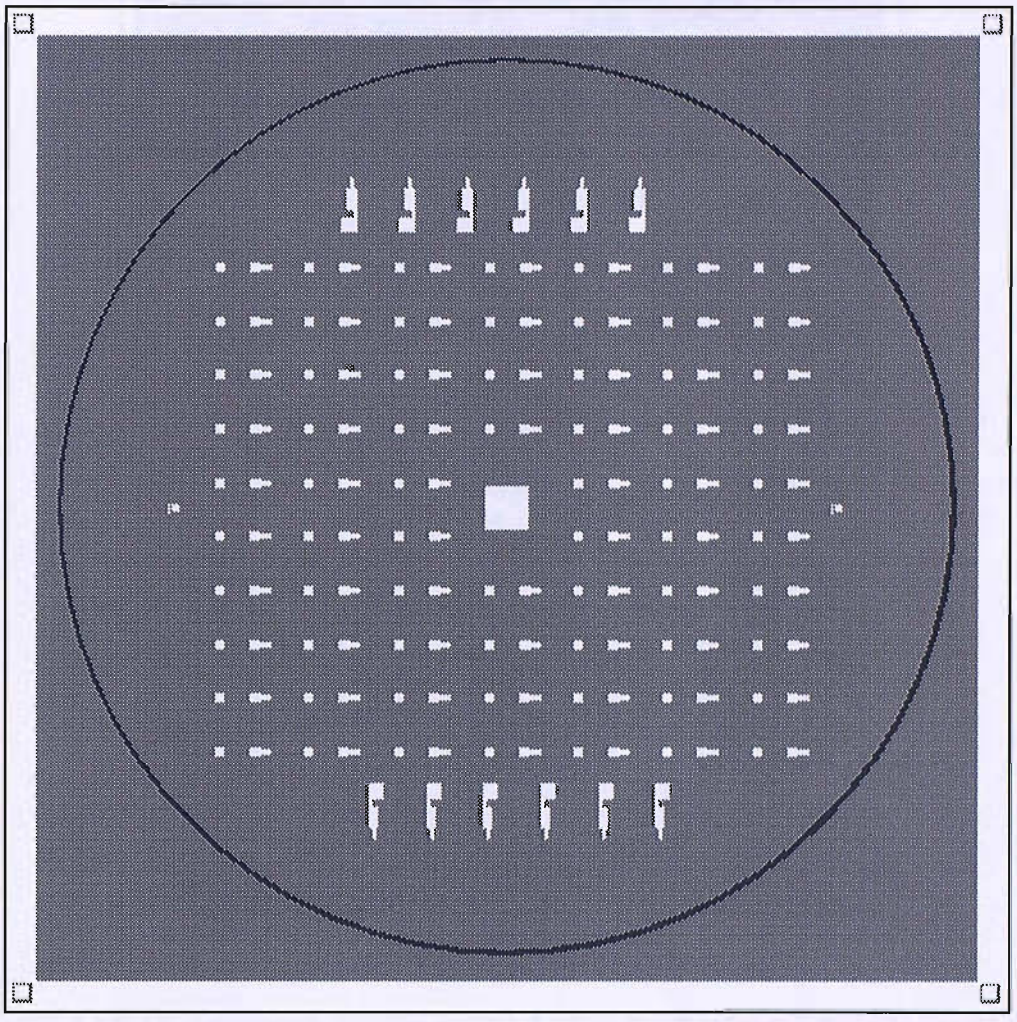

Figure J-14: The mask layout KB86M-AD of the *z* actuator with the anchor structures (3D actuator).

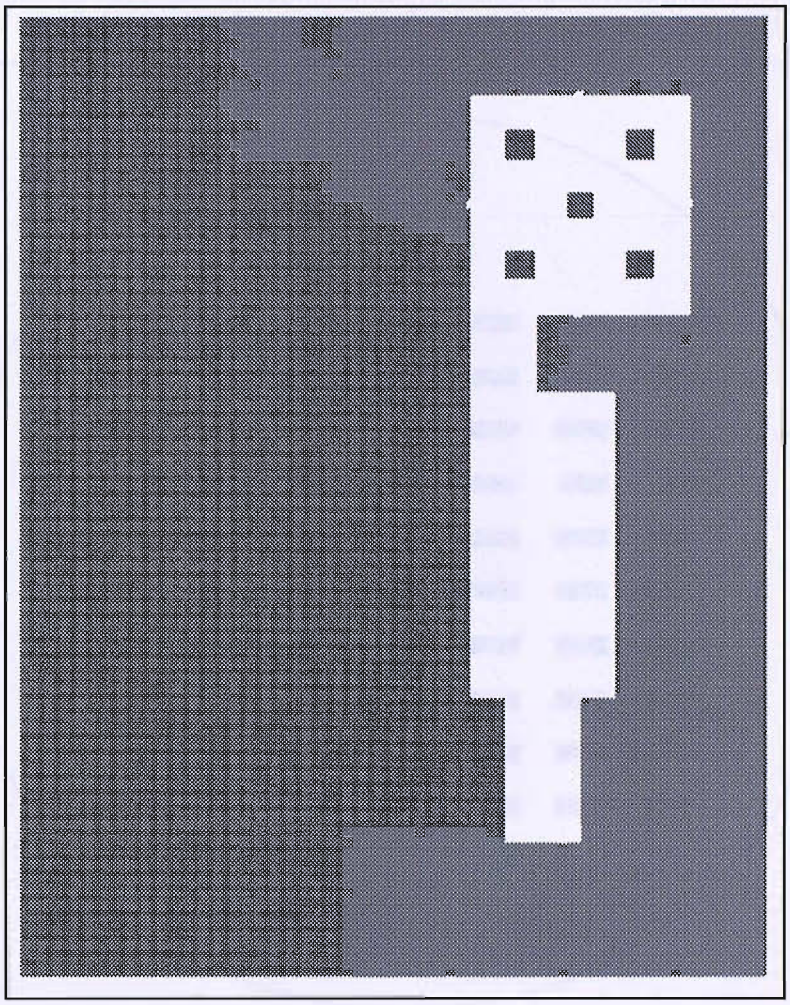

Figure J-15: One single *z* actuation device depicted and enlarged from figure C-14.

Shallow Pyrex™ Cavity (KB86M-AE)

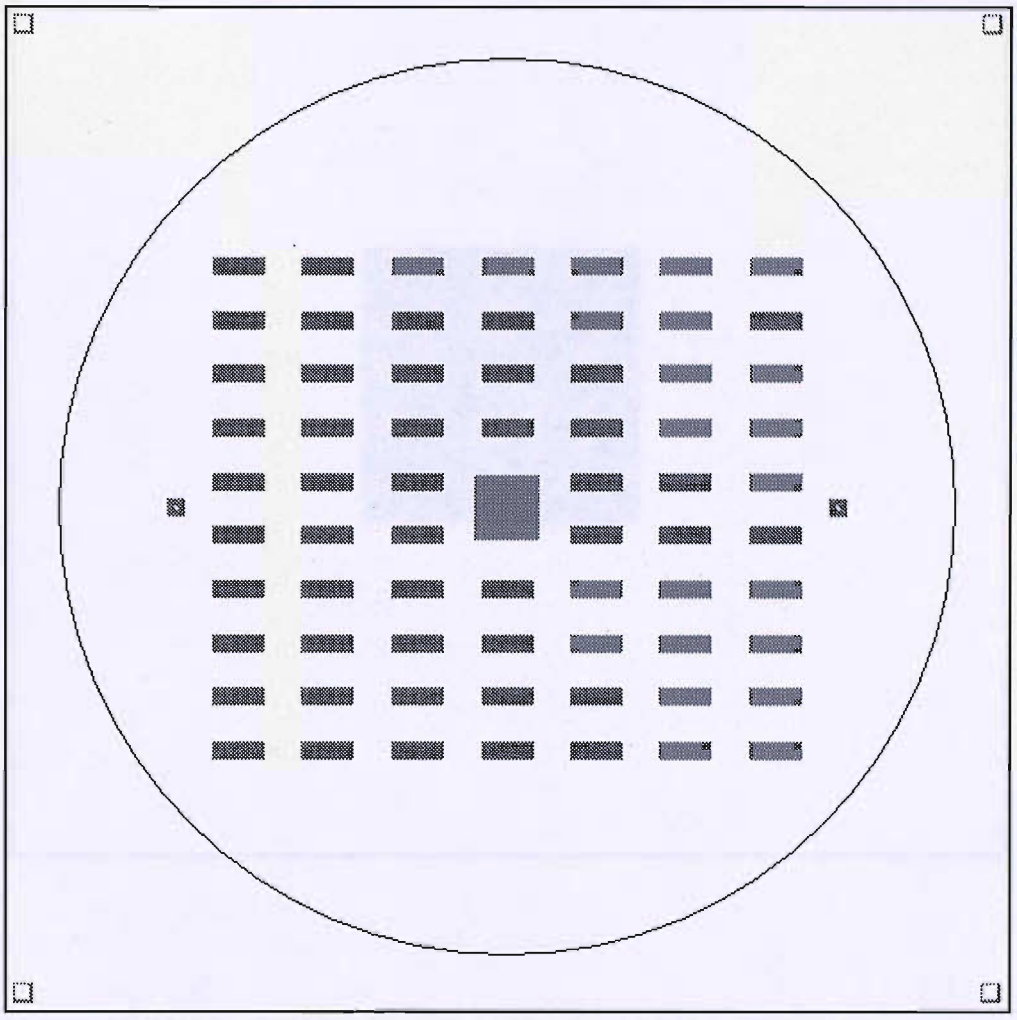

Figure J-16: The mask layout KB86M-AE of the *z* actuator with the 2.5 μm Pyrex™ cavity structures (3D actuator).

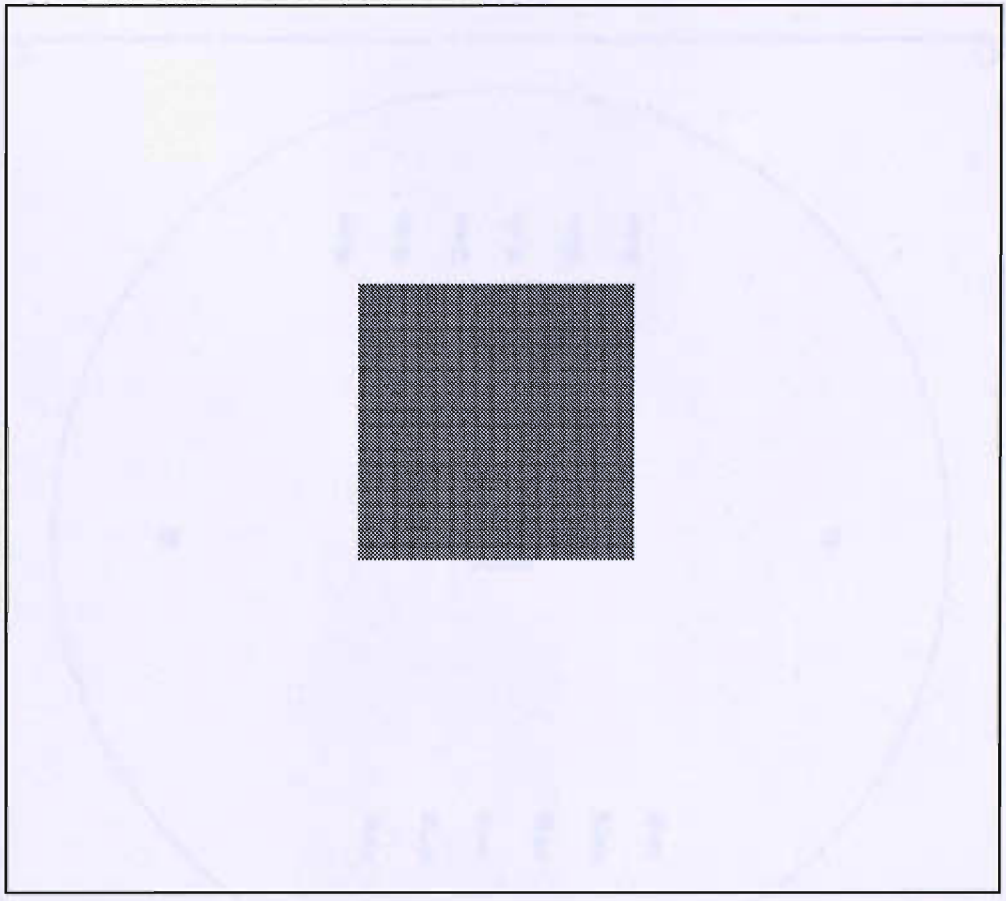

Figure J-17: One single *z* actuation device depicted and enlarged from figure C-16, showing the 2.5 μm Pyrex™ cavity area.

Deep Pyrex™ Cavity (KB86M-AF)

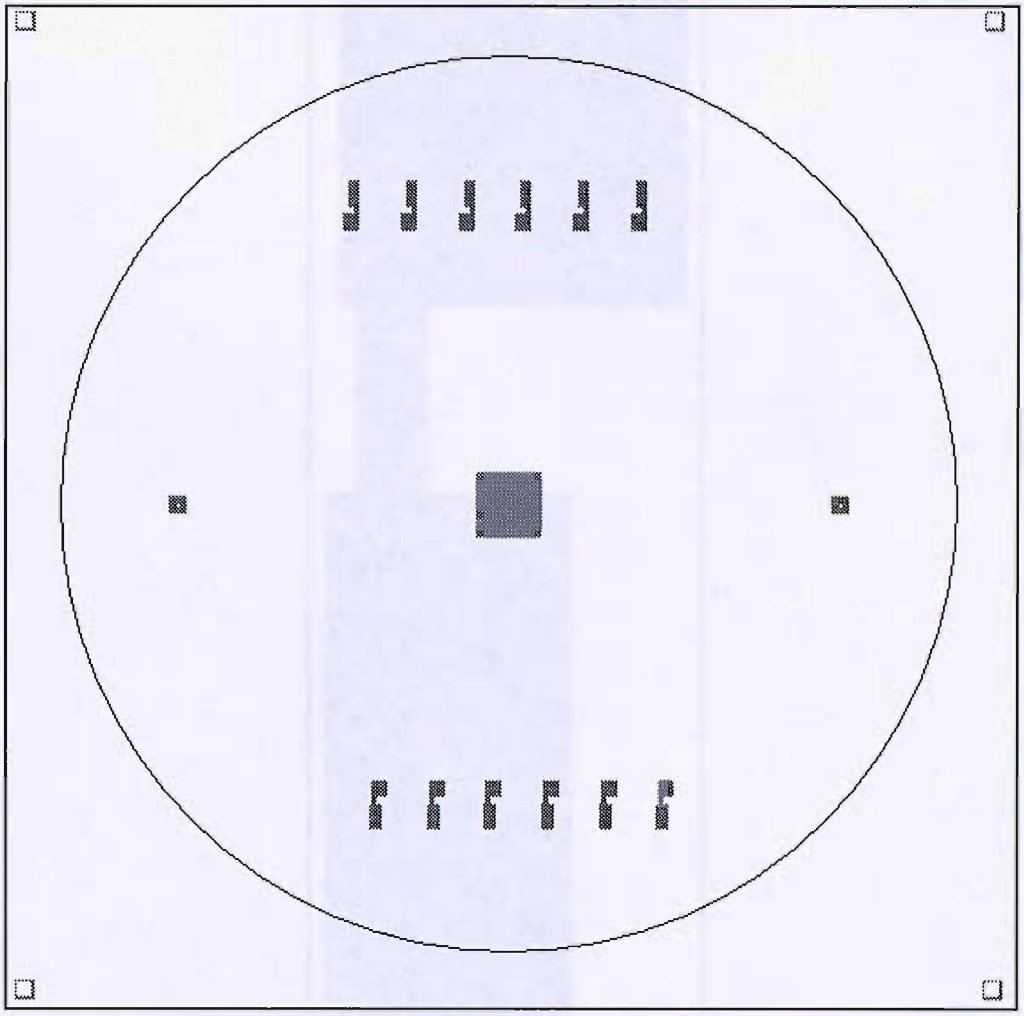

Figure J-18: The mask layout KB86M-AF of the *z* actuator with the 21 µm Pyrex™ cavity structures (3D actuator).

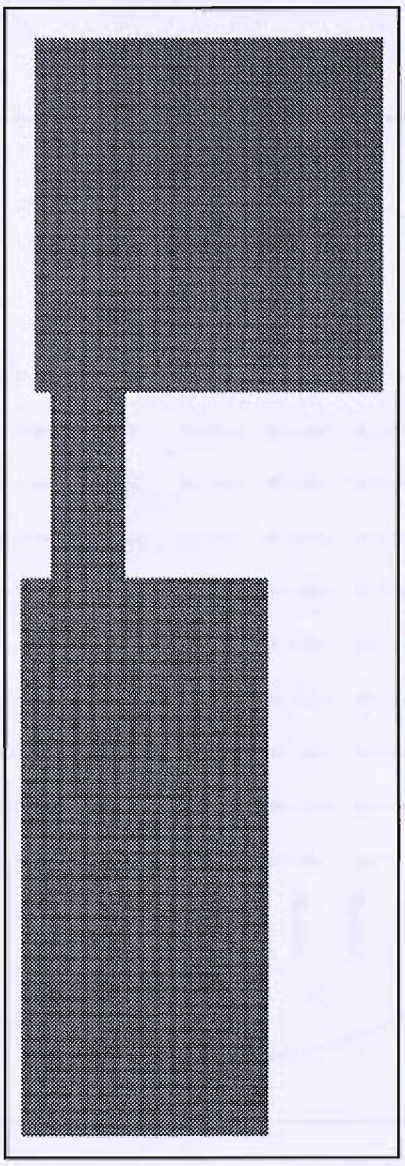

Figure J-19: One single *z* actuation device depicted and enlarged from figure C-18, showing the 21 μm Pyrex™ cavity area.

Metal Electrode Mask (KB86M-AG)

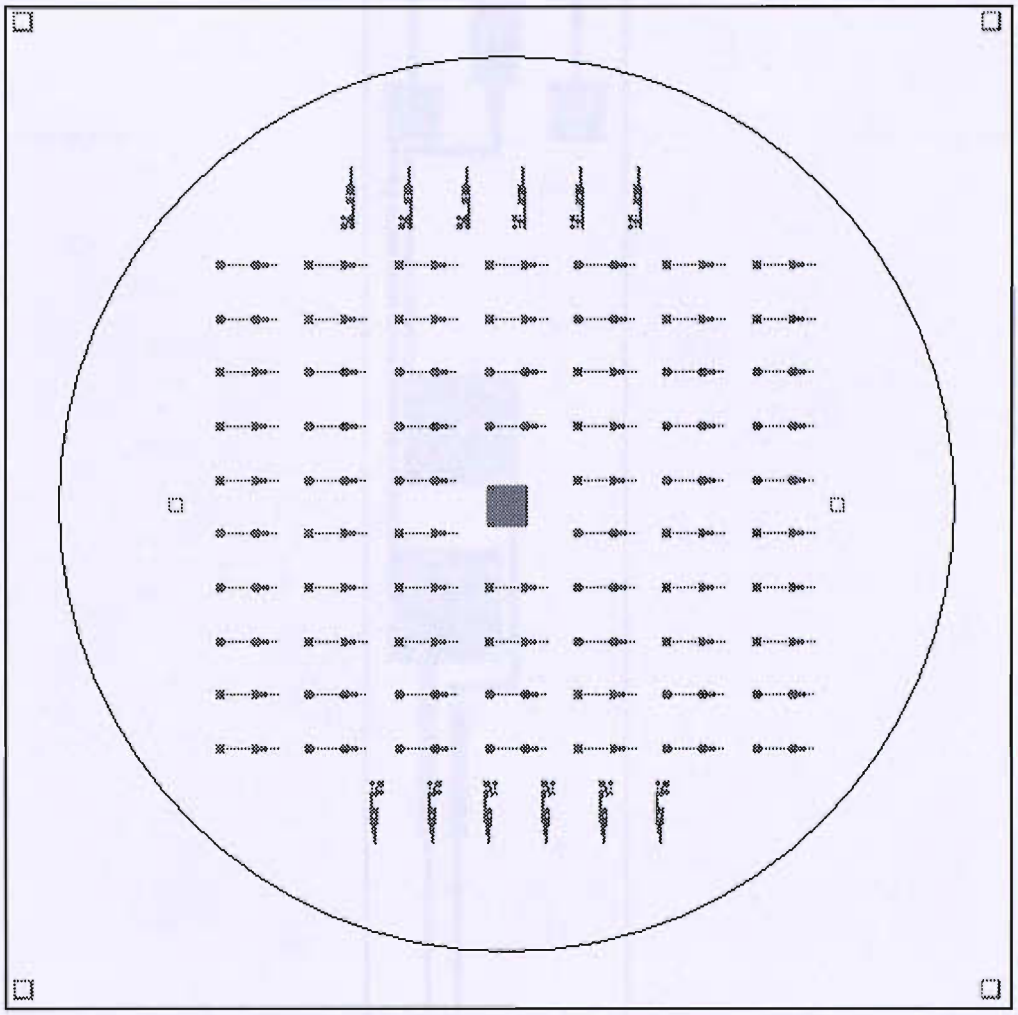

Figure J-20: The mask layout KB86M-AG of the *z* actuator with the metal electrode structures (3D actuator).

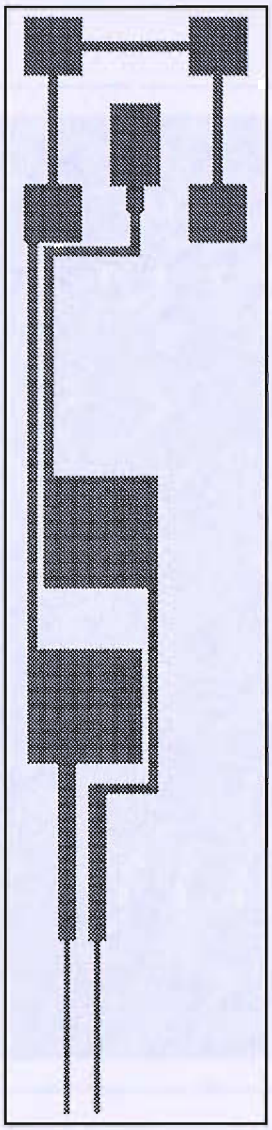

Figure J-21: One single *z* actuation device depicted and enlarged from figure C-20 showing the metal electrodes processed on the Pyrex™ wafer.

Spring Mask (KB86M-AH)

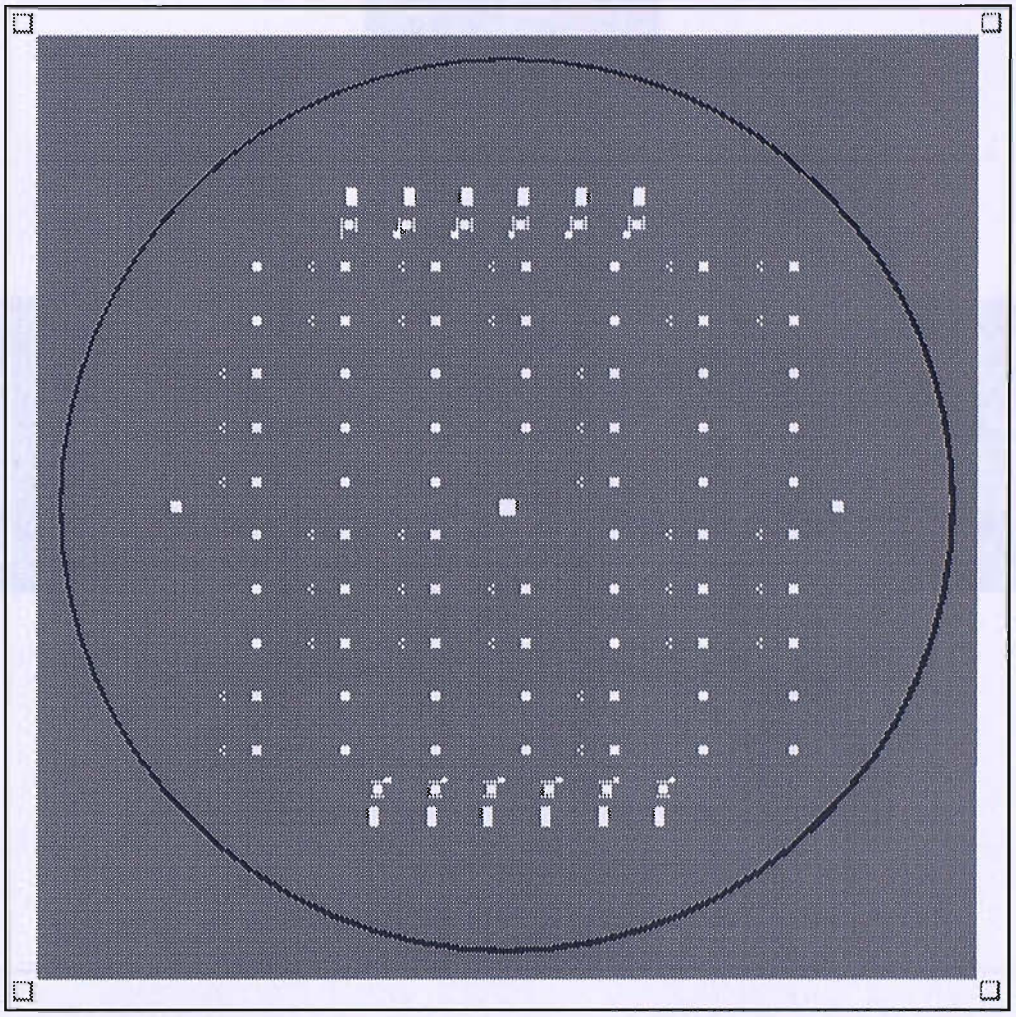

Figure J-22: The mask layout KB86M-AH of the *z* actuator with the spring structures (3D actuator).

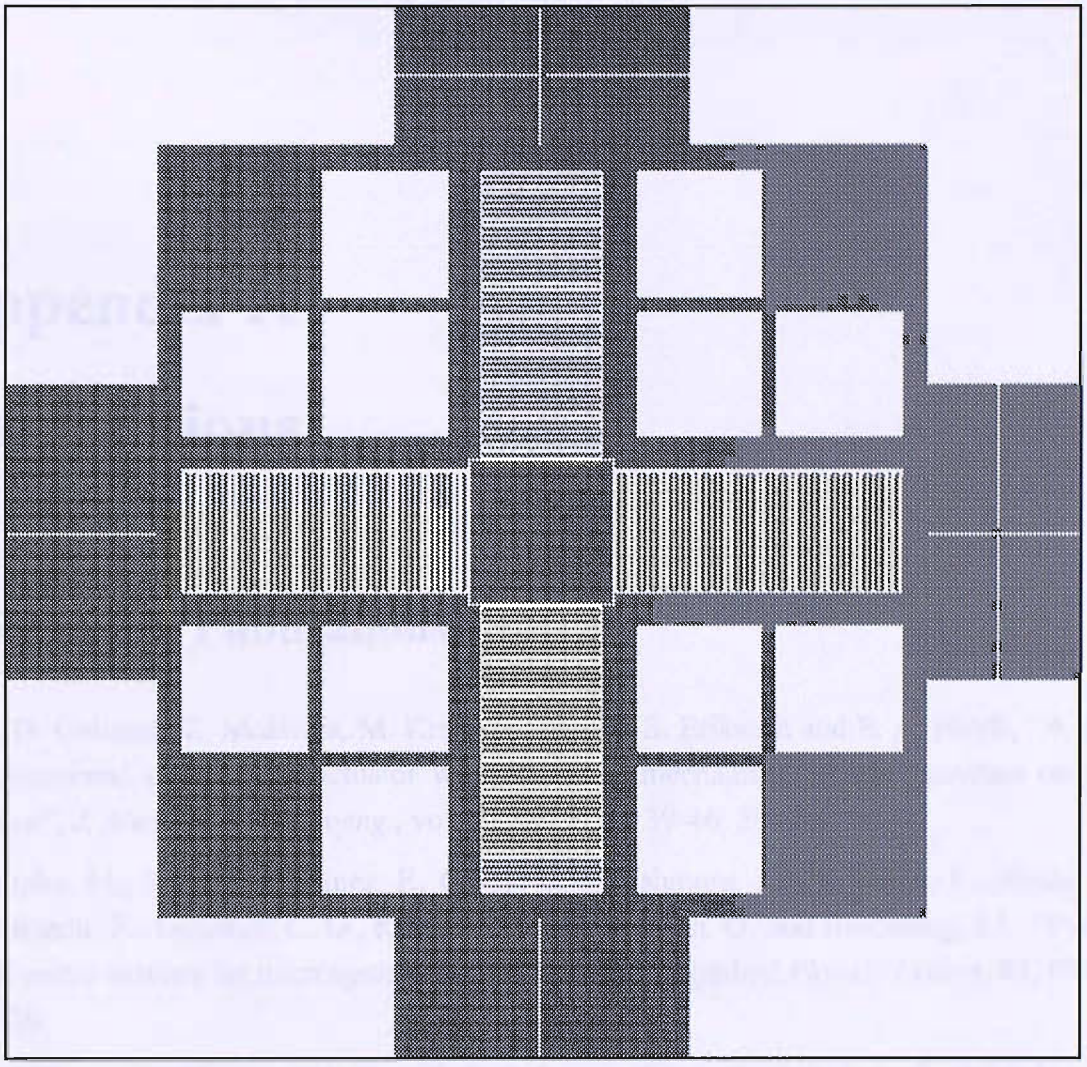

Figure J-23: One single *z* actuation device depicted and enlarged from figure C-22, showing the center mass suspended by the for meander springs.

Appendix K

Publications

K.1 Journal Publications

- C. O. Gollasch, Z. Moktadir, M. Kraft, M. Trupke, S. Eriksson and E. A. Hinds, "A three-dimensional electrostatic actuator with a locking mechanism for microcavities on atom chips", *J. Micromech. Microeng.*, vol. 15, no. 7, pp. 39-46, 2005.
- Trupke, M., Ramirez-Martinez, F., Curtis, E.A., Ashmore, J.P., Eriksson, S., Hinds, E.A. Moktadir, Z., Gollasch, C. O., Kraft, M., Vijaya Prakash, G., and Baumberg, J.J., "Pyramidal micro-mirrors for microsystems and atom chips", *Applied Physics Letters*, 88, 071116, 2006.
- S. Eriksson, M. Trupke, H.F. Powell, D. Sahagun, C.D.J. Sinclair, E.A. Curtis, B.E. Sauer, E.A. Hinds, Z. Moktadir, C.O. Gollasch and M. Kraft, "Integrated optical components on atom chips", *Eur. Phys. J. D (2005)*, vol. 35, no. 1, pp. 135-139, 2005.
- Y. Dong, M. Kraft, C. O. Gollasch and W. Redman-White, "A high-performance accelerometer with a fifth-order sigma–delta modulator", *J. Micromech. Microeng.*, vol. 15, no. 7, pp. 22-29, 2005.

K.2 Conference Publications

- C. O. Gollasch, Z. Moktadir, G. Lewis, M. Kraft, M. Trupke, S. J. Eriksson and E. A. Hinds, "Integration of a tuneable optical micro-cavity for single atom detection on an atom chip", *Proc. QELS 2007*, USA, May 2007.
- C. O. Gollasch, Z. Moktadir, G. Lewis, M. Kraft, M. Trupke, S. J. Eriksson and E. A. Hinds, "MEMS Actuators for aligning and tuning optical micro cavities on atom chips", *Proc. IET Seminar on MEMS Sensors and Actuators*, pp. 275-280, UK, May 2006.

- C. O. Gollasch, Z. Moktadir, G. Lewis, M. Kraft, M. Trupke, S. J. Eriksson and E. A. Hinds, "A one-dimensional electrostatic actuator for tuning optical cavities on atom chips", *Proc. MME 2005 Conference*, pp. 219-222, Sweden, Sept. 2005.
- C. O. Gollasch, Z. Moktadir, M. Kraft, D. Bagnall, M. Trupke, S. Eriksson, E. A. Hinds, "A three dimensional electrostatic actuator with a locking mechanism for microcavities on atom chips", *In Proceedings of 15th MicroMechanics Europe Workshop*, pp. 33-36, Leuven, Belgium 2004.
- C. O. Gollasch, Z. Moktadir, E. Koukharenko, M. Kraft, D. Bagnall, S. Eriksson, M. Trupke and E. A. Hinds, "Integration of a two-dimensional electrostatic actuator in a new generation of atom chips", *In Proceedings of Eurosensors XVIII*, pp. 23-26, Rome, Italy 2004.
- G. Lewis, Z. Moktadir, C. O. Gollasch, M. Trupke, F. Ramirez-Martinez, J. P. Ashmore, E. A. Hinds and M. Kraft, "Fabrication of patterned pyramidal micromirrors and current carrying wires for atom chips", *Proc. MME 2007 Conference*, pp. 183-186, Portugal, Sept. 2007.
- G. Lewis, Z. Moktadir, C. O. Gollasch, M. Kraft, M. Trupke, S. J. Eriksson and E. A. Hinds, "Fabrication of gold wires for atom chips by electrochemical deposition: a comparative study", *Proc. MME 2005 Conference*, pp. 56-59, Sweden, Sept. 2005.
- H.A. Rouabah, C.O. Gollasch and M. Kraft, "Design Optimisation of an Electrostatic MEMS Actuator with Low Spring Constant for an 'Atom Chip'" , *Technical Proceedings of the 2005 Nanotechnology Conference and Trade Show*, vol. 3, pp. 489-492, Anaheim, USA 2005.
- Z. Moktadir, G. V. Prakash, E. Koukharenko, C. O. Gollasch, D. Bagnall, M. Kraft, E. A. Hinds and J. Baumberg, "Fabrication of miromirrors with pyramidal shape using anisotropic etching of silicon with KOH", *In Proceedings of CLEO/IQEC 2004*, San Francisco, California, USA, 2004.
- Y. Dong, M. Kraft and C. O. Gollasch, "A High performance accelerometer with fifth-order Sigma-Delta Modulator", *In Proceedings of 15th MicroMechanics Europe Workshop*, pp. 41-44, Leuven, Belgium 2004.

References

[1] LG Electronics - www.misoblg-elite.com.

[2] E.A. Hinds and I.G. Hughes,"Magnetic atom optics: mirrors, guides, traps, and chips for atoms", *Journal of Physics D: Applied Physics*, vol. 32, R119, 1999.

[3] W. Haensel, P. Hommelhoff, T. W. Haensch, and J. Reichel, "Bose–Einstein condensation on a microelectronic chip", *Nature*, vol. 413, pp498-502, 2001.

[4] H. Ott, J. Fortagh, G. Schlotterbeck, A. Grossmann, and C. Zimmermann, "Bose-Einstein Condensation in a Surface Microtrap", *Physical Review Letter*, vol. 87, no. 23, A230401, 2001.

[5] R. Folman, T. Calarco, J. Schmiedmayer, "Quantum information processing with neutral atoms on an atom chip", *Journal of Modern Optics*, vol. 49, no. 8, pp1375-1388, 2002.

[6] M. Trupke, J. Metz, A. Beige, and E. A. Hinds, "Towards quantum computing with single atoms and optical cavities on atom chips", arXiv:quant-ph/0607197v1, 2005.

[7] P. Horak, B.G. Klappauf, P. Kazansky, "Single-atom detection by micro-cavities", *CLEO/Europe - EQEC 2003*, Munich 22-27 Jun. 2003.

[8] A. Kuhn, M. Hennrich, and G. Rempe, "Deterministic Sinlge-Photon Source for Distributed Quantum Networking", *Physical Review Letter*, vol. 89, no. 6, A067901, 2002.

[9] J. McKeever, A. Boca, A. D. Boozer, R. Miller, J. R. Buck, A. Kuzmich, and H. J. Kimble, "Deterministic Generation of Sinlge Photons from One Atom Trapped in a Cavity", *Science*, vol. 303, pp. 1992-1994, 2004.

[10] D. P. DiVincenzo, "The Physical Implementation of Quantum Computation", Fortschritte der Physic, vol. 48, pp.771-783, 2000.

[11] M.H. Anderson, J. R. Ensher, M. R. Matthews, C. E. Wieman and E. A. Cornell, "Observation of Bose-Einstein Condensation in a Dilute Atomic Vapor", *Science*, vol. 269, no. 5221, pp. 198-201, 1995.

[12] Jenny Hogan, "Computing: Quantum bits and silicon chips", *Nature*, vol. 424, pp 484-486, 2003.

[13] C. Monroe, "Quantum information processing with atoms and photons ", *Nature*, vol. 416, pp. 238-246, 2002.

[14] P. Walther, K. J. Resch, T. Rudolph, E. Schenck, H. Weinfurter, V. Vedral, M. Aspelmeyer, A. Zeilinger, "Experimental one-way quantum computing", *Nature*, vol. 434, pp. 169-176, 2005.

[15] M. H. Andersin, J. R. Ensher, M. R. Matthews, C. E. Wieman, E. A. Cornell, "Observation of Bose-Einstein Condensation in a Dilute Atomic Vapor", *Science*, vol. 269, pp. 198-201, 1995.

[16] J. D. Weinstein and K. G. Libbrecht, " Microscopic magnetic traps for neutral atoms", *Physical Review Letter*, vol. 52, no. 8, pp. 4004-4009, 1995.

[17] J. Fortagh, A. Grossmann, and C.Zimmermann, "Miniaturized Wire Trap for Neutral Atoms", *Physical Review Letter*, vol. 81, no. 24, pp. 5310-5313, 1998.

[18] J. Denschlag, D. Cassettari and Joerg Schmiedmayer, "Guiding Neutral Atoms with a Wire", *Physical Review Letter*, vol. 82, no. 10, pp. 2014-2017, 1999.

[19] J. Reichel, W. Haensel, and T. W. Heansch, "Atomic Micromanipulation with Magnetic Surface Traps", *Physical Review Letter*, vol. 83, no. 17, pp. 3398-3401, 1999.

[20] R. Folman, P. Krüger, D. Cassettari, B. Hessmo, T. Maier, and J. Schmiedmayer, "Controlling Cold Atoms using Nanofabricated Surfaces: Atom Chips", *Physical Review Letter*, vol. 84, no.20, pp4749–4752, 2000.

[21] D. Cassettari, B. Hessmo, R. Folman, T. Maier, J. Schmiedmayer, "A Beam Splitter for Guided Atoms on an Atom Chip", *Physical Review Letter*, vol. 85, no. 26, pp. 5483-5487, 2000.

[22] D. Mueller, E. A. Cornell, M. Prevedelli, P. D. D. Schwindt, A. Zozulya, D. Z. Anderson, "Waveguide atom beam splitter for laser-cooled neutral atoms", *Optics Letters*, vol. 25, no. 18, pp. 1382-1384, 2000.

[23] W. Haensel, J Reichel, P. Hommelhoff, T. W. Haensch, "Magnetic Conveyer Belt for Transporting and Merging Trapped Atom Clouds", *Physical Review Letter*, vol. 86, no. 4, pp. 608-611, 2001.

[24] E. A. Hinds, C. J. Vale, M. G. Boshier, "Two-Wire Waveguide and Interferometer for Cold Atoms", *Physical Review Letter*, vol. 86, no. 8, pp. 1462-1465, 2001.

[25] W. Haensel, J. Reichel, P. Hommelhoff, T. W. Haensch, "Trapped-atom interferometer in a magnetic microtrap", *Physical Review A*, vol. 64, A063607, 2001.

[26] E. Andersson, T. Calarco, R. Folman, M. Andersson, B. Hessmo, and J. Schmiedmayer, "Multimode Interferometer for Guided Matter Waves", *Physical Review Letter*, vol. 88, no. 10, A100401, 2002.

[27] Y.J. Wang, D. Z. Anderson, V. M. Bright, E. A. Cornell, Q. Diot, T. Kishimoto, M. Prentiss, R. A. Saravanan, S. R. Segal and S. Wu, "An Atom Michelson Interferometer on a Chip Using a Bose-Einstein Condensate", *Physical Review Letter*, vol. 94, A090405, 2005.

[28] S. Eriksson, F. Ramirez-Martinez, E. A. Curtis, B. E. Sauer, P. W. Nutter, E. W. Hill, E. A. Hinds, "Micron-sized atom traps made from magneto-otical thin films", *Applied Physics B: Laser and Optics*, vol. 79, no. 7, pp. 811-816, 2004.

[29] M. Boyd, E. W. Streed, P. Medley, G. K. Campbell, J. Mun, W. Ketterle, D. E. Pritchard, "Atom trapping with a thin magentic film", cond-mat/0608370, 2006.

[30] P. Krueger, X. Luo, M. W. Klein, K. Brugger, A. Haase, S. Wildermuth, S. Groth, I. Bar-Joseph, R. Folman, J. Schmiedmayer, "Trapping and Manipulating Neutral Atoms with Electrostatic Fields", *Physical Review Letter*, vol. 91, no. 23, A233201, 2003.

[31] G. Birkl, F. B. J. Buchkremer, R. Dumke, W. Ertmer, "Atom optics with microfabricated optical elements", *Optics Communications*, vol. 191, pp. 67-81, 2001.

[32] I. Teper, Y. J. Lin, V. Vuletic, "Resonator-Aided Single-Atom Detection on a Microfabricated Chip", *Physical Review Letter*, vol. 97, A023002, 2006.

[33] A. Haase, B. Hessmo, J. Schmiedmayer, "Detecting magnetically guided atoms with an optical cavity", *Optics Letters*, vol. 31, no. 2, pp. 268-270, 2006.

[34] P. Horak, B. G. Klappauf, A. Haase, R. Folman, J. Schmiedmayer, P. Domokos, E. A. Hinds, "Possibility of single-atom detection on a chip", *Physical Review*, vol. 67, A043806, 2003.

[35] P. A. Quinto-Su, M. Tscherneck, M. Holmes, N. P. Bigelow, "On-chip optical detection of laser cooled atoms", *Optics Express*, vol. 12., no. 21, pp. 5098-5103, 2004.

[36] M. Wilzbach, A. Haase, M. Schwarz, D. Heine, K. Wicker, S. Groth, T. Fernholz, B. Hessmo, J. Schmiedmayer, "Detecting Neutral Atoms on an Atom Chip", *Fortschritte der Physik*, vol. 54, no. 8-10, pp. 746-764, 2006.

[37] S. Eriksson, M. Trupke, H.F. Powell, D. Sahagun, C.D.J. Sinclair, E.A. Curtis, B.E. Sauer, E.A. Hinds, Z. Moktadir, C.O. Gollasch and M. Kraft, "Integrated optical components on atom chips", *Eur. Phys. J. D*, vol. 35, pp. 135-130, 2005.

[38] T. Steinmetz, Y. Colombe, D. Hunder, T. W. Haensch, A. Balocchi, R. J. Warburton, J. Reichel, "Stable fibre-based Fabry-Perot cavity", *Applied Physics Letter*, vol. 89, A111110, 2006.

[39] M. Trupke, E. A. Hinds, S. Eriksson, E. A. Curtis, Z. Moktadir, E. Kukharenka, M. Kraft, "Microfabricated high-finesse optical cavity with open access and small volume", *Applied Physics Letter*, vol. 87, A211106, 2005.

[40] M. Trupke, F. Ramirez-Martinez, E. A. Curtis, J. P. Ashmore, S. Eriksson, E. A. Hinds, Z. Moktadir, C. Gollasch, M. Kraft, G. V. Prakash, J. J. Baumberg, "Pyramidal micromirros for microsystems and atom chips", *Applied Physics Letter*, vol. 88, A071116, 2006.

[41] D. K. Armani, T. J. Kippenberg, S. M. Spillane, K. J. Vahala, "Ultra-high-Q toroid microcavity on a chip", *Nature*, vol. 421, pp. 925-928, 2003.

[42] M. Rosenblit, P. Horak, S. Helsby, R. Folman, "Singel-atom detection using whispering-gallery modes of microdisk resonators", *Physical Review A*, vol. 70, no. 5, A053808, 2004.

[43] M. Trupke, J. Metz, A. Beige, and E. A. Hinds, "Towards quantum computing with single atoms and optical cavities on atom chips", *arXiv:quant-ph/0607197*, 2006.

[44] T. Aoki, B. Dayan, E. Wilcut, W. P. Bowenb, A. S. Parkins, and H. J. Kimble, "Observation of Strong Coupling between One Atom and a Monolithic Microresonator", *arXiv:quant-ph/0606033*, 2006.

[45] T. Shimizu, H. Tokumoto, "Single Atom Detection on a Tungsten Tip", *Japan Journal Applied Physics*, vol. 38, pp. 3860-3862, 1999.

[46] S. Hoekstra, A. K. Mollema, R. Morgenstern, H. W. Wilschut, R. Hoekstra, "Single-atom detection on calcium isotopes by atom-trap trace analysis", *Physical Review A*, vol. 71, A023409, 2005.

[47] W. H. Oskay, S. A. Diddams, E. A. Donley, T. M. Fortier, T. P. Heavner, L. Hollberg, W. M. Itano, S. R. Jefferts, M. J. Delaney, K. Kim, F. Levi, T. E. Parker, J. C. Bergquist, "Single-Atom Optical Clock with High Accuracy", *Physical Review Letters*, vol. 97, A020801, 2006.

[48] ANSI/IEEE. *IEEE Standard on Piezoelectricity*, 1987. Std. 176.

[49] M. Koch, N. Harris, R. Maas, A. G.-R. Evans, N. M. White and A. Brunnschweiler, "A novel micropump design with thick-film piezoelectric actuation", *Meas. Sci. Technol.*, vol. 8, pp. 49-57, 1997.

[50] S.-J. Kim, C.-Y. Kang, J.-W. Choi, D.-Y. Kim, M.-Y. Sung, H.-J. Kim and S.-J. Yoon, "Properties of piezoelectric actuator on silicon membrane, prepared by screen printing method", *Materials Chemistry and Physics,* available online 22 November 2004.

[51] R. Bindig and G. Helke, "Application of piezoceramic multilayer actuators, experiences and solutions", *International Conference on New Actuators*, ACTUATOR, Bremen, Germany, June 2000.

[52] S. Konishi, K. Ohno, M. Muenchika, "Parallel linear actuator system with high accuracy and large stroke", *Sensors and Actuators A*, vol. 97-98, pp. 610-619, 2002.

[53] R. Yokokawa, T. Saika, T. Nakayama, H. Fujita, S. Konishi," Picoliter Controllable Syringes Driven By Parallel Motions of Electrostatic Controlled Linear Inchworm Actuator", *MEMS 2006*, Istanbul, Tuerkey, 22-26th January 2006.

[54] L. Qingquan, H. Qing-An, "Micro-electro-mechanical digital-to-analog converter based on a novel bimorph thermal actuator", *Sensors 2002, Proceedings of IEEE*, vol. 2, pp. 1036-1041, June 2002.

[55] A. Mohamed, H. Elsimar, M. Ismail, "Analysis, and optimization of a CMOS vertical thermal actuator", *Design, Test, Integration and Packaging of MEMS/MOEMS 2003*, pp.214-217, May 2003.

[56] H. Sehr, A. G.-R. Evans, A. Brunnschweiler, G. J. Ensell and T. E.-G. Niblock," Fabrication and test of thermal vertical bimorph actuators for movement in the wafer plane", *J. Micromech. Microeng.*, vol.11, no. 4, pp. 306-310, 2001.

[57] L. Que, J.-S. Park, Y.-B. Gianchandani, "Bent-beam electro-thermal actuators for high force applications", *MEMS '99. Twelfth IEEE International Conference*, pp.31-36, 1999.

[58] M. L. Sinclair, "A high force low area MEMS thermal actuator", *Thermal and Thermomechanical Phenomena in Electronic Systems, ITHERM 2000*, vol. 1, pp.127-132, 2000.

[59] R. Hickey, D. Sameoto, T. Hubbard and M. Kujath," Time and frequency response of two-arm micromachined thermal actuators", *J. Micromech. Microeng.*, vol. 13., pp.40-46, 2003.

[60] W.-C. Chen, J. Hsieh, W. Fang," A novel single-layer bi-directional out-of-plane electrothermal microactuator", *Micro Electro Mechanical Systems (MEMS),* The Fifteenth IEEE International Conference, pp. 693-697, Januar 2002.

[61] Y. Lai, J. Donald, M. Kujath and T. Hubbard," Force, deflection and power measurements of toggled microthermal actuators", *J. Micromech. Microeng.*, vol. 14, pp. 49-56, 2004.

[62] S. H. Lim, J. Choi, R. Horowitz, A. Majumdar," Design and Fabrication of a Novel Bimorph Microoptomechanical Sensor", *J. Micromech. Microeng.*, vol. 14, pp. 683-690, 2005.

[63] S. T. Todd, A. Jain, H. Qu, H. Xie," A 3-D Micromirror Utilizing Inverted-Series-Connected Electrothermal Bimorph Actuators for Piston and Tilt Motion", *Proceedings of the Particle Accelerator Conference*, 2005.

[64] I. Z. Abidine, M. Okoniewski, J. G. McRory," RF MEMS Tunable Inductor Using Bimorph Microactuators", *Proceedings of the 2005 International Conference on MEMS, NANO and Smart Systems,* ICMENS'05, 2005.

[65] T. Kawakubo, T. Nagano, M. Nishigaki, K. Abe, K. Itaya," RF-MEMS Tunable Capacitor with 3V Operation Using Folded Beam Piezoelectric Bimorph Actuator", *Journal of Microelectromechanical Systems*, vol. 15, no. 6, pp. 1759-1765, 2006.

[66] Y. Nemirovsky, O. Bochobza-Degani, "A Methodology and Model for the Pull-In Parameters of Electrostatic Actuators", *Journal of Microelectromechanical Systems*, vol. 10, no. 4, 2001.

[67] J. Cheng, J. Zhe and X. Wu," Analytical and finite element model pull-in study of rigid and deformable electrostatic microactuators", *J. Micromech. Microeng.*, vol. 14, pp. 57–68, 2004.

[68] E. S. Hung and S. D. Senturia, "Extending the Travel Range of Analog-Tuned Electrostatic Actuators", *Journal of Microelectromechanical Systems*, vol. 8, no. 4, pp. 497-505, 1999.

[69] M. S.-C. Lu and G. K. Fedder, "Closed-loop control of a parallel-plate microactuator beyond the pull-in limit," *in Tech. Dig. Solid-State Sensor, Actuator, and Microsystems Workshop*, pp. 255–258, June 2002.

[70] L. A. Rocha, E. Cretu, R. F. Wolffenbuttel, "Using Dynamic Voltage Drive in a Parallel-Plate Electrostatic Actuator for Full-Gap Travel Range and Positioning", *Journal of Microelectromechanical Systems*, vol. 15, no. 1, pp. 69-83, 2006.

[71] J. I. Seeger and B. E. Boser," Charge Control of Parallel-Plate, ElectrostaticActuators and the Tip-In Instability", *Journal of Microelectromechanical Systems*, vol. 12, no. 5, pp. 656-671, 2003.

[72] P. B. Chu and S. J. Pister," Analysis of closed-loop control of parallel-plate electrostatic microgrippers", *Robotics and Automation, 1994. Proceedings., 1994 IEEE International Conference*, vol. 1, pp. 820-825, 8-13 May 1994.

[73] W. C. Tang, "Electrostatic comb drive for resonant sensor and actuator applications", Ph.D dissertation, California Univ., CA, 1990.

[74] P. Cheung, R. Horowitz, R. Howe, "Design, Fabrication, Position Sensing, and Control of an Electrostatically-driven Polysilicon Microactuator", *IEEE Transactions on Magnetics*, vol. 32, no. 1, 1996.

[75] V. Jaecklin, C. Linder, N. F. de Rooij, J. Moret, R. Bischof, "Novel Polysilicon comb actuators for xy-stages", *Micro Electro Mechanical Systems*, Travemunede, Germany, 1992.

[76] R. Legtenberg, A. Groeneveld, M. Elwenspoek, "Comb-drive actuators for large displacements", *J. Micromech. Microeng.*, vol. 6, pp. 320–329, 1996.

[77] J. Grade, H. Jerman, T. Kenny, "Design of Large Deflection Electrostatic Actuators", *Journal of Microelectromechanical Systems*, vol. 12, no. 3, 2003.

[78] R. Syms, B. Hardcastle, R. Lawes, "Bulk micromachined silicon comb-drive electrostatic actuators with diode isolation", Sensors and Actuators A, vol. 63, pp. 61-67, 1997.

[79] J. D. Grade, H. Jerman, T. W. Kenny," Design of Large Deflection Electrostatic Actuators", *Journal of Microelectromechanical Systems*, vol. 12, no. 3, pp.335-343, 2003.

[80] Y. Zhao and T. Cui," Fabrication of high-aspect-ratio polymer-based electrostatic comb drives using the hot embossing technique", *J. Micromech. Microeng.*, vol. 13, pp. 430–435, 2003.

[81] R. Legtenberg, A. W. Groeneveld, M. Elwenspoek," Comb-drive actuators for large displacements", *J. Micromech. Microeng.*, vol. 6, pp. 320–329, 1996.

[82] W. Ye, S. Mukherjee, N. C. MacDonald," Optimal Shape Design of an Electrostatic CombDrive in Microelectromechanical Systems", *Journal of Microelectromechanical Systems*, vol. 7, no. 1, pp.16-26, 1998.

[83] T. Hirano, T. Furuhata, K. J. Gabriel, H. Fujita," Design, Fabrication, and Operation of Submicron Gap Comb-Drive Microactuators", *Journal of Microelectromechanical Systems*, vol. 1, no. 1, pp.52-59, 1992.

[84] C. Tsou, W. T. Lin, C. C. Fan, B. C. Chou," Self-Aligned Vertical Electrostatic Combdrives for Scanning Micromirrors", *18th IEEE Internation Conference on MEMS*, 2005.

[85] M. Sasaki, D. Briand, W. Noell, N. F. de Rooij, K. Hane," Three-Dimensional SOI-MEMS Constructed by Buckled Bridges and Vertical Comb Drive Actuator", *IEEE Journal of Selected Topics in Quantum Electronics*, vol. 10, no. 3, 2004.

[86] K.-H. Jeong and L. P. Lee," A novel fabrication method of a vertical comb drive using a single SOI wafer for optical MEMS applications", *TRANSDUCERS, Solid-State Sensors,*

Actuators and Microsystems, 12th International Conference, vol. 2, pp. 1462-1465, 2003.

[87] H. Xie and G. K. Fedder," Vertical comb-finger capacitive actuation and sensing for CMOS-MEMS", *Sensors and Actuators A*, vol. 95, pp.212-221, 2002.

[88] J. Kim, S. Park, D.Cho," A novel electrostatic vertical actuator fabricated in one homogeneous silicon wafer using extended SBM technology", *Sensors and Actuators A*, vol. 97-98, pp.653-658, 2002.

[89] S. Kwon, V. Milanovic,L. P. Lee," Large-Displacement Vertical Microlens Scanner With Low Driving Voltage", *IEEE Photonics Technology Letters*, vol. 14, no. 11, pp.1572-1574, 2002.

[90] J. C. Chiou, C. F. Kuo, and Y. J. Lin, "The Implementation of a Novel Magnified Cascade Configuration Using A Vertical Electrostatic Actuator", *Sixth IEEE Conference on Nanotechnoloy (IEEE-NANO 2006)*, vol. 2, pp. 913-916, 2006.

[91] C. Marxer, C. Thio, M.-A. Gretillat, N. F. de Rooij, R. Baettig, O. Anthamatten, B. Valk, P. Vogel," Vertical Mirrors Fabricated by Deep Reactive Ion Etching for Fiber-Optic Switching Applications", *Journal of Microelectromechanical Systems*, vol. 6, no. 3, pp.277-285, 1997.

[92] J. F. Saheb, J. F. Richard, R. Meingan, M. Sawan, Y. Savaria," System Integration of High Voltage Electrostatic MEMS Actuators", *3rd International IEEE-NEWCAS Conference*, 2005.

[93] M. J. Daneman, N. C. Tien, O. Solgaard, A. P. Pisano, K. Y. Lau, R. S. Mueller," Linear Microvibromotor for Positioning Optical Components", *Journal of Microelectromechanical Systems*, vol. 5, no. 3, pp.159-165, 1996.

[94] C. J. Kim, A. P. Pisano, R. S. Mueller, M. G. Lim," Polysilicon microgripper", *IEEE Solid-State Sensor and Actuator Workshop, 14th Technical Digest.*, pp. 48-51, 1990.

[95] K. Iwami, T. Ono, M. Esashi," Optical Near-Field Probe Integrated With Self-Aligned Bow-Tie Antenna and Electrostatic Actuator for Local Field Enhancement", *Journal of Microelectromechanical Systems*, vol. 15, no. 5, pp. 1201-1208, 2006.

[96] D. A. Horsley, N. Wongkomet, R. Horowitz, A. P. Pisano," Precision positioning using a microfabricated electrostatic actuator", *IEEE Transactions on Magnetics*, vol. 35, no. 2, pp. 993-999, 1999.

[97] W.-H. Juan and S. W. Pang," High-Aspect-Ratio Si Vertical Micromirror Arrays for Optical Switching", *Journal of Microelectromechanical Systems*, vol. 7, no. 2, pp. 207-213, 1998.

[98] T. Akiyama, K. Shono," A new step motion of polysilicon microstructures", *IEEE MEMS'93 Proceedings 'An Investigation of Micro Structures, Sensors, Actuators, Machines and Systems'*, pp. 272-277, 1993.

[99] T. Akiyama, K. Shono," Controlled stepwise motion in polysilicon microstructures", *Journal of Microelectromechanical Systems*, vol. 2, no. 3, pp. 106-110, 1993.

[100] P. Langlet, D. Collard, T. Akiyama, H. Fujita," A quantitative analysis of Scratch Drive Actuation for integrated X/Y motion system", *International Conference on Solid-State Sensors and Actuators - Transducers '97*, pp. 773-776, 1997.

[101] E. Quevy, L. Buchaillot, D. Collard," 3-D Self-Assembling and Actuation of Electrostatic Microstructures", *IEEE Transactions on Electron Devices*, vol. 48, no. 8, pp. 1833-1830, 2001.

[102] L. Y. Lin, J. L. Shen, S. S. Lee, and M. C. Wu," Surface-Micromachined Micro-XYZ Stages for Free-Space Microoptical Bench", *IEEE Photonics Technology Letters*, vol. 9, no. 3, pp. 345-347, 1997.

[103] S. Lee, E. Motamedi, and M. C. Wu," Surface-Micromachined Free-Space Fiber Optic Switches With Integrated Microactuators for Optical Fiber Communication Systems", *International Conference on Solid-State Sensors and Actuators - Transducers '97*, pp. 85-88, 1997.

[104] M. Föhse, T. Kohlmeier, and H. H. Gatzen, "Thinfilm technologies to fabricate a linear microactuator", *Sensors and Actuators A: Physical*, vol. 91, no. 1-2, pp. 145-149, 2001.

[105] J. Yao, S. Arney, N. MacDonald," Fabrication of High Frequency Two-Dimensional Nanoactuators for Scanned Probe Devices", *Journal of Microelectromechanical Systems*, vol. 1, no. 1, pp. 14-22, 1992.

[106] P.-F. Indermuehle, V. Jaecklin, J. Brugger, C. Linder, N. de Rooij, M. Binggeli," AFM imaging with an *xy*-micropositioner with integrated tip", *Sensors and Actuators A*, vol. 46-47, pp. 562-565, 1995.

[107] Y. Sun, D. Piyabongkarn, A. Sezen, B. J. Nelson, R. Rajamani," A high-aspect-ratio two-axis electrostatic microactuator with extended travel range", *Sensors and Actuators A*, vol. 102, pp. 49-60, 2002.

[108] C.-H. Kim and Y.-K. Kim," Micro XY-stage using silicon on a glass substrate", *J. Micromech. Microeng.*, vol. 12, pp. 103–107, 2002.

[109] L.Chu and Y. Gianchandani," A micromachined 2D positioner with electrothermal actuation and sub-nanometer capacitive sensing", *J. Micromech. Microeng.*, vol. 13, pp. 279–285, 2003.

[110] T. Fukuda and T. Tanaka," Micro electrostatic actuator with three degrees of freedom", *Proceedings, An Investigation of Micro Structures, Sensors, Actuators, Machines and Robots, IEEE MEMS 1990,* pp.153-158, 1990.

[111] Y. Xu and N. C. MacDonald," Integrated micro-scanning tunneling microscope", *Applied Physics Letter*, vol. 67, pp. 2305-2307, 1995.

[112] T. Zhou, P. Wright, J. Crawford, G. Mckinnon, Y. Zhang," MEMS 3D Optical Mirror/ Scanner", *Proceedings of the International Conference on MEMS, NANO and Smart Systems (IEEE ICMENS'03)*, pp. 1-5, 2003.

[113] Y. Ando," Development of three-dimensional electrostatic stages for scanning probe microscope", *Sensors and Actuators A*, vol. 114, no. 2-3, pp. 285-291, 2004.

[114] H. C. Chang, J. Tsai, H. C. Tsai, W. Fang," Design, fabrication, and testing of a 3-DOF HARM micromanipulator on (111) silicon substrate", *Sensors and Actuators A*, vol. 125, pp. 438-445, 2006.

[115] T. E. G. Niblock, *Mirco Scanning Probe*, Ph.D. thesis, University of Southampton, 2001.

[116] H. Sehr, A. G. R. Evans, A. Brunnschweiler, G. J. Ensell, and M. Kraft, "A 3-dimensional actuator based on a novel combination of thermally actuated planar and vertical bimorphs", *International Conference on New Actuators*, ACTUATOR, Bremen, Germany, 2000.

[117] D. Zhang, C. Chang, T. Ono, M. Esashi," A piezodriven XY-microstage for multiprobe nanorecording", *Sensors and Actuators A*, vol. 108, pp. 230-233, 2003.

[118] D. Zhang, T. Ono, M. Esashi," Piezoactuator-intergrated monolithic microstage with six degrees of freedom", *Sensors and Actuators A*, vol. 122, pp. 301-306, 2005.

[119] C.J. Vale, B.V. Hall, D.C. Lau, M.P.A. Jones, J.A. Retter and E.A. Hinds, "Atom Chips", *Europhysics News*, vol. 33, no.6, 2002.

[120] R. Folman, P. Krueger, J. Schmiedmayer, J. Denschlag and C. Henkel, "Microscopic atom optics", *Advances in Atomic, Molecular and Optical Physics*, Vol. 48, pp.263, 2002.

[121] E. Koukharenko, Z. Moktadir, D. Bagnall, M.Kraft, C. Vale, M. Jones, E. Hinds, "Microfabrication of gold wires for atom guides", *European Conference on Solid-State Transducers*, Eurosenors XVI, Portugal, 2003.

[122] G. Lewis, Z. Moktadir, C. O. Gollasch, M. Kraft, M. Trupke, S. Eriksson, E. A. Hinds, "Fabrication of gold wires for atom chips by electrochemical deposition: A comparative study", *16th MicroMechanics Europe Workshop 2005* , Schweden, Stockholm, 2005.

[123] Z. Moktadir, E. Koukharenko, M. Kraft, D.M. Bagnall, M. Jones, H. Powell and E. Hinds, "Etching techniques for the realisation optical micro-cavities on silicon for atom traps", *14th Micromechanics Europe Workshop*, MME 2003

[124] J. A. Wright, S. T.-Lucic, Y. C. Tai, W. R. McGrath, B. Bumble, and H. LeDuc, "Integrated Silicon Micromachined Waveguide Circuits For Submillimeter Wave Applications," *Symposium Proceedings: Sixth International Symposium on Space Terahertz Technology*, Pasadena, CA, pp. 387-396, March 1995

[125] Y. Uenishi, M. Tsugai, M. Mehregany, "Micro-opto-mechanical devices fabricated by anisotropic etching of (110) silicon", *Micro Electro Mechanical Systems, 1994, MEMS '94, Proceedings*, IEEE Workshop, pp. 319-324, Jan. 1994

[126] Z. Moktadir, M. P. Bruijn, R. Wiegerink, M. Elwenspoek, "Limitations of heat conductivity in cryogenic sensors due to surface roughness", *Proc. IEEE Sensors 2002*, paper 37.3, Orlando, June 11-14, 2002

[127] M. Vangbo, Ylva Baeckbund, "Precise mask alignment to the crystallographic orientation of silicon wafers using wet anisotropic etching", *J. Micromech. Microeng.*, vol. 6, pp. 279-284, June 1996.

[128] W. H. Chang, Y. C. Huang, "A new pre-etching pattern to determine <110> crystallographic orientation on both (100) and (110) silicon wafers", *Journal of Microsystem Technologies*, vol. 11, pp. 117-128, 2005.

[129] M. Trupke, E. A. Hinds, S. Eriksson, E. A. Curtis, Z. Moktadir, E. Kukharenka, M. Kraft, "Microfabricated high-finesse optical cavity with open access and small volume", *Applied Physics Letters*, vol. 87, A211106, 2005.

[130] B. Saleh and M. Teich, *Fundamentals of Photonics*, Wiley-Interscience, New York, 1991.

[131] S. Eriksson, M. Trupke, H. F. Powell, D. Sahagun, C.D.J. Sinclair, E. A. Curtis, B. E. Sauer, E. A. Hinds, Z. Moktadir, C. O. Gollasch, M. Kraft, "Integrated optical components on atom chips", *European Physics Journal D*, vol. 35, pp. 135-139, 2005.

[132] G Wu, A. R. Mirza, S. K. Gamage, L. Ukrainczyk, N. Shashidhar, G. Wruck, M. Ruda, "Design and use of compact lensed fibres for low cost packaging of optical MEMS components", *J. Micromech. Microeng.*, vol. 14, pp. 1367-1375, 2004.

[133] Y. Yunhae, C. Young, H. F. Taylor, "A high-speed tunable filter using a concave fiber mirror", *Optical Fiber Communication Conference 2005*, Technical Digest OFC/ NFOEC, vol. 3, March 2005.

[134] LG Electronics Institute of Technology (www.misob.lg-elite.com/tech_repo/SiOB.pdf), "A Silicon Optical Bench for passive alignment of fiber-optic devices", 2004.

[135] J.M. Gere and S.P. Timoshenko, *Mechanics of Materials*, Stanley Thorne, Cheltenham, 4 edition, 1999

[136] G. K. Fedder, "Simulations of Microelectromechanical Systems", Ph.D dissertation, California Univ., CA, 1994

[137] H.A. Rouabah, C.O. Gollasch and M. Kraft, "Design Optimisation of an Electrostatic MEMS Actuator with Low Spring Constant for an 'Atom Chip'" , *Technical Proceedings of the 2005 Nanotechnology Conference and Trade Show*, vol. 3, pp. 489-492, Anaheim, USA 2005.

[138] G. Zhou and P. Dowd, "Tilted folded-beam suspension for extending the stable travel range of comb-drive actuators" , *J. Micromech. Microeng.*, vol. 13, pp. 178-183, December 2003.

[139] A. Kuhn and G. Rempe, "Experimental Quantum Computation and Information", Edited by F. de Martini and C. Monroe, *Proc. Int. School of Physics Enrico Fermi, Course CXLVIII*, pp. 37-66, IOS Press, Amsterdam, 2002.

[140] Elvenspoek book from KLUNICourse(p83)

[141] C. Jia, W. Dong, C. Liu, X. Zhang, J. Zhou, Z. Zhong, H. Xue, H. Zang, B. Xu, W. Chen, "Convex corners undercutting and rhombus compensation in KOH with and without IPA solution on (110) silicon", *Journal Microelectronics*, vol. 37, pp. 1297-1301, 2006.

[142] B. Saleh and M. Teich, Fundamentals of Photonics (Wiley-Interscience, 1991).

[143] A. L. Barabasi and H. E. Stanly, "Fractal concept in surface growth" (Cambridge University Press, 1995).

[144] D. C. S. Bien, P. V. Rainey, S. J. N. Mitchell and H. S. Gamble, "Characterisation of masking materials for deep glass micromachining", *Proceedings of 13th MicroMechanics Europe Workshop 2002 (MME 2002)*, pp. 103-106, Sinaia, Romania, Oct. 6-8, 2002.

[145] X. Li, T. Abe, Y. Liu and M. Esashi, "Fabrication of high-density electrical feed-throughs by deep-reactive-ion etching of Pyrex glass", *Journal of Microelectromechanical Systems*, vol. 11, pp. 625-630, 2002.

[146] M. Stjernström and J. Roeraade, "Method for fabrication of microfluidic system in glass", *Journal of Micromechanics and Microengineering*, vol. 8, pp. 33-38, 1998.

[147] M. Bu, T. Melvin, G. J. Ensell, J. S. Wilkinson, A. G. R. Evans, "A new masking technology for deep glass etching and its microfluidic application", *Sensors and Actuators A*, vol. xx , pp. xx, 2004.

[148] T. Corman, P. Enoksson and G. Stemme, "Deep wet etching of borosilicate glass using an anodically bonded silicon substrate as mask", *Journal of Micromechanics and Microengineering*, vol. 8, pp. 84-87, 1998.

[149] X. Li, T. Abe and M. Esashi, "Deep reactive ion etching of Pyrex glass using SF6 plasma", *Sensors and Actuators A*, vol. 87, pp. 139-145, 2001.

[150] M. Bu, "Design and Fabrication of a Microfluidic Device for Polymerase Chain Reaction Application", *PhD Thesis*, University of Southampton, 2004.

[151] M. Chabloz, J. Jiao, Y. Yoshida, T. Matsuura, K. Tsutsumi, "A method to evade microloading effect in deep reactive ion etching for anodically bonded glass-silicon structures", *MEMS*, Miyazaki, Japan, 2000.

[152] O. I. B. Jena GmbH, Göschwitzer Str 22 Jena D-07745, Germany.

[153] Tanner EDA 2650 East Foothill Boulevard Pasadena CA 91107, "L-edit pro version 11".